Quantum Kinetics of charge carriers in quantum dots: applications to slow light and light amplification

Houmark-Nielsen, Jakob

Publication date:
2010

Document Version
Publisher's PDF, also known as Version of record

Ph.D. Thesis

Coherence Effects of Interacting Carriers in Self-Assembled Quantum Dots

Jakob Houmark

Supervisors: Antti-Pekka Jauho, Torben R. Nielsen, and Jesper Mørk

DTU-Nanotech, Department of Micro- and Nanotechnology
Technical University of Denmark

November 2009

Abstract

This work is a theoretical study of the quantum coherence effect Electromagnetically Induced Transparency (EIT) in self-assembled quantum dots. Quantum dots receive much of attention due to their relevance for optoelectronic devices such as lasers and optical amplifiers. Also, quantum dots are a promising candidate for practical exploitation of slow light effects based on EIT. Self-assembled quantum dots are semiconductor heterostructures and many-body effects such as phonon and Coulomb interactions influence their optical properties. The impact of Coulomb correlations is incorporated using a cluster expansion formalism truncated at Hartree-Fock level; higher order corrections and other many-body effects, such as coupling to phonons, are taken into account phenomenologically via the relaxation time approximation. The heterostructure under consideration consists of InAs quantum dots grown on top of a wetting layer sandwiched between two slabs of GaAs. The steady state and transient EIT properties of cone shaped quantum dots are examined using three different coupling-probe schemes (Ladder, V and Λ, respectively). We find that for all schemes many-body interactions have an important impact on the EIT properties. Results obtained in steady state suggest the V-type scheme as the most preferable for EIT operation. This result is quite general and could act as a pointer for experimental realization of EIT mediated slow light. The transient properties show interesting effects such as an increased robustness for quantum coherence effects and gain at the probe resonance frequency.

We also study the size and geometry dependence of the optical properties of semiconductor quantum dots using multiband $k \cdot p$ theory incorporating strain. Also here the V-type EIT scheme is found to be most favorable, and we identify an optimal height and radius of the quantum dot for efficient EIT operation. Furthermore we find that, due to the separation of the heavy and light holes, band mixing effects are relatively small. As a consequence we find a qualitative agreement between the optical transition strengths calculated using a single-band model and an eight-band model. However, a few exceptions are found, and these are relevant for the choice of EIT scheme.

Resumé

Dette arbejde er et teoretisk studie af kvantekohærenseffekten Elektromagnetisk Induceret Transparens (EIT) i selvsamlende kvantepunkter. Kvantepunkter er genstand for megen opmærksomhed grundet deres relevans for optoelektroniske komponenter såsom lasere og optiske forstærkere. De er også lovende kandidater til praktisk udnyttelse af langsomt lys baseret på EIT. Selvsamlende kvantepunkter er halvleder heterostrukturer, og mangelegemeeffekter såsom fonon og Coulomb vekselvirkninger har indflydelse på deres optiske egenskaber. Indflydelsen af Coulomb korrelationer er indkorporeret ved at bruge en klynge ekspansionsformalisme trunkeret på Hartree-Fock niveau; højere ordens korrektioner og andre mangelegemeeffekter, som f.eks. kobling til fononer, tages i betragtning fænomenologisk via relaxation time approksimationen. Den pågældende heterostruktur, består af InAs dyrket på et wetting lag placeret imellem to blokke af GaAs. Steady state og transiente EIT egenskaber ved kegleformede kvantepunkter undersøges ved at anvende tre forskellige pumpe-probe skemaer (Stige, V og Λ). Det viser sig, at mangelegemeeffekter har en vigtig indflydelse på EIT egenskaberne ved alle skemaerne. De opnåede resultater i steady state peger i retning af, at V skemaet er det mest fordelagtige i forbindelse med EIT. Dette resultat er forholdsvist generelt og kan agere som indikator for den eksperimentelle realisering af EIT medieret langsomt lys. De transiente egenskaber viser interessante effekter som for eksempel en forøget robusthed i forbindelse med kvantekohærenseffekter samt gain ved probe resonansfrekvensen.

Kvanterpunkters optiske egenskabers afhængighed af størrelse og geometri bliver også undersøgt. Vi bruger en multibånd $k \cdot p$ teori, som også inkorporerer pres. Også her viser V skemaet sig at være mest favorabelt, og vi identificerer en optimal højde og radius af kvantepunktet. Endvidere er vi nået frem til, at på grund af separationen af tunge og lette huller, er båndmixingeffekter relativt små. Som en konsekvens heraf finder vi en kvalitativ overensstemmelse mellem de optiske overgangsstyrker beregnet med henholdsvis en et-bånds- og en ottebånds model. Dog findes nogle få undtagelser, og disse er relevante for valget af EIT-skema.

Preface

This thesis is submitted in candidacy for the Ph.D degree from the Technical University of Denmark (DTU). The work was carried out in the period from May 2006 to October 2009. The project was supervised by Antti-Pekka Jauho DTU Nanotech, Department of Micro- and Nanotechnology and co-supervised by Jesper Mørk, and Torben Roland Nielsen, DTU Fotonik, Department of Photonics Engineering, DTU, Denmark.

I would like to thank my supervisors Antti-Pekka Jauho, Jesper Mørk and Torben R. Nielsen for their help and support during the project. Also I would like to thank Morten Willatzen, Benny Lassen and Daniele Barettin of the University of southern Denmark for fruitful collaboration within the field of quantum dot modeling and their hospitality during visits. My sincere gratitude goes to Per K. Nielsen for many enlightening discussions along the way as well as for proofreading this thesis.

Last but not least I would like to thank my wife Helle and my son Eskild for making the long days seem a little shorter.

List of publications

Journal Articles

- [I] **J. Houmark**, A.-P. Jauho, T. R. Nielsen and J. Mørk
  Influence of many-particle interactions on slow light phenomena in quantum dots
  J. Phys.: Conf. Ser. **107** 012005 (2008).
- [II] **J. Houmark**, T. R. Nielsen, J. Mørk and A.-P. Jauho
  Comparison of electromagnetically induced transparency schemes in semiconductor quantum dot structures: Impact of many-body interactions
  Phys. Rev. B **79**, 115420 (2009).
- [III] D. Barettin, **J. Houmark**, B. Lassen, M. Willatzen, T. R. Nielsen, J. Mørk and A.-P. Jauho
  Optical properties and optimization of electromagnetically induced transparency in strained InAs/GaAs quantum dot structures
  To appear in Phys. Rev. B **80**, ? (2009).

Conference Contributions

- **J. Houmark**, A.-P. Jauho, T. R. Nielsen and J. Mørk
  Influence of Coulomb interactions on quantum coherence in quantum dots (poster)
  Physics-based mathematical models of low-dimensional semiconductor nanostructures: Analysis and computation, 2007, Banff, Canada.
- **J. Houmark**, A.-P. Jauho, T. R. Nielsen and J. Mørk
  Comparison of EIT schemes in semiconductor quantum dots (poster)
  Slow and Fast Light (SL), 2008, Boston, Massachusetts, USA.
- **J. Houmark**, D. Barettin, B. Lassen, M. Willatzen, T. R. Nielsen, J. Mørk and A.-P. Jauho
  Analysis of quantum dot EIT based on 8-band $k \cdot p$ theory (poster)
  International Conference on the Physics of Semiconductors (ICPS-29), 2008, Rio de Janeiro, Brazil.

Contents

1 Introduction **1**
- 1.1 Electromagnetically Induced Transparency . . . 1
  - 1.1.1 EIT applications . . . 3
- 1.2 Semiconductor quantum dots . . . 5
  - 1.2.1 Quantum dot growth . . . 6
- 1.3 Outline . . . 8

2 Microscopic theory **9**
- 2.1 Observables in quantum mechanics . . . 9
- 2.2 Hamiltonian . . . 10
- 2.3 Cluster expansion and the Hartree-Fock approximation . . . 12
  - 2.3.1 Coherent evolution . . . 14
  - 2.3.2 Scattering terms . . . 16

3 Macroscopic theory **23**
- 3.1 Maxwell-Bloch equations . . . 23
- 3.2 Limiting cases . . . 25
- 3.3 System in equilibrium . . . 28
- 3.4 System in non-equilibrium . . . 31
  - 3.4.1 Transient system response . . . 32
  - 3.4.2 Steady state system response . . . 34

4 EIT - atomic approach **37**
- 4.1 Semi-classical atomic, continuous wave approach . . . 37
- 4.2 EIT features . . . 42
  - 4.2.1 γ_{31} detrimental to EIT . . . 43
  - 4.2.2 Slowdown features . . . 44
  - 4.2.3 Inhomogeneous broadening effects . . . 46

5 QD Modeling **55**
- 5.1 Quantum dot model . . . 55
  - 5.1.1 Single band effective mass Schrödinger equation . . . 56
- 5.2 Single particle properties . . . 58
  - 5.2.1 Energy spectrum . . . 58
  - 5.2.2 Dipole matrix elements . . . 60
  - 5.2.3 Inter-band dipole moment . . . 60

5.2.4 Intra-band dipole moment . . . 63
5.3 Coulomb matrix elements . . . 65
5.3.1 Hartree-Fock renormalization . . . 67
5.4 Multi-band calculations . . . 68
5.4.1 Dipole moments: Size and geometry dependence . . . 70
5.4.2 EIT properties . . . 75

6 EIT - Coulomb effects in QDs 79
6.1 EIT-schemes . . . 79
6.2 Probe duration dependency . . . 82
6.3 Steady state EIT . . . 83
6.3.1 Scheme comparison . . . 84
6.4 Transient EIT . . . 90
6.4.1 Transient response . . . 90
6.4.2 Explaining transient "wiggles" . . . 91
6.4.3 Physical understanding/use of transient spectra . . . 97
6.4.4 Coupling duration variation . . . 100

7 Conclusion and Outlook 107

A Hartree renormalization 115

B Equations of motion e-h picture 119
B.1 Hamiltonian . . . 120
B.2 General approach . . . 120
B.3 Coherences . . . 122
B.3.1 Interband polarization: $P_{\alpha,\beta}$ . . . 122
B.3.2 Intraband hole-hole polarization: $\tilde{P}_{\beta,\kappa}$ . . . 128
B.3.3 Intraband electron-electron polarization: $\bar{P}_{\alpha,\gamma}$ . . . 136
B.4 Populations . . . 142
B.4.1 Electron: n^e_α . . . 142
B.4.2 Hole: n^h_β . . . 146

C Material parameters 153
C.1 InAs/GaAs . . . 153
C.2 QD and QD array parameters . . . 153

D Computational parameters 155

Chapter 1

Introduction

This thesis evolves around the study of the quantum coherence phenomenon Electromagnetically Induced Transparency (EIT) in semiconductor quantum dots. The EIT effect allows one the possibility of manipulating light pulses, where semiconductor quantum dots offers a compact, convenient and efficient medium for doing so. This chapter contains a brief review of the EIT principle and its applications as well as an introduction to semiconductor quantum dots.

1.1 Electromagnetically Induced Transparency

Electromagnetically induced transparency is an effect for making an otherwise optically thick medium transparent to a weak (probe/signal) laser field by applying another strong (coupling) field. Equivalently one could say that EIT is the cancelation of absorption of a weak field tuned to resonance of a transition by coupling it coherently to another transition by means of a strong also resonant laser field.

Fano interference

The foundations of EIT were laid in an experiment carried out in 1961 by U. Fano [1], which was the first coherence interference experiment. An illustration of the experiment is shown in Fig. 1.1. Excitation takes place between some lower state and a continuum ionizing state ($|i\rangle$). It also takes place between the lower state and an autoionized state ($|a\rangle$). Once in the autoionizing state the atom relaxes to the ionizing state. Hence there are two routes to the final state. Fano found that interference between these two paths lead to asymmetric peaks in the excitation spectra and that the "transition probability vanishes on one side of the resonance", thus signifying that coherence effects had canceled the absorption.

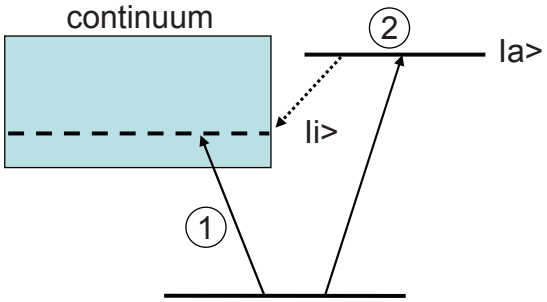

***Figure 1.1**: Fano Interference: Two excitation paths to the same ionizing state ($|i\rangle$) within a continuum leads to a cancelation of absorption due to destructive interference between the two paths.*

Physics of EIT

The concept of Electromagnetic Induced Transparency was first introduced in 1990 by Harris, Field, and Imamoglu [2]. EIT occurs in multilevel systems interacting with coherent electromagnetic fields. The first experimental realization was performed in Sr vapor using pulsed lasers in 1991 [3]. The simplest system which display the EIT effect are certain three level systems shown in Fig. 1.2. We can describe EIT in terms of an interference effect between two routes to

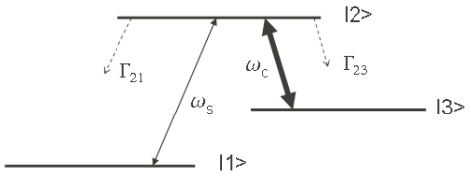

(a) Λ – *scheme*

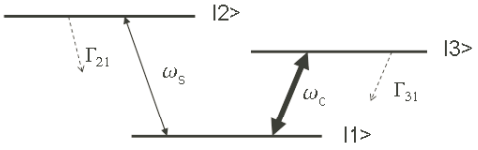

(b) V-scheme

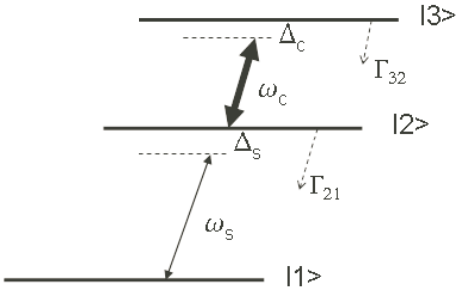

(c) Ladder-scheme

***Figure 1.2**: Configurations displaying EIT. ω_s,ω_c and Δ_s,Δ_c refer to the frequency and detuning of the signal/probe and the coupling field, respectively. The detuning is only displayed in case of the Ladder scheme.*

excitation of the upper probe level (level $|2\rangle$ in Fig. 1.2). The probe can excite population by the direct $|1\rangle - |2\rangle$ route. Alternatively the population can reach $|2\rangle$ via the $|1\rangle - |2\rangle - |3\rangle - |2\rangle$ pathway (or by higher order variants) in

which the population is moved between $|2\rangle$ and $|3\rangle$ by the coupling field. Since the coupling is very strong the two pathways are equally probable, and due to Fano-like destructive interference, the direct probe route is canceled or reduced. Under this situation, we say an initial opaque $|1\rangle - |2\rangle$ transition has been made transparent to a probe laser beam by the presence of another strong coupling laser. This description of EIT is in the so called bare-state picture. We can also view the EIT process through the dressed state picture. In the dressed state picture the intense coupling field dresses the system and forms a coherent superposition of the two upper states (see Fig. 1.3) resembling an Autler-Townes splitting [4] of the $|2\rangle$ level. The transition probability amplitude $|1\rangle - |2\rangle$ in the bare picture becomes a sum of the amplitudes $|1\rangle - |2d\rangle$ and $|1\rangle - |3d\rangle$. Since the latter two transitions both couple to the same final state they can interfere destructively via the Fano effect.

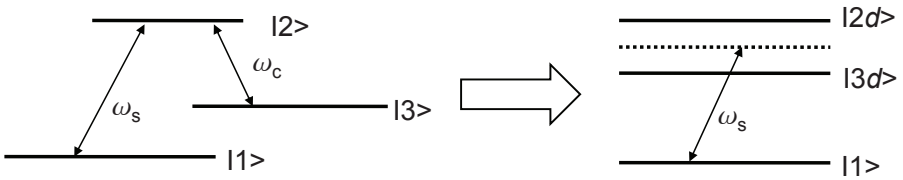

Figure 1.3: *Λ-scheme in the dressed state picture. The intense coupling beam creates a doublet of states labeled $|2d\rangle$ and $|3d\rangle$, consisting of a coherent superposition of the bare states $|2\rangle$ and $|3\rangle$.*

1.1.1 EIT applications

The reduction in absorption is accompanied by a rapid change of the refractive index (see Fig. 1.4) and a subsequent modification of the group velocity of a propagating light beam. The refractive index change accompanied by low absorption can be used in nonlinear optical processes, like wave mixing where new frequencies are generated at other frequencies than those of the applied laser fields. Usually the generated fields suffer from reabsorption and are thus very small. EIT can provide transitions that do not reabsorb. For instance Hahn *et al.* [5] utilized the EIT effect to generate sum-frequency radiation in atomic Zn and Hakuta *et al.* [6] used a dc EIT effect to realize second harmonic generation in atomic H. The concept of lasing without inversion (LWI) in three -and multi level systems [7, 8] has its roots in the EIT effect. A laser traditionally requires a population inversion due to the fact that the lasing medium experiences stimulated absorption as well as emission. However, the EIT effect allows stimulated absorption of radiation from lower states to be reduced more effectively compared with a competing stimulated emission of radiation from upper states, thus realizing laser actions without population inversion. LWI has been experimentally demonstrated in atomic gases, e.g. Rb [9] and Cs [10]. For a thorough review of the LWI concept we point the reader to [11].

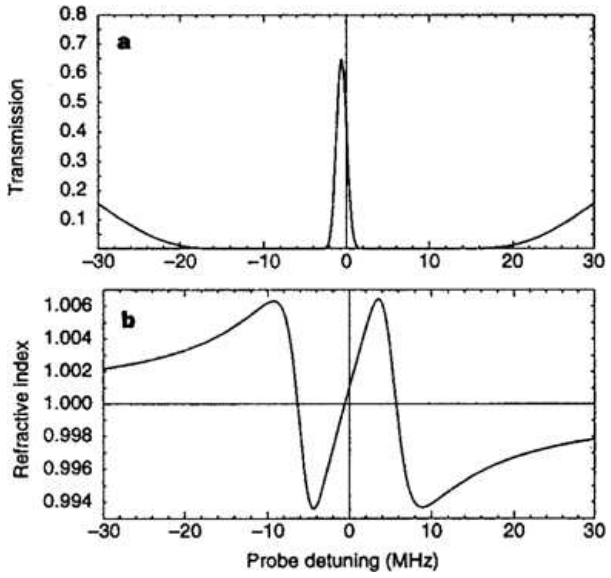

***Figure 1.4**: Transmission and refractive index in the presence of the EIT effect. The figure is taken from [12].*

Slow light via EIT

The modification in group velocity can be utilized to slow down the speed of the probe field. Experiments performed in ultra-cold Na vapor showed that the speed of light could be reduced to that of a cyclist [12] and even completely stopped [13]. The possibility of controlling the speed of light open up a plethora of potential applications for both studying fundamental science as well as direct application. Slow light has been suggested for creating an optical black hole [14], an analogue to the real black hole so that one could study gravitational phenomena from the comfort of one's own laboratory. EIT has also been proposed to serve in quantum entanglement experiments [15] and other studies of fundamental quantum processes [16].

On the application side an opto-electronic device capable of controlling the speed of light could find many uses. One, highly relevant for the present work, is the potential ability to store and release light pulses at will. This could be used in an all-optical buffer [17, 18], a critically missing element in realizing all-optical networks. Also, an adjustable delay or phase-shifter would enable a technology jump within various kinds of microwave signal processing, e.g., optically fed phased-array antennas [19] as well as optical clock distribution on high-speed electronic chips. A reduced speed of light also implies higher local intensity and within sensing and measurement technology one aims to apply this effect for realizing engineered media with increased sensitivity towards an optical beam or reduced device size. Common for these applications is that they are only relevant if they can be realized at room temperature and brought out into the field. Ultra-cold atomic clouds can hardly be considered to satisfy those demands. Solid state implementations, such as semiconductor heterostructures

are on the other hand highly relevant in this context, as they provide possibilities for cheap production and monolithic integration with existing technology.

The first experimental realization of EIT in solids was done using ruby [20], for quantum wells several reports have followed [21–24], whereas for quantum dots, to our knowledge, only a single report exists [25]. Common for recent semiconductor experiments is that they do not rely on "classical" EIT schemes, meaning that they have not been based on the interference between the bare states of e.g. the quantum dot, but rather on virtual transitions, depending on the existence of an exciton complex. However, these experiments are still well described using the "classical" EIT theory and this work concerns the more traditional EIT schemes.

1.2 Semiconductor quantum dots

A key feature in realizing a slow-light medium using the physical effect of EIT is the availability of a medium with discrete resonances. This is naturally achieved in atoms due to the discrete orbital energies, while the level structure of semiconductors is of a continuous nature. However, quantum dots (QDs) represent a way of realizing discrete resonances in a semiconductor medium. Semiconductor quantum dots are like atoms in many aspects. Where quantum wells and quantum wires represent confinement in one and two dimensions, quantum dots represent the ultimate three dimensional confinement. QD structures consists of thousands of atoms in which the density of states is a set of delta functions. The resulting electron spectrum is therefore discrete and depends on the material system, shape and size of the QD. The ability to tailor the electronic and optical properties is at the center of QD research. As is seen in Fig. 1.5 QD emitters can e.g. be made to cover the whole visible spectrum.

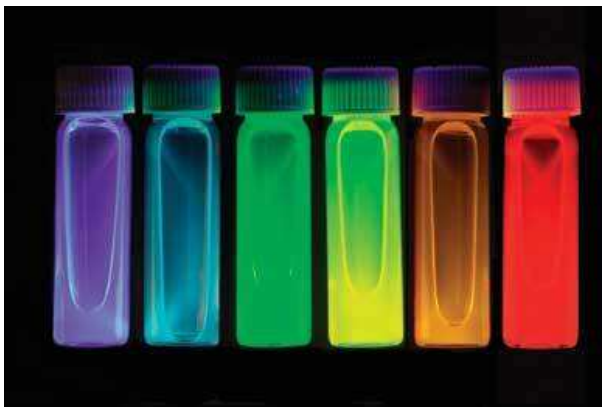

***Figure 1.5**: Vials of fluorescent CdSe nanocrystal QDs suspended in hexane. The emission wavelength depends on the size of the QD, which ranges from* 2 nm *(blue) to* 8 nm *(red).*

1.2.1 Quantum dot growth

Various different techniques can be used to generate the three dimensional confinement in semiconductor materials. Among the dominating methods are: Chemical synthesis of nanocrystal QDs [26], lithographic definition and etching [27] used in conjunction with metallic gate electrodes as method of confinement, and last but not least, epitaxially grown (also known as self assembled) QDs. The latter technique is based on the principle of embedding a low bandgap material within a material of higher bandgap. Through band bending effects this creates a confining potential for both electrons and holes, allowing spatially localized states inside the QDs. In this work we consider self-assembled QDs based on the Stranski-Krastanow (S-K) growth technique [28,29]. The S-K growth mode is based on either molecular beam epitaxy (MBE) or metal organic vapor phase epitaxy (MOVPE). The first step consists of placing a layer of high bandgap material (GaAs) on a substrate. In the second step a very thin layer (termed the epitaxy layer), usually only a few monolayers thick, of low bandgap semiconductor (InAs) is evaporated onto the the first. The InAs has a larger lattice constant than the GaAs and therefore the epitaxy layer is grown under compressive strain with a subsequent increase in surface energy. The addition of more InAs material results in a metastable state consisting of several mono-layers. At a certain critical thickness the epitaxial layer is able to minimize the surface energy by relaxing into a thin 2d layer and 3d islands on top. These islands are denoted self-assembled QDs and the thin layer below them is denoted the wetting layer (WL). This step of the process is illustrated in Fig. 1.6, where a scanning electron microscope image shows an isolated InAs dot and an atomic force micrograph displays the random distribution of QDs of varying size on the WL. The last step of the process consists of evaporating a final layer of GaAs on top embedding the InAs structure. QD structures of this kind have

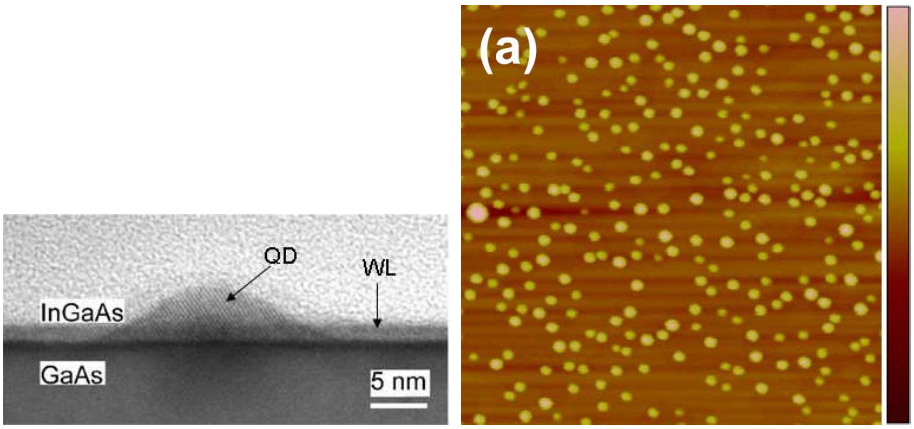

***Figure 1.6**: Left: Transmission electron microscope image of a single InGaAs/GaAs QD. Taken from [30]. Right: Topographic atomic force micrograph depicting a surface area of* 1×1 μm *of uncapped QDs. The color scale runs from 0 to 20 nm. Taken from [31].*

been studied for the fabrication of laser devices working in the telecom relevant

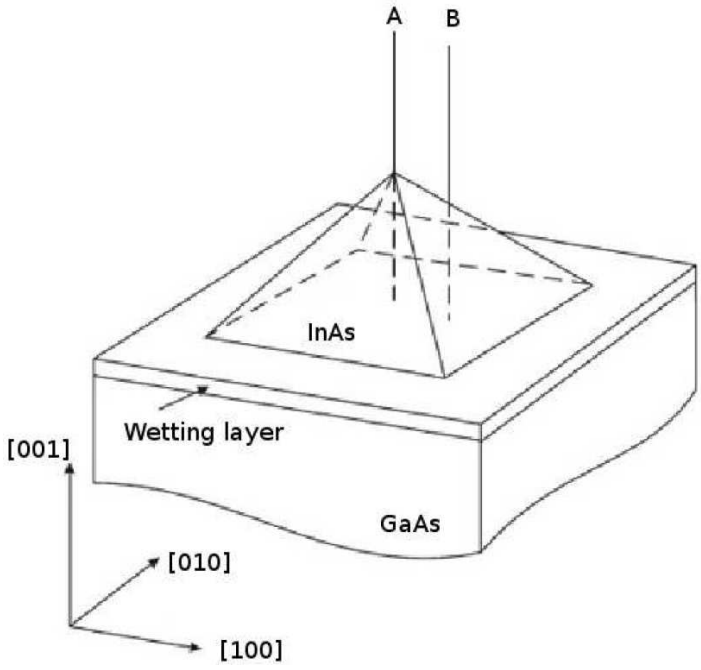

***Figure 1.7**: Schematic geometry of InAs/GaAs quantum dots. Figure is taken from [37].*

$1.3 - 1.55$ μm wavelength range, and interesting results have been achieved using active regions based on the arrays of quantum dots, showing superior laser characteristics such as ultra-low threshold current densities [32, 33], ultrahigh temperature stability [34], very high differential efficiency [35], small α-factor and chirp [36].

Depending on growth conditions, such as temperature and crystallographic orientation of the substrate, the S-K grown QDs can be manipulated in geometrical shape, size and density. Various different geometries has been realized; from lens-shaped QDs over spherical and ellipsoidal dots to pyramidal structures, depending on growth conditions. In Fig. 1.7 we show a schematic illustration of a pyramidal shaped QD. However, the self-assembly method has a drawback. Fluctuation in size, geometry and/or chemical composition leads to inhomogeneity of the dot species resulting in broadening of the optical spectrum of a dot ensemble. The inhomogeneous broadening plays a detrimental role in respect to their use as active medium in an EIT setup. It is viewed as the major obstacle which has to be overcome before a QD slow light device based on EIT can be fabricated.

The view of quantum dots as artificial atoms reflects the historical development of the field and explains the extensive application of atomic models [38, 39] used in relation with QDs and in particular EIT [40–43]. Quantum dots are semiconductor structures and many-body effects such as phonon and Coulomb interactions influence their optical properties in a way the atomic models cannot account for. Present theoretical work in this area [44–47] has been touching

upon the transient EIT properties, but the effort has been far from exhaustive. It is the aim of this thesis to abridge this gap and investigate the properties of various EIT schemes that can be realized in QDs in the presence of many-body interactions in both transient and steady state.

1.3 Outline

The remainder of this thesis is organized as follows. The second part reviews the theoretical background for studying quantum coherence in semiconductor structures. First we consider the microscopic theory which leads to the semiconductor Bloch equations (SBE). The microscopic expectation values enter a macroscopic description of laser pulse propagation in the QD system. How to extract propagation characteristics from a microscopic calculation is the topic of the third chapter. We then review the atomic approach to EIT in which the quantum dot is treated effectively as a noninteracting three level atom. This treatment serves as the background for understanding the more complex many-body results. Chapter five is devoted to establishing the QD model and furthermore explores the impact of band mixing and strain on the QD optical properties. Paper III is based on the last part of this chapter. The sixth chapter contains results from both the steady state and transient EIT regimes that can be addressed depending on the duration of the coupling field. Paper I and II are based on the steady state results presented in this chapter, whereas for the transient results a paper is being prepared. The final chapter contains the summary and an outlook.

Chapter 2

Microscopic theory

We here present the theoretical background needed for studying quantum coherence phenomena in semiconductors. The method applied is known as the cluster expansion scheme (for thorough review see e.g. [48]), which is based on single-time density matrices.

2.1 Observables in quantum mechanics

Consider a single-particle operator O, describing some observable quantity of the semiconductor system. In second quantization this operator is written as

$$O = \sum_{ij} O_{ij} a_i^\dagger a_j \,, \tag{2.1.1}$$

where O_{ij} is the single-particle matrix element and a can be either a fermion or boson operator. What is measured in experiments is the expectation value of O, defined by tracing[1] over the density operator of the system ρ_0

$$\begin{aligned} \langle O(t) \rangle &= \mathrm{Tr}[O\rho_0(t)] = \mathrm{Tr}[Ou(t,t_0)\rho_0(t_0)u^\dagger(t,t_0)] \\ &= \mathrm{Tr}[u^\dagger(t,t_0)Ou(t,t_0)\rho_0(t_0)] = \mathrm{Tr}[O(t)\rho_0(t_0)]. \end{aligned} \tag{2.1.2}$$

In the above $u(t,t_0)$ is a general time propagation operator, that propagates a state from t_0 to t. It is possible to focus on a single subset of the system (in this case the carriers) and trace out all other degrees of freedom [49]. In doing so we may write

$$\langle O(t) \rangle = \sum_{ij} O_{ij} \mathrm{Tr}\left[a_i^\dagger(t) a_j(t) \rho_0(t_0) \right] = \sum_{ij} O_{ij} \left\langle a_i^\dagger(t) a_j(t) \right\rangle \,. \tag{2.1.3}$$

The bracket $\langle ... \rangle$ denotes the quantum-statistical ensemble average with respect to the initial state of the system $\rho_0(t_0)$ in thermal equilibrium. The bracketed

[1] The trace is performed over the entire Fock space spanned by many-particle states.

object is the second quantization equivalent of the reduced single-particle density matrix, which we shall define as $\rho_{ij}(t) = \langle a_j^\dagger(t) a_i(t) \rangle$. In the present treatment we are only concerned with equal time operators and therefore drop the explicit time dependence from the second quantization operators, we write $\rho_{ij}(t) = \langle a_j^\dagger a_i \rangle$.

We wish to study the the coherences and populations of the carriers in a combined QD-WL system. These quantities are the elements of the reduced density matrix. The diagonal components ($\rho_{ii}(t)$) correspond to the occupation of the state $|i\rangle$, whereas the off-diagonal components correspond to the coherences that are related to microscopic polarization components.

2.2 Hamiltonian

To move further we need to specify the Hamiltonian for the combined QD and WL system. The Hamiltonian for interacting carriers in a semiconductor being irradiated by a classical external light field is

$$H = H_0 + H_{c-f} + H_C \,, \tag{2.2.4}$$

here H_0 describes the quadratic, time independent contribution to the Hamiltonian, H_{c-f} is the carrier-field interaction and H_C is the Coulomb interaction amongst the carriers. Lattice vibrations (phonons) and their interaction with the carriers are not treated explicitly, instead they are included on a phenomenological level.

The contributions to H_0 come from the kinetic energy of the carriers and the interaction with the static lattice. Assuming that the solution to this complex problem is known, we use the eigenstates of H_0 as the single-particle basis $\{|\varphi_i\rangle\}$ in which to expand the Hamiltonian

$$H = \sum_{ij} h_{ij} c_i^\dagger c_j + \frac{1}{2} \sum_{klmn} V_{klmn} c_k^\dagger c_l^\dagger c_m c_n \,, \tag{2.2.5}$$

where h_{ij} is the matrix element of the single-particle Hamiltonian $h = h_0 + h_{c-f}$, thus combining the single-particle components of the Hamiltonian and V_{klmn} is the matrix element of the two-particle Coulomb interaction. The second quantization operators that creates and annihilates a fermion in state i are denoted $c_i^\dagger$ and c_i, respectively. We do not give the explicit form of the matrix elements of the different operators, this is done at a later time. For the time being it is sufficient to note that the diagonal components of h are the single particle energies, i.e. $h_0(\mathbf{r})\varphi_i(\mathbf{r}) = \epsilon_i \varphi_i(\mathbf{r})$ and the off-diagonal components are generated by the (explicitly time dependent) carrier-field interaction that induce transitions between the states. The matrix elements are formally constructed

as

$$\begin{aligned} h_{ij} &= \langle i|\, h\, |j\rangle \\ &= \int \mathrm{d}\boldsymbol{r}\, \varphi_i^*(\boldsymbol{r}) h(\boldsymbol{r}) \varphi_j(\mathbf{r})\,, \end{aligned} \tag{2.2.6}$$

$$\begin{aligned} V_{klmn} &= \langle kl|\, V\, |mn\rangle \\ &= \iint \mathrm{d}\boldsymbol{r}\mathrm{d}\boldsymbol{r}'\, \varphi_k^*(\boldsymbol{r})\varphi_l^*(\boldsymbol{r}') V(\boldsymbol{r},\boldsymbol{r}')\varphi_m(\mathbf{r}')\varphi_n(\mathbf{r})\,. \end{aligned} \tag{2.2.7}$$

In order to establish an equation of motion for the density matrix ($\langle c_i^\dagger c_j\rangle$) we consider first its elementary building blocks. The Fermionic annihilation and creation operators obey the following three anti-commutation[2] relations:

$$\{c_i, c_j^\dagger\} = \delta_{ij}\,, \qquad \{c_i, c_j\} = 0\,, \qquad \{c_i^\dagger, c_j^\dagger\} = 0\,. \tag{2.2.8}$$

Using the Heisenberg equation of motion along with the above commutation relations we arrive at the following differential equation for the elementary operators

$$i\hbar \frac{d}{dt} c_i^\dagger = [c_i^\dagger, H] = -\sum_l h_{li} c_l^\dagger + \sum_{lmn} V_{lmni} c_l^\dagger c_m^\dagger c_n\,, \tag{2.2.9}$$

$$i\hbar \frac{d}{dt} c_j = [c_j, H] = \sum_l h_{jl} c_l - \sum_{lmn} V_{jlmn} c_l^\dagger c_m c_n\,. \tag{2.2.10}$$

In deriving the above we used the fact that the Coulomb interaction is translational invariant, i.e. $V(\boldsymbol{r},\boldsymbol{r}') = V(|\ \boldsymbol{r}-\boldsymbol{r}'\ |) = V(\boldsymbol{r}',\boldsymbol{r})$, which leads to the identity $V_{klmn} = V_{lknm}$.

The equation of motion for the single-particle density matrix is found by using the product rule for differentiating $c_i^\dagger c_j$ along with the equation of motion for the elementary operators

$$\begin{aligned} i\hbar \frac{d}{dt}\langle c_i^\dagger c_j\rangle = &-\sum_l \Big(h_{li}\,\langle c_l^\dagger c_j\rangle - \langle c_i^\dagger c_l\rangle\, h_{jl}\Big) \\ &+ \sum_{lmn} \Big(V_{lmni}\,\langle c_l^\dagger c_m^\dagger c_n c_j\rangle - V_{jlmn}\,\langle c_i^\dagger c_l^\dagger c_m c_n\rangle\Big)\,. \end{aligned} \tag{2.2.11}$$

The above differential equation for the single-particle density matrix illustrates what is known as the hierarchy problem. The two point correlation function $\langle c_i^\dagger c_j\rangle$ couples to four-point correlation functions e.g. $\langle c_i^\dagger c_l^\dagger c_m c_n\rangle$, whose equation of motion also will have to be solved. By differentiating $\langle c_i^\dagger c_l^\dagger c_m c_n\rangle$ with respect to time and applying the equations of motion for the elementary single point operators it is seen that the four-point expectation values connects to correlation functions of even higher order (a six-point expectation value). The coupling to higher order products is infinite and so the set of equations never

[2] We use curly brackets to define the anti-commutator $\{A, B\} \equiv AB + BA$, for two operators A and B.

closes, this is the hierarchy problem of many-body theory. There are different ways to overcome this obstacle, but they all rely on some approximation scheme for the higher order terms so that the set of equations can be closed. Two widely used methods are the cluster expansion and the Green's function approach. The cluster expansion scheme relies on the systematic factorization of the expectation values of higher order operators into products of lower order equal time correlation functions (e.g. the density matrix) ultimately cutting off at some level, thereby closing the equations. For a review on the cluster expansion scheme applied to semiconductor optics see [48,50]. The Green's function approach is based on the generalization of the single-time density matrix into a two-time correlation function. Instead of keeping all types of interactions and truncating at a certain level in the higher order products, only select contributions (one usually chooses to include contributions so that the general conservation laws are obeyed) are included but kept to infinite order. For a textbook treatment see e.g. [51, 52]. The two methods each have their advantages depending on the problem one wishes to solve. In case of the Hamiltonian considered here the two methods coincide at the level of the Hartree-Fock approximation. The following theoretical approach does not attempt to calculate terms beyond this approximation and so we choose to use the cluster expansion scheme since it is particularly intuitive.

2.3 Cluster expansion and the Hartree-Fock approximation

To progress the theoretical development the above very compact form (Eq. (2.2.11)) must be made more transparent and we do so by expressing the different components of the Hamiltonian in terms of real space field operators. The Hamiltonian governing the motion of the electrons in the static lattice has the following appearance

$$H_0 = \int \mathrm{d}\boldsymbol{r}\, \psi^\dagger(\boldsymbol{r}) h_0(\boldsymbol{r}) \psi(\boldsymbol{r})\,, \tag{2.3.12}$$

where the single-particle hamiltonian is

$$h_0(\boldsymbol{r}) = -\frac{\hbar^2}{2m}\nabla^2 + eU(\boldsymbol{r})\,. \tag{2.3.13}$$

The second quantization operators that creates and annihilates a particle at space point $(\boldsymbol{r})$ is expanded in a single-particle basis $\{|\nu\rangle\}$ as

$$\psi(\boldsymbol{r}) = \sum_\nu \langle \boldsymbol{r}|\nu\rangle\, c_\nu\ , \qquad \psi^\dagger(\boldsymbol{r}) = \sum_\nu \langle \boldsymbol{r}|\nu\rangle^*\, c_\nu^\dagger\ . \tag{2.3.14}$$

The real space/spin representation of $|\nu\rangle$ is given by $\langle \boldsymbol{r}|\nu\rangle = \varphi_\nu(\boldsymbol{r}) = \phi_\alpha^b(\boldsymbol{r})\chi_\sigma$, where $\phi_\alpha^b(\boldsymbol{r})$ is the wave function of the electron in the spatial state α, b and χ_σ is a spin function. If we choose the eigenstates of the single-particle Hamiltonian

h_0 as basis, the general state label ν would cover spin (σ), band index (b) and a spatial quantum number signifying either a state localized within the quantum dot with quantum number l found at position $\boldsymbol{R}$ $(\boldsymbol{R}, l)$ or a two-dimensional momentum corresponding to a delocalized state in the WL with sub-band index n $(\mathbf{k}, n)$. For now we collect all spatial quantum numbers in the label α i.e. $\nu = \{b, \sigma, \alpha\}$, later we will also use α exclusively for localized states, but it will be clear from context when that is the case. Also, the spin index σ unless explicitly stated is tacitly contained within the spatial quantum number. H_0 thus becomes

$$H_0 = \sum_{\nu} \epsilon_\nu c_\nu^\dagger c_\nu \,. \tag{2.3.15}$$

The interaction energy of the carriers with the classical electromagnetic field

$$H_{c-f}(\boldsymbol{r}) = \int \mathrm{d}\boldsymbol{r}\, \psi^\dagger(\boldsymbol{r}) h_{c-f}(\boldsymbol{r}) \psi(\boldsymbol{r}), \tag{2.3.16}$$

is taken within the dipole approximation

$$h_{c-f} = -\boldsymbol{D} \cdot \boldsymbol{E}(t)\,, \tag{2.3.17}$$

where $\boldsymbol{D} = e\boldsymbol{r}$ is the dipole operator. Writing H_{c-f} in the $|\nu\rangle$ basis and introducing the projection of the dipole matrix element along the direction of the electrical field $\mu_{\nu\nu'} = \int \mathrm{d}\boldsymbol{r}\, \varphi_\nu^*(\boldsymbol{r}) e\boldsymbol{r} \cdot \hat{\boldsymbol{e}}_{\boldsymbol{E}} \varphi_{\nu'}(\boldsymbol{r}) = \int \mathrm{d}\boldsymbol{r}\, {\phi_\alpha^b}^*(\boldsymbol{r}) e\boldsymbol{r} \cdot \hat{\boldsymbol{e}}_{\boldsymbol{E}} \phi_{\alpha'}^{b'}(\boldsymbol{r}) \delta_{\sigma,\sigma'}$, we get

$$H_{c-f} = -\sum_{\nu_1 \neq \nu_2} \mu_{\nu_1\nu_2} E(t) c_{\nu_1}^\dagger c_{\nu_2}\,. \tag{2.3.18}$$

In the above we assume that the symmetry of the eigenstates is such that there is no dipole moment between identical states. As for the Coulomb interaction H_C its form remains unchanged from Eq. (2.2.7) for completeness we present it anyway

$$H_C = \frac{1}{2} \sum_{\nu_1\nu_2\nu_3\nu_4} V_{\nu_1\nu_2\nu_3\nu_4} c_{\nu_1}^\dagger c_{\nu_2}^\dagger c_{\nu_3} c_{\nu_4}\,, \tag{2.3.19}$$

where the Coulomb matrix elements

$$\begin{aligned} V_{\nu_1\nu_2\nu_3\nu_4} &= \int\!\!\int \mathrm{d}\boldsymbol{r}\mathrm{d}\boldsymbol{r}'\, \varphi_{\nu_1}^*(\boldsymbol{r}) \varphi_{\nu_2}^*(\boldsymbol{r}') V(\boldsymbol{r}-\boldsymbol{r}') \varphi_{\nu_3}(\mathbf{r}') \varphi_{\nu_4}(\mathbf{r}) \\ &= \int\!\!\int \mathrm{d}\boldsymbol{r}\mathrm{d}\boldsymbol{r}'\, {\phi_{\alpha_1}^{b_1}}^*(\boldsymbol{r}) {\phi_{\alpha_2}^{b_2}}^*(\boldsymbol{r}') V(\boldsymbol{r}-\boldsymbol{r}') \phi_{\alpha_3}^{b_3}(\mathbf{r}') \phi_{\alpha_4}^{b_4}(\mathbf{r}) \delta_{\sigma_1,\sigma_4} \delta_{\sigma_2,\sigma_3} \end{aligned} \tag{2.3.20}$$

are diagonal in spin, and the bare Coulomb interaction potential is $V(\boldsymbol{r}-\boldsymbol{r}') = \frac{e^2}{4\pi\epsilon_0|\boldsymbol{r}-\boldsymbol{r}'|}$.

Hartree-Fock approximation

Now that the matrix elements of the Hamiltonian are specified we can insert them directly into Eq. (2.2.11), but before doing so we need to address the hierarchy problem. The Hartree-Fock (H-F) approximation is the lowest order approximation to the four-point correlation function $\langle c^\dagger_{\nu_1} c^\dagger_{\nu_2} c_{\nu_3} c_{\nu_4} \rangle$. Generally we can write the four-point correlation function as its value within the H-F approximation plus a deviation that contains all higher order corrections

$$\langle c^\dagger_{\nu_1} c^\dagger_{\nu_2} c_{\nu_3} c_{\nu_4} \rangle = \langle c^\dagger_{\nu_1} c^\dagger_{\nu_2} c_{\nu_3} c_{\nu_4} \rangle_{HF} + \langle c^\dagger_{\nu_1} c^\dagger_{\nu_2} c_{\nu_3} c_{\nu_4} \rangle_{\delta} \ . \tag{2.3.21}$$

The H-F approximation is a mean field theory where one assumes the particles can be treated as independent and only interacting with the average field of the other particles. In this case the four point operator terms are factorized according to Wick's theorem[3]:

$$\langle c^\dagger_{\nu_1} c^\dagger_{\nu_2} c_{\nu_3} c_{\nu_4} \rangle_{HF} = \langle c^\dagger_{\nu_1} c_{\nu_4} \rangle \langle c^\dagger_{\nu_2} c_{\nu_3} \rangle - \langle c^\dagger_{\nu_1} c_{\nu_3} \rangle \langle c_{\nu_2} c_{\nu_4} \rangle \ . \tag{2.3.22}$$

The first term represent the direct interaction (Hartree), because is gives the classical expectation value of the interaction between two densities. The second term (Fock), is a quantum mechanical correction due to the indistinguishability of the particles.

If we return to the equation of motion for the density matrix (Eq. (2.2.11)) and insert the expression for the four point operator (Eq. (2.3.21)) we see that the Hartree-Fock part which consist of two-point correlation functions can be absorbed into the first line of Eq. (2.2.11). In other words we can split the equation of motion of the density matrix into two parts; a coherent (single-particle) part and a scattering part

$$\frac{\partial \rho(t)}{\partial t} = \left.\frac{\partial \rho(t)}{\partial t}\right|_{coh} + \left.\frac{\partial \rho(t)}{\partial t}\right|_{scatt} \ . \tag{2.3.23}$$

The coherent part governs the time evolution of the independent carriers (within the H-F approximation) under the action of the coherent light field, whereas the scattering part contains all higher order terms. It is the remainder, what is left out in the H-F approximation, of performing the single particle decomposition. The scattering part describes the decay processes that tends to dephase polarization components and redistribute carriers both within and across the bands.

2.3.1 Coherent evolution

Using Eq. (2.3.22) to decompose the higher order terms in Eq. (2.2.11) while separating the density matrix into microscopic polarization components $p_{\nu_1\nu_2} =$

[3] Wicks theorem states that for non-interacting particles higher order correlation functions can be factorized into products of single-particle correlation functions, making all possible pairings while changing sign when two fermion operators are interchanged.

$\langle c^\dagger_{\nu_2} c_{\nu_1}\rangle$ $(\nu_1 \neq \nu_2)$ and populations $n_{\nu_1} = \langle c^\dagger_{\nu_1} c_{\nu_1}\rangle$, we arrive at the semiconductor Bloch equations (SBE)

$$i\hbar \frac{\partial}{\partial t} p_{\nu_1\nu_2}(t)\bigg|_{coh} = \left[\tilde{\epsilon}_{\nu_1}(t) - \tilde{\epsilon}_{\nu_2}(t)\right] p_{\nu_1\nu_2}(t) + \left[n_{\nu_2}(t) - n_{\nu_1}(t)\right] \Omega_{\nu_1\nu_2}(t) + \sum_{\nu_3 \neq \nu_1,\nu_2} \left[\Omega_{\nu_1\nu_3}(t) p_{\nu_3\nu_2}(t) - p_{\nu_1\nu_3}(t)\Omega_{\nu_3\nu_2}(t)\right] , \quad (2.3.24)$$

$$i\hbar \frac{\partial}{\partial t} n_{\nu_1}(t)\bigg|_{coh} = \sum_{\nu_3 \neq \nu_1} \left[\Omega_{\nu_1\nu_3}(t) p_{\nu_3\nu_1}(t) - \Omega_{\nu_3\nu_1}(t) p_{\nu_1\nu_3}(t)\right] . \quad (2.3.25)$$

We have introduced a renormalized energy $\tilde{\epsilon}_\nu(t)$ and a generalized Rabi energy $\Omega_{\nu_1\nu_2}(t)$ defined as

$$\tilde{\epsilon}_\nu(t) = \epsilon_\nu + \sum_{\nu_3\nu_4} \left[V_{\nu\nu_4\nu_3\nu} - V_{\nu\nu_4\nu\nu_3}\right] \rho_{\nu_3\nu_4}(t) , \quad (2.3.26)$$

$$\Omega_{\nu_1\nu_2}(t) = -\mu_{\nu_1\nu_2} E(t) + \sum_{\nu_3\nu_4} \left[V_{\nu_1\nu_4\nu_3\nu_2} - V_{\nu_1\nu_4\nu_2\nu_3}\right] \rho_{\nu_3\nu_4}(t) . \quad (2.3.27)$$

The impact of the Coulomb interaction is to couple the different components of the density matrix, for instance the renormalization of the Rabi energy means that a given polarization $p_{\nu_1\nu_2}$ interacts with all other polarization components, resulting in a formidable amount of couplings. As the equations stand now, in their most general form, it constitutes a great task to solve them. To make this a more feasible job certain simplifications can be applied. A very common approach is to disregard energetically unfavorable scattering events i.e. scattering of carriers across the bandgap. In a semiconductor with a relatively wide bandgap such processes will be highly improbable, and so we set $V_{\nu_1\nu_2\nu_3\nu_4} = V_{\nu_1\nu_2\nu_3\nu_4}\delta_{b_1,b_4}\delta_{b_2,b_3}$. The number of carriers in each band is constant as a consequence thereof and hence no recombination can be attributed to the Coulomb interaction within this approximation. It is convenient for both conceptual and computational reasons to move from the electron-electron (c-v) picture and recast the above equation in the electron-hole (e-h) picture. The e-h picture is defined by introducing the concept of a hole as the absence of a valence electron, so that the field operators that create a hole is related to the valence band electron annihilation operator as:

$$\psi_v(\boldsymbol{r}) = \sum_{\alpha,\sigma} \phi^v_\alpha(\boldsymbol{r}) \chi_\sigma c_{v,\alpha,\sigma} = \sum_{\alpha,\sigma} \phi^{h\,*}_\alpha(\boldsymbol{r}) \chi_{-\sigma}{}^* b^\dagger_{\alpha,-\sigma} = \psi^\dagger_h(\boldsymbol{r}) , \quad (2.3.28)$$

and vice versa for the hole annihilation operator. $c_{v,\alpha,\sigma}$ removes a valence band electron in state α,σ and $b_{\alpha,-\sigma}$ generates a hole in state $\alpha,-\sigma$. For further reference we shall keep the spin label hidden within the spatial quantum number α unless explicitly stated otherwise. The conduction band electron operators remain unchanged. Applying the transformation has the following consequences:

$$n_c = n_e \qquad \epsilon_c = \epsilon_e \quad (2.3.29)$$

$$n_v = 1 - n_h \qquad \epsilon_v = -\epsilon_h , \quad (2.3.30)$$

i.e. the probability of finding a valence band electron equals the probability of not finding a hole and the hole energy changes sign.

When substituting into Eq. (2.3.24) one ends up with several constant terms arising from the factor 1 in the definition of the hole population ($n_v = 1 - n_h$) this can be understood as the contribution from Coulomb interaction with the fully occupied valence band. Considering for instance the hole energy $\tilde{\epsilon}_h$, large constant terms such as $\sum_{\nu_3\nu_4} [V_{\nu\nu_4\nu_3\nu} - V_{\nu\nu_4\nu\nu_3}]$ enter the expression. Typically one argues that such contributions are already accounted for in the model of the free particle part, i.e. the band structure calculation, which is based on measured semiconductor parameters such as band gaps and effective masses. And so one can absorb the constant terms in the free energy ϵ_h. Upon transforming to the e-h picture, while disregarding contributions from the full valence band in the expressions for the renormalized energies, Eq. (2.3.24) retains its overall structure, however one now has five equations, three polarization equations (two intra-band polarization and one inter-band) and two population equations (that are identical). The polarization equations differ from each other by only a few sign changes[4]. The full set of equations can be found in appendix B. The equations of motion are there derived based on transforming to the the e-h picture at Hamiltonian level. The removal of the full valence band is then performed upon normal ordering of the Hamiltonian, where one disregards constants and absorbs two-operator terms only retaining contributions that contain four operators. Removing all references to the full valence band has the consequence that in equilibrium the Coulomb interaction does not contribute, one only has contributions in non-equilibrium situations. For further discussions we shall use the e-h picture.

2.3.2 Scattering terms

The Hartree-Fock approximation fails to account for correlations between the particles. All additional interaction effects beyond the mean field approximation are contained in the scattering terms. Therefore the SBE as they stand now, do not include e.g. decay of the polarizations (dephasing), relaxation of the excited carriers nor screening effects. As mentioned in the beginning of this chapter various approaches can be applied to model the scattering terms on various levels of sophistication each approach having their own pros and cons. Depending on the physical situation at hand, i.e. the strength and time dynamics of the applied electrical fields, different sources dominate the above effects and hence the choice of model. Dephasing arises from scattering events within the system (Coulomb) or interaction with a surrounding environment, i.e. lattice vibrations (phonons). In the low excitation regime the dephasing is dominated by the phonon interaction, at elevated carrier densities the Coulomb interaction is dominant. In this work we restrain ourselves to treat the scattering terms on a phenomenological basis. This approach, known as the phenomeno-

[4]The equation of motion for inter-band polarizations contain an additional 1 in the Pauli blocking factor, stemming from the transformation: $(n_v - n_c) = (1 - n_h - n_e)$.

logical relaxation time approximation, uses effective scattering rates extracted from experiments. This corresponds to modeling the decay of the polarization as that of a single exponential. Other more elaborate theories would include the dynamics of the scattering processes, also referred to as quantum kinetics. In these approaches one accounts for the (fast but) finite duration of the scattering process, effectively resulting in the system having a memory of the scattering events. Ultrafast dynamics are studied using femtosecond excitations with intensive pulses, where a quantum kinetic treatment of the relaxation and dephasing is generally needed. These models lead to exotic effects such as excitation induced dephasing [53, 54].
Extensive work is done in this field, for a thorough review we point the reader to Ref. [55].

In the relaxation time approximation the scattering term for the microscopic polarizations is modeled using a fixed characteristic dephasing time[5] $T_2 = 1/\gamma_d$. The dephasing mechanism is assumed to be dominated by interaction with phonons, and thus T_2 is highly temperature dependent. Choosing a fixed rate means we cannot include dynamically changing dephasing rates occurring due to a gradually increasing carrier density (such as in an carrier exciting EIT scheme). The scattering term has the following appearance

$$\left.\frac{\partial}{\partial t} p_{\nu_1\nu_2}(t)\right|_{scatt} = -\gamma_d p_{\nu_1\nu_2}. \tag{2.3.31}$$

The values of the decoherence rates at various temperatures are extracted from measurements of the homogeneous broadening linewidth from experiments on InGaAs QDs [56–59] and ranges from several hundreds of picoseconds at 7 K to hundreds of femtoseconds at room temperature (see Table 2.1).

Temperature [K]	T_2
7	630 ps
25	170 ps
50	37 ps
75	11 ps
100	6 ps
200	0.66 ps
300	290±80 fs

***Table 2.1**: T_2 values extracted from homogeneous broadening linewidth measurements on InGaAs QDs [56–59] at various temperatures.*

Within the relaxation time approximation we include the population scattering term as:

$$\begin{aligned}\left.\frac{\partial}{\partial t} n_\nu(t)\right|_{scatt} = &-\gamma_{c-c}[n_\nu(t) - f_\nu(\mu_p^b, T_p)] \\ &-\gamma_{c-p}[n_\nu(t) - f_\nu(\mu_L^b, T_L)] - \gamma_{nr} n_\nu(t)\,.\end{aligned} \tag{2.3.32}$$

[5] The dephasing time T_2 is also referred to as the transverse relaxation time.

The first term represents carrier-carrier scattering mediated by the Coulomb interaction. In general, carrier-carrier scattering is the most efficient process for thermalizing the carriers. It is assumed to be the fastest scattering mechanism, but depends on carrier density, the mechanism generally acts on the sub picosecond timescale [60]. For the purpose here we set the characteristic time constant $\tau_{c-c} = 1/\gamma_{c-c} = 0.5 \cdot 10^{-12}$ s, following Refs. [46,47]. This scattering mechanism leads to relaxation of the carrier distribution toward a Fermi-Dirac distribution function $f_\nu(\mu_p^b, T_p)$ parameterized by a chemical potential μ_p^b and a plasma temperature T_p

$$f_\nu(\mu_p^b, T_p) = \left[\exp\left(\frac{\tilde{\epsilon}_\nu - \mu_p^b}{k_B T_p}\right) + 1\right]^{-1}, \tag{2.3.33}$$

where $\tilde{\epsilon}_\nu$ is the renormalized energy of the state and k_B is the Boltzmann's constant. The chemical potential and plasma temperature can be determined from the instantaneous carrier distribution by utilizing that the carrier-carrier intra-band scattering mechanism conserves both the particle density and total energy. The chemical potential of either the electrons μ_p^e or holes μ_p^h is uniquely determined by requiring

$$\begin{aligned} N_{tot}^b &= \frac{1}{A}\sum_\alpha n_\alpha^b + \frac{1}{A}\sum_{\mathbf{k}} n_{\mathbf{k}}^b \\ &= N_{dot}\sum_l f_l(\mu_p^b, T_p) + \frac{1}{A}\sum_{\mathbf{k}} f_{\mathbf{k}}(\mu_p^b, T_p)\,, \end{aligned} \tag{2.3.34}$$

where N_{tot}^b is the total particle density of either electrons or holes. In the above α refers to localized dot states ($\boldsymbol{R}$, l), whereas $\mathbf{k}$ refers to delocalized WL states. A is the normalization area of the WL. We assume the dots can be treated independent of position, and replace the summation over position $\boldsymbol{R}$ by N_{dot}, the density of dots. The plasma temperature is found from the total energy density

$$\begin{aligned} E_{tot} &= \frac{1}{A}\sum_{\alpha,b} \tilde{\epsilon}_\alpha^b n_\alpha^b + \frac{1}{A}\sum_{\mathbf{k},b} \tilde{\epsilon}_{\mathbf{k}}^b n_{\mathbf{k}}^b \\ &= N_{dot}\sum_{l,b} \tilde{\epsilon}_l^b f_l(\mu_p^b, T_p) + \frac{1}{A}\sum_{\mathbf{k},b} \tilde{\epsilon}_{\mathbf{k}}^b f_{\mathbf{k}}(\mu_p^b, T_p)\,. \end{aligned} \tag{2.3.35}$$

The second term in (2.3.32) describes electron-phonon scattering. Generally this mechanism acts on a timescale that is an order of magnitude slower than Coulomb scattering [60], i.e. on the order of picoseconds. Following Refs. [45,46], we set the characteristic time constant $\tau_{c-p} = 1/\gamma_{c-p} = 5.0 \cdot 10^{-12}$ s. This scattering mechanism leads to equilibration of the carrier distribution with the phonon bath at the fixed lattice temperature T_L. The corresponding Fermi distribution function can be determined by utilizing the particle-conservation

property of electron-phonon scattering[6]

$$N^b_{tot} = \frac{1}{A}\sum_{\alpha} n^b_{\alpha} + \frac{1}{A}\sum_{\mathbf{k}} n^b_{\mathbf{k}} = N_{dot}\sum_{l} f_l(\mu^b_L, T_L) + \frac{1}{A}\sum_{\mathbf{k}} f_{\mathbf{k}}(\mu^b_L, T_L)\,. \tag{2.3.36}$$

The energy in the carrier-phonon interaction is not conserved. Energy is exchanged between the carriers and the lattice. To account for this the temperature entering the distribution function is fixed at the lattice temperature T_L.

The third term accounts for non radiative carrier loss i.e. the relaxation towards the equilibrium situation, the filled valence band. This occurs on a much longer timescale, namely nanoseconds. Following Refs. [47, 61], we set $\tau_{nr} = 1/\gamma_{nr} = 1.0 \cdot 10^{-9}$ s.

[6] As in the case of Coulomb scattering, promotion/demotion of carriers across the bandgap is highly unlikely and by disregarding such processes one obtains particle conservation within the bands.

Generalized semiconductor Bloch equations

Collecting everything the semiconductor Bloch equations in the e-h picture become:

$$
\begin{aligned}
&(b_1 = e, b_2 = h):\\
&i\hbar\frac{\partial}{\partial t}p_{\nu_1\nu_2}(t) = [\tilde{\epsilon}_{\nu_1}(t) + \tilde{\epsilon}_{\nu_2}(t)]\, p_{\nu_1\nu_2}(t) + [1 - n_{\nu_2}(t) - n_{\nu_1}(t)]\, \Omega_{\nu_1\nu_2}(t)\\
&\qquad + \sum_{\nu_3\neq\nu_1,\nu_2} [\Omega_{\nu_1\nu_3}(t)p_{\nu_3\nu_2}(t) - p_{\nu_1\nu_3}(t)\Omega_{\nu_3\nu_2}(t)]\\
&\qquad - i\hbar\gamma_d p_{\nu_1\nu_2}\,, \qquad (2.3.37)\\
&(b_1 = e, b_2 = e):\\
&i\hbar\frac{\partial}{\partial t}p_{\nu_1\nu_2}(t) = [\tilde{\epsilon}_{\nu_1}(t) - \tilde{\epsilon}_{\nu_2}(t)]\, p_{\nu_1\nu_2}(t) + [n_{\nu_2}(t) - n_{\nu_1}(t)]\, \Omega_{\nu_1\nu_2}(t)\\
&\qquad + \sum_{\nu_3\neq\nu_1,\nu_2} [\Omega_{\nu_1\nu_3}(t)p_{\nu_3\nu_2}(t) - p_{\nu_1\nu_3}(t)\Omega_{\nu_3\nu_2}(t)]\\
&\qquad - i\hbar\gamma_d p_{\nu_1\nu_2}\,, \qquad (2.3.38)\\
&(b_1 = h, b_2 = h):\\
&i\hbar\frac{\partial}{\partial t}p_{\nu_1\nu_2}(t) = [\tilde{\epsilon}_{\nu_2}(t) - \tilde{\epsilon}_{\nu_1}(t)]\, p_{\nu_1\nu_2}(t) + [n_{\nu_1}(t) - n_{\nu_2}(t)]\, \Omega_{\nu_1\nu_2}(t)\\
&\qquad + \sum_{\nu_3\neq\nu_1,\nu_2} [\Omega_{\nu_1\nu_3}(t)p_{\nu_3\nu_2}(t) - p_{\nu_1\nu_3}(t)\Omega_{\nu_3\nu_2}(t)]\\
&\qquad - i\hbar\gamma_d p_{\nu_1\nu_2}\,, \qquad (2.3.39)\\
&(b_1 = e/h, b_2 = b_1):\\
&i\hbar\frac{\partial}{\partial t}n_{\nu_1}(t) = \sum_{\nu_3\neq\nu_1} [\Omega_{\nu_1\nu_3}(t)p_{\nu_3\nu_1}(t) - \Omega_{\nu_3\nu_1}(t)p_{\nu_1\nu_3}(t)]\\
&\qquad - i\hbar\gamma_{c-c}[n_{\nu_1}(t) - f_{\nu_1}(\mu_p^{b_{\nu_1}}, T_p)] - i\hbar\gamma_{c-p}[n_{\nu_1}(t) - f_{\nu_1}(\mu_L^{b_{\nu_1}}, T_L)]\\
&\qquad - i\hbar\gamma_{nr} n_{\nu_1}(t)\,, \qquad (2.3.40)
\end{aligned}
$$

where

$$\tilde{\epsilon}_\nu(t) = \epsilon_\nu \pm \sum_{\nu_3\nu_4} [V_{\nu\nu_4\nu_3\nu} - V_{\nu\nu_4\nu\nu_3}]\,(1 - 2\delta_{\nu_3\nu_4}\delta_{b_{\nu_3}h})\rho_{\nu_3\nu_4}(t) \qquad (2.3.41)$$

$$\Omega_{\nu_1\nu_2}(t) = -e\mu_{\nu_1\nu_2}E(t) + \sum_{\nu_3\nu_4} [V_{\nu_1\nu_4\nu_3\nu_2} - V_{\nu_1\nu_4\nu_2\nu_3}]\,(1 - 2\delta_{\nu_3\nu_4}\delta_{b_{\nu_3}h})\rho_{\nu_3\nu_4}(t)\,, \qquad (2.3.42)$$

are the Hartree-Fock renormalized single particle energy and generalized Rabi frequency, respectively. In the expression for the renormalized energy '+' refers to electrons and '−' is for hole states.

In this work the SBE are solved using a fourth order Runge-Kutta method. The number of equations is lowered by the fact that we disregard subband structure in the WL and subsequently all intra-band polarizations involving the WL due to a negligible dipole moment. Following a similar vein we disregard polarization

components between WL and dot states. Another way to simplify the equations is only to include those polarizations that are being optically driven i.e. are in resonance with the electrical field(s), however as we will investigate different EIT schemes which involves switching between signal and coupling transitions we include all possibilities.

Chapter 3

Macroscopic theory

In this section it is shown how the microscopic quantities enter a macroscopic description. Slow light based on EIT is about propagation of light pulses which ultimately means we must relate the microscopic results to macroscopic theory (the Maxwell's equations). We explore the wave propagation aspects of using a continuous wave (c-w) or pulsed coupling field and treat the issue of how to extract and utilize the material response in these limits. These two scenarios correspond to the steady state and transient situations, respectively.

3.1 Maxwell-Bloch equations

Constitutive relations are ubiquitous in physics. In optics the central physical quantity is the polarization response of a medium under the influence of an applied electric field $\mathbf{E}$. The polarization $\mathbf{P}$ can be described in terms of a power series in the field (to ease the notation we suppress both spatial and temporal dependencies), i.e.

$$\mathbf{P} = \mathbf{P}^{(0)} + \mathbf{P}^{(1)} + \mathbf{P}^{(2)} + ..., \tag{3.1.1}$$

where $\mathbf{P}^{(1)}$ is linear in the field, $\mathbf{P}^{(2)}$ is quadratic, and so on. $\mathbf{P}^{(0)}$ is independent of the field, and represents permanent static polarizations present in some crystals and molecules. In this work we will not treat materials with built in polarizations. The linear polarization governs linear-optical phenomena, i.e. it corresponds to the regime where the optical properties of a medium are independent of field intensity. The most general linear relation between $\mathbf{P}(t)$ and $\mathbf{E}(t)$ is written as

$$\mathbf{P}^{(1)}(t) = \epsilon_0 \int_{-\infty}^{\infty} \mathrm{d}t' \, \boldsymbol{\chi}^{(1)}(t,t')\mathbf{E}(t') \,, \tag{3.1.2}$$

where the linear response function or susceptibility $\boldsymbol{\chi}^{(1)}(t,t')$ is a tensor of the second rank and a function of the two times t and t'. We take both $\mathbf{P}^{(1)}(t)$ and $\mathbf{E}(t)$ to be real, and consequently so is $\boldsymbol{\chi}^{(1)}(t,t')$. The susceptibility is required

to vanish at $t' > t$ so as to satisfy the principle of causality. The causality principle states that the polarization $\mathbf{P}(t)$ at time t cannot be affected by fields acting in the future, i.e. , $t' > t$. The susceptibility contains knowledge of the system and can in principle be calculated using microscopic theory.

The polarization enters the wave equation for the electrical field, which in a nonmagnetic dielectric medium (without free charges) looks like

$$\begin{aligned} \nabla \times (\nabla \times \mathbf{E}) + \frac{1}{{c_0}^2}\frac{\partial^2}{\partial t^2}\mathbf{E} &= -\mu_0 \tfrac{\partial^2}{\partial t^2}\mathbf{P} \\ \nabla(\nabla \cdot \mathbf{E}) - \nabla^2\mathbf{E} + \frac{1}{{c_0}^2}\frac{\partial^2}{\partial t^2}\mathbf{E} &= -\mu_0 \tfrac{\partial^2}{\partial t^2}\mathbf{P}\,. \end{aligned} \tag{3.1.3}$$

This equation is simplified by making the paraxial approximation $\nabla(\nabla \cdot \mathbf{E}) \simeq 0$, which assumes that a wave vector makes a non appreciable angle with a direction of propagation and is valid when a wavelength is short in comparison with a characteristic transverse dimension, e.g. a spot size, of an incident beam. In a homogeneous and isotropic medium this criterion is always fulfilled. Via the definition of the displacement field $\mathbf{D} = \epsilon_0\mathbf{E} + \mathbf{P}$, the wave equation becomes

$$-\nabla^2\mathbf{E} + \mu_0\frac{\partial^2}{\partial t^2}\mathbf{D} = 0\,. \tag{3.1.4}$$

This expression tells us how the electromagnetic wave behaves under the influence of the polarization $\mathbf{P}$. That polarization must still be determined. The relation between the microscopic field-induced atomic coherences and the macroscopic field-induced polarization is described using semiclassical theory. The macroscopic polarization is derived from a spatial averaging of microscopic charge imbalances. The leading contribution of a multi-pole expansion of the polarization is given by the dipole term. The macroscopic polarization is found as a quantum mechanical ensemble average of the dipole operator, in addition to the electromagnetic average taken on basis of a single elementary cell. We treat the QD system as a homogeneous medium, meaning that the system consisting of randomly placed QDs on top of a WL is modeled using an elementary cell that contains a suitable amount of QDs. If the QD system is sufficiently dilute, so that the dot wave functions are not overlapping, they can be treated as independent[1]. The summation running over dot positions and the cell average will in the large area limit lead to a constant QD density and a microscopic calculation for a single dot. The macroscopic polarization is then calculated from Eq. (2.1.3) as

$$\begin{aligned} \mathbf{P}(t) &= \frac{1}{V}\sum_{\text{elem.cell}}\sum_{\nu_1\nu_2}\boldsymbol{\mu}_{\nu_1\nu_2}p_{\nu_1\nu_2} \\ &= \frac{1}{w}\Big(N_{\text{dot}}\sum_{\alpha_1\alpha_2}\boldsymbol{\mu}_{\alpha_1\alpha_2}P_{\alpha_1\alpha_2}(t) + \frac{1}{A}\sum_{\mathbf{k}}\left[\boldsymbol{\mu}_{\mathbf{k}}P_{\mathbf{k}}(t) + c.c.\right]\Big)\,. \end{aligned} \tag{3.1.5}$$

N_{dot} is the two-dimensional density of the dots in the WL plane, A is the quantization area, and w is the thickness of the active region which is determined

[1] Coulomb interaction may couple the dots, but we shall later on justify the independent dot assumption.

by the height of the QD's. We have assumed that dipole moments between dot and WL states can be neglected, and that the only non-zero inter-band dipole components between WL states exists between states of the wave vector k.

From the Semiconductor Bloch Equations we see that the field drives the polarization, which in turn drives the field. In general this set of coupled nonlinear equations known as the Maxwell-Bloch equations have to solved selfconsistently.

For the remainder of this section we shall focus on the Maxwell equations and assume the solution of the microscopic Bloch part, either as the polarization $\mathbf{P}$ or in terms of its expansion in the complex susceptibility tensor $\boldsymbol{\chi}$

$$\mathbf{P} = \epsilon_0 \boldsymbol{\chi}^{(1)} \mathbf{E} + \epsilon_0 \boldsymbol{\chi}^{(2)} \mathbf{E}\mathbf{E} + \epsilon_0 \boldsymbol{\chi}^{(3)} \mathbf{E}\mathbf{E}\mathbf{E} + \dots , \tag{3.1.6}$$

where we still suppress both spacial and time dependencies as well as integration over time variables. In an inversion symmetric material the second order nonlinear response vanishes, and as the QD's under consideration here are centrosymmetric we drop this term.

We are considering EIT experiments, which means the total electrical field consists of a probe and a coupling field $\mathbf{E} = \mathbf{E}_p + \mathbf{E}_c$ (generally) having distinct polarization and propagation directions, so that the total polarization can be written as

$$\mathbf{P} = \epsilon_0 \boldsymbol{\chi}^{(1)} \mathbf{E}_c + \epsilon_0 \boldsymbol{\chi}^{(1)} \mathbf{E}_p + \epsilon_0 \boldsymbol{\chi}^{(3)} \mathbf{E}_c \mathbf{E}_c \mathbf{E}_c + \boldsymbol{\chi}^{(3)} \epsilon_0 \mathbf{E}_p \mathbf{E}_p \mathbf{E}_p + \dots , \tag{3.1.7}$$

where the continuation ... contains all possible combinations and permutations of the electrical fields to any order.

3.2 Limiting cases

If the susceptibility depends on the spatial position either directly (material inhomogeneity) or because of a nonlinear response, usually a general explicit solution of the wave equation (3.1.3) cannot be given. Instead one would have to propagate the electromagnetic wave, i.e. solve the combined Maxwell-Bloch equations selfconsistently. In a slow light setup, this would generally be the case. What we seek here is to consider limiting cases where the wave propagation characteristics of the probe field can be found by direct solution of the Maxwell equations. First of all we shall assume the optical medium to be homogeneous. Disregarding spatial inhomogeneities means that we cannot treat reflection at interfaces, internal backscattering nor inter-dot coupling via the light field.

The next assumption we shall make is that the optical response is isotropic. This means that the resulting polarization is polarized in the same direction(s)

as the electrical field(s). We can write[2]

$$\mathbf{E} = \mathbf{E}_p + \mathbf{E}_c = \hat{\boldsymbol{e}}_p E_p + \hat{\boldsymbol{e}}_c E_c \tag{3.2.8}$$

$$\mathbf{P} = \hat{\boldsymbol{e}}_p P + \hat{\boldsymbol{e}}_c P\,, \tag{3.2.9}$$

where $\hat{\boldsymbol{e}}_p$ and $\hat{\boldsymbol{e}}_c$ are unit vectors in direction of the respective electrical fields. We have split the polarization into two parts depending on its direction. The two components both contain terms coupling probe and coupling fields. In isotropic media $\boldsymbol{\chi}^{(3)}$ terms that involve the probe field to second order generate a polarization in direction of the coupling beam[3] and vice versa, under the assumption that the probe is much weaker than the coupling terms of second and higher order in the probe field can be omitted. We can write the two polarization contributions as

$$\mathbf{P}_p = \hat{\boldsymbol{e}}_p P_p = \epsilon_0 \boldsymbol{\chi}^{(1)} \mathbf{E}_p + \epsilon_0 \boldsymbol{\chi}^{(3)} \mathbf{E}_p \mathbf{E}_c \mathbf{E}_c + \epsilon_0 \boldsymbol{\chi}^{(3)} \mathbf{E}_c \mathbf{E}_p \mathbf{E}_c + ... \tag{3.2.10}$$

$$\mathbf{P}_c = \hat{\boldsymbol{e}}_c P_c = \epsilon_0 \boldsymbol{\chi}^{(1)} \mathbf{E}_c + \epsilon_0 \boldsymbol{\chi}^{(3)} \mathbf{E}_c \mathbf{E}_c \mathbf{E}_c + \epsilon_0 \boldsymbol{\chi}^{(5)} \mathbf{E}_c \mathbf{E}_c \mathbf{E}_c \mathbf{E}_c \mathbf{E}_c + \tag{3.2.11}$$

We have introduced the probe induced polarization $\mathbf{P}_p$ and coupling induced polarization $\mathbf{P}_c$ each acting as a driving term for the corresponding electrical field. This separation is obvious if the two fields have orthogonal polarizations, but even if the two fields have the same polarization direction, one can often separate the resulting polarization response if the carrier frequencies are sufficiently far from each other. The probe induced polarization contains terms to any order in the coupling field and linear in the probe field, whereas the coupling induced polarization only contains terms to all orders in the coupling field. This allows for a simple interpretation of the two polarization contributions. We can consider this as corresponding to two different experiments/calculations; one where only the coupling field is present ($\mathbf{P}^{coupl} = \mathbf{P}_c$), and one where both probe and coupling fields are applied to the sample ($\mathbf{P}^{tot} = \mathbf{P}_c + \mathbf{P}_p$). This allows us to extract the probe induced polarization as the difference between two such calculations

$$\mathbf{P}_p = \mathbf{P}^{tot} - \mathbf{P}^{coupl}\,. \tag{3.2.12}$$

We take a step further and collect all terms linear in the probe

$$\begin{aligned} \mathbf{P}_p &= \mathbf{P}_p^L + \mathbf{P}_p^{NL} \\ &= \epsilon_0 \boldsymbol{\chi}^{(1)} \mathbf{E}_p + \epsilon_0 \boldsymbol{\chi}^{(3)} \mathbf{E}_p \mathbf{E}_c \mathbf{E}_c + \epsilon_0 \boldsymbol{\chi}^{(5)} \mathbf{E}_p \mathbf{E}_c \mathbf{E}_c \mathbf{E}_c \mathbf{E}_c + ... + \mathbf{P}_p^{NL} \\ &= \epsilon_0 \boldsymbol{\chi}_D^{(1)} \mathbf{E}_p \; + \mathbf{P}_p^{NL}\,. \end{aligned} \tag{3.2.13}$$

[2] Anisotropy effects can be neglected if the medium is sufficiently dilute so that the resulting (weak) probe induced polarization is small, which allows us to disregard the part of the electrical field generated with a polarization different to the original direction. This assumption is obviously not satisfied for the strong coupling field. The event where the anisotropy of the material results in coupling induced polarization components pointing in direction of the probe, generally has to be given the full self consistent Maxwell-Bloch treatment unless the carrier frequencies of the applied electrical fields (and thus also those of the resulting polarizations) are sufficiently far apart.

[3] For a thorough review of the susceptibility tensors in various crystal symmetries see e.g. Boyd(2003) [62].

We have shown only a few of the possible combinations between probe and coupling that contain the probe field to first order, but collected all of them into an effective "dressed" linear susceptibility $\boldsymbol{\chi}_D^{(1)}$. All higher order terms are lumped into $\mathbf{P}_p^{NL}$, which by construction is a small quantity and therefore can be disregarded. For future reference we shall adopt the scalar nature of the dressed linear susceptibility in the notation and to ease the notation even further simply use the label χ.

The coupling field is strong and therefore it experiences a non-linear system response, in general a numerical evaluation would therefore be needed. If for instance the coupling field is absorbed and thus varied spatially, the dressed susceptibility would include an explicit position dependence and thus the optical medium experienced by the probe would be inhomogeneous. We hence seek out situations where propagation effects in the coupling field can be disregarded. Such would be the case when the coupling field is c-w and propagates perpendicular to the WL plane and thus only interacts with a thin slab of material, or when the coupling field connects two empty states, thus rendering the transition transparent allowing the field to propagate without attenuation.

Slowly varying envelope (SVEA) approximation

Now focusing on the probe induced polarization, assuming the probe field propagates in the z direction and that the field amplitude is sufficiently small as to neglect non-linear effects, the expression for the electrical field and induced polarization reads

$$\mathbf{E}_p = \tfrac{1}{2}\hat{\boldsymbol{e}}_p(E_p^{(+)} + E_p^{(-)}) = \tfrac{1}{2}\hat{\boldsymbol{e}}_p\tilde{\mathcal{E}}_p e^{i(k_p z - \omega_p t)} + c.c.\,, \tag{3.2.14}$$

$$\mathbf{P}_p = \tfrac{1}{2}\hat{\boldsymbol{e}}_p(P_p^{(+)} + P_p^{(-)}) = \tfrac{1}{2}\hat{\boldsymbol{e}}_p\tilde{\mathcal{P}}_p e^{i(k_p z - \omega_p t)} + c.c.\,. \tag{3.2.15}$$

We have decomposed the electrical field and the polarization into positive and negative frequency parts and written the fields in terms of slowly varying part $\tilde{\mathcal{E}}_p$ and $\tilde{\mathcal{P}}_p$, a carrier frequency ω_p and wave number k_p. It is convenient to focus on one of the two complex fields, and we choose the positive part. Recall that the physical field is retrieved easily

$$\mathbf{E}_p = \hat{\boldsymbol{e}}_p \mathrm{Re}[E_p^{(+)}]\,, \qquad \mathbf{P}_p = \hat{\boldsymbol{e}}_p \mathrm{Re}[P_p^{(+)}]\,. \tag{3.2.16}$$

To simplify the notation we shall drop the super script and write the complex fields as E_p and P_p.

Envelope functions for the E-field and the polarization, i.e. $\tilde{\mathcal{E}}_p$ and $\tilde{\mathcal{P}}_p$, are both functions of a transverse coordinate $\mathbf{r}_t$, a longitudinal coordinate z, and a time t. In general, both envelopes are complex functions which can be expressed as follows

$$\tilde{\mathcal{E}}_p(\mathbf{r}_t, z, t) = \mathcal{E}_p(\mathbf{r}_t, z, t)e^{i\phi_p(\mathbf{r}_t, z, t)} \tag{3.2.17}$$

$$\tilde{\mathcal{P}}_p(\mathbf{r}_t, z, t) = \mathcal{P}_p(\mathbf{r}_t, z, t)e^{i\phi_p(\mathbf{r}_t, z, t)}\,, \tag{3.2.18}$$

where $\mathcal{E}_p$ and ϕ_p are a modulus and phase of $\tilde{\mathcal{E}}_p$. Under the slowly varying amplitude and phase approximations which mean that the modulus and phase of envelopes $\tilde{\mathcal{E}}_p$ and $\tilde{\mathcal{P}}_p$ both vary very slowly on scales of an optical wavelength and an optical period it follows

$$\frac{\partial \mathcal{E}_p}{\partial t} \ll \omega_p \mathcal{E}_p \,, \quad \frac{\partial \mathcal{E}_p}{\partial z} \ll k_p \mathcal{E}_p \tag{3.2.19}$$

$$\frac{\partial \phi_p}{\partial t} \ll \omega_p \phi_p \,, \quad \frac{\partial \phi_p}{\partial z} \ll k_p \phi_p \tag{3.2.20}$$

$$\frac{\partial \mathcal{P}_p}{\partial t} \ll \omega_p \mathcal{P}_p \,. \tag{3.2.21}$$

Substituting Eq. (3.2.17) into the wave equation and eliminating terms according to Eqs. (3.2.19 - 3.2.21) we end up with the paraxial wave equation for the slowly varying electrical field envelope [63]

$$\left(\nabla^2_{\mathbf{r}_t} + 2ik_p \left[\frac{\partial}{\partial z} + \frac{n_b}{c_0}\frac{\partial}{\partial t}\right]\right) \tilde{\mathcal{E}}_p(\mathbf{r}_t, z, t) = -\frac{k_p^2}{n_b^2 \epsilon_0} \tilde{\mathcal{P}}_p(\mathbf{r}_t, z, t) \,. \tag{3.2.22}$$

We have included the effect of a passive background by introducing the background refractive index n_b, which means that $k_p = \frac{\omega_p n_b}{c_0}$. The paraxial wave equation can be simplified by employing a local plane wave (i.e. annular-plane-wave) approximation under a large Fresnel number [64]. Effectively this means that instead of solving a full three-dimensional (with a transverse Laplacian included) wave equation, we can neglect the transverse Laplacian term in Eq. (3.2.22) leading to a one dimensional equation. Furthermore by transforming into the frame of a pulse moving with the reduced speed of light $c = c_0/n_b$ by introducing the delayed time $t' = t - z/v_g$ and position $z' = z$ we get the simple form for the slowly varying wave equation

$$\frac{\partial}{\partial z'} \tilde{\mathcal{E}}_p(z', t') = i \frac{\omega_p}{2 n_b \epsilon_0 c_0} \tilde{\mathcal{P}}_p(z', t') \,. \tag{3.2.23}$$

3.3 System in equilibrium

Consider a situation where only a weak probe field is interacting with the QD system. If the probe is sufficiently weak the system is unperturbed by the action of the field and remains in equilibrium. In the expression for the linear polarization response Eq. (3.1.2) perform the following transformation to new time variables t'' and τ

$$t'' = \frac{t + t'}{2} \quad \text{and} \quad \tau = t - t' \,. \tag{3.3.24}$$

In an equilibrium situation the linear response function $\chi(t'', \tau)$ cannot depend on absolute times t'', only on the relative time τ, we can therefore write the response function with only one argument $\chi(\tau)$ so that the polarization become

$$P_p(z, t) \;=\; \epsilon_0 \int_{-\infty}^{\infty} \mathrm{d}\tau \; \chi(\tau) E_p(z, t - \tau) \,, \tag{3.3.25}$$

where we assumed propagation along the z-direction and skipped the vector notation since we are dealing with a single polarization direction. Using the Wigner coordinate representation (Eq.(3.3.24)) the expression for the polarization becomes a convolution in the time domain, and consequently a product in frequency space thereby making the wave equation directly solvable. We begin by inserting the expression for the electrical field in the frequency domain[4]

$$\begin{aligned} P_p(z,t) &= \epsilon_0 \int_{-\infty}^{\infty} \frac{\mathrm{d}\omega}{2\pi} \int_{-\infty}^{\infty} \mathrm{d}\tau\ \chi(\tau) E_p(z,\omega) e^{-i\omega(t-\tau)} \\ &= \epsilon_0 \int_{-\infty}^{\infty} \frac{\mathrm{d}\omega}{2\pi}\, \chi(\omega) E_p(z,\omega) e^{-i\omega t} \qquad (3.3.26) \\ &= \int_{-\infty}^{\infty} \frac{\mathrm{d}\omega}{2\pi}\, P_p(z,\omega) e^{-i\omega t}\,, \qquad (3.3.27) \end{aligned}$$

with

$$P_p(z,\omega) = \epsilon_0 \chi(\omega) E_p(z,\omega). \qquad (3.3.28)$$

A similar relation holds for the slowly varying components since

$$\begin{aligned} E_p(z,\omega) &= \int_{-\infty}^{\infty} \mathrm{d}t\, \tilde{\mathcal{E}}_p(z,t) e^{i(k_p z - \omega_p t)} e^{i\omega t} \\ &= e^{ik_p z} \tilde{\mathcal{E}}_p(z,\Omega)\,, \text{ with } \Omega = \omega - \omega_p\,. \qquad (3.3.29) \end{aligned}$$

Inserting this into Eq. (3.3.26) and using the definition of the slowly varying fields according to Eq. (3.2.15 and 3.2.15) we get

$$\begin{aligned} \tilde{\mathcal{P}}_p(z,t) &= \epsilon_0 \int_{-\infty}^{\infty} \frac{\mathrm{d}\omega}{2\pi}\, \chi(\omega) \tilde{E}_p(z,\Omega) e^{-i(\omega-\omega_p)t} \\ &= \epsilon_0 \int_{-\infty}^{\infty} \frac{\mathrm{d}\Omega}{2\pi}\, \chi(\Omega+\omega_p) \tilde{E}_p(z,\Omega) e^{-i\Omega t}\,, \qquad (3.3.30) \end{aligned}$$

allowing us to identify the relation between the Fourier transform of the slowly varying components

$$\tilde{\mathcal{P}}_p(z,\Omega) = \epsilon_0 \chi(\Omega+\omega_p) \tilde{\mathcal{E}}_p(z,\Omega)\,. \qquad (3.3.31)$$

[4] We introduced the Fourier transformation $f(\omega)$ of a function $f(t)$ as

$$f(t) = \int_{-\infty}^{\infty} \frac{\mathrm{d}\omega}{2\pi}\, f(\omega) e^{-i\omega t}\,,\ f(\omega) = \int_{-\infty}^{\infty} \mathrm{d}t\ f(t) e^{i\omega t}\,.$$

The slowly varying wave equation in frequency space thus becomes

$$\begin{aligned}\frac{\partial}{\partial z'}\tilde{\mathcal{E}}_p(z',\Omega) = i\frac{\omega_p}{2n_b c_0}\tilde{\mathcal{P}}_p(z',\Omega) = i\frac{\omega_p}{2n_b c_0}\chi(\Omega+\omega_p)\tilde{\mathcal{E}}_p(z',\Omega)\\ \Downarrow\\ \tilde{\mathcal{E}}_p(z',\Omega) = \tilde{\mathcal{E}}_p(0,\Omega)e^{i\frac{\omega_p}{2n_b c_0}\chi(\Omega+\omega_p)z'}\,.\end{aligned} \tag{3.3.32}$$

Inserting this expression back into Eq. (3.3.29) shows that the wave propagates with the complex[5] propagation constant $k(\omega)$ given by

$$k(\omega) = \frac{\omega_p}{c_0}\left(n_b + \frac{\chi(\omega)}{2n_b}\right)\,. \tag{3.3.33}$$

Wave propagation characteristics such as absorption and refraction can thus be directly related to the susceptibility $\chi(\omega)$. The intensity of the electrical field is proportional to the absolute square of the electrical field

$$\begin{aligned}I_p(z,\omega) \propto& |E_p(z,\omega)|^2\\ \propto& E_p(0,\omega)^2 e^{ik(\omega)z}e^{-ik(\omega)^* z}\\ =& I(0,\omega)e^{-2\mathrm{Im}[k(\omega)]z} = I_p(0,\omega)e^{-\alpha(\omega)z}\,,\end{aligned} \tag{3.3.34}$$

thus the intensity is attenuated with the absorption coefficient

$$\alpha(\omega) = 2\mathrm{Im}[k(\omega)] = \frac{\omega_p}{c_0}\frac{\chi''(\omega)}{n_b}\,. \tag{3.3.35}$$

The wave number of the probe field is real part of the propagation constant

$$k'(\omega) = \frac{\omega_p}{c_0}n(\omega)\,, \tag{3.3.36}$$

with refractive index

$$n(\omega) = n_b + \frac{\chi'(\omega)}{2n_b}\,. \tag{3.3.37}$$

In the stationary frame the probe envelope propagates with the group velocity defined by

$$v_g = \frac{c_0}{n(\omega_p) + \omega_p \left.\frac{\partial n(\omega)}{\partial\omega}\right|_{\omega=\omega_p}}\,. \tag{3.3.38}$$

As long as the first derivative of the refractive index remains constant within the spectral bandwidth of the pulse we can speak of a definite group velocity, if this is not the case the probe pulse will not retain its shape and the concept of group velocity becomes cluttered.

[5] For a complex quantity we adopt the following notation for the real and imaginary part: $k(\omega) = k'(\omega) + ik''(\omega)$.

From the group velocity the general concept of transit time T through an optical medium of length L can be considered

$$T = L/v_g. \tag{3.3.39}$$

We define a slow-down factor S as the ratio of the transit time through the medium to the to the transit time of the same pulse traveling the same distance in vacuum:

$$S = \frac{T}{T_{vac}} = \frac{c_0}{v_g} = n(\omega_p) + \omega_p \left.\frac{\partial n(\omega)}{\partial \omega}\right|_{\omega=\omega_p}. \tag{3.3.40}$$

By making $\partial n(\omega)/\partial\omega$ large and positive we can achieve slow light. Slow light effects make use of the rapid variation in the refractive index that occurs in the vicinity of a material resonance. The maximum slowdown is found at the frequency for which the slope of the refractive index is largest. Notice, that the slowdown factor obtained away from resonance ($\frac{\partial n'}{\partial \omega} \approx 0$) is given by the background refractive index.

To conclude this section we mention that $\chi(\omega)$ can be found using Eq. (3.3.28). Inserting the expression for the field we note that the explicit spatial dependence drops out and $\chi(\omega)$ can be extracted from the Semiconductor Bloch equations as the ratio between the polarization and the applied electrical field in the frequency domain: $\chi(\omega) = \frac{P_p(\omega)}{\epsilon_0 E_p(\omega)}$.

3.4 System in non-equilibrium

If the system is driven out of equilibrium, e.g. by the action of a coupling beam in an EIT experiment, the system response changes drastically from the simple picture discussed above. The dressed linear response function, which we shall refer to simply as $\chi(t, t')$ is now a genuine two time function. This means the material response to a particular frequency is no longer unique, it now depends on the physical situation, i.e. both coupling and probe fields. In a stationary system the polarization response at a given frequency is proportional only to the probe pulse spectrum at that frequency not its temporal development, this is generally not case in non-equilibrium. We can always write the Fourier transform of the polarization as

$$P_p(\omega) = \epsilon_0 \int_{-\infty}^{\infty} \mathrm{d}t' \, \chi(\omega, t') E_p(t') \, , \tag{3.4.41}$$

where $\chi(\omega, t')$ is the dynamical system response Fourier transformed with respect to the first argument. We see that the response at a given frequency depends on the temporal evolution of the probe field $E_p(t)$. In the following we shall consider two different regimes of a non-equilibrium situation. The steady state regime, where, in certain cases, the system response is governed by the

single time susceptibility and the genuinely transient regime, where the system response function is a function of two times. Whichever regime is relevant depends on the coupling field.

3.4.1 Transient system response

If the action of the coupling beam is such that the system never approaches a steady state we are in the transient regime. This criterion is set by the dephasing time, so that a transient situation is addressed when the coupling pulse duration is comparable to, or less than, the dephasing time. As a result of the transient behavior, the wave equation cannot be directly solved. Only in the limit of an optically thin material, where propagation effects can be disregarded, one can derive expressions for absorption and refraction. Therefor wave propagation characteristics, such as slowdown factors, which in principle can be extracted in the thin sample limit approach cannot be related to actual wave propagation. Instead one should rather be solving the combined Maxwell-Bloch equations.

We shall consider two different situations where quantities such as absorption and refraction can be derived. Depending on the probe field we get either a frequency or a time dependent absorption coefficient.

Finite probe: Frequencial absorption coefficient $\alpha(\omega; E_p(t))$

Consider the slowly varying wave equation in the frequency domain, i.e. the Fourier transform of Eq. (3.2.23). For a sufficiently thin sample one can use a first order Taylor expansion as a forward discretization scheme

$$\begin{aligned}\tilde{\mathcal{E}}_p(z'+\Delta z,\Omega) &\simeq \tilde{\mathcal{E}}_p(z',\Omega)+\frac{\partial}{\partial z}\tilde{\mathcal{E}}_p(z',\Omega)\Delta z \\ &= \tilde{\mathcal{E}}_p(z',\Omega)+i\frac{\omega_p}{2n_b\epsilon_0 c_0}\tilde{\mathcal{P}}_p(z',\Omega)\Delta z \\ &= \tilde{\mathcal{E}}_p(z',\Omega)\left[1+i\frac{\omega_p}{2n_b\epsilon_0 c_0}\frac{\tilde{\mathcal{P}}_p(z',\Omega)}{\tilde{\mathcal{E}}_p(z',\Omega)}\Delta z\right] . \end{aligned} \tag{3.4.42}$$

If we know $\tilde{\mathcal{E}}_p(z'=0,\Omega)$ and $\tilde{\mathcal{E}}_p(z'=L,\Omega)$ we may, in general define the complex propagation constant:

$$\tilde{\mathcal{E}}_p(L,\Omega)=\tilde{\mathcal{E}}_p(0,\Omega)e^{ik(\Omega)L} . \tag{3.4.43}$$

For small $L=\Delta z$ we have

$$\tilde{\mathcal{E}}_p(\Delta z,\Omega)=\tilde{\mathcal{E}}_p(0,\Omega)\left[1+ik(\Omega)\Delta z\right] , \tag{3.4.44}$$

and by comparing to Eq. (3.4.42) and inserting into the full expression for electrical field we find

$$k(\omega)=\frac{\omega_p}{c_0}\left(n_b+\frac{1}{2n_b}\frac{\tilde{\mathcal{P}}_p(z',\Omega)}{\epsilon_0\tilde{\mathcal{E}}_p(z',\Omega)}\right) . \tag{3.4.45}$$

What this equation tells us is that we can find the dynamic absorption and refraction spectra for any probe pulse in the same manner as we find the susceptibility for stationary systems. Namely by calculating $P_p(t)$ from the SBE, performing a Fourier transform and dividing by the probe spectrum. Also it is apparent that the system response function is not something one can get at easily, it is buried within an integral. Absorption and refraction for a finite probe pulse are found from Eq. (3.4.45) as:

$$\begin{aligned}\alpha(\omega;E_p(t)) &= \frac{\omega}{c_0 n_b}\mathrm{Im}\left[\frac{P_p(\omega)}{\epsilon_0 E_p(\omega)}\right] = \frac{\omega}{c_0 n_b}\mathrm{Im}\left[\frac{\epsilon_0\int_{-\infty}^{\infty}\mathrm{d}t\ \chi(\omega,t)E_p(t)}{\epsilon_0 E_p(\omega)}\right] \\ &= \frac{\omega}{c_0 n_b}\mathrm{Im}\left[\chi_{\mathrm{eff}}(\omega;E_p(t))\right]\ , \qquad (3.4.46)\\ n(\omega;E_p(t)) &= n_b + \frac{1}{2n_b}\mathrm{Re}\left[\frac{P_p(\omega)}{\epsilon_0 E_p(\omega)}\right] = n_b + \frac{1}{2n_b}\mathrm{Re}\left[\frac{\epsilon_0\int_{-\infty}^{\infty}\mathrm{d}t\ \chi(\omega,t)E_p(t)}{\epsilon_0 E_p(\omega)}\right] \\ &= n_b + \frac{\omega}{c_0 n_b}\mathrm{Re}\left[\chi_{\mathrm{eff}}(\omega;E_p(t))\right]\ . \qquad (3.4.47)\end{aligned}$$

To connect to the equilibrium results we have defined the effective susceptibility $\chi_{\mathrm{eff}}(\omega;E_p(t)) \equiv \frac{P_p(\omega)}{\epsilon_0 E_p(\omega)}$ which we generally shall refer to as simply the susceptibility. This quantity isnot unique because it depends on both the coupling beam and the shape and time of application of the probe beam. Note, that in the equilibrium limit the expression for the effective susceptibility equals that of the original susceptibility.

Continuous wave probe: Temporal absorption coefficient $\tilde{\alpha}(t;\omega_p)$

Consider the slowly varying wave equation in the time domain, i.e. Eq. (3.2.23). In the thin sample limit, one can apply similar arguments as above to find

$$\tilde{\mathcal{E}}_p(z'+\Delta z,t') = \tilde{\mathcal{E}}_p(z',t')\left[1 + i\frac{\omega_p}{2n_b\epsilon_0 c_0}\frac{\tilde{\mathcal{P}}_p(z',t')}{\tilde{\mathcal{E}}_p(z',t')}\right]\ . \qquad (3.4.48)$$

Corresponding to a slowly varying temporal absorption coefficient

$$\tilde{\alpha}(t) = \frac{\omega_p}{c_0 n_b}\mathrm{Im}\left[\frac{\tilde{\mathcal{P}}_p(z',t')}{\epsilon_0\tilde{\mathcal{E}}_p(z',t')}\right]\ . \qquad (3.4.49)$$

When employing a c-w probe field this can be interpreted as the instantaneous system response at time t at the probe frequency, i.e. $\tilde{\alpha}(t;\omega_p)$.

One could be inclined to think that calculating the system response using c-w probes of various frequencies could be superimposed to get the system response to a wavepacket. This is of course the case in equilibrium, but as we saw from the treatment above, calculating the system response to a probe pulse based on the response to a superposition of plane waves would not hold, since in the transient regime the system response depends on the temporal development of the probe field. As we seek to model slow light EIT experiments, which inevitably involves a probe pulse, that per se excludes the c-w probe approach.

3.4.2 Steady state system response

If the QD system is driven out of equilibrium by a continuous wave (c-w) coupling beam of frequency Ω the system will eventually reach a steady state with respect to some rotating frame. Floquet theory provides a tool to systematically describe the states in a system that is driven by a time periodic field. It is the temporal analogue of what Bloch theory is for spatially periodic systems (for a review see e.g. [65]). Consider a system governed by the time periodic Hamiltonian $H(t) = H(t+T)$. The Floquet states are periodic with period T and are thus the steady states of the system, in the sense that if a state is prepared in a Floquet state it remains there. Due to the periodic coupling field $\chi(t,t')$ the susceptibility function, which essentially is two-particle correlation function, can be expanded in Floquet states so that it can effectively be written as

$$\begin{aligned}\chi(t,t') =& \sum_n \chi_n(t-t')e^{in\Omega(t+t')} \\ =& \chi_0(t-t') + \sum_{n\neq 0} \chi_n(t-t')e^{in\Omega(t+t')}\,, \end{aligned} \tag{3.4.50}$$

The difference time functions $\chi_n(t-t')$ is found by solving for the Floquet components in the expansion of the microscopic correlation function, but we are here merely interested in arguing on basis of their general properties. It is obvious that if we can disregard the higher order terms, the susceptibility is a function of time differences only and all results from the equilibrium treatment carries over and the c-w coupling situation can be used for wave propagation characterization.

The second term of Eq. (3.4.50) gives rise to sideband generation spaced by the driving frequency Ω. To see this consider the probe induced polarization

$$P_p(t) = \epsilon_0 \int_{-\infty}^{\infty} \mathrm{d}t' \left[\chi_0(t-t') + \sum_{n\neq 0} \chi_n(t-t')e^{in\Omega(t+t')}\right] E_p(t')\,. \tag{3.4.51}$$

Assume a probe field of the form $E_p(t) = \sum_j E_j e^{-i\omega_j t}$, where E_j are the components of a Fourier expansion.

$$\begin{aligned} P_p(t) =& \epsilon_0 \int_{-\infty}^{\infty} \mathrm{d}t' \sum_{n,j} \chi_n(t-t')e^{in\Omega(t+t')}E_j e^{-i\omega_j t'} \\ =& \epsilon_0 \sum_{n,j} E_j e^{-i(\omega_j - n\Omega)t} \int_{-\infty}^{\infty} \mathrm{d}t'\, \chi_n(t-t')e^{i(\omega_j - n\Omega)(t-t')} \\ =& \epsilon_0 \sum_{n,j} E_j e^{-i(\omega_j - n\Omega)t} \chi_n(\omega_j - n\Omega)\,. \end{aligned} \tag{3.4.52}$$

If the probe and coupling frequencies are comparable, sidebands will be generated far from the central frequency of the probe, under the assumption that the

probe is spectrally narrow and that the functions χ_n mainly have contributions around the central frequency, the sidebands will therefore not have any weight in the spectral area of the probe beam. On the other hand, if the probe field is spectrally wide it will contain frequency components at the sideband frequencies and is thus able to "talk" to the side bands. Another way to think of this is, that if the probe is temporally short enough it can resolve the optical period imposed by driving field. Even in the event of a c-w probe, if the sidebands are generated close enough to the central frequency then one cannot disregard their contribution and one has a transient situation.

A practical way to check if one can disregard the sidebands, is to calculate the ratio $\frac{P_p(\omega)}{\epsilon E_p(\omega)}$ for probe beams of varying length and time of application. If the above assumption is not valid the dynamical responses would differ, on the other hand if the responses are identical is means that the ratio $\frac{P_p(\omega)}{\epsilon E_p(\omega)}$ can be related to a single time susceptibility, and thus can be used for propagation characterization. Disregarding the sidebands is common practice in atomic physics based treatments [63,66], in which the rotating wave approximation is performed. The validity of the rotating wave approximation can only be assumed for spectrally narrow pulses and when the coupling and probe transitions are comparable, however in semiconductors the two incident fields can have significantly different frequencies thus rendering the atomic treatment, and the rotating wave approximation, moot.

Chapter 4

EIT - atomic approach

In this chapter we present the simplest model one can use to describe QD EIT phenomena - the non-interacting atomic three-level model. Within this model, in steady state using a c-w probe field, one can derive an analytical expression for the susceptibility. This furthermore allows for a rudimentary treatment of inhomogeneous broadening effects that occur in a QD array and their impact on EIT.

4.1 Semi-classical atomic, continuous wave approach

As the quantum dot is usually described as an "artificial" atom, it is natural to extend the treatment from atomic physics to the semiconductor regime considering the QD as an isolated three-level system disregarding many-body interactions. We here discuss the case where the energy levels are arranged in the so called Ladder-scheme (see Fig. 4.1), the derivation follows a similar pattern for the two other configurations and is textbook material, see e.g. [67]. An intense near resonant c-w electromagnetic field, termed the coupling field, drives the $|2\rangle$-$|3\rangle$ transition. Another also near resonant, but much weaker c-w probe field, is applied to the $|1\rangle$-$|2\rangle$ transition. It is assumed that the two fields cannot drive each others transitions, e.g. due to angular momentum selection rules and that the transition $|1\rangle$-$|3\rangle$ is dipole forbidden.

The Hamiltonian governing the system is in first quantization:

$$H = H_0 + H_{c-f}, \text{ where} \tag{4.1.1}$$

$$H_{c-f} = -\boldsymbol{\mu} \cdot \boldsymbol{E}(t). \tag{4.1.2}$$

H_0 is the electronic Hamiltonian of the QD in absence of any fields, with eigenvalues $\hbar\omega_1, \hbar\omega_2$ and $\hbar\omega_3$. H_{c-f} represents the carrier-field interaction within the dipole approximation. The electronic dipole moment operator $\boldsymbol{\mu}$ and its matrix

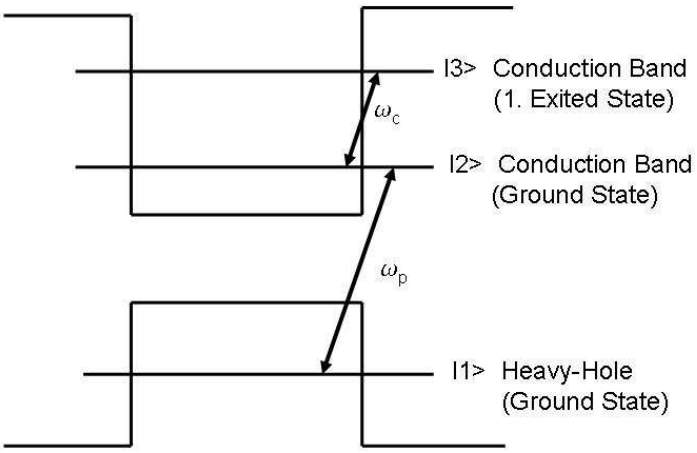

***Figure 4.1**: Generic example of a Ladder scheme in a quantum dot.*

elements in the basis of the bare states are defined by

$$\boldsymbol{\mu} = e\boldsymbol{r} \tag{4.1.3}$$

$$\boldsymbol{\mu}_{ij} = e\langle i|\boldsymbol{r}|j\rangle, \tag{4.1.4}$$

here e is the electron charge and $i, j = 1, 2, 3$.

The electrical fields are written as a superposition of standing waves:

$$\mathbf{E}(t) = \tfrac{1}{2}\sum_k \boldsymbol{E}_k \left(\mathrm{e}^{-i\omega_k t} + \mathrm{e}^{i\omega_k t}\right) \tag{4.1.5}$$

The summation should be taken over indices p and c, so that $\boldsymbol{E}_k = \hat{e}_k E_k$ and ω_k represents the direction, magnitude and frequency of either the probe or the coupling field.

Next we insert the expression for the electrical fields into H_{c-f}. Writing the Hamiltonian in the bare state basis, we get:

$$\begin{aligned} H_{c-f} = & -\hbar\Big[\Omega_c(\mathrm{e}^{-i\omega_c t} + \mathrm{e}^{i\omega_c t})|3\rangle\langle 2| \\ & +\Omega_p(\mathrm{e}^{-i\omega_p t} + \mathrm{e}^{i\omega_p t})|2\rangle\langle 1| + \mathrm{h.c.}\Big]. \end{aligned} \tag{4.1.6}$$

We have introduced the complex Rabi frequencies of the coupling $\Omega_c = \frac{\boldsymbol{\mu}_{32}\cdot\boldsymbol{E}_c}{2\hbar}$ and probe $\Omega_p = \frac{\boldsymbol{\mu}_{21}\cdot\boldsymbol{E}_p}{2\hbar}$ fields.

It is useful to move to the interaction picture, thereby letting the time evolution of the state vector depend only on the interaction Hamiltonian H_{c-f}. The interaction picture Hamiltonian H_{c-f}^{int} is obtained through the unitary transformation

$$H_{c-f}^{\mathrm{int}} = U_0^{\dagger} H_{c-f} U_0, \text{ where} \tag{4.1.7}$$

$$U_0 = \mathrm{e}^{-iH_0 t/\hbar}. \tag{4.1.8}$$

Applying the transformation, we get

$$\begin{aligned} H_{c-f}^{\text{int}} &= -\hbar\Big[\Omega_c e^{i\omega_3 t}e^{-i\omega_2 t}(e^{-i\omega_c t}+e^{i\omega_c t})|3\rangle\langle 2| + \\ &\quad +\Omega_p e^{i\omega_2 t}e^{-i\omega_1 t}(e^{-i\omega_p t}+e^{i\omega_p t})|2\rangle\langle 1| + \text{h.c.}\Big] \\ &= -\hbar\Big[\Omega_c e^{i\Delta_c t}|3\rangle\langle 2| + \Omega_p e^{i\Delta_p t}|2\rangle\langle 1| + \text{h.c.}\Big]. \end{aligned} \tag{4.1.9}$$

In the last step we used the rotating wave approximation, which amounts to keeping only the most energy-conserving terms in the Hamiltonian. Also, we defined the coupling and probe laser detunings as $\Delta_c = \omega_{32} - \omega_c$ and $\Delta_p = \omega_{21} - \omega_p$, where $\omega_{32} = \omega_3 - \omega_2$ and $\omega_{21} = \omega_2 - \omega_1$ are the transition frequencies.

The coherent dynamics of the system is derived from the density matrix [67] [68]

$$\left.\frac{d}{dt}\rho_{ij}\right|_{coh} = -i/\hbar[H_{c-f}^{\text{int}}, \rho]_{ij}\,, \tag{4.1.10}$$

while the incoherent or scattering part is incorporated as [1]

$$\left.\frac{d}{dt}\rho_{11}\right|_{scatt} = \Gamma_{21}\rho_{11} \tag{4.1.11}$$

$$\left.\frac{d}{dt}\rho_{22}\right|_{scatt} = (\Gamma_{32}-\Gamma_{21})\rho_{22} \tag{4.1.12}$$

$$\left.\frac{d}{dt}\rho_{33}\right|_{scatt} = -\Gamma_{32}\rho_{33} \tag{4.1.13}$$

$$\left.\frac{d}{dt}\rho_{21}\right|_{scatt} = -(\frac{1}{2}\Gamma_{21}+\gamma_{21}^{\text{ph}})\rho_{21} \tag{4.1.14}$$

$$\left.\frac{d}{dt}\rho_{31}\right|_{scatt} = -(\frac{1}{2}\Gamma_{32}+\gamma_{31}^{\text{ph}})\rho_{31} \tag{4.1.15}$$

$$\left.\frac{d}{dt}\rho_{32}\right|_{scatt} = -(\frac{1}{2}\Gamma_{21}+\frac{1}{2}\Gamma_{32}+\gamma_{32}^{\text{ph}})\rho_{32}. \tag{4.1.16}$$

In light of the atomic treatment we have included Γ_{ij} that describe the population transfer rate from state $|i\rangle$ to $|j\rangle$ and γ_{ij}^{ph} which is the linewidth broadening due to "pure" dephasing. This should be taken in the sense that the transverse relaxation rate T_2 of a given transition is defined as:

$$\frac{1}{T_2} = \frac{1}{2T_1}+\frac{1}{T_2^*}, \tag{4.1.17}$$

where the pure dephasing $\frac{1}{T_2^*}$ corresponds to γ_{ij}^{ph} of that transition. The two broadening effects above can be collected in one total decoherence rate $\gamma_{ij} = \frac{1}{T_2}$, in other words; one effective rate of decay of the polarizations

$$\gamma_{ij} = \frac{1}{2}(\gamma_i+\gamma_j)+\gamma_{ij}^{\text{ph}}, \tag{4.1.18}$$

where $1/\gamma_i$ is the lifetime of the i'th state; $\gamma_i = \sum_l \Gamma_{il}$.

[1] Since ρ is Hermitian, we here list only the lower half of the off-diagonal elements.

The equations of motion for the density matrix become:

$$\frac{d}{dt}\rho_{11} = i\Omega_p^* \mathrm{e}^{-i\Delta_p t}\rho_{21} - i\Omega_p \mathrm{e}^{i\Delta_p t}\rho_{12} + \Gamma_{21}\rho_{22} \tag{4.1.19}$$

$$\frac{d}{dt}\rho_{22} = i\Omega_p \mathrm{e}^{i\Delta_p t}\rho_{12} + i\Omega_c^* \mathrm{e}^{-i\Delta_c t}\rho_{32} - i\Omega_p^* \mathrm{e}^{-i\Delta_p t}\rho_{21} - i\Omega_c \mathrm{e}^{i\Delta_c t}\rho_{23} + \\ +(\Gamma_{32} - \Gamma_{21})\rho_{22} \tag{4.1.20}$$

$$\frac{d}{dt}\rho_{33} = i\Omega_c \mathrm{e}^{i\Delta_c t}\rho_{23} - i\Omega_c^* \mathrm{e}^{-i\Delta_c t}\rho_{32} - \Gamma_{32}\rho_{33} \tag{4.1.21}$$

$$\frac{d}{dt}\rho_{21} = i\Omega_p \mathrm{e}^{i\Delta_p t}(\rho_{11} - \rho_{22}) + i\Omega_c^* \mathrm{e}^{-i\Delta_c t}\rho_{31} - \gamma_{21}\rho_{21} \tag{4.1.22}$$

$$\frac{d}{dt}\rho_{31} = i\Omega_c \mathrm{e}^{i\Delta_c t}\rho_{21} - i\Omega_p \mathrm{e}^{i\Delta_p t}\rho_{32} - \gamma_{31}\rho_{31} \tag{4.1.23}$$

$$\frac{d}{dt}\rho_{32} = i\Omega_s^* \mathrm{e}^{-i\Delta_p t}\rho_{31} + i\Omega_c \mathrm{e}^{i\Delta_c t}(\rho_{22} - \rho_{33}) - \gamma_{32}\rho_{32} \tag{4.1.24}$$

In order to find the system response to the probe field, we look at the probe induced polarization. The total polarization is according to Eq. (3.1.5)

$$\mathbf{P}(t) = \frac{1}{w} N_{\mathrm{dot}} \left(\boldsymbol{\mu}_{12}\rho_{21} e^{-i\omega_{31}t} + \boldsymbol{\mu}_{23}\rho_{32} e^{-i\omega_{32}t} + \mathrm{c.c.} \right) . \tag{4.1.25}$$

We have used that the system is constructed so that only transitions $|1\rangle - |2\rangle$ and $|2\rangle - |3\rangle$ are dipole allowed. Furthermore, the time dependent exponentials represent the conversion of ρ back into the Schrödinger picture.

In the atomic approach it is assumed that one can use the equilibrium response when calculating the susceptibility. In other words we can use Eq. (3.3.25) from which it follows that the probe induced polarization is

$$\begin{aligned} \mathbf{P}_p(t) &= \epsilon_0 \int_{-\infty}^{\infty} \mathrm{d}\tau \ \chi(\tau)\mathbf{E}_p(t-\tau) \\ &= \frac{1}{2}\epsilon_0 \chi(\omega_p)\boldsymbol{E}_p \, e^{-i\omega_p t} + \mathrm{c.c.}\,, \end{aligned} \tag{4.1.26}$$

By comparing the two expressions for the polarization considering terms that are directed along the probe field polarization direction and oscillate near the probe frequency, we see that the susceptibility can be extracted as

$$\begin{aligned} \frac{1}{w} N_{\mathrm{dot}}\mu_{12}\rho_{21} e^{-i\omega_{31}t} &= \frac{1}{2}\epsilon_0 \chi(\omega_p) E_p \, e^{-i\omega_p t} \\ &\Downarrow \\ \chi(\omega_p) &= \frac{2}{w} N_{\mathrm{dot}} \epsilon_0 E_p \mathrm{e}^{-i\Delta_p t}\mu_{12}\rho_{21}. \end{aligned} \tag{4.1.27}$$

To find the ρ_{21} component we need to solve the system of coupled differential equations defined by equations (4.1.19)-(4.1.24). First we eliminate the exponential time dependencies by defining the slow-varying density matrix components

$\tilde{\rho}_{ij}$ as

$$\rho_{21} = \tilde{\rho}_{21}e^{i\Delta_p t} \quad (4.1.28)$$
$$\rho_{31} = \tilde{\rho}_{31}e^{i(\Delta_p+\Delta_c)t} \quad (4.1.29)$$
$$\rho_{32} = \tilde{\rho}_{32}e^{i\Delta_c t}. \quad (4.1.30)$$

As for the diagonal components, they remain unchanged.

The equations of motion for the density matrix now become

$$\frac{d}{dt}\rho_{11} = i\Omega_p^*\tilde{\rho}_{21} - i\Omega_p\tilde{\rho}_{12} + \Gamma_{21}\rho_{22} \quad (4.1.31)$$
$$\frac{d}{dt}\rho_{22} = i\Omega_p\tilde{\rho}_{12} + i\Omega_c^*\tilde{\rho}_{32} - i\Omega_p^*\tilde{\rho}_{21} - i\Omega_c\tilde{\rho}_{23} + (\Gamma_{32} - \Gamma_{21})\rho_{22} \quad (4.1.32)$$
$$\frac{d}{dt}\rho_{33} = i\Omega_c\tilde{\rho}_{23} - i\Omega_c^*\tilde{\rho}_{32} - \Gamma_{32}\rho_{33} \quad (4.1.33)$$
$$\frac{d}{dt}\tilde{\rho}_{21} = i\Omega_p(\rho_{11} - \rho_{22}) + i\Omega_c^*\tilde{\rho}_{31} - (\gamma_{21} + i\Delta_p)\tilde{\rho}_{21} \quad (4.1.34)$$
$$\frac{d}{dt}\tilde{\rho}_{31} = i\Omega_c\tilde{\rho}_{21} - i\Omega_p\tilde{\rho}_{32} - \big(\gamma_{31} + i(\Delta_p + \Delta_c)\big)\tilde{\rho}_{31} \quad (4.1.35)$$
$$\frac{d}{dt}\tilde{\rho}_{32} = i\Omega_s^*\tilde{\rho}_{31} + i\Omega_c(\rho_{22} - \rho_{33}) - (\gamma_{32} + i\Delta_c)\tilde{\rho}_{32}. \quad (4.1.36)$$

This set of equations cannot be solved analytically. However, we are at the moment not interested in transient behavior, only in the steady state. The steady state solution can be found by solving the homogeneous linear system of equations, but a few simplifying approximations can be made, so as to get a nice short analytical answer.

We assume that $|\Omega_p| \ll |\Omega_c|$, that is, the probe field is much weaker than the coupling field. If we expand the master equation in terms of Ω_p, the weak field allows us to keep only terms of the lowest orders. Another consequence is that only a very small fraction of the population is contained within the exited states. Given the initial condition; the unexcited QD, we find, by inspection, for the diagonal elements

$$\rho_{11} = 1 - \mathcal{O}(|\Omega_p|^2) + ... \quad (4.1.37)$$
$$\rho_{22} = \mathcal{O}(|\Omega_p|^2) + ... \quad (4.1.38)$$
$$\rho_{33} = \mathcal{O}(|\Omega_p|^2) + ... \quad (4.1.39)$$
$$(4.1.40)$$

Since we are looking for the linear response, we need only keep terms to first order in the probe field. And so the diagonal elements become

$$\rho_{11} \simeq 1 \quad (4.1.41)$$
$$\rho_{22} = \rho_{33} \simeq 0. \quad (4.1.42)$$

This approximation can only be made for non-carrier exciting schemes. The reason is that the strong coupling laser would otherwise pump carriers from the

ground state $|1\rangle$ into one of the excited states and the assumption $\rho_{11} \simeq 1$ would not be valid.

Using the above expansion, keeping only the lowest order components, we get for the equations for the off-diagonal elements

$$\begin{aligned}
0 &= i\Omega_p(1-0) + i\Omega_c^*\tilde{\rho}_{31} - (\gamma_{21} + i\Delta_p)\tilde{\rho}_{21} && (4.1.43)\\
0 &= i\Omega_c\tilde{\rho}_{21} - i\Omega_p\tilde{\rho}_{32} - \big(\gamma_{31} + i(\Delta_p + \Delta_c)\big)\tilde{\rho}_{31} && (4.1.44)\\
0 &= i\Omega_p^*\tilde{\rho}_{31} + i\Omega_c(0-0) - (\gamma_{32} + i\Delta_c)\tilde{\rho}_{32} && (4.1.45)\\
&\Downarrow \\
\tilde{\rho}_{21} &= i\frac{\Omega_p + \Omega_c^*\tilde{\rho}_{31}}{\gamma_{21} + i\Delta_p} && (4.1.46)\\
\tilde{\rho}_{31} &= i\frac{\Omega_c\tilde{\rho}_{21} - \Omega_p\tilde{\rho}_{32}}{\gamma_{31} + i(\Delta_p + \Delta_c)}. && (4.1.47)\\
\dot{\tilde{\rho}}_{32} &= i\frac{\Omega_p^*\tilde{\rho}_{31}}{(\gamma_{32} + i\Delta_c)} && (4.1.48)
\end{aligned}$$

This closed set of equations is further reduced by noting that the second term in the numerator of (4.1.47) has an $O(|\Omega_p|^2)$ dependency, and thus can be dropped. We end up with the following coupled set of equations:

$$\begin{aligned}
\tilde{\rho}_{21} &= i\frac{\Omega_p + \Omega_c^*\tilde{\rho}_{31}}{\gamma_{21} + i\Delta_p} && (4.1.49)\\
\tilde{\rho}_{31} &= i\frac{\Omega_c\tilde{\rho}_{21}}{\gamma_{31} + i(\Delta_p + \Delta_c)}. && (4.1.50)
\end{aligned}$$

Solving for $\tilde{\rho}_{21}$ and multiplying by $\mathrm{e}^{i\Delta_p t}$ to transform back to the original density matrix component

$$\begin{aligned}
\rho_{21} &= i\frac{\mathrm{e}^{i\Delta_p t}\Omega_p}{\gamma_{21} + i\Delta_p}\frac{1}{1 + \frac{|\Omega_c|^2}{(\gamma_{31}+i(\Delta_p+\Delta_c))(\gamma_{21}+i\Delta_p)}}\\
&= i\mathrm{e}^{i\Delta_p t}\Omega_p\frac{\gamma_{31} + i(\Delta_p + \Delta_c)}{(\gamma_{31} + i(\Delta_p + \Delta_c))(\gamma_{21} + i\Delta_p) + |\Omega_c|^2}. && (4.1.51)
\end{aligned}$$

The final expression for the susceptibility is found by inserting into (4.1.27)

$$\begin{aligned}
\chi(\omega) &= i\frac{2N_{\mathrm{dot}}}{w\epsilon_0 E_p}\mu_{12}\Omega_p\frac{\gamma_{31} + i(\Delta_p + \Delta_c)}{(\gamma_{31} + i(\Delta_p + \Delta_c))(\gamma_{21} + i\Delta_p) + |\Omega_c|^2}\\
&= i\frac{N_{\mathrm{dot}}|\mu_{12}|^2}{w\epsilon_0}\frac{\gamma_{31} + i(\Delta_p + \Delta_c)}{(\gamma_{31} + i(\Delta_p + \Delta_c))(\gamma_{21} + i\Delta_p) + |\Omega_c|^2}\,. && (4.1.52)
\end{aligned}$$

In the last step we used the definition of the Rabi frequency.

4.2 EIT features

In this section we will examine the central features of the susceptibility of an EIT medium. A thorough discussion can also be found in [66]. We focus on

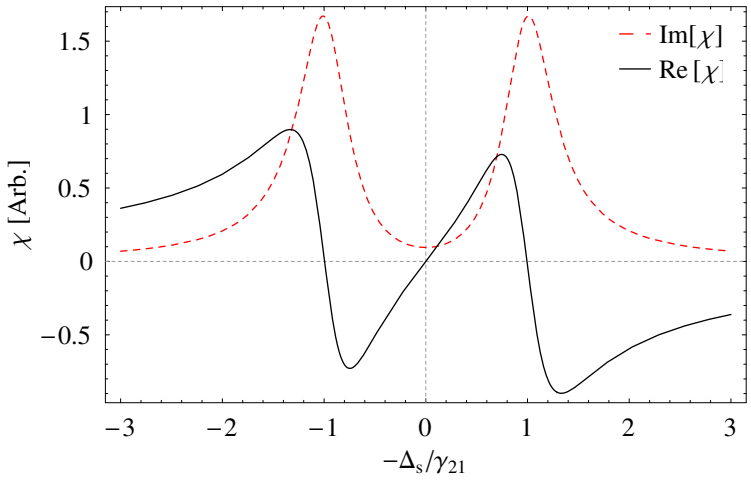

Figure 4.2: *Real (χ') and imaginary (χ'') parts of the susceptibility given in arbitrary units for a Ladder scheme, shown as a function of probe detuning: $\Omega_c = 2\gamma_{21}$ and $\gamma_{31} = 0.2\gamma_{21}$.*

the Ladder scheme, however the general results are the same no matter what scheme is used.

We calculate the susceptibility as a function of probe detuning, with the coupling laser on resonance ($\Delta_c = 0$). This is depicted in Fig. 4.2 in the case of ($\gamma_{31} = 0.2\gamma_{21}$). Most noteworthy is the dip in the imaginary part of the susceptibility around zero detuning, often referred to as the "transparency window". This feature is what gives the EIT effect its name in the first place. Notice also how the transparency is accompanied by a drastic change in χ', which follows from the Kramers-Kronig relations. At resonance we have a large positive slope, i.e. a large slow-down of the incident field.

4.2.1 γ_{31} detrimental to EIT

The main parameter that limits EIT is the decoherence rate of the uncoupled transition $|1\rangle$-$|3\rangle$. This is illustrated in Fig. 4.3, for $\Delta_c = 0$.

As γ_{31} increases, the EIT effect is seen to dwindle. At $\gamma_{31}/|\Omega_p| \gtrsim 2$ EIT has completely vanished and we are left with regular anomalous dispersion.

One can re-enter the EIT regime by increasing the coupling power, as is illustrated in fig 4.4. However, as we pull the absorption peaks farther away from each other increasing the transparency window, the slope of the susceptibility around $\Delta_p = 0$ becomes smaller and the light is slowed less.

For application purposes the intensity should be chosen such that the bandwidth of the propagating pulse fits nicely within the transparency window. In this context it should be remarked, that pulling the absorption peaks apart also results in a larger range over which the slope of the susceptibility is constant,

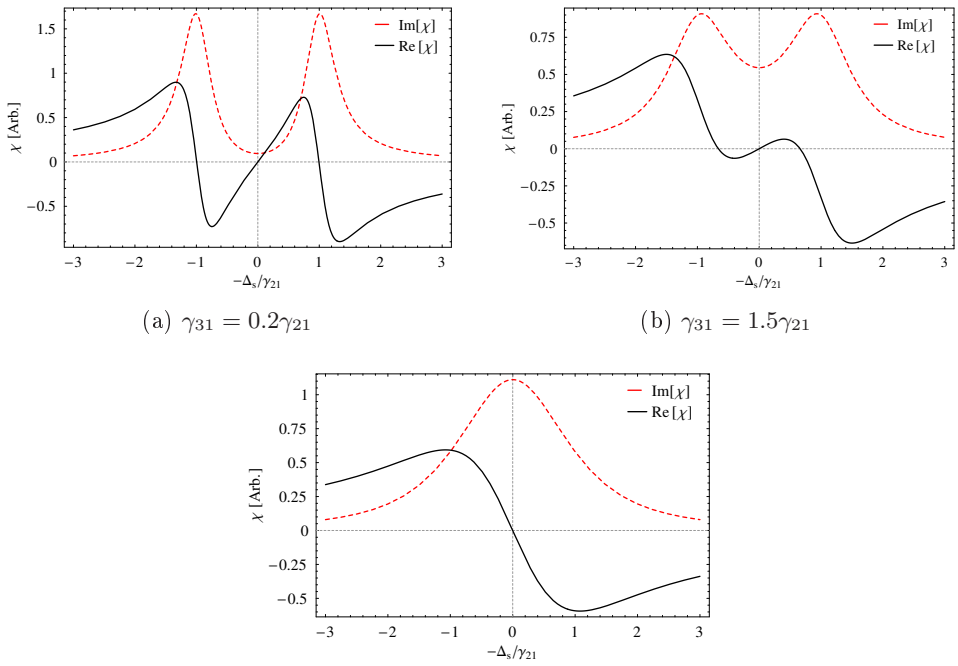

(a) $\gamma_{31} = 0.2\gamma_{21}$

(b) $\gamma_{31} = 1.5\gamma_{21}$

(c) $\gamma_{31} = 5\gamma_{21}$

Figure 4.3: *Susceptibility calculated for various values of* γ_{31}*. In all cases* $\Omega_c = 2\gamma_{21}$*.*

and thus a propagating pulse would experience less distortion.

4.2.2 Slowdown features

In order to calculate slowdown values we need to introduce numerical values for the parameters entering Eq. (4.1.52) and the background refractive index. The dephasing values for different lattice temperatures are taken from Table 2.1, and the dipole moments are chosen to be $|\mu_{12}| = 20.4$ Åe and $|\mu_{23}| = 24.6$ Åe following ref. [18] for a disc shaped InAs QD. In light of the later SBE treatment we take the same dephasing value for all transitions, the remaining parameters are all listed in Appendix C.

First we investigate the effect of coupling detuning. The slowdown calculated at 300 K using a probe power density of 7 MW/cm^2 is given in Fig. 4.5. We use the contour plot to identify the points of maximum slow-down. Somewhat surprisingly the greatest slowdown does not occur when both fields are resonant, i.e. at ($\Delta_p = 0$,$\Delta_c = 0$), but instead at ($\Delta_p = \mp 1.8$ meV,$\Delta_c = \pm 3.9$ meV). To verify that these detuning values can actually be used in a slow light experiment we calculate the absorption spectrum. The absorption is shown in Fig. 4.6. Here we see that the points of maximum slowdown is in fact accompanied by low absorption. In the present case (300 K) the difference between the maximum value of slow-down compared to its value at zero detuning is quite small (from 48.9 to 52.9), at lower temperatures the difference is more pronounced (see Table

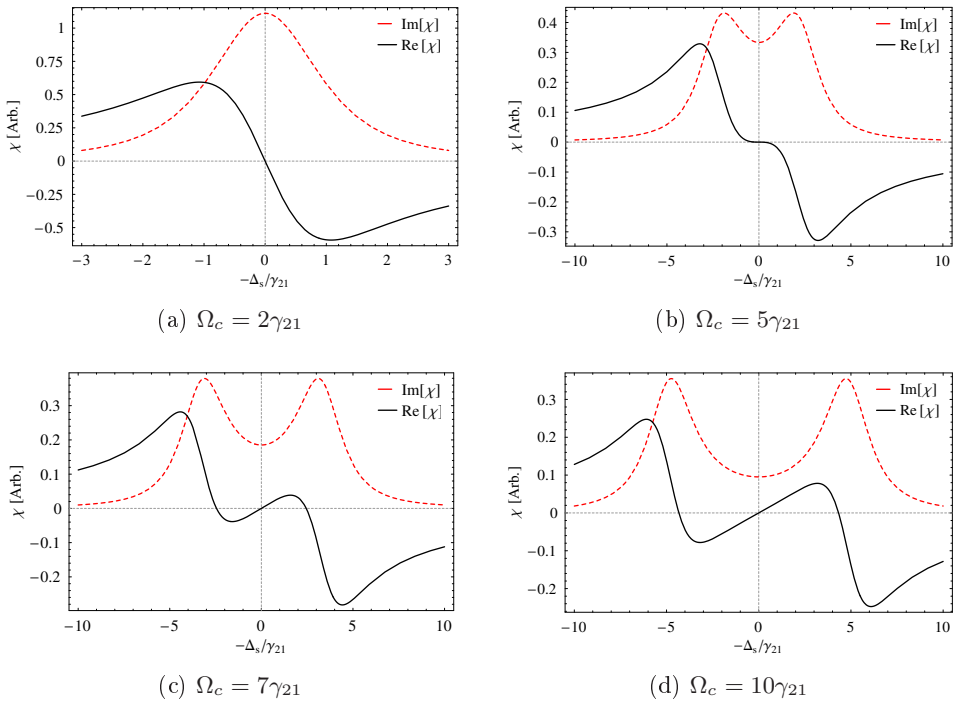

(a) $\Omega_c = 2\gamma_{21}$ (b) $\Omega_c = 5\gamma_{21}$

(c) $\Omega_c = 7\gamma_{21}$ (d) $\Omega_c = 10\gamma_{21}$

***Figure 4.4**: Susceptibility calculated for various values of Ω_c. In all cases $\gamma_{31} = 5\gamma_{21}$.*

4.1). We shall see later that inhomogeneous broadening effect requires one to use

Temperature [K]	Laser intensity [MW/cm^2]	Slow-down at (0,0)	Max slow-down
25	0.0005	1.47×10^6	2.34×10^6
50	0.001	1.54×10^5	2.0×10^5
100	0.03	10775	13781
300	7	48.9	52.9

***Table 4.1**: Slowdown values calculated at various temperatures. The values of the probe intensities are taken at the respective points of maximum slow-down in accordance to Fig. 4.7.*

so large coupling intensities, that this feature becomes blurred out. Therefore we use the situation with both lasers on resonance.

The dependency of coupling laser intensity is investigated in Fig. 4.7. We see that very large slowdown factors can be attained at low temperatures. At elevated temperatures large dephasing effects set in, and heavily suppress the attainable slowdown factor. Notice that the slowdown has a global maximum, and falls off when increasing the coupling power past this point.

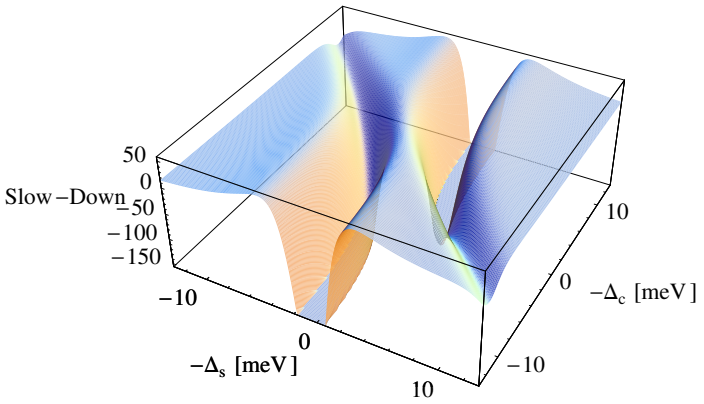

(a) 3D Plot.

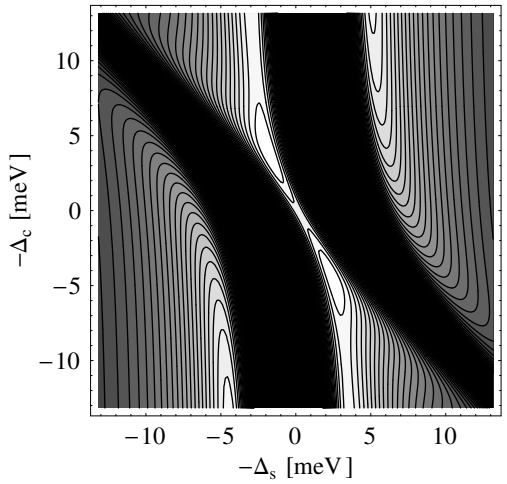

(b) Contour Plot. Negative values are colored black.

***Figure 4.5**: Slowdown as function of probe and coupling detuning at 300 K using a coupling power density of 7 MW/cm^2.*

4.2.3 Inhomogeneous broadening effects

The above calculations are based on the assumption that all QDs are completely identical and have similar surroundings. This, however is not case for an actual QD array. Variations, in e.g. size, density, strain and chemical composition, mean that the dots have different energy level structures, effectively resulting in an inhomogeneous broadening of the transition linewidths. Cutting edge growth methods (Stranski-Krastanow) measure the broadening of the hole ground state to electron ground state, i.e the $|1\rangle$ - $|2\rangle$ transition, to be around 20 meV [69].

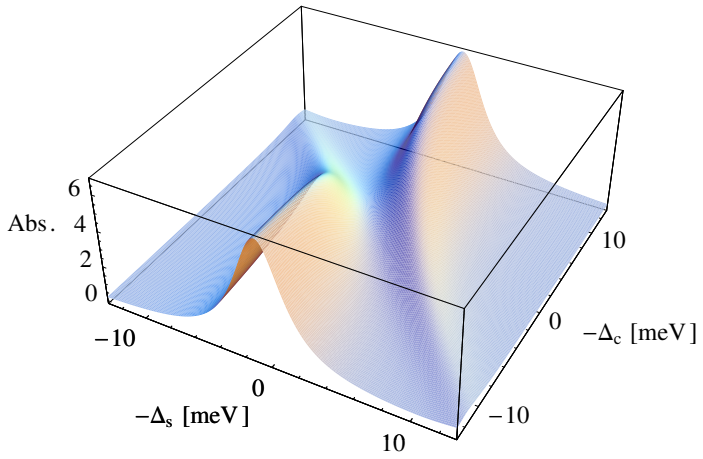

(a) 3D Plot.

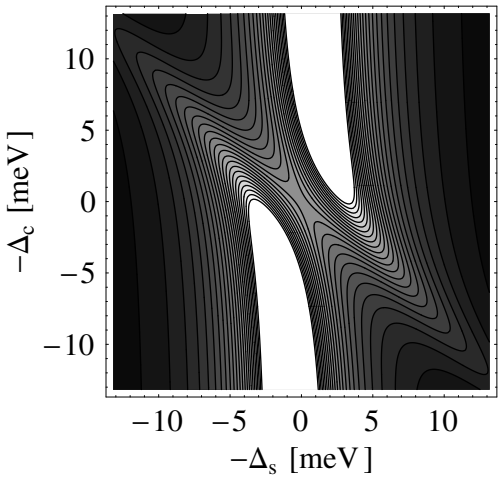

(b) Contour Plot. Large values are shown in white.

***Figure 4.6**: Absorption as function of probe and coupling detuning at 300 K using a coupling power density of 7 MW/cm^2.*

This linewidth is much larger than the homogeneous broadening linewidth, and is temperature independent.

The effect of the nonuniform dot distribution is that the incoming light no longer can be characterized by a single detuning parameter. Instead the light experiences different detunings when interacting with different dots, and the overall slowdown factor is reduced. To see this consider an ensemble made up of equal amounts of two different dot species (Type I and Type II). The probe and coupling laser are aligned to only one dot type (Type I). The coupling frequency is kept constant, while the probe frequency is varied around the resonance value

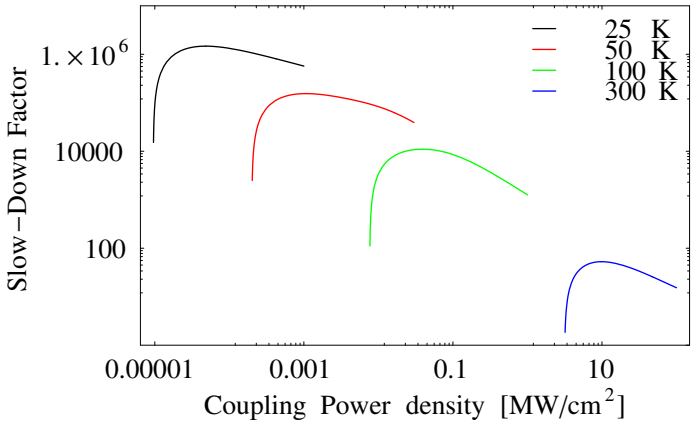

***Figure 4.7**: Slowdown as a function of coupling laser power, calculated for various temperatures. In all cases both probe and coupling laser are on resonance.*

of the Type I dot. The slowdown factor for the two dot types is shown in Fig. 4.8. It is seen that the slowdown for the misaligned case can even be negative at the

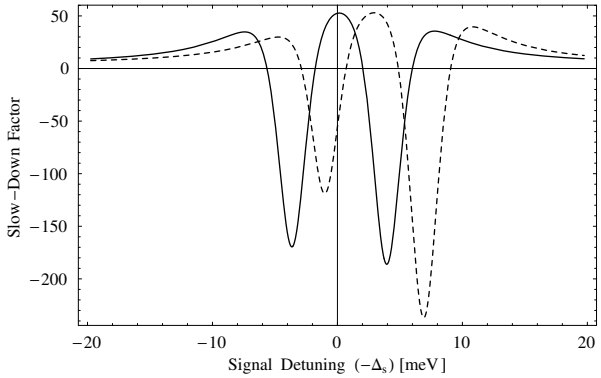

***Figure 4.8**: Slowdown calculated for two different quantum dots species. The solid line refers to a Type I dot which is on resonance with the coupling field, and the dashed line refers to a Type II dot which is detuned with respect to the coupling field. The probe detuning is taken with respect to the $|1\rangle - |2\rangle$ transition frequency of Type I.*

probe wavelength, thereby canceling the positive slowdown generated by the aligned dots.

As a first step we let only the $|1\rangle$-$|2\rangle$ transition, that is ω_{21}, fluctuate and keep ω_{32} constant. We write

$$\omega_{21} = \omega_{21}^0 + \delta\omega_{21}, \text{ so that} \tag{4.2.53}$$

$$\Delta_p = \omega_{21}^0 + \delta\omega_{21} - \omega_p. \tag{4.2.54}$$

The average system response experienced by the probe field is the combined response of all dot species

$$\langle\chi(\omega)\rangle = \sum_{\omega_{21}} P(\omega_{21})\chi(\omega, \omega_{21}). \tag{4.2.55}$$

$P(\omega_{21})$ represents the probability for finding a dot with an energy splitting of ω_{21}.
Modeling the variation as a Gaussian distribution centered about ω_{21}^0 and taking the probe laser to be tuned to this central frequency, we get for the average susceptibility

$$\langle\chi(\omega)\rangle = \int \mathrm{d}\ \delta\omega_{21} \frac{1}{\sqrt{2\pi}\Gamma_{\mathrm{inh}}} \mathrm{e}^{-\frac{\delta\omega_{21}^2}{2\Gamma_{\mathrm{inh}}}} \times i\frac{N_{\mathrm{dot}}|\mu_{12}|^2}{w\epsilon_0} \frac{\gamma_{31} + i(\delta\omega_{21} + \Delta_c)}{(\gamma_{31} + i(\delta\omega_{21} + \Delta_c))(\gamma_{21} + i\delta\omega_{21}) + |\Omega_c|^2}. \tag{4.2.56}$$

where $\Gamma_{\mathrm{inh}} = \frac{1}{2\sqrt{2\ln(2)}}\gamma_{\mathrm{inh}}$ in which $\hbar\gamma_{\mathrm{inh}}$ is the FWHM inhomogeneous broadening linewidth.
Slowdown factors incorporating various degrees of broadening are depicted in Fig. 4.9 as a function of coupling laser intensity. Non-uniformity is seen to have

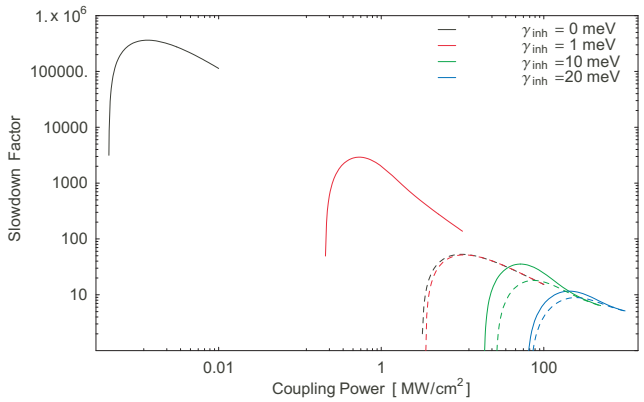

***Figure 4.9**: Slowdown factors calculated for various values of inhomogeneous broadening at 50 K (solid curves) -and room temperature (dashed curves).*

a heavy impact, especially on systems kept at low temperature. The reason is that the broadening acts as to smear out the variations in $\chi(\omega)$. At low temperatures the variations in susceptibility happens over a small spectral range much smaller than the inhomogeneous broadening. To suppress the smearing effect one needs to enlarge the transparency window to a size comparable to γ_{inh}, this is done at the expense of slowdown.
The slow-down at 25 K as a function of probe and coupling detuning is shown in Fig. 4.10. We used an inhomogeneous broadening of 10 meV and a coupling power density of 40 MW/cm^2, corresponding to the point of maximum slowdown found by inspecting Fig. 4.9. The accompanying absorption spectrum is shown in Fig. 4.11.

There is no direct empirical evidence pointing to the size of the broadening of the $|2\rangle$ - $|3\rangle$ transition. To take this into account we first of all assume that the broadening is attributed to only size fluctuations. This allows us to couple ω_{21}

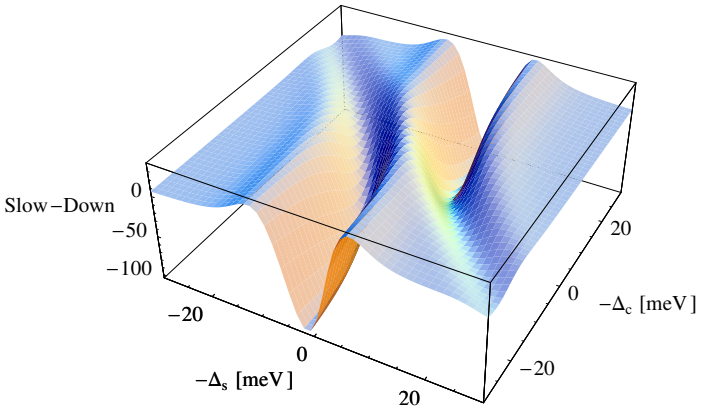

(a) 3D Plot.

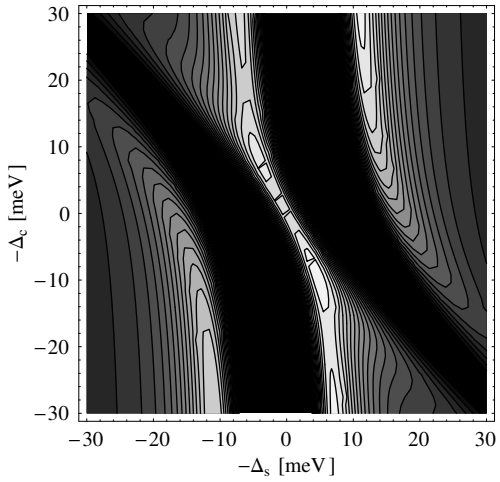

(b) Contour Plot. Negative values are colored black.

***Figure 4.10**: Slowdown as function of probe and coupling detuning at 50 K using a homogeneous broadening of 10 meV and a coupling power density of 40 MW/cm^2.*

and ω_{32}. Shrinking or enlarging a dot shifts the energy levels up or down, the main point is that ω_{32} moves in the same direction as ω_{21}. With this in mind it makes sense to express $\delta\omega_{32}$ as a linear function of $\delta\omega_{21}$:

$$\delta\omega_{32} \quad = \quad k\delta\omega_{21}. \tag{4.2.57}$$

The linearity constant k is found by considering the size dependency of the three lowest (non-degenerate) energy levels in a dot. For simplicity we model the dot as an infinite spherical confinement potential with radius r, for which the three

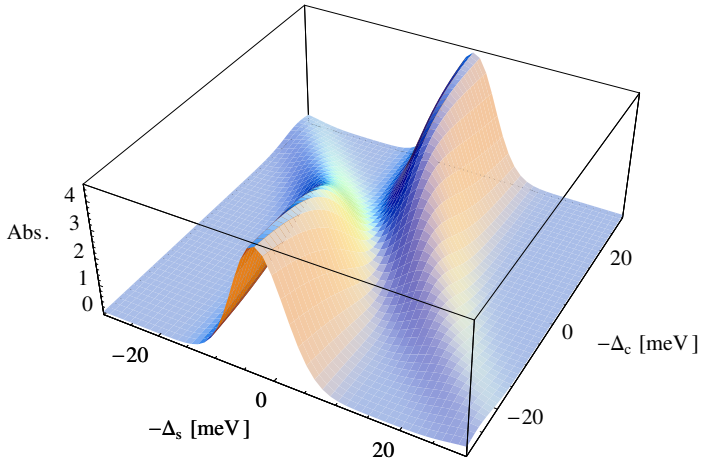

(a) 3D Plot.

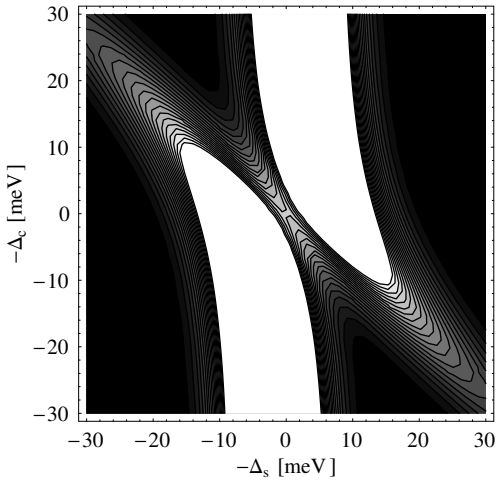

(b) Contour Plot. Large values are all shown in white.

***Figure 4.11**: Absorption as function of probe and coupling detuning at 50 K using a homogeneous broadening of 10 meV and a coupling power density of 40 MW/cm^2.*

lowest and non-degenerate energy levels are given as

$$E_1 = \hbar^2\pi^2/2mr^2 \quad (4.2.58)$$

$$E_2 = 4E_1 \quad (4.2.59)$$

$$E_3 = 9E_1, \quad (4.2.60)$$

where m is the mass of the confined particle. From the above we gather $E_{21} = E_2 - E_1 = 3E_1$ and $E_{32} = E_3 - E_2 = 5E_1$ which can be written as

$$E_{32} = 5/3E_{21}. \quad (4.2.61)$$

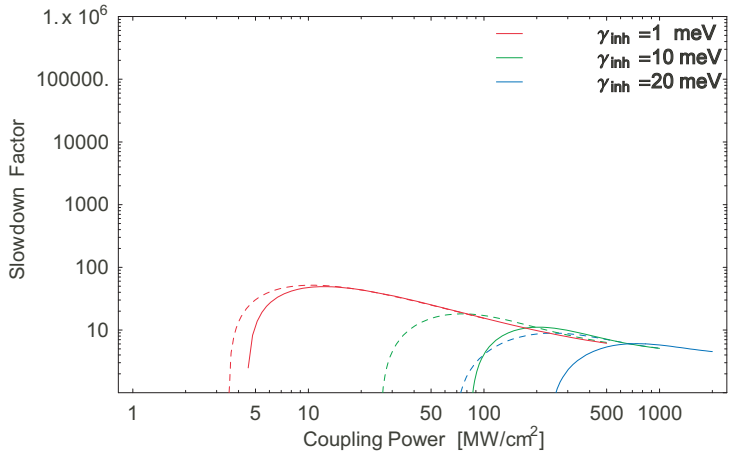

Figure 4.12: *Slowdown factor calculated for various values of inhomogeneous broadening at room temperature. Dashed curves corresponds to only probe broadening, solid curves include coupling broadening as* $\delta\omega_{32} = 5/3\delta\omega_{21}$.

A small change in size shifts E_{21} by an amount δE_{21} and E_{32} by $\delta E_{32} = 5/3\delta E_{21}$. Using $k = 5/3$ we get the relation $\omega_{32} = \omega_{32}^0 + 5/3\delta\omega_{21}$ and insert into the expression for the susceptibility. When both fields are resonant with their respective transitions we get

$$\langle\chi(\omega)\rangle = \int \mathrm{d}\ \delta\omega_{21} \frac{1}{\sqrt{2\pi}\Gamma_{\mathrm{inh}}} \mathrm{e}^{-\frac{\delta\omega_{21}^2}{2\Gamma_{\mathrm{inh}}}} \\ i\frac{N_{\mathrm{dot}}|\mu_{12}|^2}{w\epsilon_0} \frac{\gamma_{31} + i(\delta\omega_{21} + 5/3\delta\omega_{21})}{(\gamma_{31} + i(\delta\omega_{21} + 5/3\delta\omega_{21}))(\gamma_{21} + i\delta\omega_{21}) + |\Omega_c|^2}. \tag{4.2.62}$$

We plot the slowdown as function of coupling laser intensity. This is shown in Fig. 4.12. As expected including more broadening effects further deteriorates the slowdown. However, the general EIT features are still visible. The slowdown and accompanying absorption as function of probe and coupling detunings are shown in Figs. 4.13 and 4.14.

In conclusion we note that inhomogeneous broadening effects seriously impairs slowdown in semiconductor QD systems. If we can reduce the size variation by 80%, the inhomogeneous broadening will be smaller than homogeneous broadening due to carrier dephasing at room temperature.

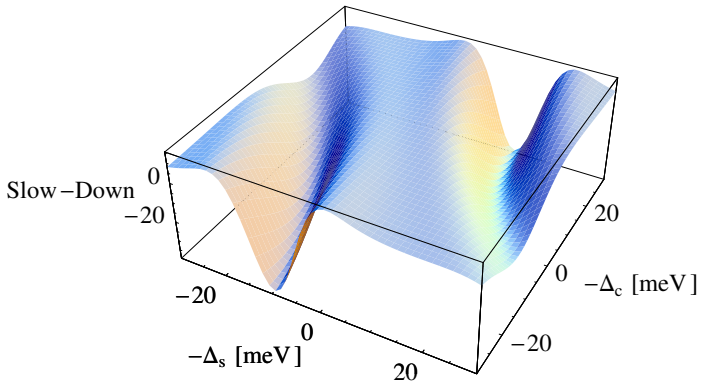

(a) 3D Plot.

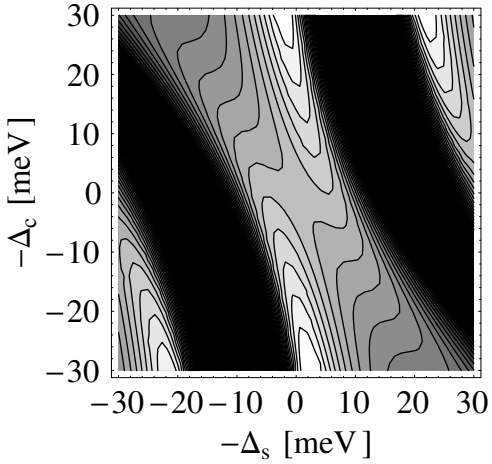

(b) Contour Plot. Negative values are colored black.

***Figure 4.13**: Slowdown as a function of probe and coupling detuning at 300 K using a coupling power density of 300 MW/cm^2. The inhomogeneous broadening of 10 meV is incorporated in both probe and coupling detunings.*

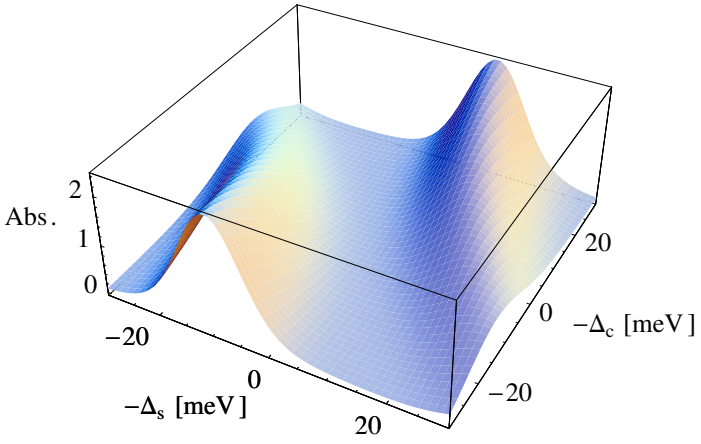

(a) 3D Plot.

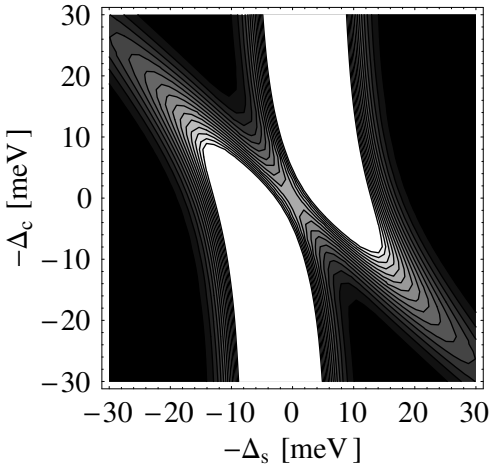

(b) Contour Plot. Large values are all shown in white.

***Figure 4.14**: Absorption as a function of probe and coupling detuning at 300 K using a coupling power density of 300 MW/cm^2. The inhomogeneous broadening of 10 meV is incorporated in both probe and coupling detunings.*

Chapter 5

QD Modeling

In this chapter we present the QD model along with its single- and two particle properties. This entails both optical dipole matrix elements as well as Coulomb elements. We also study the impact of strain and band mixing on the optical properties of Qds using eight band $\vec{k} \cdot \vec{p}$ theory and analyze size and geometry dependence of the dipole moments.

5.1 Quantum dot model

The heterostructure under consideration consists of randomly distributed identical InAs QDs residing on a wetting layer (WL), sandwiched between two slabs of GaAs. We assume the QD density is sufficiently dilute so that they can be treated independently. The starting point for a theoretical description of the

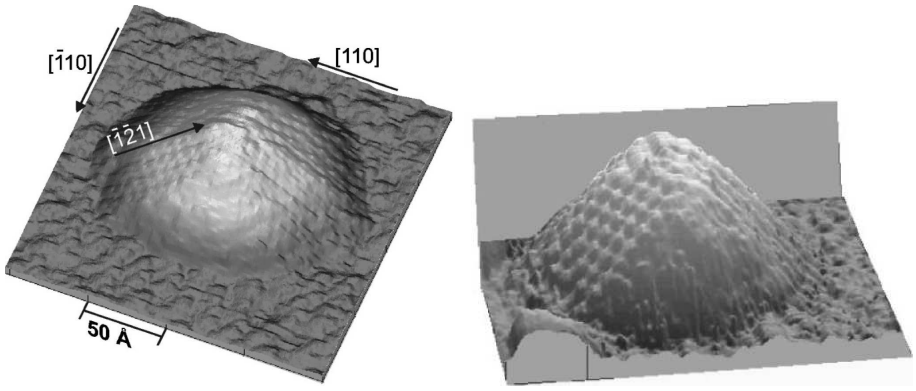

***Figure 5.1**: STM image of uncapped InAs dot grown on GaAs substrate. From Ref. [70].*

QD carrier system is the non-interacting single-particle states. It is a complicated task on its own to compute from first principles these single-particle states for a given confinement situation that depends on the QD geometry, the strain profile and possible composition variations within the QD. At varying levels of

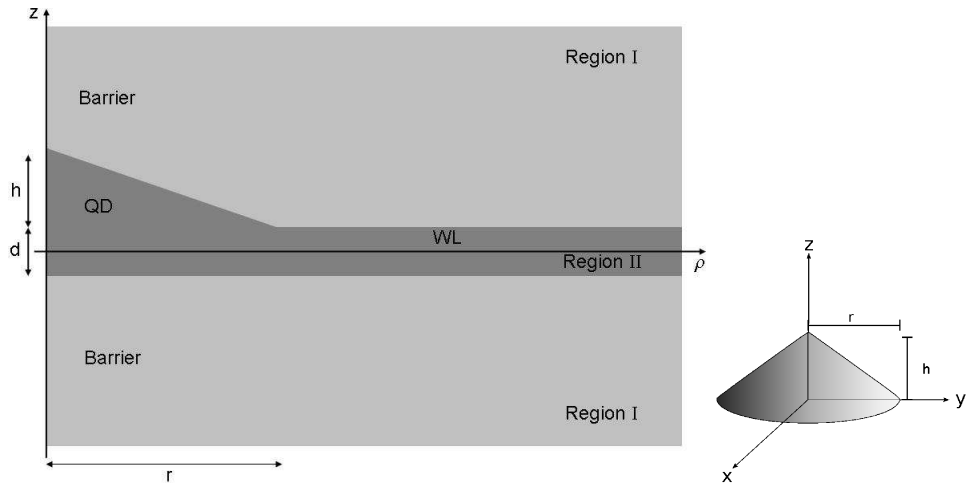

Figure 5.2: *Computational domain used for solving the effective mass Schrödinger equation Eq. (5.1.4) and an isolated conical QD.*

sophistication different schemes can be employed for calculating the single particle properties. From the atomistic tight-binding [71] and pseudopotential [72] approaches across multiband $k \cdot p$ theory [73] to the simple effective mass approximation [74]. The results of this thesis are mainly based on the effective mass model however we shall also show results obtained using eight band $k \cdot p$ theory.

For simplicity we model the QD as a rotationally symmetric cone, which roughly agrees with experimental findings for uncapped [29, 70, 75, 76] as well as capped [77] QDs.

We show in Fig. 5.1 a few STM (Scanning Tunneling Microscope) images of uncapped InAs QDs grown on a GaAs (001) substrate. In the example shown here the QDs have a typical diameter of 9 nm, a height above the WL of 3 nm, and the thickness of the WL is typically a few monolayers, illustrating the resemblance to a lens or cone shape. In the following we shall consider a QD having a cylindrical symmetric confinement potential with spatial extension defined by the physical dimensions of the cylindrical symmetric QD. The computational setup is illustrated in Fig. 5.2.

5.1.1 Single band effective mass Schrödinger equation

Strain together with spatial confinement lifts the degeneracy of the light and heavy hole band at the Γ-point that exists in bulk III-V semiconductors pushing the light hole band towards lower energies. Therefore modeling the valence band states using only a single band, i.e. the heavy hole band is a good starting approximation [78].

We seek solutions to the single[1] band effective mass Schrödinger equation for

[1] It is common to refer to the number of Bloch states used to expand the wavefunction

the envelope function $\psi_\nu(\boldsymbol{r})$

$$\left(-\frac{\hbar^2}{2}\boldsymbol{\nabla}\cdot\left[\frac{1}{m^*_\nu(\boldsymbol{r})}\boldsymbol{\nabla}\right]+V_\nu(\boldsymbol{r})\right)\psi_\nu(\boldsymbol{r})=E_\nu\psi_\nu(\boldsymbol{r}). \tag{5.1.1}$$

Here V_ν is the confinement potential created by band bending effects from sandwiching low bandgab InAs in high bandgap GaAs, and m^*_ν is the position dependent effective mass.

Using a single band effective mass approximation for QDs with cylindrical symmetric confinement potential allows to separate the azimuthal dependency from the radial and axial, thereby reducing the dimensionality of the problem. This leads to the following ansatz for the wave functions

$$\Psi_\nu(\boldsymbol{r})=\psi_\nu(\boldsymbol{r})u_\nu(\boldsymbol{r})=\Phi_\nu(\phi)f_\nu(\rho,z)u_\nu(\boldsymbol{r}) \tag{5.1.2}$$

where ψ_ν is the full envelope function and u_ν is the lattice periodic Bloch function containing information about the underlying atomistic structure. $f_\nu(\rho,z)$ is the envelope in the (ρ,z)-plane and $\Phi_\nu(\phi)$ is the azimuthal envelope function. Due to the rotational symmetry the Hamiltonian commutes with the generator of rotations about the z-axis L_z. Thus the z-component of angular momentum is a good quantum number and the azimuthal envelope functions are equal to the eigenstates of L_z, i.e.

$$\Phi_\nu(\phi)=\frac{1}{\sqrt{2\pi}}e^{im\phi}, \tag{5.1.3}$$

with the integer m being the angular momentum in the z-direction. Ultimately we can write the Schrödinger equation for a given angular momentum m as

$$\left(-\frac{\hbar^2}{2\rho}\partial_\rho\left[\frac{\rho}{m^*_b(\rho,z)}\partial_\rho\right]-\frac{\hbar^2}{2}\partial_z\left[\frac{1}{m^*_b(\rho,z)}\partial_z\right]+\frac{\hbar^2m^2}{2m^*_b(\rho,z)\rho^2}+V_b(\rho,z)\right)f_m(\rho,z)=E_mf_m(\rho,z), \tag{5.1.4}$$

where b is the band index. The position dependent effective mass and confinement potential are constants within each domain (I and II) and jump whenever an internal boundary is crossed, hence

$$m^*_b(\rho,z)=\begin{cases} m^{\mathrm{I}}_b, & (\rho,z)\in\mathrm{I}\\ m^{\mathrm{II}}_b, & (\rho,z)\in\mathrm{II},\end{cases}$$

The confinement potential is set to zero inside the the QD (region I) and equal to the band offset outside the dot (region II).

$$V_b(\rho,z)=\begin{cases} 0, & (\rho,z)\in\mathrm{I}\\ \Delta E_b, & (\rho,z)\in\mathrm{II}.\end{cases}$$

under consideration. In a single band model a valence band state is expressed using a single valence band Bloch function and a conduction band state is expanded onto a single conduction band Bloch function. More elaborate models will expand the wavefunction onto more Bloch functions.

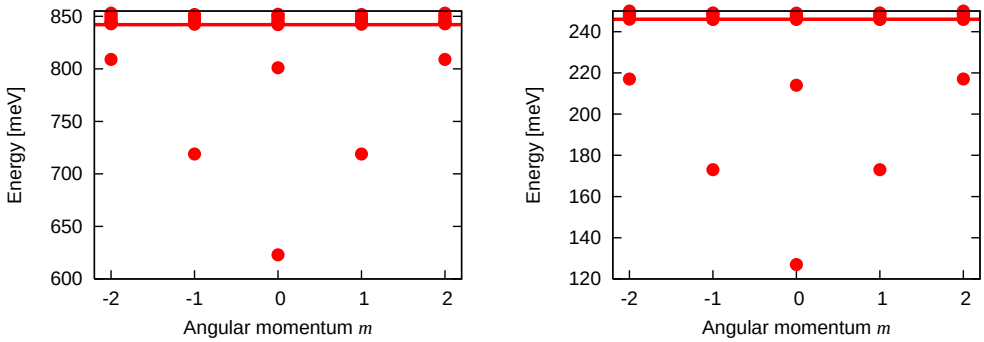

(a) Electron energy. (b) Hole energy.

***Figure 5.3**: Energy spectrum for electrons (left panel) and holes (right panel) obtained from solving Eq. (5.1.4). The zero point is taken at the top of the heavy hole band. The solid line indicates the onset of the WL continuum. Notice that the energies are degenerate both in spin and $\pm m$.*

The eigenfunctions and corresponding eigenvalues are obtained by numerical solution of Eq. (5.1.4) using COMSOL. The appropriate boundary conditions are such that for angular momentum $m \neq 0$ Dirichlet boundary conditions are used, while for $m = 0$ Neumann boundary conditions must in addition be implemented at the domain boundary $(\rho = 0; z)$ [79].

5.2 Single particle properties

We focus on a cone shaped dot of height $h = 3$ nm and radius $r = 9$ nm residing on a WL of thickness $d = 1.2$ nm. The remaining computational parameters are listed in Table C.1. The reason for choosing this particular dot is that it contains an s, p and d shell in both bands, and as we shall see later from the dipole section rules, it allows access to a number of different EIT schemes.

5.2.1 Energy spectrum

The resulting energy spectrum is shown in Fig. 5.3. We find six bound states localized within the dot as well as a continuum of delocalized WL states and several quasi-bound states residing at the onset of the continuum. Each state is doubly degenerate due to spin, also the rotational symmetry causes states of opposite angular momentum $(\pm m)$ to coincide energetically. The bound states show a clear shell structure, it is therefore natural to label the shells in analogy with atomic physics, i.e. s, p, d. The WL states are identified by the fact that they are generally unaffected by the existence of the dot potential. It is found that the envelope of a WL state is practically zero in the dot region which means it as also a solution to the "pure" WL problem, the quantum well. The quasi-bound states are identified by the fact that their envelope functions have

significant amplitude both in the dot- and the WL region and therefore overlap with both QD-states and WL-states. As these states are neither localized nor delocalized we choose, in the present work to disregard them. For a detailed description see e.g. Ref. [80]. However, the quasi-bound states are of interest in more elaborate quantum kinetic models where they can act as mediators in scattering between dot and WL states. A surface plot of the QD ground state (s-state) and a WL state is shown in Fig. 5.4.

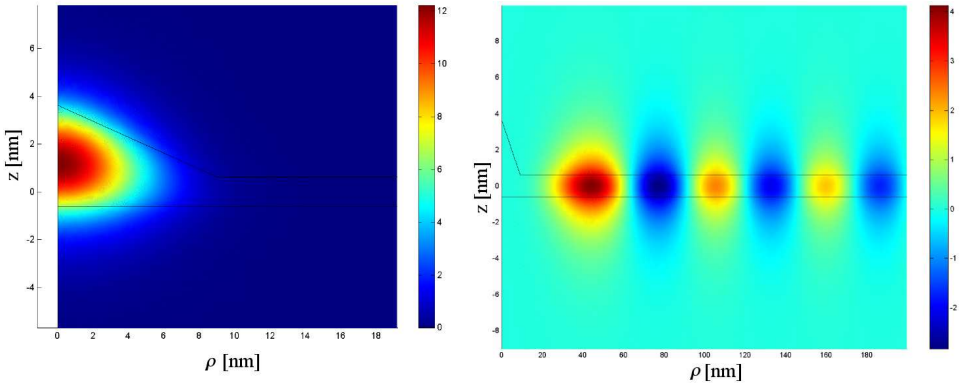

(a) QD s-state (b) WL-state

***Figure 5.4**: Surface plot of the unnormalized envelope functions for an electron s-state and a WL state. The solid lines indicate the boundary between the barrier and the dot material. Note the different scales used in the two plots.*

Even though we refer to the delocalized states as a continuum they still constitute a discrete set, where the energy spacing between states is determined by the artificial outer boundary of the computational domain. In order to treat the WL as a true continuum one needs a continuous variable (such as a two dimensional momentum $\boldsymbol{k}$ in a quantum well) to label and designate the set of states. To meet this end we choose to model the WL states as quantum well states. That is; 2D plane waves in the QD/WL plane using a parabolic dispersion with effective masses from Table C.1. For the strong confinement in the growth direction we use an infinite potential well and consider only the lowest subband. This is a good approximation as long as the WL thickness is small[2]. The length of the well is fitted to match the WL envelope functions obtained from the solutions to the original Schrödinger equation. The WL envelope function can be written as

$$\psi^b_{\boldsymbol{k}}(\boldsymbol{r}) = \xi^b_{WL}(z)\varphi_{\boldsymbol{k}}(\boldsymbol{\rho}) = \frac{1}{\sqrt{A}}\xi^b_{WL}(z)e^{i\boldsymbol{k}\cdot\boldsymbol{\rho}}\,, \tag{5.2.5}$$

with $\boldsymbol{\rho}$ being the position vector in the WL plane, and A the WL normalization area. It should be emphasized that the present approach for handling the WL states has the obvious flaw that the quasi bound states are lost, and that the combined set of QD and WL states are no longer orthogonal. The consequences of the latter will be treated in the section on Coulomb matrix elements.

[2]The inter-subband spacing of an infinite well of length d is inversely proportional to d^2.

5.2.2 Dipole matrix elements

The dipole matrix element $\boldsymbol{\mu}_{\nu\nu'}$, that enters as the coupling strength in the carrier-field Hamiltonian, between state ν and ν' is defined as

$$\begin{aligned}\boldsymbol{\mu}_{\nu\nu'} &= \langle\nu|\, e\boldsymbol{r}\,|\nu'\rangle \\ &= e\int \mathrm{d}\boldsymbol{r}\,\Psi^*_\nu(\boldsymbol{r})\boldsymbol{r}\Psi_{\nu'}(\boldsymbol{r}) \\ &= e\int \mathrm{d}\boldsymbol{r}\,[\psi_\nu(\boldsymbol{r})u_\nu(\boldsymbol{r})]^*\boldsymbol{r}\psi_{\nu'}(\boldsymbol{r})u_{\nu'}(\boldsymbol{r})\,. \end{aligned} \tag{5.2.6}$$

This integral cannot, however be evaluated in all cases. As pointed out in Ref. [81] the expectation value for the dipole moment operator is not well defined for infinitely extended Bloch states. Instead one can make use of the relation between position $\boldsymbol{r}$ and momentum $\boldsymbol{p}$

$$\boldsymbol{p} = m_0\frac{\partial}{\partial t}\boldsymbol{r} = \frac{m_0}{i\hbar}[\boldsymbol{r}, H_0]\,, \tag{5.2.7}$$

where H_0 is the quadratic time independent Hamiltonian of Chapter 2. Using the above relation we get

$$\boldsymbol{p}_{\nu\nu'} = im_0\omega_{\nu\nu'}\boldsymbol{r}_{\nu\nu'}\,, \tag{5.2.8}$$

$$\boldsymbol{\mu}_{\nu\nu'} = e\boldsymbol{r}_{\nu\nu'}\,, \tag{5.2.9}$$

with $\omega_{\nu\nu'} = \frac{1}{\hbar}(\epsilon_\nu - \epsilon_{\nu'})$. The $\boldsymbol{p}$ elements are then evaluated in the following manner:

$$\begin{aligned}\langle\nu|\boldsymbol{p}|\nu'\rangle &= \int d\boldsymbol{r}\,[\psi_\nu(\boldsymbol{r})u_\nu(\boldsymbol{r})]^*\,\boldsymbol{p}\psi_{\nu'}(\boldsymbol{r})u_{\nu'}(\boldsymbol{r}) \\ &= \int d\boldsymbol{r}\,[\psi_\nu(\boldsymbol{r})u_\nu(\boldsymbol{r})]^*\,\{\psi_{\nu'}(\boldsymbol{r})[\boldsymbol{p}u_{\nu'}(\boldsymbol{r})] + u_{\nu'}(\boldsymbol{r})[\boldsymbol{p}\psi_{\nu'}(\boldsymbol{r})]\} \\ &\approx \langle\psi_\nu|\psi_{\nu'}\rangle\,\langle u_\nu|\boldsymbol{p}|u_{\nu'}\rangle + \langle\psi_\nu|\boldsymbol{p}|\psi_{\nu'}\rangle\,\langle u_\nu|u_{\nu'}\rangle\ . \end{aligned} \tag{5.2.10}$$

In the last step we used the fact that the envelope functions are slowly varying on the scale of a unit cell.

5.2.3 Inter-band dipole moment

In a single band model when considering inter-band dipole moments, i.e. between states belonging to different bands, the second term in Eq. (5.2.10) drop out due to the orthogonality of the Bloch functions. We are left with

$$\boldsymbol{p}^{bb'}_{\alpha\alpha'} = \langle\psi^b_\alpha|\psi^{b'}_{\alpha'}\rangle\,\langle u_b|\boldsymbol{p}|u_{b'}\rangle\ , \tag{5.2.11}$$

where b is the band index and α can refer to both dot and WL states. The first part involves the overlap between envelope functions. The latter part involving the momentum operator and Bloch functions can be evaluated from tabulated values. The momentum matrix element is found using the symmetry properties

of the zincblende InAs lattice. The $u_b, u_{b'}$ states consist only of s-like orbitals for the conduction band and p-like orbitals for the valence band. Using the conventional nomenclature; the conduction band state is designated S and a valence band state built of p orbitals aligned along the x-axis is called X. The matrix element $\langle S|p_x|X\rangle = (im_0/\hbar)P$ is found using the Kane energy $E_P = 2m_0P^2/\hbar$. Symmetry dictates the following non-zero elements:

$$\langle S|p_x|X\rangle\,, \qquad \langle S|p_y|Y\rangle\,, \qquad \langle S|p_z|Z\rangle\ . \tag{5.2.12}$$

In the single band model we consider only the heavy hole band. The valence band state u_v entering Eq. (5.2.11) is thus constructed of linear combinations of X and Y states only:

$$u_v = -\frac{1}{\sqrt{2}}(X + iY)\,. \tag{5.2.13}$$

Consequently we get the following general expression for the inter-band dipole matrix element

$$\mu^x_{\nu\nu'} = -e\frac{1}{2\omega_{\nu\nu'}}\sqrt{\frac{E_p}{m_0}}\,\langle\psi_\nu|\psi_{\nu'}\rangle \tag{5.2.14}$$

$$\mu^y_{\nu\nu'} = -ie\frac{1}{2\omega_{\nu\nu'}}\sqrt{\frac{E_p}{m_0}}\,\langle\psi_\nu|\psi_{\nu'}\rangle \tag{5.2.15}$$

$$\mu^z_{\nu\nu'} = 0\,. \tag{5.2.16}$$

We see that the maximum dipole moment is found when electron and hole envelopes are equal.

WL-WL dipole

The selection rules for dipole moments involving two WL states is dictated by the envelope overlap integral

$$\begin{aligned}\langle\psi^b_{\boldsymbol{k}}|\psi^{b'}_{\boldsymbol{k}'}\rangle &= \frac{1}{A}\int \mathrm{d}\boldsymbol{r}\,[\xi^b_{WL}(z)e^{i\boldsymbol{k}\cdot\boldsymbol{\rho}}]^*\xi^{b'}_{WL}(z)e^{i\boldsymbol{k}'\cdot\boldsymbol{\rho}} \\ &= \int \mathrm{d}z\,[\xi^b_{WL}(z)]^*\xi^{b'}_{WL}(z)\delta_{\boldsymbol{k}\boldsymbol{k}'}\,,\end{aligned} \tag{5.2.17}$$

yielding the well known $\boldsymbol{k}$ selection rule.

Dot-WL dipole

The envelope function overlap between dot- and WL states is not evaluated explicitly. Instead we follow an argument often used in the literature: In the limit where the hole and electron envelopes are identical the overlap between a localized dot state and a plane wave is, due to the orthogonality of the states in a given band, by construction zero. When we move away from the equal envelope assumption the overlap becomes finite, but as long as the envelopes are not too different it is still small, and we can choose to neglect these dipole components.

Dot-dot dipole

Due to the cylindrical symmetry selection rules can be obtained on the basis of the azimuthal dependency of envelope wave functions.

$$\int \mathrm{d}\phi \, [\Phi_\nu(\phi)]^* \Phi_{\nu'}(\phi) = \int \mathrm{d}\phi \, \frac{1}{\sqrt{2\pi}} e^{-im\phi} \frac{1}{\sqrt{2\pi}} e^{im'\phi} = \delta_{m,m'} \, . \tag{5.2.18}$$

The envelope overlap is therefore

$$\langle \psi^b_\alpha | \psi^{b'}_{\alpha'} \rangle = \int \mathrm{d}z \mathrm{d}\rho \, \rho [f^b_\alpha(\rho, z)]^* f^{b'}_{\alpha'}(\rho, z) \Big|_{\Delta m=0} \, , \tag{5.2.19}$$

where $\Delta m = m - m'$.

From Eq. (5.2.19) it follows that one expects the largest dipole moments between states having similar envelopes and thus belonging to the same "shell" index, i.e. between $s-s, p-p, d-d$, such transitions are also referred to as "direct" transitions. In Fig. 5.5 we show a selection of inter-band transitions within the dot.

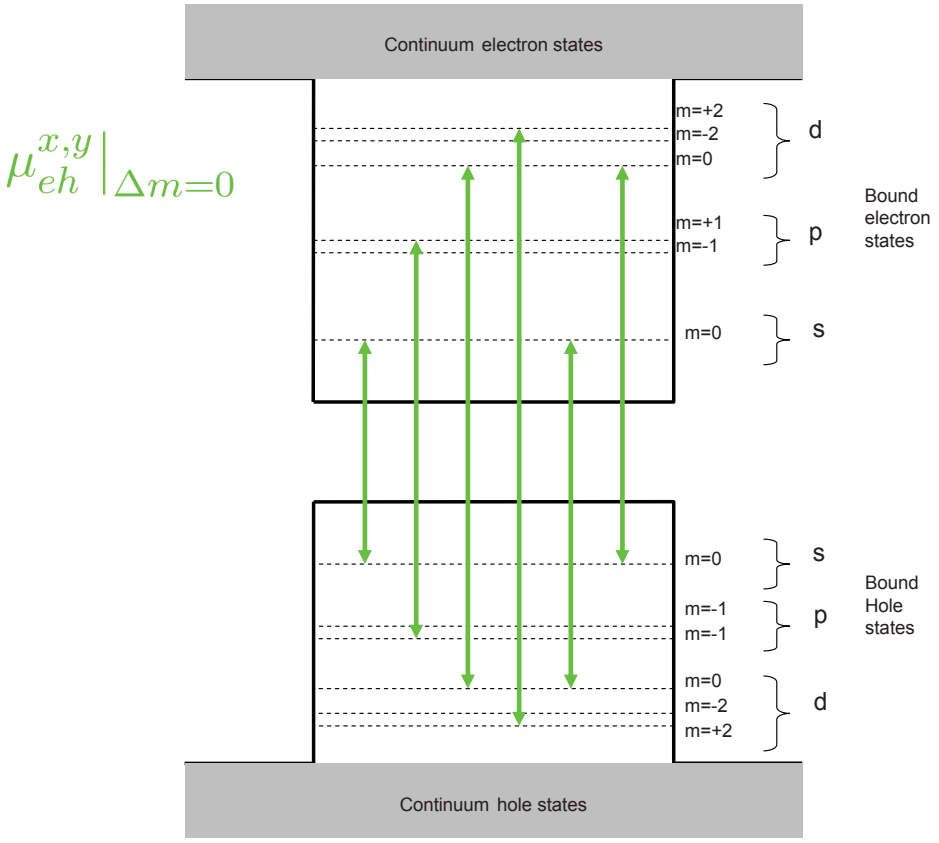

***Figure 5.5**: A selection of dipole allowed inter-band transitions. For illustrative purposes the degenerate set of states $m = \pm 1, \pm 2$ have been split.*

5.2.4 Intra-band dipole moment

For the case of intra-band dipole moments the $\boldsymbol{p}$ element between Bloch states belonging to the same band are equal to zero and so the first term in Eq. (5.2.10) drop out. We need to consider the second term involving the $\boldsymbol{p}$ matrix elements between envelope functions. This approach is convenient when WL states are involved since they are eigenstates of the momentum operator, however when two dot states are under consideration it is easier to return to the original expression for the dipole moment (Eq. (5.2.6)). In the single band model for intra-band dipoles we can use the fact that $|u_b|^2$ varies rapidly and integrates to unity over a unit cell

$$\begin{aligned}\mu_{\nu\nu'} &= e\int \mathrm{d}\boldsymbol{r}\,[\Phi_\alpha(\phi)f^b_\alpha(\rho,z)u_b(\boldsymbol{r})]^*\boldsymbol{r}\Phi_{\alpha'}(\phi)f^b_{\alpha'}(\rho,z)u_b(\boldsymbol{r})\\ &\approx e\int \mathrm{d}\boldsymbol{r}\,[\Phi_\alpha(\phi)f^b_\alpha(\rho,z)]^*\boldsymbol{r}\Phi_{\alpha'}(\phi)f^b_{\alpha'}(\rho,z)\\ &= e\,\langle\psi_\nu|\boldsymbol{r}|\psi_{\nu'}\rangle\ . \end{aligned} \tag{5.2.20}$$

This integral is well defined since we are dealing with localized dot states.

WL-WL dipole

From the nature of the WL states, i.e. being eigenstates of the momentum operator, the $\boldsymbol{p}$ element lying in the WL plane vanishes, and since we disregard subband structure so does the p_z element.

Dot-WL dipole

Intra-band dipoles between dot and WL can be disregarded through the following consideration: For the WL states we do not think of them as plane waves, but instead as plane waves orthogonalized to the QD states (see e.g. [82] for a thorough derivation). The orthogonalized plane wave (OPW) states remain approximative eigenstates of the $\boldsymbol{p}$ operator in the plane of the WL[3], which means

$$\langle\psi^b_\alpha|p_x|\psi^{b,\mathrm{OPW}}_{\boldsymbol{k}'}\rangle \simeq p_x(\boldsymbol{k}')\,\langle\psi^b_\alpha|\psi^{b,\mathrm{OPW}}_{\boldsymbol{k}'}\rangle\ , \tag{5.2.21}$$

leaving us with an overlap integral between a localized dot state and an OPW state, which is zero by construction. For the p_z element we consider relatively shallow dots, in which the potential in the z-direction varies only slowly when moving in the radial direction. One can then approximate the dot envelope function $f(z,\rho)$ using a product of independent functions $\xi^b_a(z)g^b_\alpha(\rho)$ (see e.g. Ref. [83,84]). Under this assumption we can split the integral into a z-dependent part involving the momentum operator, and an in-plane overlap integral between a dot- and a WL state. As the the two states are orthogonal the in-plane overlap integral is zero, thus allowing us to also disregard this part of the $\boldsymbol{p}$ element.

[3] One can show for the OPW states, that *on average* momentum conservation is restored, so that $\langle\boldsymbol{k}|\boldsymbol{k}'\rangle \propto \delta(\boldsymbol{k}-\boldsymbol{k}')$.

Dot-dot dipole

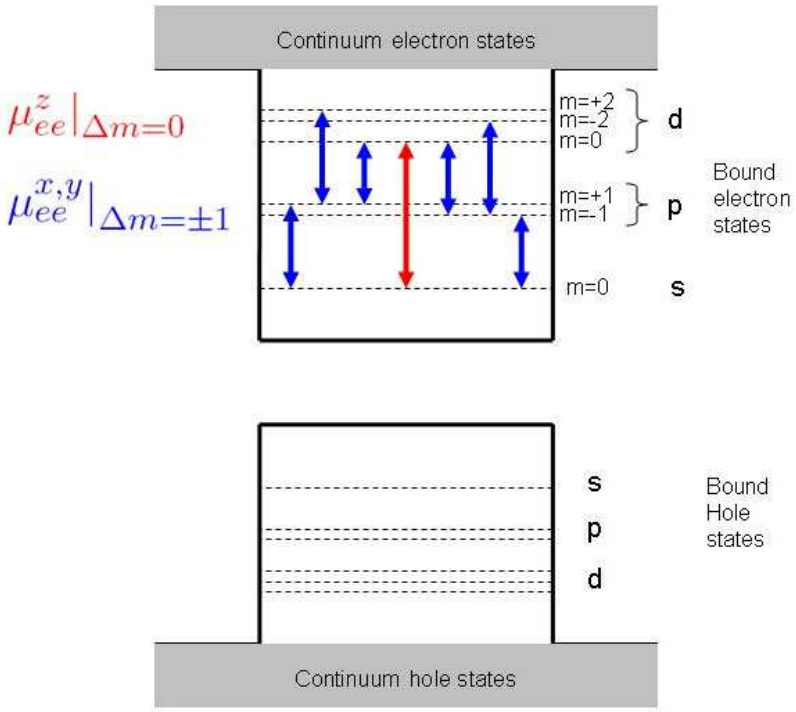

***Figure 5.6**: Dipole allowed intra-band transitions. The selection rules are similar for holes. For illustrative purposes the degenerate set of states $m = \pm 1, \pm 2$ have been split.*

Selection rules for intra-band dipole moments involving two dot states are found from the azimuthal dependency of the wave functions. First we consider the in-plane part of the dipole moment, e.g. μ^x. For the x-component the angular integration over the envelope functions gives only a non-zero contribution for states which differ in angular momentum by one unit

$$\begin{aligned}\int \mathrm{d}\phi\,[\Phi_\nu(\phi)]^* \cos(\phi)\Phi_{\nu'}(\phi) &= \int \mathrm{d}\phi\,\frac{1}{\sqrt{2\pi}} e^{-im\phi}\cos(\phi)\frac{1}{\sqrt{2\pi}} e^{im'\phi} \\ &= \frac{1}{2} \quad \text{for} \quad \Delta m = m - m' = \pm 1\,. \end{aligned} \tag{5.2.22}$$

Similar relations hold for μ^y. For the dipole moment in the z-direction we have a simple overlap integral as in Eq.(5.2.18), resulting in the $\Delta m = 0$ selection rule as for the inter-band dipole moment.

To summarize the intra-band dipole moments are:

$$\mu^x_{\nu\nu'} = \frac{e}{2}\int \mathrm{d}z\mathrm{d}\rho\,\rho^2 [f^b_\alpha(\rho,z)]^* f^b_{\alpha'}(\rho,z)\Big|_{\Delta m=\pm 1} \tag{5.2.23}$$

$$\mu^y_{\nu\nu'} = -i\frac{e}{2}\int \mathrm{d}z\mathrm{d}\rho\,\rho^2 [f^b_\alpha(\rho,z)]^* f^b_{\alpha'}(\rho,z)\Big|_{\Delta m=\pm 1} \tag{5.2.24}$$

$$\mu^z_{\nu\nu'} = e\int \mathrm{d}z\mathrm{d}\rho\,\rho [f^b_\alpha(\rho,z)]^* f^b_{\alpha'}(\rho,z)\Big|_{\Delta m=0}\,. \tag{5.2.25}$$

The intra-band dipole moments are illustrated in Fig. 5.6.

5.3 Coulomb matrix elements

In the following we shall consider an ensemble of identical quantum dots and assume that the states of different QDs are non-overlapping. This assumption is valid for relatively low QD densities where the mean QD spacing is much larger than the QD radius[4].

The Coulomb matrix elements read

$$V_{\nu_1\nu_2\nu_3\nu_4} = \int\int \mathrm{d}\boldsymbol{r}\mathrm{d}\boldsymbol{r}'\, \Psi^*_{\nu_1}(\boldsymbol{r})\Psi^*_{\nu_2}(\boldsymbol{r}')V(\boldsymbol{r}-\boldsymbol{r}')\Psi_{\nu_3}(\mathbf{r}')\Psi_{\nu_4}(\mathbf{r})\,, \tag{5.3.26}$$

where $V(\boldsymbol{r}-\boldsymbol{r}') = e^2/4\pi\epsilon|\boldsymbol{r}-\boldsymbol{r}'|$ is the bare Coulomb potential with background dielectric constant $\epsilon = \epsilon_0\epsilon_r$. With the help of the Fourier transform of the Coulomb potential we can introduce the in-plane Coulomb matrix elements with the two-dimensional momentum $\boldsymbol{q}$

$$V(\boldsymbol{r}-\boldsymbol{r}') = \frac{1}{A}\sum_{\boldsymbol{q}} V_{\boldsymbol{q}} e^{i\boldsymbol{q}\cdot(\boldsymbol{\rho}-\boldsymbol{\rho}')}e^{-q|z-z'|}, \quad V_{\boldsymbol{q}} = \frac{e^2}{2\varepsilon}\frac{1}{q}\,, \tag{5.3.27}$$

where A is the quantization area, $\boldsymbol{q} = (q_x, q_y)$ is the 2D or in-plane wavevector, and $\boldsymbol{\rho} = (x, y)$ is the in-plane position vector.

To avoid heavy numerics we, instead of calculating Coulomb matrix elements directly from the states obtained via effective mass theory, choose an approximation. As discussed above for shallow QDs it becomes a good approximation to assume that the electronic envelope function can be factored into a product of functions for each spatial direction. The in-plane part can be approximated by a harmonic oscillator as shown in Refs. [85, 86]. Evidence of the validity of this approximation is the practically equidistantly spaced QD energy spectrum. The effective envelope for the z-direction is taken as the ground state for an infinite well, whose center is offset by 1.2 nm compared to the WL envelopes. The width of the well is extrapolated from the original wave functions. The full dot wave function therefore is written as

$$\Psi_\nu(\boldsymbol{r}) = \xi^b_D(z)\varphi^b_l(\boldsymbol{\rho})u_b(\boldsymbol{r})\,, \tag{5.3.28}$$

where b is the band index, the in-plane quantum number $l = (n, m)$ covers a shell index ($n = 0, 1, 2, ...$) determining the energy $E_n = (n+1)E^b_{HO}$ of a given shell (s,p,d,...), with E^b_{HO} being the constant energy spacing between the shells of the harmonic oscillator. The second index m characterizes the two-dimensional angular momentum. Utilizing the product assumption for both dot and WL

[4] In this work we consider QD densities of $5 \cdot 10^{10}$ cm^{-2} corresponding to an average dot separation of 50 nm.

states along with the Fourier representation of the Coulomb potential allows us to split the integral

$$\begin{aligned} V_{\nu_1\nu_2\nu_3\nu_4} =& \frac{1}{A}\sum_{\boldsymbol{q}} V^{b_1 b_2}_{\sigma_1\sigma_2\sigma_3\sigma_4}(\boldsymbol{q})\delta_{b_1,b_4}\delta_{b_2,b_3} \\ & \times \int \mathrm{d}\boldsymbol{\rho}\,[\varphi^{b_1}_{\alpha_1}(\boldsymbol{\rho})]^* e^{-i\boldsymbol{q}\cdot\boldsymbol{\rho}}\varphi^{b_4}_{\alpha_4}(\boldsymbol{\rho}) \\ & \times \int \mathrm{d}\boldsymbol{\rho}'\,[\varphi^{b_2}_{\alpha_2}(\boldsymbol{\rho}')]^* e^{i\boldsymbol{q}\cdot\boldsymbol{\rho}'}\varphi^{b_3}_{\alpha_3}(\boldsymbol{\rho}')\,, \end{aligned} \tag{5.3.29}$$

with the form factor

$$V^{b_1 b_2}_{\sigma_1\sigma_2\sigma_3\sigma_4}(\boldsymbol{q}) = \frac{e^2}{2\varepsilon}\frac{1}{q}\int \mathrm{d}z\mathrm{d}z'[\xi^{b_1}_{\sigma_1}(z)\xi^{b_2}_{\sigma_2}(z')]^* e^{-iq|z-z'|}\xi^{b_2}_{\sigma_3}(z')\xi^{b_1}_{\sigma_4}(z)\ , \tag{5.3.30}$$

for $\sigma = D, WL$ and $\alpha = \{(\boldsymbol{R}, l), \boldsymbol{k}\}$. The delta functions in band index arise from the envelope approximation in the single band model, showing that only pairs having the same band index contribute. Generally the Coulomb matrix elements involve calculating in-plane overlap integrals of the type

$$\langle \varphi^b_\alpha | e^{i\boldsymbol{q}\cdot\boldsymbol{\rho}} | \varphi^b_{\alpha'}\rangle\ . \tag{5.3.31}$$

The above in-plane integrals in case of two dot states read

$$\begin{aligned} \langle \alpha | e^{i\boldsymbol{q}\cdot\boldsymbol{\rho}} | \alpha'\rangle &= \int \mathrm{d}\boldsymbol{\rho}\,[\varphi^b_\alpha(\boldsymbol{\rho})]^* e^{i\boldsymbol{q}\cdot\boldsymbol{\rho}}\varphi^b_{\alpha'}(\boldsymbol{\rho}) = \int \mathrm{d}\boldsymbol{\rho}\,[\varphi^b_l(\boldsymbol{\rho}-\boldsymbol{R})]^* e^{i\boldsymbol{q}\cdot\boldsymbol{\rho}}\varphi^b_{l'}(\boldsymbol{\rho}-\boldsymbol{R}') \\ &= \int \mathrm{d}\boldsymbol{\rho}\,[\varphi^b_l(\boldsymbol{\rho})]^* e^{i\boldsymbol{q}\cdot(\boldsymbol{\rho}+\boldsymbol{R})}\varphi^b_{l'}(\boldsymbol{\rho}+\boldsymbol{R}-\boldsymbol{R}') \\ &= \langle l | e^{i\boldsymbol{q}\cdot\boldsymbol{\rho}} | l'\rangle\, e^{i\boldsymbol{q}\cdot\boldsymbol{R}}\delta_{\boldsymbol{R},\boldsymbol{R}'} \end{aligned} \tag{5.3.32}$$

where the final step comes from the assumption that states localized on different QDs do not overlap.

For combinations of QD and WL states, we find

$$\begin{aligned} \langle \alpha | e^{i\boldsymbol{q}\cdot\boldsymbol{\rho}} | \boldsymbol{k}'\rangle &= \int \mathrm{d}\boldsymbol{\rho}\,[\varphi^b_\alpha(\boldsymbol{\rho})]^* e^{i\boldsymbol{q}\cdot\boldsymbol{\rho}}\varphi^b_{\boldsymbol{k}'}(\boldsymbol{\rho}) = \int \mathrm{d}\boldsymbol{\rho}\,[\varphi^b_l(\boldsymbol{\rho}-\boldsymbol{R})]^* e^{i\boldsymbol{q}\cdot\boldsymbol{\rho}}\varphi^b_{\boldsymbol{k}'}(\boldsymbol{\rho}) \\ &= \langle \alpha | e^{i\boldsymbol{q}\cdot\boldsymbol{\rho}} | \boldsymbol{k}'\rangle\, e^{i(\boldsymbol{k}'+\boldsymbol{q})\cdot\boldsymbol{R}}. \end{aligned} \tag{5.3.33}$$

And for two WL states it follows trivially

$$\langle \boldsymbol{k} | e^{i\boldsymbol{q}\cdot\boldsymbol{\rho}} | \boldsymbol{k}'\rangle = \delta_{\boldsymbol{k},\boldsymbol{q}+\boldsymbol{k}'}\ . \tag{5.3.34}$$

The overlap integrals involve either two harmonic oscillator states or a combination of a plane wave and a harmonic oscillator state. These integrals have analytical solutions which have been tabulated in Ref. [82].

The main point in applying the wave function product approximation for the dot states is that the evaluation of Coulomb elements becomes semi-analytical

thus significantly decreasing the computational effort. For the approximated envelope functions employed here we find the resulting Coulomb elements involving solely QD states only differed by maximally 5% from those based the original QD states. As for the WL states the result of using non-orthogonalized plane waves comes about in Coulomb elements involving a combination of WL and dot states. The missing orthogonality results in an overestimation of the overlap integral and thus also the matrix element in question (see e.g. Ref. [44]).

5.3.1 Hartree-Fock renormalization

The ensemble average that enters in the expression for macroscopic polarization Eq. (3.1.5) relies on the fact that we can treat the dots independently, i.e. without referring to a particular position $\boldsymbol{R}$. The Coulomb interaction couples a given dot with both WL and the dots surrounding it thereby deviating from the independent dot picture. We show in Appendix A that for a random and sufficiently dilute distribution of dots, global charge neutrality restores the independent dot picture while the absence of local charge neutrality leads only to energy corrections from interactions between states within the same dot.

The renormalization of the energy of a given state $\tilde{\epsilon}_\nu$ and Rabi energy $\Omega_{\nu\nu'}$ stems from the Hartree-Fock terms

$$\tilde{\epsilon}_\nu = \epsilon + \Delta_\nu^{\mathrm{HF}}\,, \tag{5.3.35}$$

$$\Omega_{\nu\nu'} = -\mu_{\nu\nu'}E(t) + \Delta_{\nu\nu'}^{\mathrm{HF}}\,. \tag{5.3.36}$$

The HF shifts are defined as

$$\begin{aligned}\Delta_\nu^{\mathrm{HF}} &= \Delta_\nu^{\mathrm{H}} + \Delta_\nu^{\mathrm{F}} \\ &= \pm\sum_{\nu_1\nu_2}\left[V_{\nu\nu_2\nu_1\nu} - V_{\nu\nu_2\nu\nu_1}\right](1-2\delta_{\nu_1,\nu_2}\delta_{b_1,h})\rho_{\nu_1\nu_2} \qquad (5.3.37)\\ \Delta_{\nu\nu'}^{\mathrm{HF}} &= \Delta_{\nu\nu'}^{\mathrm{H}} + \Delta_{\nu\nu'}^{\mathrm{F}} \\ &= \sum_{\nu_1\nu_2}\left[V_{\nu\nu_2\nu_1\nu'} - V_{\nu\nu_2\nu'\nu_1}\right](1-2\delta_{\nu_1,\nu_2}\delta_{b_1,h})\rho_{\nu_1\nu_2}\,. \qquad (5.3.38)\end{aligned}$$

To lighten the notation we will skip the $(1-2\delta_{\nu_1,\nu_2}\delta_{b_1,h})$ part and remember that when ever we encounter a hole population it comes with a minus sign. In the following we shall also drop the $\pm$ in front of the energy renormalization term and put it back in when stating a result.

Hartree renormalization

From Appendix A we find that the Hartree energy shifts of the WL states vanish due to global charge neutrality

$$\Delta_{b,\boldsymbol{k}}^{\mathrm{H}} = 0\,. \tag{5.3.39}$$

For the same reason the Hartree energy shift of a localized dot state is only attributed to interaction with charges and intra-band polarization components on the same dot

$$\Delta^{\mathrm{H}}_{b,l} = \pm \sum_{b_1,l_1,l_2} V^{bb_1}_{ll_1l_2l} \rho^{b_1}_{l_1l_2} \,. \tag{5.3.40}$$

For the Rabi energy renormalization the Hartree term is only non-zero for QD intra-band polarizations ($b = b'$).

$$\Delta^{\mathrm{H}}_{b,l,l'} = \sum_{b_1,l_1,l_2} V^{bb_1}_{ll_1l_2l'} \rho^{b_1}_{l_1l_2} \,. \tag{5.3.41}$$

Fock renormalization

In the Fock terms, the summation over different QD positions can be performed directly and the phase factors are seen to disappear. The resulting Fock energy shifts contain contributions from both QD and WL

$$\Delta^{\mathrm{F}}_{b,l} = \pm \left[\sum_{l_1l_2} V^{bb}_{ll_2ll_1} \rho^{b}_{l_1l_2} + \sum_{\boldsymbol{k}_1} V^{bb}_{l\boldsymbol{k}_1l\boldsymbol{k}_1} n^{b}_{\boldsymbol{k}_1} \right] , \tag{5.3.42}$$

$$\Delta^{\mathrm{F}}_{b,\boldsymbol{k}} = \pm \left[N \cdot \sum_{l_1l_2} V^{bb}_{\boldsymbol{k}l_2\boldsymbol{k}l_1} \rho^{b}_{l_1l_2} + \sum_{\boldsymbol{k}_1} V^{bb}_{\boldsymbol{k}\boldsymbol{k}_1\boldsymbol{k}\boldsymbol{k}_1} n^{b}_{\boldsymbol{k}_1} \right] . \tag{5.3.43}$$

As for the Fock Rabi energy shifts we find

$$\Delta^{\mathrm{F}}_{b,b',l,l'} = -\sum_{l_1l_2} V^{bb'}_{ll_2l'l_1} \rho^{bb'}_{l_1l_2} - \sum_{\boldsymbol{k}_1} V^{bb'}_{l\boldsymbol{k}_1l'\boldsymbol{k}_1} \rho^{bb'}_{\boldsymbol{k}_1} \,, \tag{5.3.44}$$

$$\Delta^{\mathrm{F}}_{b,b',\boldsymbol{k}} = N \cdot \sum_{l_1l_2} V^{bb'}_{\boldsymbol{k}l_2\boldsymbol{k}l_1} \rho^{bb'}_{l_1l_2} + \sum_{\boldsymbol{k}_1} V^{bb'}_{\boldsymbol{k}\boldsymbol{k}_1\boldsymbol{k}\boldsymbol{k}_1} \rho^{bb'}_{\boldsymbol{k}_1} \,. \tag{5.3.45}$$

The Coulomb terms $V^{bb'}_{\boldsymbol{k}l_2\boldsymbol{k}l_1}$ in Eq. (5.3.43) and Eq. (5.3.45) are associated with an additional factor $1/A$ so that the QD density $N_{\mathrm{dot}} = N/A$ enters in these expressions.

5.4 Multi-band calculations

In this section we study the impact of strain and band mixing on the optical properties of isolated cone shaped QDs, i.e. disregarding the WL structure. The effect of band mixing is determined by comparing results obtained via eight band $\boldsymbol{k} \cdot \boldsymbol{p}$ theory with results using a single band model. It is beyond the scope of this work to give a complete treatment of the underlying theory. Instead we point the reader to the thesis work by D. Barettin [87] which also

covers the results presented here, the textbook treatments mentioned in the beginning of this chapter, and to Ref. [88] for a description of the eight-band Hamiltonian and Ref. [89] for the strain dependent part. In the eight-band model the wavefunction Ψ_n of the n'th localized dot state is given by a linear combination of the eight Bloch states weighted by an envelope function,

$$\Psi_n = \sum_{i=1}^{8} \psi_i^{(n)} u_i \,, \tag{5.4.46}$$

where $\psi_i^{(n)}$ are the envelope functions and u_i are the Bloch states. The eight-band model includes the conduction band, heavy-holes, light-holes and spin-orbit split-off bands around the Γ point of the Brillouin zone.

In the following we explicitly present the one-band models as due to their simplicity these are most open to interpretation. The one-band eigenvalue equation for the envelope functions reads $H_\lambda \phi_\lambda = E_\lambda \phi_\lambda$ where H_λ, ϕ_λ and E_λ are the Hamiltonian, the envelope wave function and the energy, respectively. λ denotes either the conduction band or the heavy holes, i.e., $\lambda = \{e, hh\}$. The Hamiltonian is

$$H_\lambda = H_\lambda^k(\boldsymbol{r}_\lambda) + H_\lambda^b(\boldsymbol{r}_\lambda) + H_\lambda^\epsilon(\boldsymbol{r}_\lambda) \,, \tag{5.4.47}$$

where $H_\lambda^k(\boldsymbol{r}_\lambda)$ is the kinetic part, $H_\lambda^b(\boldsymbol{r}_\lambda)$ is the energy of the unstrained band edge, and $H_\lambda^\epsilon(\boldsymbol{r}_\lambda)$ is the strain dependent part.

The kinetic part is given by:

$$H_s(\boldsymbol{r}_\lambda) = \frac{\hbar^2}{2m_0}\left(\boldsymbol{k}\frac{1}{m_\lambda(\boldsymbol{r})}\boldsymbol{k}\right), \tag{5.4.48}$$

where $\hbar$ is Planck's constant, m_0 is the is the free-electron mass, $\boldsymbol{k}$ is the wave vector operator and m_λ is the effective masses of either the conduction band electron or heavy hole in units of m_0. Material parameters used for calculations in this section are taken from [90].

In the one-band model the strain Hamiltonian for a zincblende crystal structure is given by

$$H_e^\epsilon(\boldsymbol{r_e}) = a_c(\boldsymbol{r})\varepsilon_H(\boldsymbol{r}), \tag{5.4.49}$$

$$H_{hh}^\epsilon(\boldsymbol{r}_{hh}) = -a_v(\boldsymbol{r})\varepsilon_H(\boldsymbol{r}) + \frac{b}{2}\varepsilon_B(\boldsymbol{r}), \tag{5.4.50}$$

where a_c (a_v) and b are the conduction (valence)-band hydrostatic deformation potential and b is the shear deformation potential, respectively [91]. The hydrostatic and biaxial strain components read

$$\varepsilon_H(\boldsymbol{r}) = \varepsilon_{xx}(\boldsymbol{r}) + \varepsilon_{yy}(\boldsymbol{r}) + \varepsilon_{zz}(\boldsymbol{r}), \tag{5.4.51}$$

$$\varepsilon_B(\boldsymbol{r}) = \varepsilon_{xx}(\boldsymbol{r}) + \varepsilon_{yy}(\boldsymbol{r}) - 2\varepsilon_{zz}(\boldsymbol{r}), \tag{5.4.52}$$

where ε_{ik} is the strain tensor. The strain fields are found by minimizing the elastic strain energy [92]. The above expressions show that strain has a profound different impact on the conduction band than on the valence band. The

conduction band only experiences the homogeneous hydrostatic strain, which only serves to shift the energy. The valence band electrons also experiences a inhomogeneous contribution from the biaxial strain component, which affects the spatial dependence of the envelope wave function.

Dipole moments are calculated from the momentum matrix element $\boldsymbol{p}_{nm}$ as in Eq. (5.2.10), for a generalized multi-band model it reads:

$$\begin{aligned}\boldsymbol{p}_{nm} &\equiv \langle \Psi_n | \boldsymbol{p} | \Psi_m \rangle \\ &= \sum_{i,j=1}^{N} \left(\langle \psi_i^{(n)} | \boldsymbol{p} | \psi_j^{(m)} \rangle \delta_{ij} + \langle \psi_i^{(n)} | \psi_j^{(m)} \rangle \langle u_i | \boldsymbol{p} | u_j \rangle \right) \\ &\equiv \boldsymbol{p}_{nm}{}^{(\psi)} + \boldsymbol{p}_{nm}{}^{(u)}, \end{aligned} \tag{5.4.53}$$

where $N = 1$ or 8. $\boldsymbol{p}^{(\psi)}$ and $\boldsymbol{p}^{(u)}$ are the envelope and the Bloch parts of the momentum matrix element, respectively. It is usual to consider only the Bloch part $\boldsymbol{p}^{(u)}$ since the envelope part $\boldsymbol{p}^{(\psi)}$ is usually an order of magnitude smaller, as shown in [93] and further corroborated by our own findings. The intra-band dipole moment for the single band models is a special case as only $\boldsymbol{p}^{(\psi)}$ is non-zero. Here Eq. (5.2.20) is used instead.

5.4.1 Dipole moments: Size and geometry dependence

We investigate the size and geometry dependence of the dipole moments by considering two cases. We consider QDs with a fixed aspect ratio between the radius r and height h (see illustration in Fig. 5.2) and vary the volume, or we fix the volume and vary the aspect ratio. The results presented in Fig. 5.7 and Fig. 5.8 are related to a set of QDs with fixed aspect ratio $r = 2h$. We focused on the first twelve bound states for both bands. Since all the states are at least doubly degenerate (spin degeneracy), we consider six energy levels (labeled from 1 to 6) for both bands. In the one-band model, due to the conical quantum-dot symmetry along with the assumption of atomistic isotropy, level 2 and level 3 are degenerate for both the conduction and the valence band, level 4 and level 5 are degenerate for the valence band, and level 5 and level 6 are degenerate for the conduction band. In the upper part of Fig. 5.7 and Fig. 5.8 we show the energy levels and inter-band dipole moments relevant for EIT operation corresponding to a dot with $h = 7.5$ nm for the four different models: one-band model without strain, one-band model with strain, eight-band model without strain and eight-band model with strain. Throughout this section we consider only one polarization direction; within the QD growth plane, right handed circularly polarized.

In Figs. 5.7 and 5.8 the thicknesses of the lines indicating the transitions, are proportional to the corresponding dipole moments. Obviously, an eight-band model calculation leads to a higher valence-band density-of-states as compared to a one-band calculation. Hence, also more interband transitions result, in a given energy range, when using an eight-band model. In other words; the additional bandstructure generates more interband transitions since we no longer

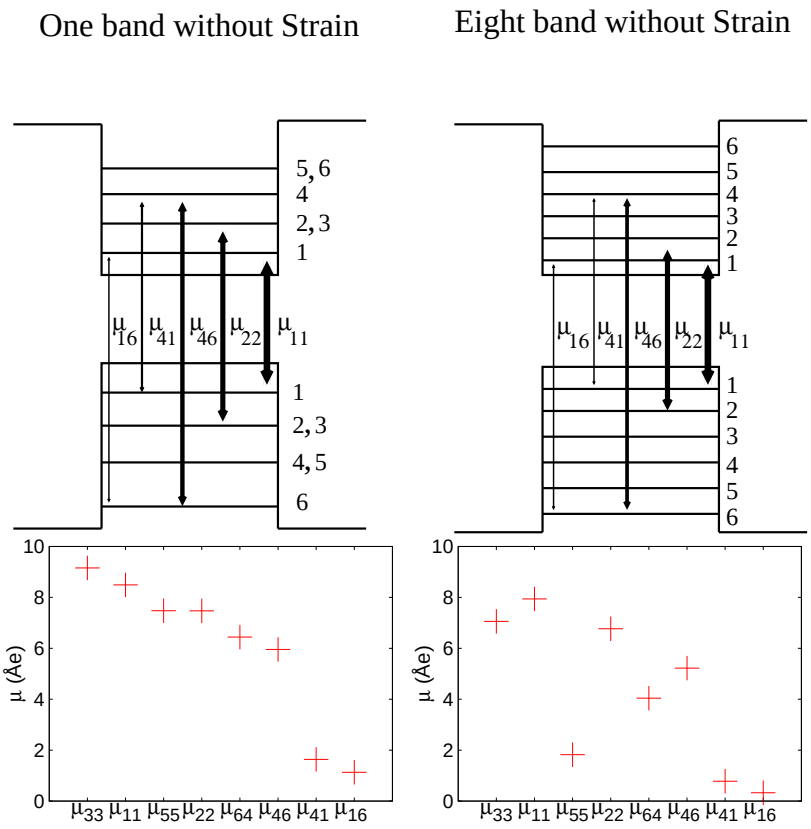

***Figure 5.7**: Energy level structure and relevant dipole moments for EIT (top) and values of the eight strongest interband dipole moments (bottom) for one-band (left) and eight-band (right) model without strain for a dot with $h = 7.5$ nm. From [94].*

have the strict selection rules as for single band. We have chosen to show in the bottom part of Fig. 5.7 and Fig. 5.8 only the strongest eight dipole-matrix elements for both one-band and eight-band models. First, we observe that there is a qualitative agreement between dipole-moment results for the one-band and eight-band models with strain (Figure 5.8). This is due to the fact that in the eight-band model the biaxial strain component of Eq. (5.4.52) shifts heavy-holes (light-holes) to higher (lower) energies. As a consequence the valence-band groundstate and the first excited states are predominantly heavy-holes like giving rise to a general better agreement between the one-band model and the eight-band model. The only notable discrepancies are observed for the EIT relevant transitions μ_{46} and μ_{41}. Second, the inclusion of strain reduces the strength of the dipole moments significantly. This is because there is a non-trivial influence of strain on the wave functions. The conduction-band states are only affected by the hydrostatic strain component of Eq. (5.4.51) giving rise more or less to a constant shift in the effective potential inside the dot while the valence band states, in addition to the hydrostatic strain, are also affected by the biaxial strain component (see Eq. (5.4.52)). The latter component is highly inhomogeneous inside the dot. In the eight-band model there is a third contribution from ϵ_{xz} and ϵ_{yz} strain components [89] but this term is not as

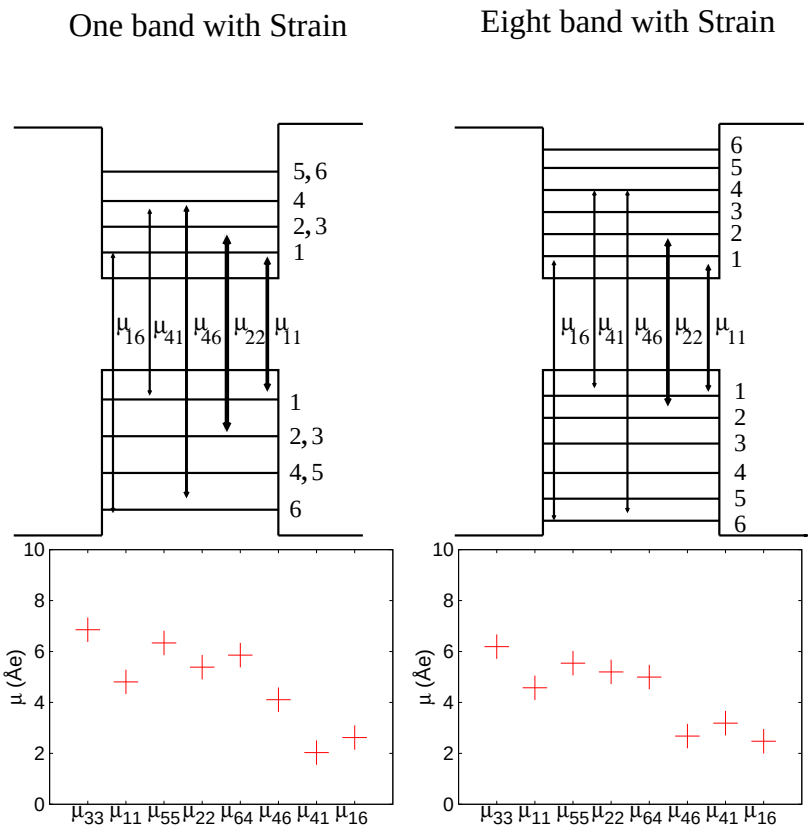

***Figure 5.8**: Energy level structure and relevant dipole moments for EIT (top) and values of the eight strongest interband dipole moments (bottom) for one-band (left) and eight-band (right) model with strain for a dot with $h = 7.5$ nm.From [94].*

significant as the biaxial of Eq. (5.4.52).

In order to understand the influence of strain on the dipole moment we compare in Fig. 5.9 the valence-band groundstate probability density $|\Psi|^2$ (eight-band model) with and without the influence of the strain field for a quantum dot with height $h = 11.5$ nm and radius $r = 23$ nm. While in the case without strain the groundstate shows a *s-like* shape, the biaxial-strain component modifies the hole wave function into a toroidal shape moving it away from the center of the dot where the potential is stronger. This drastically reduces the overlap between the envelope functions ψ_i of the conduction and valence band and consequently the corresponding dipole moments.

The reduction of the dipole moment due to strain is evident in Fig. 5.10 where we plot the interband dipole moment μ_{11} between the conduction- and the valence-band ground states for the four different models as a function of h. In the models with strain we have a maximum around $h = 5$ nm, while the dipole moments for the two models without strain grow monotonically with increasing height and eventually reach a plateau value corresponding to the bulk value of 16.8 Åe. The monotonic increase of the dipole moments can be understood based on Eq. (5.2.8). Without strain the momentum matrix elements $\boldsymbol{p}$ (mainly

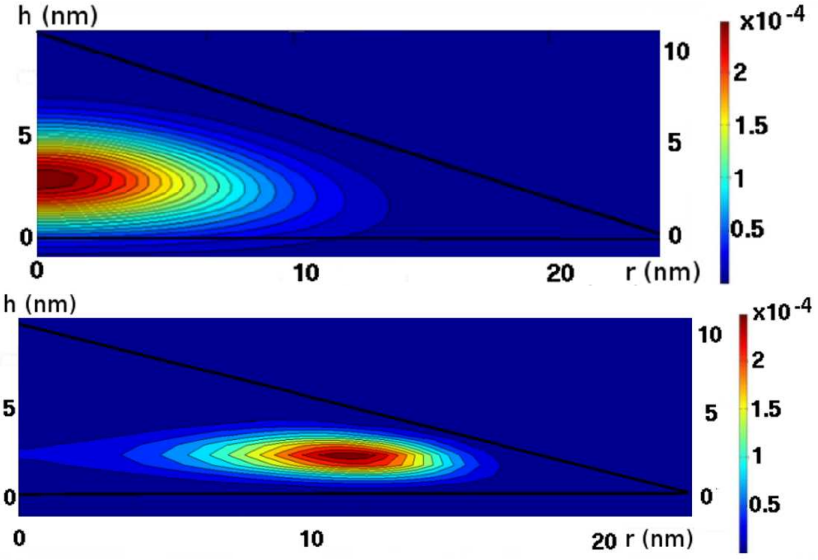

***Figure 5.9**: Probability density $|\Psi|^2$ of the valence-band groundstate for the eight-band model without (up) and with (down) strain. The dimensions of the quantum dot are $h = 11.5$ nm and $r = 23$ nm. From [94].*

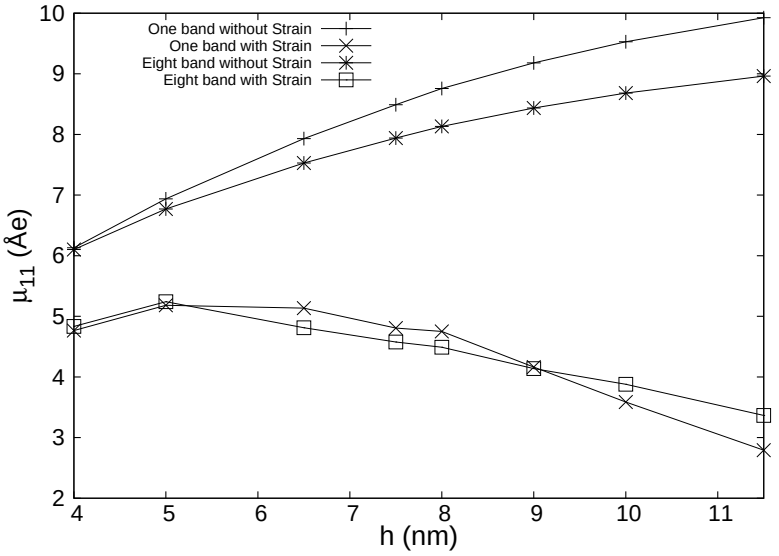

***Figure 5.10**: Interband μ_{11} dipole moments as a function of h for the four different models. From [94].*

determined by $\boldsymbol{p}^{(u)}$) remains constant with increasing height whereas the energy difference ω_{nm} decreases. The presence of strain reduces the overlap of electron and hole distributions as a result of the increased displacement of the hole wave functions away from the center leading to the observed decrease in the dipole moments.

In Fig. 5.11 we plot the energies of the first six levels in the conduction (top)

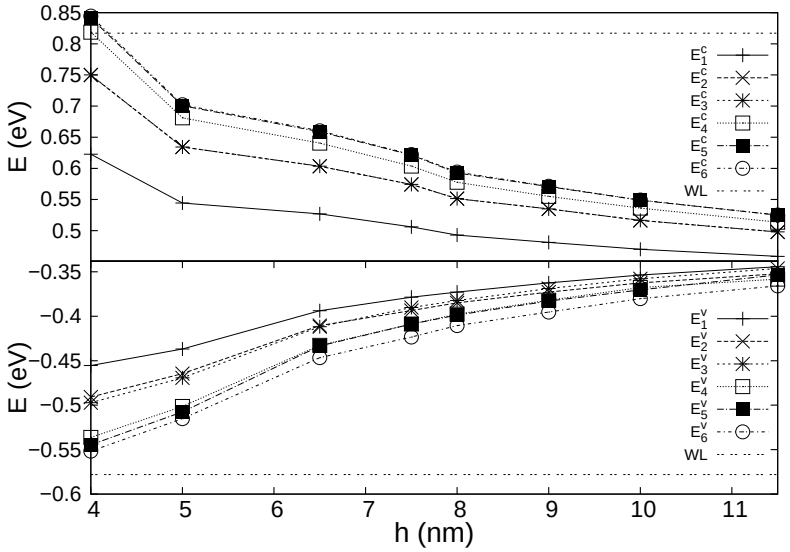

***Figure 5.11**: Energies of the six considered levels in conduction (top) and valence (bottom) band as a function of h with fixed aspect ratio $r = 2h$ for the eight-band model with strain. The onset of continuous wetting layer states (WL) is also indicated (dashed-horizontal line). From [94].*

and valence band (bottom) as a function of the height h. The wave functions of the confined states are characterized (in the eight-band model) by eight envelopes weighted differently depending on the state. As mentioned above, the biaxial strain is inhomogeneous and this, combined with the differently spatially distributed envelope functions, leads to a higher sensitivity against strain as compared to a one-band model. Further, the inhomogeneity of the strain field grows with volume, especially for the biaxial-strain component of Eq. (5.4.52). These coupled strain-band mixing effects lead to energy crossings in the valence band. We have also indicated where the wetting layer continuum starts (WL). The WL dashed lines in Fig. 5.11 are computed using a Ben-Daniel Duke approach for a 0.5 nm InAs quantum-well embedded in GaAs [95]. We observe that the last three considered conduction-band levels for the smallest quantum dot lie above the lower bound of the wetting layer continuum states.

The EIT relevant dipole moments for the eight-band model are shown in the upper part of Fig. 5.12 as a function of h. The bottom part gives the related energy differences ΔE. The strain reduces the dipole-moment strengths with increasing volume because of the decreasing wave function overlap (similar to what was found for μ_{11}).

This geometry effect is indeed mainly a function of the dot volume as Fig. 5.13 shows. Here, we refer to a second set of quantum dots with different aspect ratios (r/h) having the same volume ($V = 226.19$ (nm)^3). The interband dipole moments (top) and relative energy differences (bottom) are depicted as a function of aspect ratio and evidently results are rather insensitive to the aspect ratio.

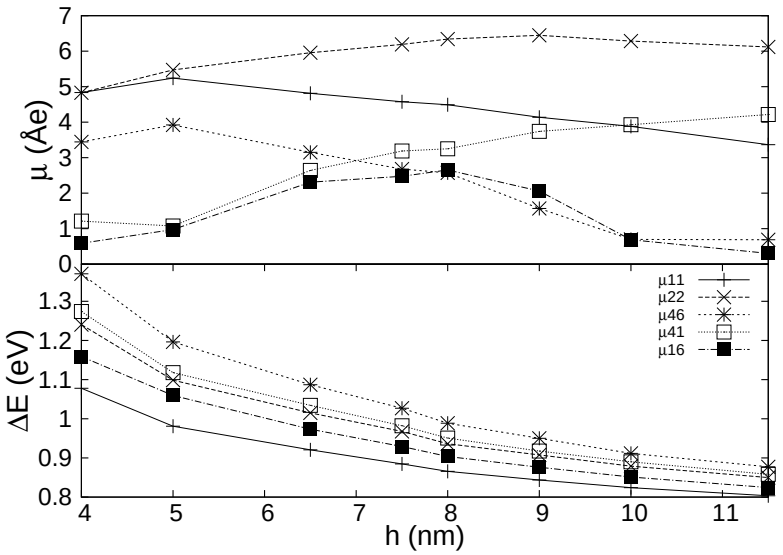

***Figure 5.12**: Interband dipole moments μ (top) and band energy difference ΔE (bottom) as a function of the height h with fixed aspect ratio $r = 2h$. From [94].*

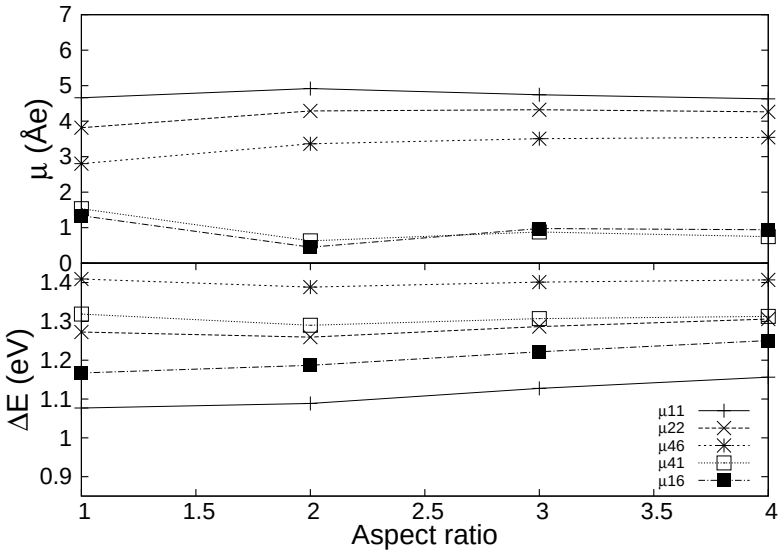

***Figure 5.13**: Interband dipole moments μ (top) and relative band energy difference ΔE (bottom) as a function of the aspect ratio (r/h) at constant volume. From [94].*

5.4.2 EIT properties

In this section we consider right-handed circularly polarized light for both the coupling and probe fields and investigate the slow light characteristics upon propagation through several stacked layers of QD material. We assume that one can disregard propagation effects in the coupling field. We use a c-w coupling beam and apply the rotating wave approximation so that a single time susceptibility can be extracted. Otherwise the system response is calculated

using the procedure presented in Chapter 2 and 3, using a dephasing rate corresponding to a lattice temperature of 200 K and disregarding Coulomb effects.

The possible interband EIT schemes are illustrated in Fig. 5.8 (top). By combining the shown EIT relevant transitions a variety of different V as well as Λ-schemes can be accessed. As noted in a previous section there are very few differences between dipole moments predicted by the one-band strained model and the eight-band strained model, however the deviations that do exist, appears for transitions that could be used in connection with EIT. The one-band strained model significantly overestimates μ_{46}, a transition that would otherwise seem attractive to use for EIT. Furthermore, μ_{41} is very small in all but the eight-band strained model. To illustrate the impact of these differences we have in Fig. 5.14 shown absorption spectra for an EIT scheme constructed using μ_{41} as probe and μ_{46} as coupling transition. It is seen that using eight-band

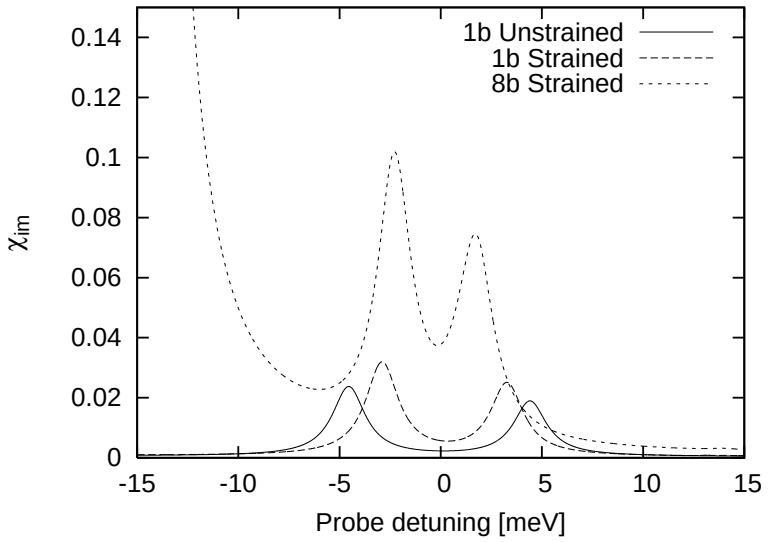

Figure 5.14: *EIT absorption spectrum calculated using μ_{41} as probe and μ_{46} as coupling transition for different models: one-band unstrained (full line), one-band strained (dashed line) and eight-band strained (dotted line). The additional feature in the eight-band strained calculation is due to the nearby lying μ_{55} resonance. From [94].*

strained bandstructure results in an altered EIT behavior. The signature feature, the split peaks, are higher and closer together, a direct consequence of the magnitudes of the involved dipole moments. These significant differences between the spectra justifies focusing on the results of the more accurate eight-band strained bandstructure model. A V and Λ scheme can be realized using μ_{41} as coupling transition and either of the two transitions μ_{11} or μ_{46} for the probe field. Two similar schemes can be accessed using the same probe transitions and μ_{16} for the coupling field. As is evident from Fig. 5.13 the dipole moments are relatively unchanged by varying shape (aspect ratio), we choose to focus on $r/h = 2$ since the common probe transitions (μ_{11} and μ_{46}) are maximized for this geometry and consider volume dependencies.

We see that for small dots ($h < 5$ nm) the dipole moments addressed by the coupling beam are relatively small (on the order of 1 nm) and therefore dots of this size are not suitable for EIT operation. As the dot increases in size both coupling transitions become stronger, the two probe transitions, however begins to decrease. The dipole μ_{46} is always the smaller of the two probe transitions, and the fact that it drops off faster suggests that one should aim at using μ_{11}, ground state to ground state, as probe transition.

To quantify the above discussion we show in Fig. 5.15 the slowdown factor as a function of coupling intensity calculated for three different dot volumes ($h = 6.5\text{ nm}, 8\text{ nm}, 10\text{ nm}$) for each of the two remaining EIT schemes[5]. For every dot type we see that the V-scheme prevails, it has the lowest coupling power requirements and the largest obtainable slowdown value. The first observation can be understood from Fig. 5.12 where the V-scheme coupling transition μ_{41} is always the larger. Since both schemes utilize the same probe transition one could be inclined to think that they should display the same maximum slowdown value. The reason they do not, is that the coupling beam, although detuned, is exciting carriers into the levels connected by the probe beam. The presence of the carriers serve to block the probe transition. As indicated in the lower part of Fig. 5.12, the coupling beam in the Λ case is less detuned from the probe transition than in the V case, and thus more carriers are excited into the electron and hole ground states, resulting in a smaller effective probe transition strength. It is apparent that the best tradeoff between maximum slowdown and coupling intensity is found using the V scheme for dots having a relatively large height, in the region around 8 nm.

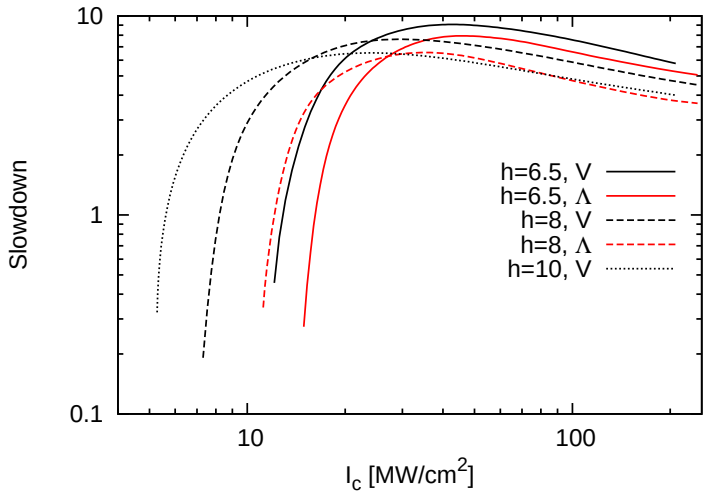

***Figure 5.15**: (Color online) Slowdown versus coupling beam intensity calculated for three different dot sizes. The black curve refers to the V scheme whereas the red curve is for Λ configuration. From [94].*

[5]for the $h = 10$ nm dot, in the case of the Λ scheme no EIT behavior is found due to its weak coupling transition. Slowdown results for this dot/EIT setup has therefore been omitted in Fig. 5.15.

Chapter 6

EIT - Coulomb effects in QDs

This chapter explores the steady state and transient properties of QD EIT. Different EIT schemes are compared in order to identify a preferable setup. Two different kinds of models are used; a many-body model, that includes Coulomb effects and an atomic model without interactions. For the atomic model this entails that population scattering is disregarded. All results presented in this chapter are calculated for the same lattice temperature and hence have the same effective dephasing rate, that is using a T_2 value of 0.66 ps corresponding to 200 K.

6.1 EIT-schemes

The single band QD model to be used in all coming EIT simulations was presented in the previous chapter. The resulting energy level structure along with three different EIT-schemes are shown schematically in Fig. 6.1. The dipole selection rules allow for the realization of the three archetypical EIT schemes; Ladder, V and Λ. In all cases the probe is polarized in the WL plane (x-direction), this is also the case for the control beam in the V and Λ schemes. In the Ladder scheme the coupling field connects states $|e0\rangle$ and $|e5\rangle$ and is polarized in the growth direction of the QD's (z-direction). Inevitably this means that the coupling field is traveling in the WL plane, however as the coupling field is connecting two empty transitions it experiences no absorption, and propagation effects can be disregarded. The reason for choosing this particular transition for the coupling is due to the almost equidistant energy level spacings. If we use an in-plane polarized field we can connect the various intra-band shells of the dot, e.g. $s-p$ or $p-d$, however the resulting susceptibility deviates from the expected result. The fact that the energy levels are nearly equidistantly spaced means that the coupling connects both the $s-p$ and $p-d$ intra-band transitions, an effective four-level Ladder type scheme, a scheme that does not exhibit the desired transparency effect. An example of such a setup, where the coupling field is tuned to the $s-p$ electron intra-band transition is shown in Fig. 6.2. The calculation is based on the non-interacting model using a c-w

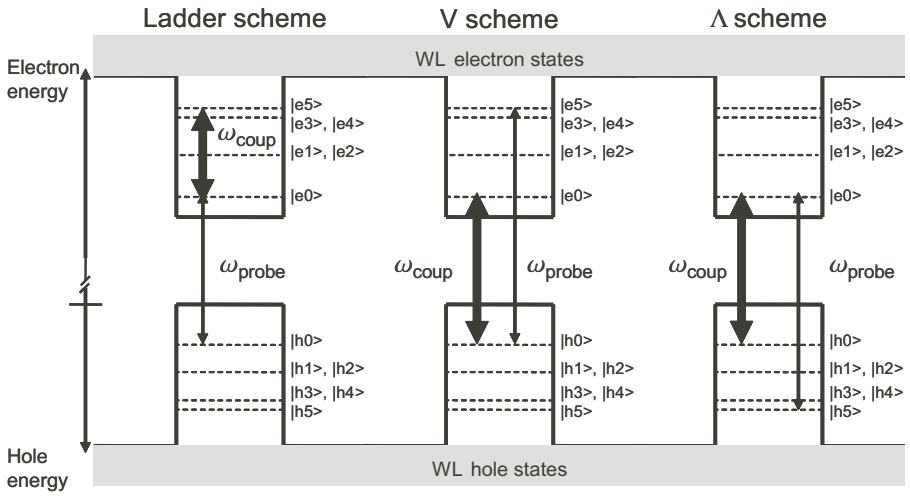

***Figure 6.1**: Schematic quantum dot level structure and three possible EIT configurations.*

coupling beam. Instead of displaying an absorption dip, the spectrum has peak around the resonance frequency. This is due to the states in the d-shell that are also being addressed by the coupling field. They introduce alternative decay pathways to the system and that effectively destroy the destructive interference between the available paths, which is at the origin of EIT. In the single band

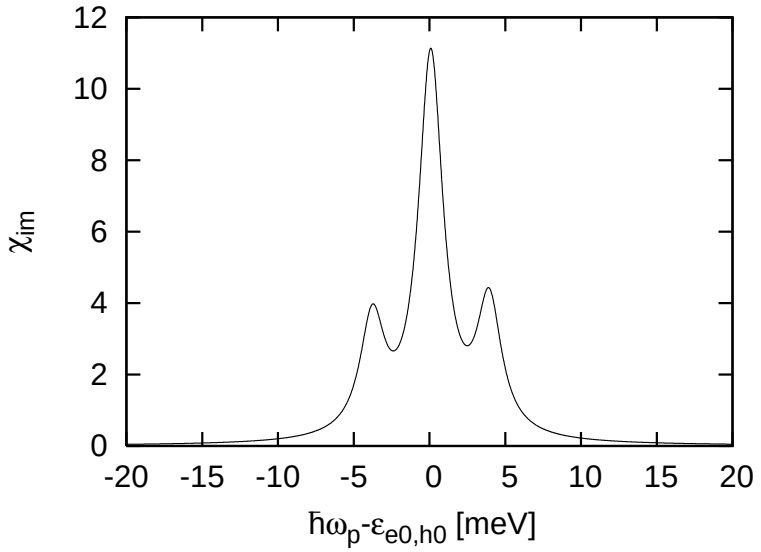

***Figure 6.2**: Imaginary part of the susceptibility for a Ladder type scheme using a coupling beam tuned to the $s-p$ electron intra-band transition. The calculation is based on the non-interacting model.*

model without strain the "indirect" inter-band transitions connecting states belonging to different shells are very small and schemes involving such transitions hardly display the EIT effect. In order to facilitate a comparison between different EIT configurations, the strength of the inter-band transitions connecting

$|e0\rangle$ and $|h5\rangle$ as well as $|e5\rangle$ and $|h0\rangle$ have been increased so as to match the results obtained via eight band $k \cdot p$ theory including strain. This entails that the transitions in question are enlarged so that they have a magnitude of around $2/3$ relative to the bright $|e0\rangle - |h0\rangle$ inter-band transition[1].

To illustrate the inter-band transitions, we plot the absorption spectrum for the dot using an x-polarized probe in Fig. 6.3. The figure also shows the outcome of including Coulomb interactions, resulting in excitonic shifts of the transitions as well as the redistribution of oscillator strengths. Since the peaks of the spectrum including Coulomb effects are generally higher than those disregarding Coulomb effects, it might seem as if the oscillator sum rule is not obeyed. However, the discrepancy is caused by redistribution of oscillator strength from the WL transitions, which are not shown in the figure.

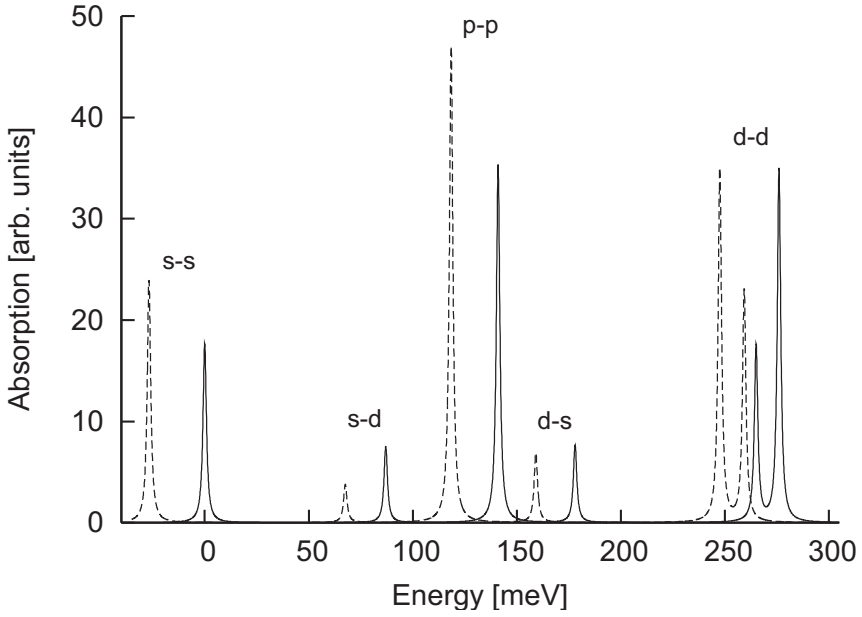

***Figure 6.3**: QD absorption spectrum using a homogeneous broadening corresponding to 200 K. Solid line refers to the spectrum disregarding Coulomb interactions, the dotted line shows the spectrum when Coulomb interactions are included. The zero point of the probe energy is taken as the energy of the non-interacting ground state to ground state (s-s) resonance. Also indicated on the figure is which type of states, that the different transitions connect. The first letter refers to the electron state, the second to the hole.*

[1]Late in the process it has been realized that inter-band dipole moments are calculated based on bulk parameters, i.e. using the value of the InAs bandgap for $\omega_{\nu\nu'}$ in Eq. (5.2.8). This entails that the inter-band dipoles used in the following calculations should be scaled by roughly a factor $1/2 - 1/3$.

6.2 Probe duration dependency

The non-equilibrium system responses (which we shall refer to as the susceptibility) derived in Chapter 3 depend on both the probe and the coupling beam. In the steady state limit, for a probe of sufficient duration, the system response collapses into a single time function, and there should be no dependency on the temporal structure of the probe nor the actual time the probe is applied. We illustrate the probe duration dependency in Fig. 6.4 for the non-interacting Ladder scheme using gaussian shaped probe pulses of varying duration (FWHM) Δt_p peaking around the same time t_p. In the non-interacting Ladder scheme the energy of the coupling transition is 222 meV, corresponding to a coupling field period of 0.023 ps.

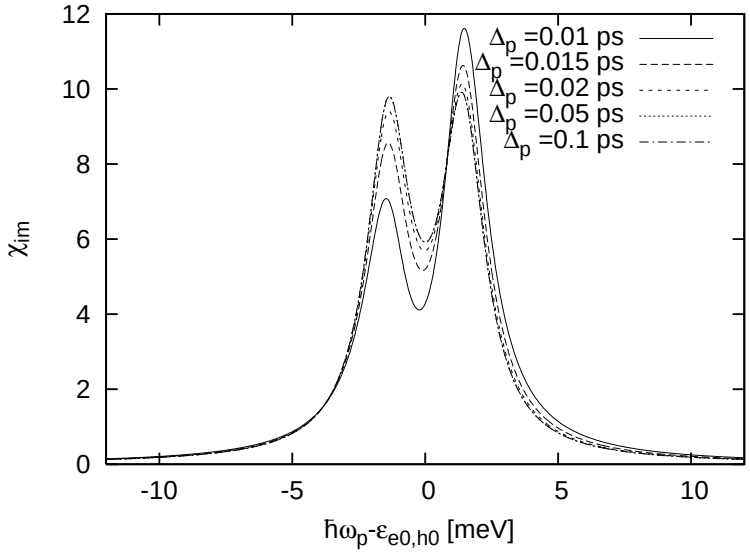

***Figure 6.4**: Imaginary part of the susceptibility calculated using five different probe durations all peaking around the same time.*

From the figure it is seen that probes with a duration longer than twice the coupling field period, i.e. 0.05 ps, gives the same dynamic susceptibility. If we use a shorter and thus spectrally wider pulse the system response is influenced by the sidebands generated by the coupling field. This is illustrated in Fig. 6.5, showing different responses when the system is probed at different times t_p using a $\Delta t_p = 0.01$ ps pulse. As the Ladder scheme involves the smallest coupling frequency (the transition is of intra-band type) it is for this scheme the sideband influence occurs using the longest probe durations. In the other schemes, which use high-frequency inter-band transitions, this effect occurs for much shorter probe pulses for which the even the SVEA is invalid. Since we aim to compare the slowdown capabilities of the different schemes we will throughout this chapter use a probe pulse of 0.1 ps (FWHM) duration, so that the response functions can be used for wave propagation characterization.

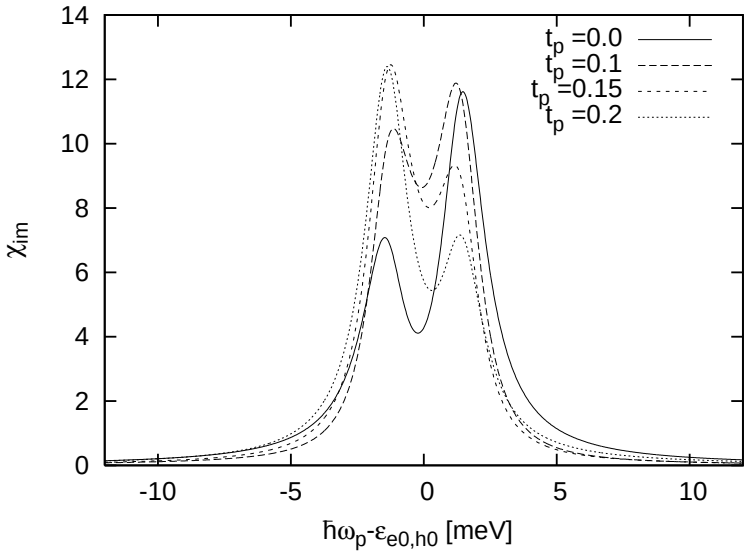

***Figure 6.5**: Imaginary part of the susceptibility calculated using a probe duration (FWHM) of 0.01 ps applied at 4 different times t_p. The times are taken relative to the peak probe times of Fig. 6.4.*

6.3 Steady state EIT

We obtain steady state results by using a c-w coupling beam. At times much larger than the inverse of the dephasing rate the system is assumed to have reached a steady state and is then probed using a temporally narrow gaussian shaped pulse (see Fig. 6.6). This is a sufficient condition when considering the

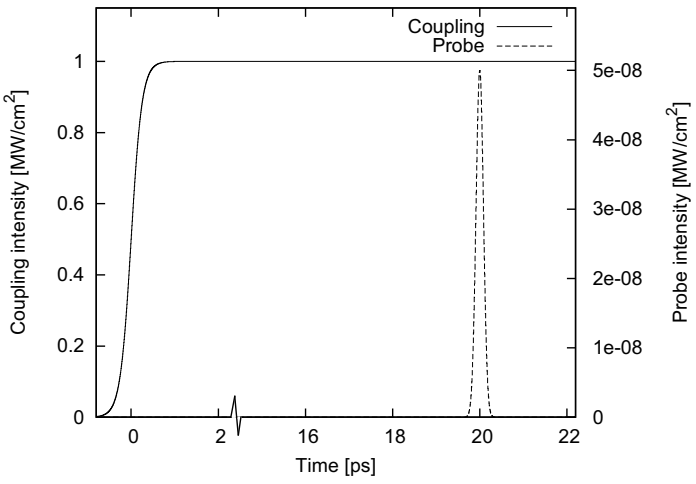

***Figure 6.6**: Example of coupling and probe field setup used for steady state simulations.*

atomic models, however when interactions are taken into account new timescales enter the problem and one has to wait for the population scattering mechanisms

to die out. An example of this is shown in Fig. 6.7.

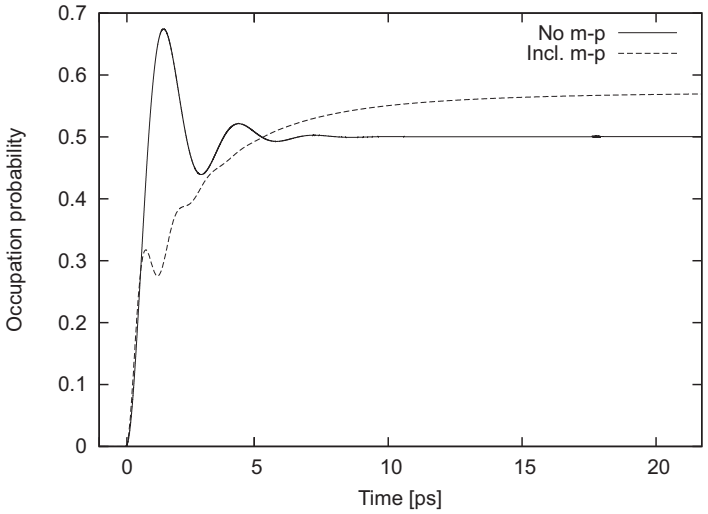

***Figure 6.7**: Temporal evolution of the electronic ground state in the atomic and interacting model under action of a c-w pump of intensity* 1 MW/cm^2. *The fields are tuned to resonance of the bare transition (atomic model) and the zero density exciton transition (interacting model), respectively.*

In the case of the carrier exciting schemes, because of the in-plane polarized coupling beam, the WL is being optically pumped. Since the WL band edge is quite far detuned (338 meV) from the driving field, this happens by only by a small amount. However, owing to scattering and the continuous nature of the WL over the course of time, a non negligible amount of carriers will accumulate in the WL. But since this buildup is slow on the timescales we are considering (pico seconds), we can safely assume the carrier density to be constant during the action of the probe so that we are dealing with a system in quasi-equilibrium. In the Hartree-Fock treatment we disregard screening effects. Following [82] screening effects come into play at WL carrier densities around 10^{12} cm^{-1}. Even for the largest coupling powers, we only reach values around 10^{11} cm^{-1} and the Hartree-Fock approximation is still valid. However, as we are employing the (fixed) relaxation time approximation, we cannot account for additional contributions to dephasing and carrier scattering rates due to the Coulomb interaction of the excited carriers.

6.3.1 Scheme comparison

The optical response for the three different schemes using a coupling field with an intensity of 26 MW/cm^2 is shown in Fig. 6.8 illustrating both the interacting and the non-interacting cases. An immediate difference between the atomic and many-body approach is the change in probe field energy towards negative detuning. This is due to the excitonic shift of the various probe transitions. An apparent feature of the Ladder scheme (Fig. 6.8a) is that the peaks of the imag-

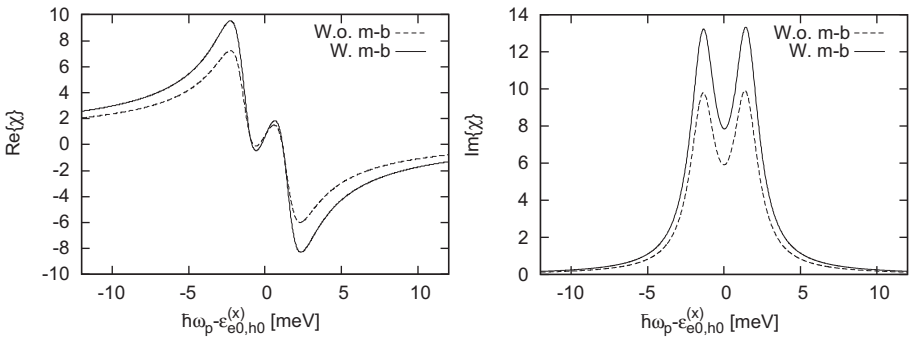

(a) Ladder scheme.

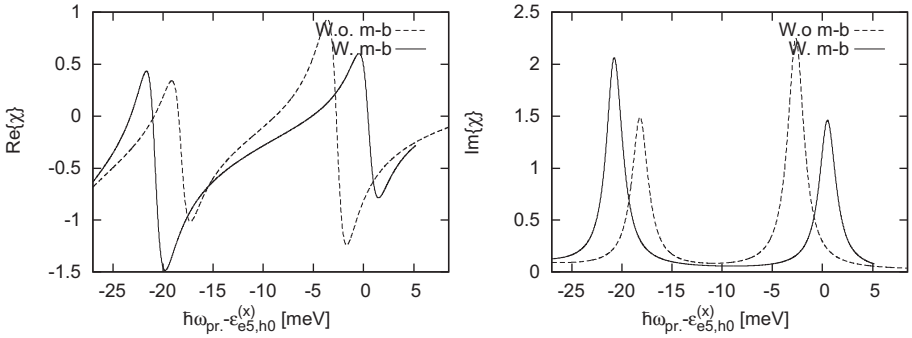

(b) V scheme.

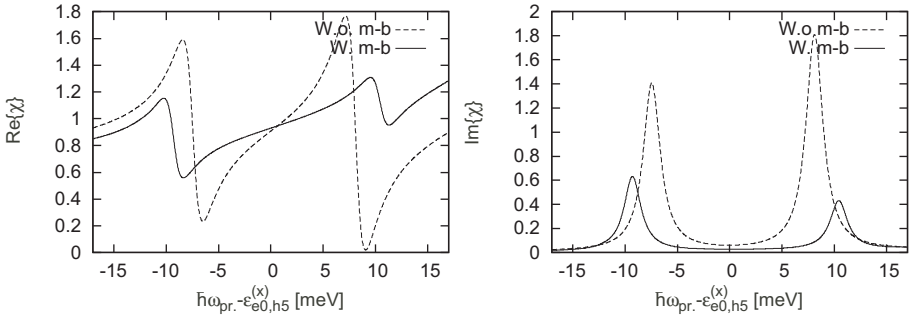

(c) Λ scheme.

Figure 6.8*: Ladder, V and Λ schemes using a coupling field intensity of* $26\ \mathrm{MW/cm^2}$*: Complex susceptibility vs. probe energy. The dashed line corresponds to the atomic model, i.e., without many-body interactions, while the solid line is evaluated with many-body interactions. The energy is measured relative to the zero density excitonic resonances* $\epsilon^{(x)}_{e0,h0}$*,* $\epsilon^{(x)}_{e5,h0}$ *and* $\epsilon^{(x)}_{e0,h5}$*, respectively. To facilitate a comparison between the two cases, the noninteracting spectra have been shifted accordingly. From [96].*

inary part of the susceptibility are highest for the many-body model. While the distance between the peaks remains the same one can readily see that a larger area is covered by the many-body spectrum. This is evidence that oscillator strength has been shifted into the $|e0\rangle - |h0\rangle$ transition, in other words it has been Coulomb enhanced. Considering the real part of the susceptibility, the enhancement of the probe transition results in more pronounced features, notably a larger slope at zero detuning. Both curves are generally shifted upwards from the zero point; this behavior is due to transitions in the vicinity of the probe which are contributing to the background index of the area in question.

The optical responses for V and Λ schemes are shown in Fig. 6.8b and Fig. 6.8c, respectively. For the interacting case the coupling field has been tuned to the zero density exciton resonance of the coupling transition. The asymmetry in the peak heights of the imaginary part of the susceptibility has different origin for the interacting and noninteracting cases. The skewness in the atomic model is due to the fact that we are not dealing with a closed three level system. The control field pumping the $|e0\rangle - |h0\rangle$ is also connecting the dipole allowed $|e5\rangle - |h5\rangle$ transition, however severely negatively detuned. Effectively we are dealing with two EIT schemes, the original V (Λ) and a detuned Λ (V) scheme. In general a negatively detuned Λ or V EIT scheme has a prominent shift in peak height towards positive detunings (resembling an optical Stark shift). What is seen in the two figures is an admixture of the symmetric peaks owing to the resonant V (Λ) scheme and a Stark shifted transition. Further evidence of this effect has been obtained by altogether disallowing the "conflicting" transition in which case one recovers the symmetric result. In the models including interactions the same asymmetry should be expected, but it is countered by a negative shift in resonance energy induced by the Coulomb interaction with the excited carriers. This means that the coupling is detuned positively with respect to the resonance, and hence the asymmetry tends towards negative probe energy. The probe transitions in these cases are not enhanced rather they are suppressed by the inclusion of many-body effects; this can be seen by the fact that the features are generally smaller in magnitude than in the atomic model and is also evident from the equilibrium absorption spectrum (Fig. 6.3). The splitting of the peaks is larger though, showing that the effective Rabi frequency is higher, owing to the Coulomb enhancement of the $|e0\rangle - |h0\rangle$ coupling transition.

Slowdown factor

As a basis for comparing the slow light capabilities of the different schemes we examine the slowdown factor S calculated at the frequency of the probe transition, i.e. the absorption minimum. To make a just comparison, we detune the coupling field used in the many-body V and Λ models from the zero density exciton resonance, so that the peaks of $\mathrm{Im}[\chi(\omega)]$ become symmetric signifying that the coupling field is on resonance at the time the system is probed. However, the amount of detuning for this to be realized depends on the intensity of the coupling field. Changing the intensity in turn changes the amount of carriers

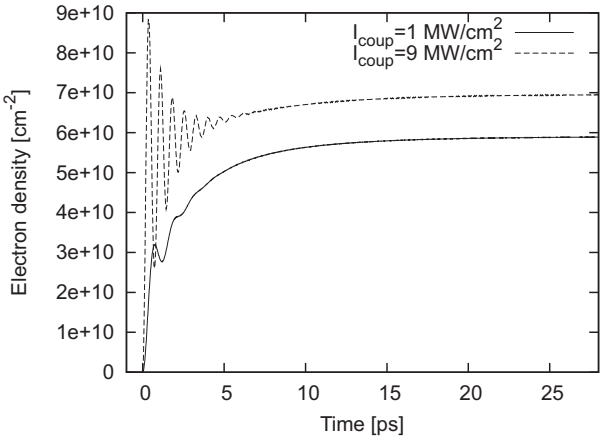

***Figure 6.9**: Temporal development of the total electron density for a coupling intensity of* 1 MW/cm^2 *(solid line) and* 9 MW/cm^2 *(dotted line).*

being excited and thus the excitonic shift, which results in different detuning for different intensities. To illustrate this, we show in Fig. 6.9 the temporal development of the total electron density for two different coupling intensities both tuned to the resonance frequency of the zero density exciton transition.

In Fig. 6.10 we show the temporal development of the electron ground state and first excited state during the action of a coupling beam resonant with the zero density exciton energy and one detuned by 3.85 meV. Both beams have an intensity of 9 MW/cm^2. In the case where the coupling field is tuned to the zero density exciton resonance at the beginning of the excitation, the coupling beam is on resonance and carriers are excited very effectively, which is evidenced by the almost complete Rabi half-cycle. As the states are being populated the field becomes detuned resulting in faster Rabi oscillations. In the case where the coupling field starts out being detuned the carrier excitation is inefficient at first, but then as carriers are excited the field tunes into resonance. Each situation gives rise to a different temporal development of the carrier distribution, however it is seen that the action of the two fields ultimately leads to nearly the same quasi-equilibrium carrier distribution.

Fig. 6.11 depicts the maximum achievable slowdown factor and the corresponding absorption coefficient $\alpha(\omega)$ as a function of coupling power for all three schemes. A striking feature of Fig. 6.11 is that the inclusion of many-body effects leads to different results depending on the choice of EIT scheme. The results of the carrier-exciting V and Λ setups are seen to differ fundamentally from the Ladder scheme. Inspecting the absorption coefficient plot we see two plateaus, corresponding to the maximum (minimum) absorption in the absence (presence) of EIT. The transition from the upper to the lower plateau happens across fewer orders of magnitude in the coupling power for the Ladder scheme than the other two schemes. Here the absorption coefficient drop is solely due to the quantum coherence effect setting in, whereas the transition for Λ and V happens across a significantly larger relative range. At low coupling power

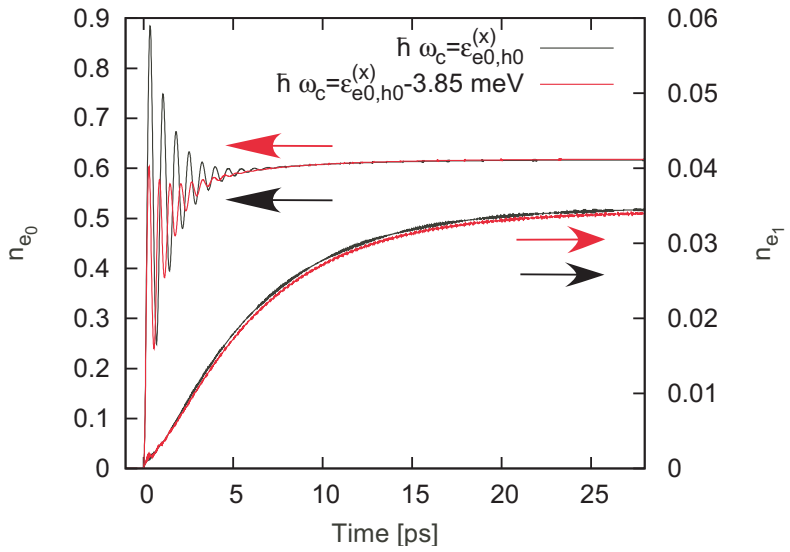

***Figure 6.10**: Temporal development of the population of the electron ground state n_{e_0} and first excited stated n_{e_1} for two different coupling beams. The black curve is for a* $9\ \mathrm{MW/cm^2}$ *beam tuned to the zero density exciton energy of the s-s transition, the red curve is for a coupling beam of similar amplitude detuned by* 3.85 meV*. The additional oscillating structure mainly visible in plots for n_{e_1} is a consequence of not performing the rotating wave approximation.*

the absorption drop is driven by the excitation of carriers occupying the probe transition. As evidenced by the slowdown plot, the EIT effect sets in at larger coupling powers, only when we are near the lower plateau. The largest slowdown values are achieved using the Ladder scheme, for which the slowdown factor is increased significantly when interactions are included. This is due to Coulomb enhancement of the $|e0\rangle - |h0\rangle$ resonance probed in this scheme. The slowdown effect is seen to disappear at the same value of coupling power for both cases, which indicates that the coupling transition ($|e0\rangle - |e5\rangle$) utilized in the Ladder configuration is unchanged by the inclusion of many-body effects. On contrary, for the carrier-exciting schemes V and Λ, many-body effects have a significant impact on the coupling threshold.

Both V and Λ schemes show largest slowdown values for the non-interacting model. On the other hand, the noninteracting model overestimates the minimum required coupling power for observing slow light by roughly a factor of two compared to the more realistic case of interacting particles. As both schemes utilize the same coupling transition they experience the same coupling power threshold, in both the interacting as well as the non-interacting case. The shift in required coupling power can be attributed solely to the Rabi energy enhancement of the coupling transition. This conclusion is reached by inspecting the absorption spectrum in absence of a coupling field. By comparing the height of the $|e0\rangle - |h0\rangle$ resonance (coupling transition used in both schemes) with and without interactions we find that the dipole moment of the transition is enlarged by roughly a factor of 1.2. If we, in the atomic model, enlarge the

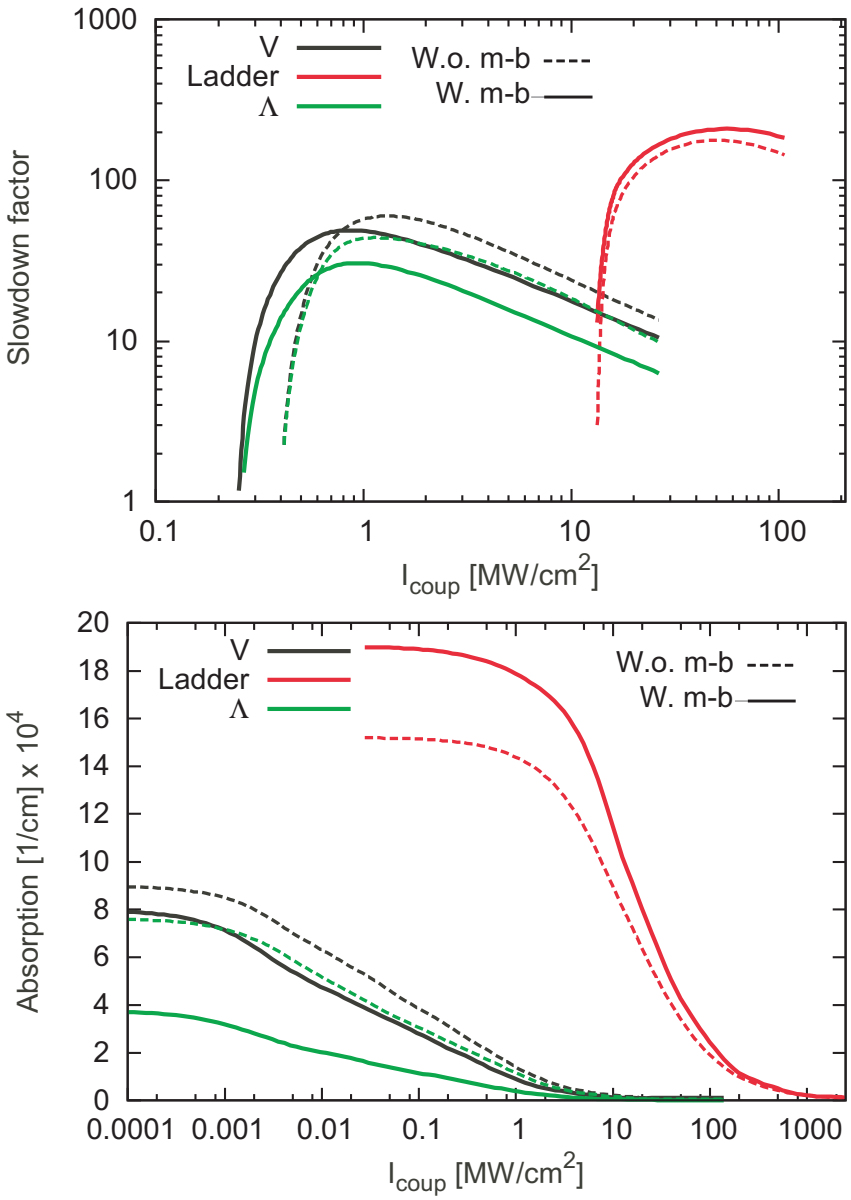

***Figure 6.11**: Maximum slowdown factor and corresponding absorption coefficient vs. coupling intensity for various EIT-schemes. The dashed curves are for the independent particle (atomic) model, while the solid curves include many-body interactions. From [96].*

coupling dipole moment by the same amount, we end up with a result having the same minimal requirement on coupling power as the interacting case.

The V scheme is preferable to the Λ scheme, due to its higher slowdown values. The reason is twofold. Firstly, based on observations from the absorption spectrum without coupling, we find that the two probe transitions are both Coulomb suppressed, however the Λ scheme to a higher degree than V. Secondly the fact that the V probe connects a hole ground state to an electron excited state results

in a larger Pauli blocking factor (the third term in Eq. (2.3.37)) as compared to the Λ scheme. Fig. 6.12 demonstrates this for the interacting case utilizing a coupling intensity of 2.5 MW/cm^2. For the interacting model the redistribu-

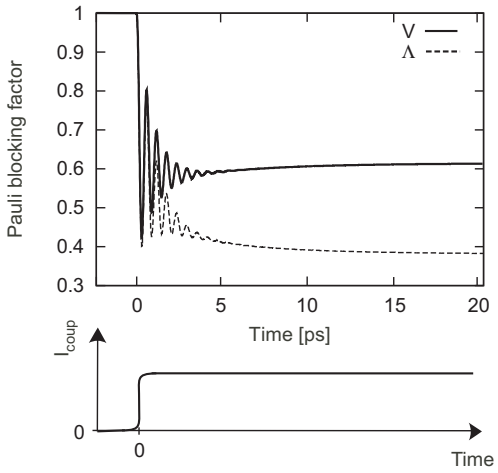

***Figure 6.12**: Temporal development of the Pauli probe blocking factors for Λ and V schemes at coupling intensity 2.5 MW/cm^2. Shown in the figure are the Rabi oscillations of the populations at the onset of the coupling field and the relaxation towards their stationary value. Also shown is an illustration of the "turn on" of the coupling laser. From [96].*

tion of carriers plays a crucial role; the smaller effective electron mass leads to a larger energy spacing of the electronic levels, which means that the electron excited states become less populated than their hole counterparts. In the case presented here the hole ground state is seen to be depleted and carriers are redistributed into the higher lying energy states. For electrons the redistribution is less prominent, and as the coupling field excites more and more carriers, electrons accumulate in the ground state. Thus the Pauli blocking factor seen by the probe in the V configuration is always the larger, which ultimately translates into an increased slowdown factor. This result is quite general and could act as a pointer for experimental realization of EIT mediated slow light.

6.4 Transient EIT

We investigate the transient behavior by using a coupling pulse with a temporal width comparable to the dephasing time of the system. To obtain a temporally well resolved system response, we apply a short probe pulse of temporal length less than the inverse of the dephasing rate.

6.4.1 Transient response

The frequency and time dependent linear response function $\chi(\omega;\tau)$ is measured relative to the peak of the coupling pulse ($\tau > 0$ indicates that the probe

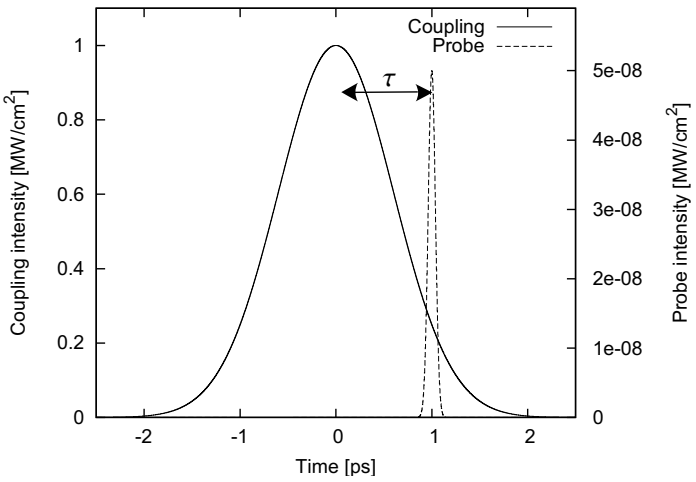

***Figure 6.13**: Example of coupling and probe field setup used for simulations in a transient regime.*

pulse arrives after the peak of the coupling pulse). Unless otherwise stated all results presented use a gaussian shaped coupling and probe beam with duration (FWHM) of $\Delta t_c = 2.0$ ps and $\Delta t_p = 0.1$ ps, respectively. The setup is illustrated in Fig. 6.13.

Fig. 6.14 shows a few "snapshots" of transient spectra calculated for the Λ scheme using a coupling power of 9MW/cm^2. The full sequence is found in Fig. 6.26 at the end of this chapter.

An obvious feature present in both the independent and interacting models is the oscillations seen in the imaginary part of the susceptibility, resulting in the existence of gain at multiple frequencies at certain times. One could be lead to think that the oscillations are due to Rabi flopping induced by the coupling laser leading to population inversion in the probe transition, however as seen in Fig. 6.21 there is no such inversion taking place. Also, this argument would only explain gain at the resonance frequency, and does not account for the existence of more than one gain peak hinting to that fact that we are dealing with a coherent phenomenon.

6.4.2 Explaining transient "wiggles"

Transient gain at the center frequency has been reported theoretically in atomic systems using a c-w probe [97] , also there has been experimental reports on transient gain and three peak structure in Rb vapor [98,99] also using c-w probe fields.

In the following we shall rely on an atomic model, using a simple 3 level system, to explain the transient behavior. Consider the non-carrier exciting Ladder scheme depicted in Fig. 1.2a subjected to electrical fields similar in shape and

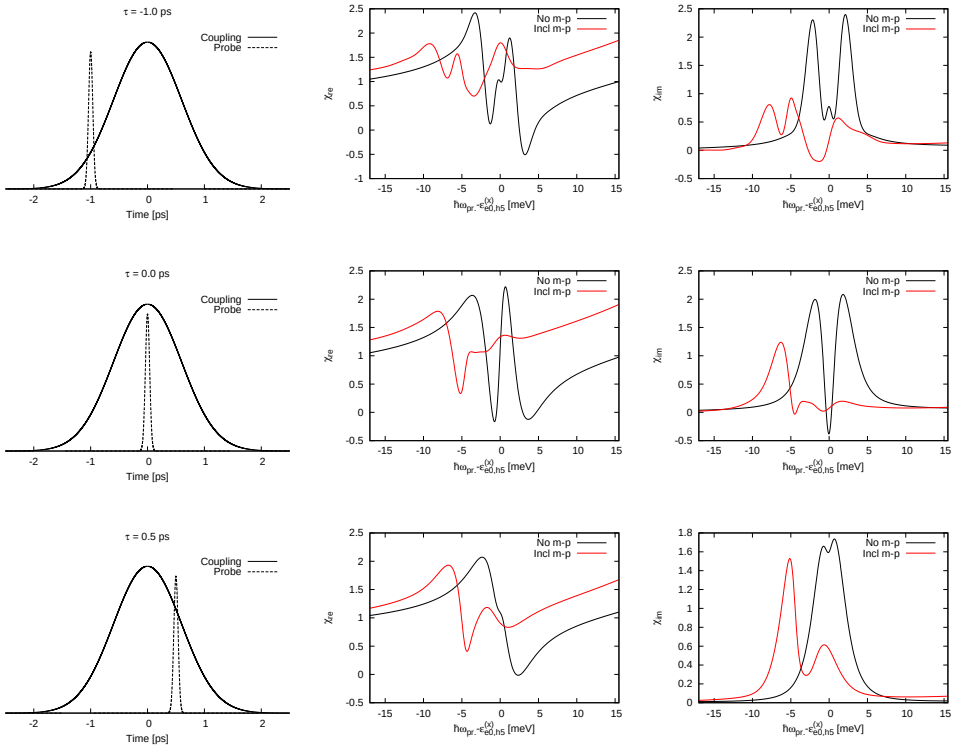

***Figure 6.14**: Three snapshots of the time dependent susceptibility for Λ scheme at coupling intensity 9 MW/cm^2. Left panel shows an illustration of the envelopes of the probe and coupling field intensities. Middle panel shows the real part, rightmost the imaginary. The black curves are for the independent particles, while the red curves are including many-body interactions. In the interacting cases the coupling beam has been tuned to the zero density exciton resonance. The non-interacting results has been shifted in order to better enable a comparison of the spectral features.*

magnitude to the ones used in the above simulations (Fig. 6.26) for the Λ-scheme. The model parameters are listed in Table 6.1. This approach assumes a non-carrier exciting scheme, however we see that the qualitative insight obtained using the simple non-carrier exciting model carries over to the more complicated cases where carriers are excited. It is important to note that, that the following model employs the rotating wave approximation, where sideband generation is disregarded. Since we can qualitatively understand the transient spectra using this rudimentary model, it is clear that the wiggly spectrum present in the full models in which the sidebands are accounted for, is not attributed to the presence of the sidebands. The equations of motion in the rotating wave approximation to first order in the probe field, setting $\rho_{11}^{(0)} = 1$ and all other populations to zero, has the following appearance in the rotating frame (see e.g.

***Table 6.1**: Parameter values and conversion*

SBE parameter	SI units	units of γ
γ	1.5 ps^{-1}	1 γ
γ_{13}	1.5 ps^{-1}	1 γ
Δt_c	2.0 ps	3 γ^{-1}
Δt_p	0.1 ps	0.15 γ^{-1}
Ω_c	8.5 ps^{-1}	5.66 γ

Eq. (4.1.34 - 4.1.35):

$$\frac{\partial}{\partial t}\tilde{\rho}_{21}^{(1)}(t) = (i\delta_p - \gamma)\tilde{\rho}_{21}^{(1)}(t) + i\Omega_p(t)/2 + i\Omega_c(t)\tilde{\rho}_{31}^{(1)}(t)/2 \tag{6.4.1}$$

$$\frac{\partial}{\partial t}\tilde{\rho}_{31}^{(1)}(t) = [i(\delta_p - \delta_c) - \gamma_{31}]\tilde{\rho}_{31}^{(1)}(t) + i\Omega_c(t)^*\tilde{\rho}_{21}^{(1)}(t)/2\ . \tag{6.4.2}$$

$\Omega_p(t)$ and $\Omega_c(t)$ are the real Rabi frequencies of the slowly varying envelopes of the signal and coupling fields, defined as $\Omega_p(t) = \mu_{12}\tilde{\mathcal{E}}_p(t)/\hbar$ and $\Omega_c(t) = \mu_{23}\tilde{\mathcal{E}}_c(t)/\hbar$, with central frequencies ω_p and ω_c, respectively. The detunings are defined as: $\delta_s = \omega_s - \omega_{12}$ and $\delta_c = \omega_c - \omega_{32}$. $\gamma \equiv \gamma_{21}$ and γ_{31} is the decoherence of the $|1\rangle - |2\rangle$ and $|1\rangle - |3\rangle$ transition, respectively. The matrix element $\tilde{\rho}_{21}^{(1)}(t)$ describes the (slowly varying) time development of the dipole coherence between states $|1\rangle$ and $|2\rangle$ and is proportional to the polarization induced by the signal beam. Whereas $\tilde{\rho}_{31}^{(1)}(t)$ describes the non-radiative coherence between states $|1\rangle$ and $|3\rangle$. We can find the probe absorption for a probe applied at time τ according to (3.4.46)

$$\alpha(\delta_s;\tau) \propto \mathrm{Im}\left[\frac{\tilde{\rho}_{21}^{(1)}(\delta_p)}{\Omega_p(\delta_p)}\right]\ . \tag{6.4.3}$$

Here $\tilde{\rho}_{21}^{(1)}(\delta_p)$ and $\Omega_p(\delta_p)$ are the Fourier transforms of $\tilde{\rho}_{21}^{(1)}(t)$ and $\Omega_p(t)$. For the sake of comparison all variables are taken relative to the decoherence rate of the probe transition γ. As can be seen from the above equations the probe absorption is interconnected with the real part of the non-radiative coherence via the coupling field $\Omega_c(t)$. In the absence of a coupling field, equation (6.4.1) reduces to free decay of the dipole coherence. The non-radiative coherence enters as a driving term in the equation for the probe coherence by virtue of the coupling pulse $\Omega_c(t)$. In order to observe EIT one must have a non-vanishing $\tilde{\rho}_{31}^{(1)}(t)$, which evidently means that $\Omega_c > \gamma_{31}$. Furthermore, the interaction time, given by the duration of the coupling field, must be sufficiently long for the two coherences to affect each other. The non-radiative coherence may be present however the total nonlinear driving term drop out when $\Omega_c(t)$ is zero. In other words a short coupling pulse effectively reduces the coherent interaction time.

If the coupling beam duration is sufficiently long, the temporal development of the coherences will be dominated by the decay imposed by the dephasing rates of the system as shown in Fig. 6.17 resulting in the regular steady state EIT

absorption spectrum.

The transient situation occurs when the ratio $\frac{\partial \Omega_c(t)}{\partial t}/\gamma_{31}$ is large, or in other words, when the coupling spectral bandwidth is larger than the decoherence rate of the non-radiative coherence. In this case the absorption is then not only determined by the state of the system at the time of the probe pulse, but also by the temporal evolution of coupling beam after the application of the probe pulse.

The aim is here not a complete parametric examination of the influence of coupling beam shape on the transient EIT behavior. We retain the discussion to gaussian shaped pulses. In Fig. 6.15 we show an example of absorption spectra calculated at various times using the parameters listed in Table 6.1.

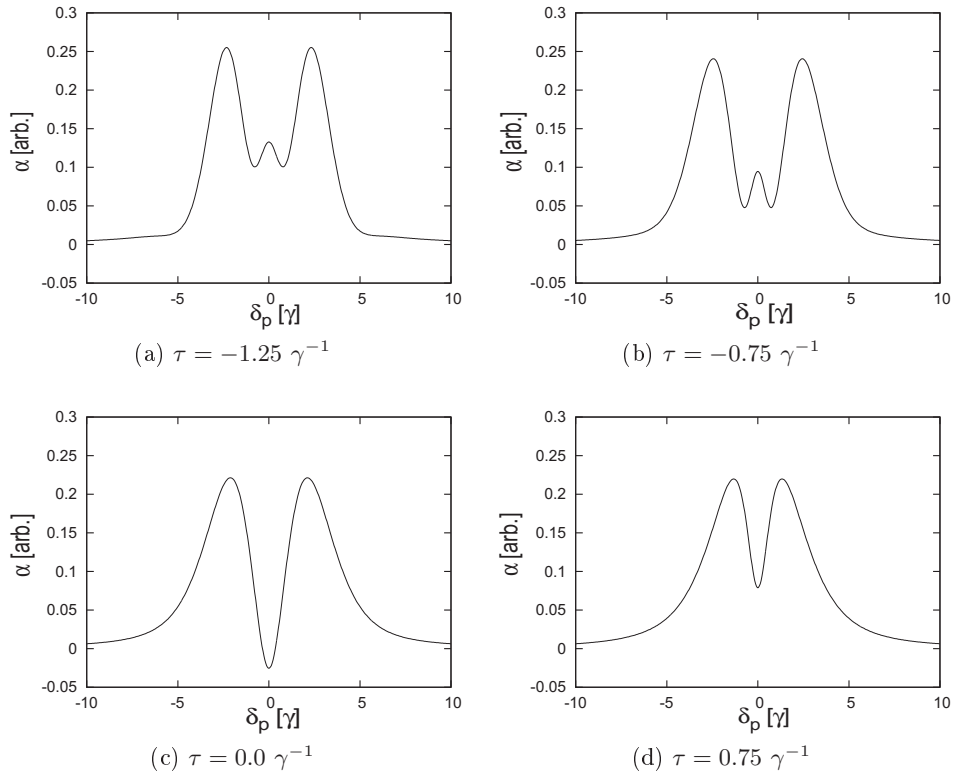

(a) $\tau = -1.25\ \gamma^{-1}$ (b) $\tau = -0.75\ \gamma^{-1}$

(c) $\tau = 0.0\ \gamma^{-1}$ (d) $\tau = 0.75\ \gamma^{-1}$

***Figure 6.15**: Absorption spectrum at various times τ relative to the peak of the coupling pulse. Simulation parameters are listed in Table 6.1.*

If we apply the probe early we see oscillations in the spectrum. Fig. 6.16 shows that if the induced dipole and the non-radiative coherence have a long interaction time (which is the case for a probe applied before the peak of the coupling pulse), they have time to act back on each other, resulting in oscillations in the time domain. If we probe at later times the interaction is damped by the coupling field envelope giving only one spectral dip, but with gain. At the latest of times we recapture the standard EIT behavior displaying a single absorption dip resembling the spectrum of the steady state calculation. Note the difference

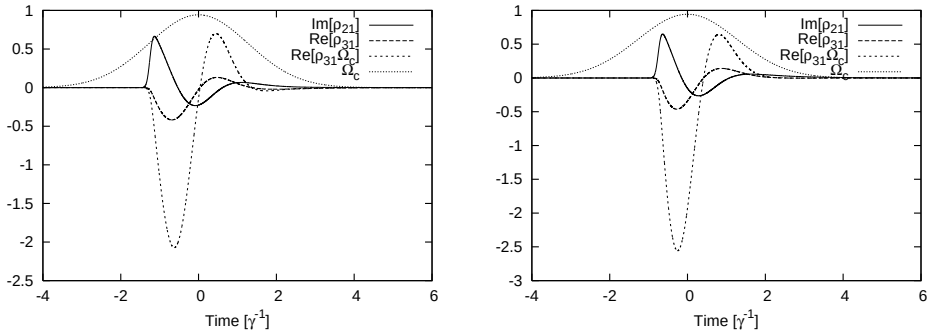

(a) $\tau = -1.25\ \gamma^{-1}$ (b) $\tau = -0.75\ \gamma^{-1}$

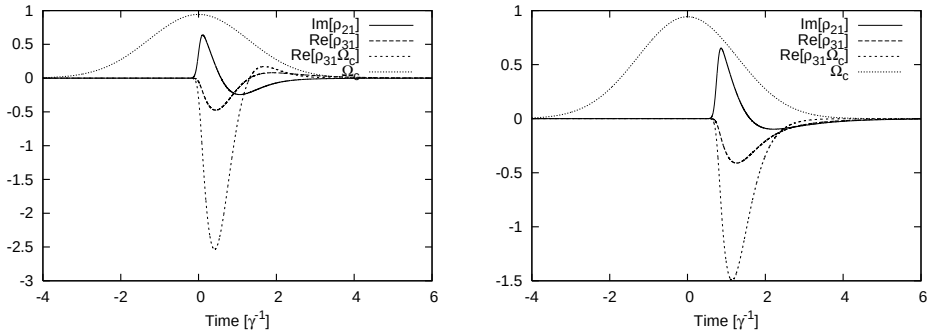

(c) $\tau = 0.0\ \gamma^{-1}$ (d) $\tau = 0.75\ \gamma^{-1}$

***Figure 6.16**: Temporal development of coherences at various probe delays. The coupling field envelope is shown as the dotted curve.*

in the time domain between the $\tau = 0.75\ \gamma^{-1}$ result and the steady state result (Fig. 6.17). In steady state the driving term is maximized and constant resulting in damped oscillations of a single frequency of the dipole coherence, however in the transient case the coupling field affects the driving term by applying a time dependent damping/amplification, in other words it adds interference.

It is seen in Fig. 6.15 how the spectra do not display the same behavior when probing symmetrically ($\tau = \pm 0.75\ \gamma^{-1}$) around the peak of the coupling beam. More oscillations are seen when probing prior to the coupling maximum as opposed to probing after the coupling maximum, showing the difference between a positive and negative slope of Ω_c, corresponding to an amplification or damping of the interaction.

For larger Rabi frequencies the slope of Ω_c is increased allowing the coupling beam to affect the interference pattern even more. The effect of more oscillations for larger coupling power can be understood through this vein. The larger a pump area the probe can interact with, the larger a coherence is built up i.e. more temporal oscillations can be performed. This means that schemes that experience Rabi enhancement (Λ and V) will have more oscillations in their spectra when including interactions, which is evidenced in Figs. 6.26 and 6.27.

With all this in mind we can now discuss the results from all schemes interacting

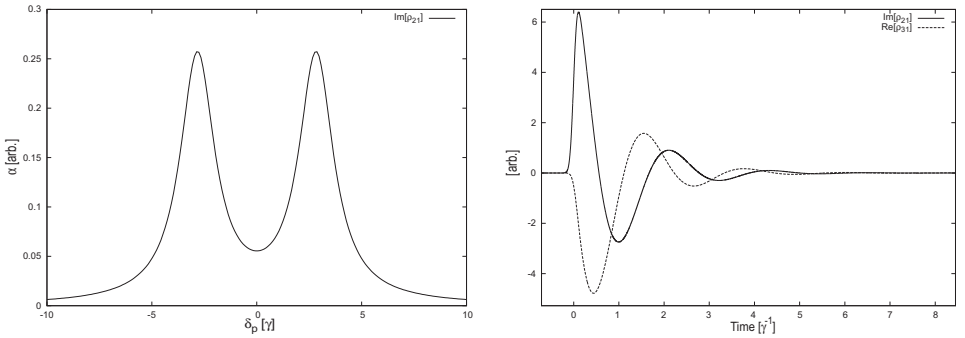

***Figure 6.17**: Time development of coherences (right) and resulting absorption spectrum (left) for the parameter choice displayed in Table 6.1 using a c-w coupling beam.*

as well as noninteracting. Fig. 6.18 shows a few "snapshots" for the Ladder and V scheme using a coupling intensity of 90MW/cm^2. As for the Λ case the full set of spectra (Fig. 6.27) is found at the end of this chapter.

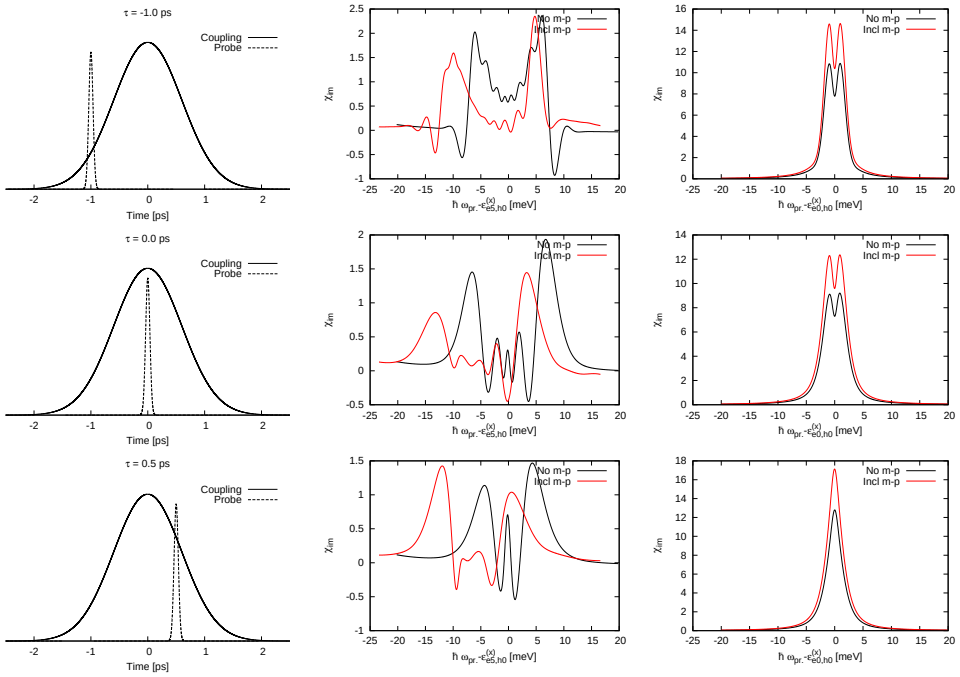

***Figure 6.18**: Three snapshots of the time evolution of the imaginary part of the susceptibility at coupling intensity 90 MW/cm^2. Left panel shows an illustration of the envelopes of the probe and coupling field intensities. Middle panel refers to V configuration, rightmost is Ladder. The black curves are for the independent particles, while the red curves are including many-body interactions. In the interacting cases the pump beam has been tuned to the zero density exciton resonance of the given transition. The non-interacting results has been shifted in order to better enable a comparison of the spectral features.*

An apparent feature of the Ladder scheme is that the overall spectral features

remain EIT-like at all times, reflecting the fact that the Rabi frequency of the coupling beam is just about powerful enough for quantum coherence effects to set in. As also observed in the steady state calculations the absorption peaks have the same separation, showing that the coupling transition remains unchanged by the inclusion of many-particle interactions. The explanation is the same as in steady state; the Ladder scheme is using an empty intra-band transition as pump, and one cannot expect Coulomb enhancement, simply because no carriers are involved. The spectral features of the Λ and V scheme are quite different, not only when comparing models with and without interactions, they also differ a lot from steady state EIT spectra through their oscillatory appearance. The transient oscillations that appear in the spectra we can understand from the treatment above. In the non-interacting case the outer peaks are generally symmetric (of the same height), At certain times in the interacting case, they appear skewed. This is particularly pronounced at times where the spectrum approaches EIT-like features. The reason for this asymmetry is that the coupling is detuned from the zero density excitonic resonance. During the action of the coupling field, carriers are excited and (if the the coupling field is powerful enough) perform Rabi oscillations, this introduces a time dependent detuning of the coupling frequency. This problem does not occur in the Ladder scheme where, due to the lack of carriers, the shift in the coupling transition frequency remains constant. An important point to notice is that the distance between the outer peaks is larger for the interacting model. Evidence that the pump transition has been enhanced, since in regular steady state EIT the distance between the peaks is related to the Rabi frequency Ω_c so larger distance suggests a higher effective Ω_c.

For the interacting cases the slopes of the peaks appear "softer" on side, than on the other, this feature is particularly prominent at times where the spectrum is most EIT-like also the spectra are not symmetric around the central excitonic resonance, they have a tendency to be smeared out towards the positive detuning side. The simple model can help explaining these observations, which are two sides of the same story. If we detune the coupling beam in the simple model, the spectral peak heights become asymmetric around the central resonance, in the same manner as in steady state EIT. The outer peaks remain separated by the same amount, but with the shifts in peak height comes a change in the distance between the inner peaks. This change tends to compress the distance between peaks that are being enlarged, and expand the distance between peaks that are being shrunk. This is illustrated in Fig. 6.19.

6.4.3 Physical understanding/use of transient spectra

In relation to EIT what use can we make of the transient spectra and refractive indexes? As discussed in Chapter 3 transient spectra reflects the actual absorption in a thin slab experiment. However, using the transient refractive index e.g. for calculating a group velocity is ill defined, since the concept of group velocity only makes sense for a pulse for which the refractive index varies monotonously,

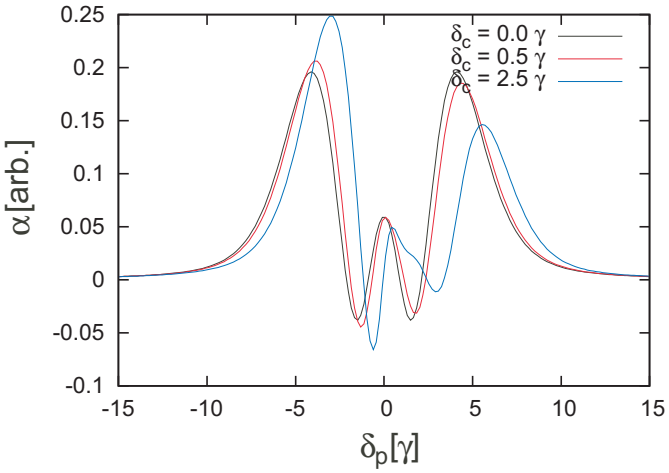

***Figure 6.19**: Absorption spectrum calculated for different detunings of the coupling beam for the simple three level model.*

which is clearly not the case we present here. In fact we only see the EIT effect in the cases where the probe is significantly shorter than the pump, which means that the probe spectrum is far from lying inside the EIT transparency window and thus it would be wrong to speak of a group velocity. If we increase the temporal width of the pulse, but maintain a short coupling pulse (so that the system remains transient) we will not get an EIT like spectrum out. Simply because the probe most of the time is addressing the unperturbed medium, i.e. seing a regular absorption peak. The only case we can make the probe pulse duration sufficiently long to fit spectrally within the transparency window is when the pump pulse is even longer, in which case we will be approaching the steady state situation.

Slowdown

Knowing that the transient susceptibility cannot be used for extracting propagation characteristics such as the group velocity, we nonetheless present plots of a slowdown factor. One can think of it as an effective slowdown factor, constructed formally the same way as in steady state. We can use it as an indicator of the quality of quantum coherence in the system, so that the slowdown as function of coupling power becomes a "phase diagram" indicating the size of- and whether or not quantum coherence effects are present. This should be understood in the sense that a positive slowdown factor corresponds to the existence of quantum coherence effects, whereas sub zero values tell us that quantum coherence effects have died out. For the purpose here, we define the maximum achievable slowdown factor S_{max}, calculated at times τ_{max} where the spectrum is most EIT-like, i.e. when the spectrum displays a double peaked structure along with zero absorption, for example around $\tau = -0.25$ ps in Fig. 6.26. A plot showing the maximum slowdown factor for the three different schemes is

presented in Fig. 6.20.

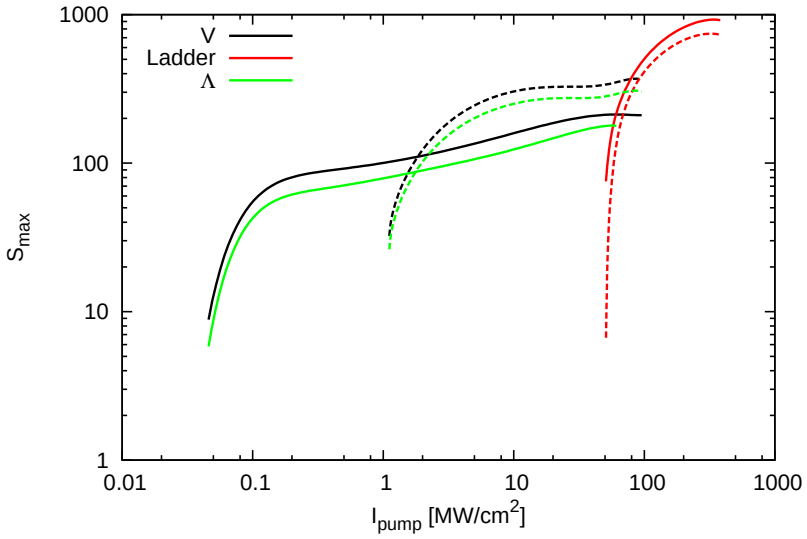

Figure 6.20: *Maximum effective slowdown factor vs. coupling pulse peak intensity for various EIT-schemes. The dashed curves are for the independent particles, while the solid curves include many-body interactions.*

The reason for the apparent absence of a slowdown maximum and oscillatory behavior of the Λ and V slowdown curves stems from the fact that these schemes involve excitation of carriers. During the action of the pump, the relevant electron and hole occupations undergo Rabi oscillations. As the probe connects to either of these states, the Pauli blocking factor relating to the probe transition also oscillates, its local minima (maxima) falling at the peak (valley) of the population oscillations (see e.g. Fig. 6.21). As τ_{max} changes with varying coupling power, so does the Pauli blocking factor, resulting in an oscillatory behavior of the slowdown curve. As in the steady state calculations the V-scheme is seen to produce the largest slowdown factors also in the transient situation this is due to a favorable carrier redistribution mechanism resulting in larger Pauli blocking factors for the V-scheme, which is evidenced in Fig. 6.21.

It is important to note that the inclusion of many-particle effects in a transient situation has profoundly different effect as compared to the steady state. In a transient regime the system seems more robust in the sense that coherence effects are retained longer in the system. The minimum coupling power required for observing EIT is seen to shift by roughly a factor of 10, when comparing the interacting and non-interacting models for the carrier exciting schemes. Showing that the non-interacting model clearly over estimates the coupling power requirement. In steady state this shift is only around a factor of 2.

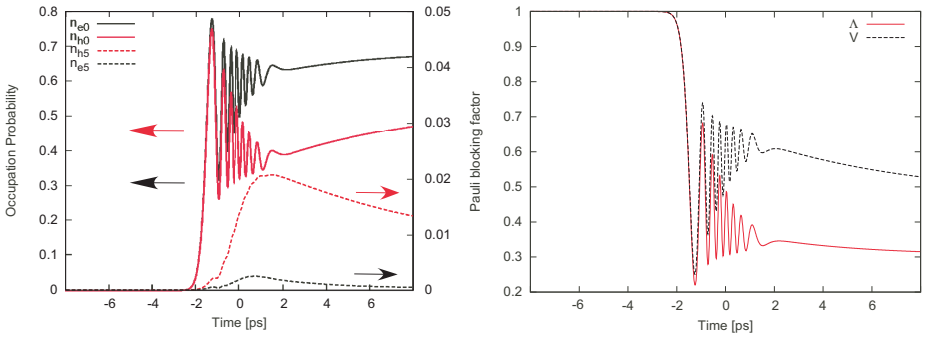

***Figure 6.21**: (Left) temporal development of occupation probabilities for coupling intensity* 60 MW/cm^2 *in the interacting case. (Right) the corresponding Pauli blocking factors for* Λ *and* V *schemes. Notice that the* V*-scheme has the larger blocking factor at all times. The Pauli blocking factors never become negative and thus there is no population inversion.*

6.4.4 Coupling duration variation

In order to make a connection between the transient and steady state regimes, we show here calculations for the V and Ladder scheme at three different probe times ($\tau = -0.5$ ps, $\tau = 0.0$ ps and $\tau = 0.5$ ps) using a constant coupling intensity of 90 MW/cm^2 while varying the duration of the coupling pulse (Δt_c). For each calculation the absorption (imaginary part of the transient susceptibility) and slowdown factor at the frequency of the probe transition is evaluated. The frequency of the probe and coupling transition are easily identified in the non-interacting cases and also for the Ladder scheme (as it remains constant). For the V scheme when including Coulomb interactions this is not as straightforward as both transition frequencies experience time dependent shifts and are thus unknown. To this end we tune the coupling field to the zero exciton resonance, whereas the probe transition frequency is taken to be the center point between the two outermost peaks/dips of the given absorption spectrum, e.g. around -6 meV in the spectrum for $\tau = 0.5$ ps in Fig. 6.27.

The results are presented in Figs. 6.22-6.25. As the coupling duration increases the results of the three different probe times approach each other. When they coincide we are approaching the steady state regime (given a probe applied around the peak time of the coupling field).

In the Ladder scheme we are only barely entering the EIT regime, which is why we see no oscillations in either absorption nor slowdown. This should be compared to the V case where many oscillations are seen in both curves reflecting the fact that the coupling beam is strong enough to enter the multi peaked EIT regime (see e.g. Fig. 6.27 for the $\Delta t_c = 2$ ps case). As the Ladder scheme does not involve excitation of carriers every change in absorption is due to coherence effects. For these two reasons it is easier to draw conclusions from the Ladder scheme plots. It can be seen that transient effects gives rise to lower absorption and larger slowdown values as compared to steady state (corresponding to large

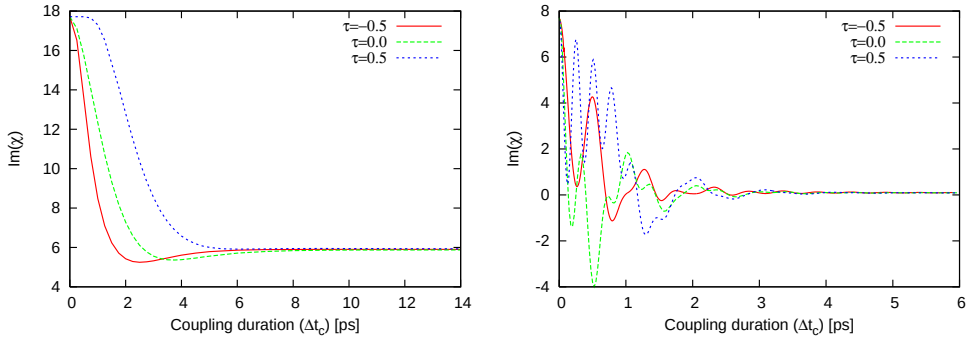

Figure 6.22: *Imaginary part of the susceptibility for the non-interacting Ladder (left)- and V scheme (right) for various coupling durations.*

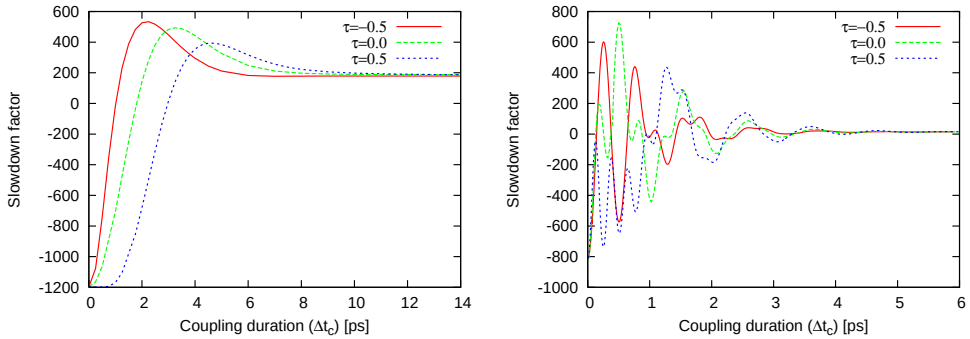

Figure 6.23: *Slowdown calculated for the non-interacting Ladder (left)- and V scheme (right) for various coupling durations.*

Δt_c) for certain coupling lengths and probe times, in particular early probe times. The question remains if this could be harnessed in an actual slow light propagation experiment. Both the non-interacting model (Fig. 6.22) and the interacting Fig. (6.24) suggests an early probe using a coupling duration around 2 ps, a few times longer than the dephasing time of the system. We see that if we choose a late probe ($\tau = 0.5$ ps) we can never obtain an enhancement of the EIT effect by entering the transient regime. This goes for both models.

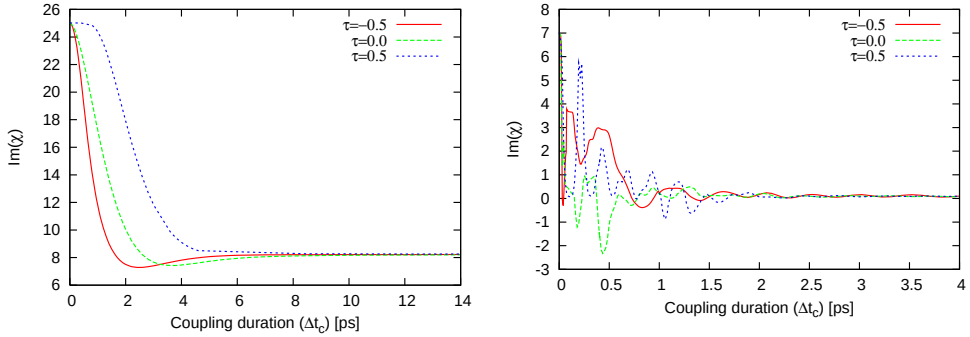

Figure 6.24: *Imaginary part of the susceptibility for the interacting Ladder (left)- and V scheme (right) for various coupling durations.*

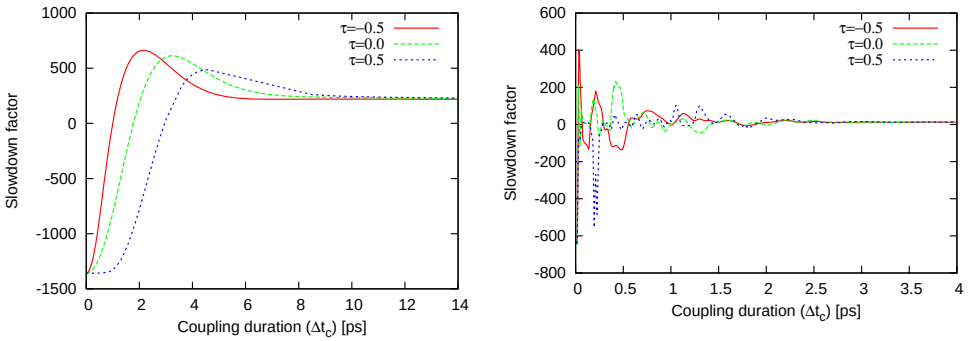

***Figure 6.25**: Slowdown calculated for the interacting Ladder (left)- and V scheme (right) for various coupling durations.*

When considering the absorption plots for the V-scheme, it is difficult to distinguish between coherence effects and simple bleaching. Particularly the late probe case ($\tau_p = 0.5$ ps), is dominated by bleaching effects for short coupling durations. The absorption dips can in fact be attributed to EIT for $\tau_p = (-0.5 \text{ ps}, 0.0 \text{ ps})$, however in the late probe case the oscillations in absorption is only the result of optical pumping. This can be seen by the fact that the slowdown factor remains negative, reflecting the fact that the absorption spectra in these cases show only the resonance peak, but of lower magnitude due to Pauli blocking. It is important to note that in the non-interacting model the most pronounced EIT effects are obtained at a coupling duration of $\Delta t_c \approx 0.55$ ps for a probe applied at the peak of the coupling pulse ($\tau = 0.0$ ps), which is in contrast to the findings for the Ladder scheme. A similar feature is also seen in the interacting case, but here it occurs around $\Delta t_c \approx 0.45$ ps due to the Coulomb increased Rabi frequency.

When comparing absorption and slowdown for the non-interacting and interacting models it seen that the inclusion of Coulomb effects results in even more oscillatory structure. This is attributed to the fact that the coupling Rabi frequency is Coulomb enhanced.

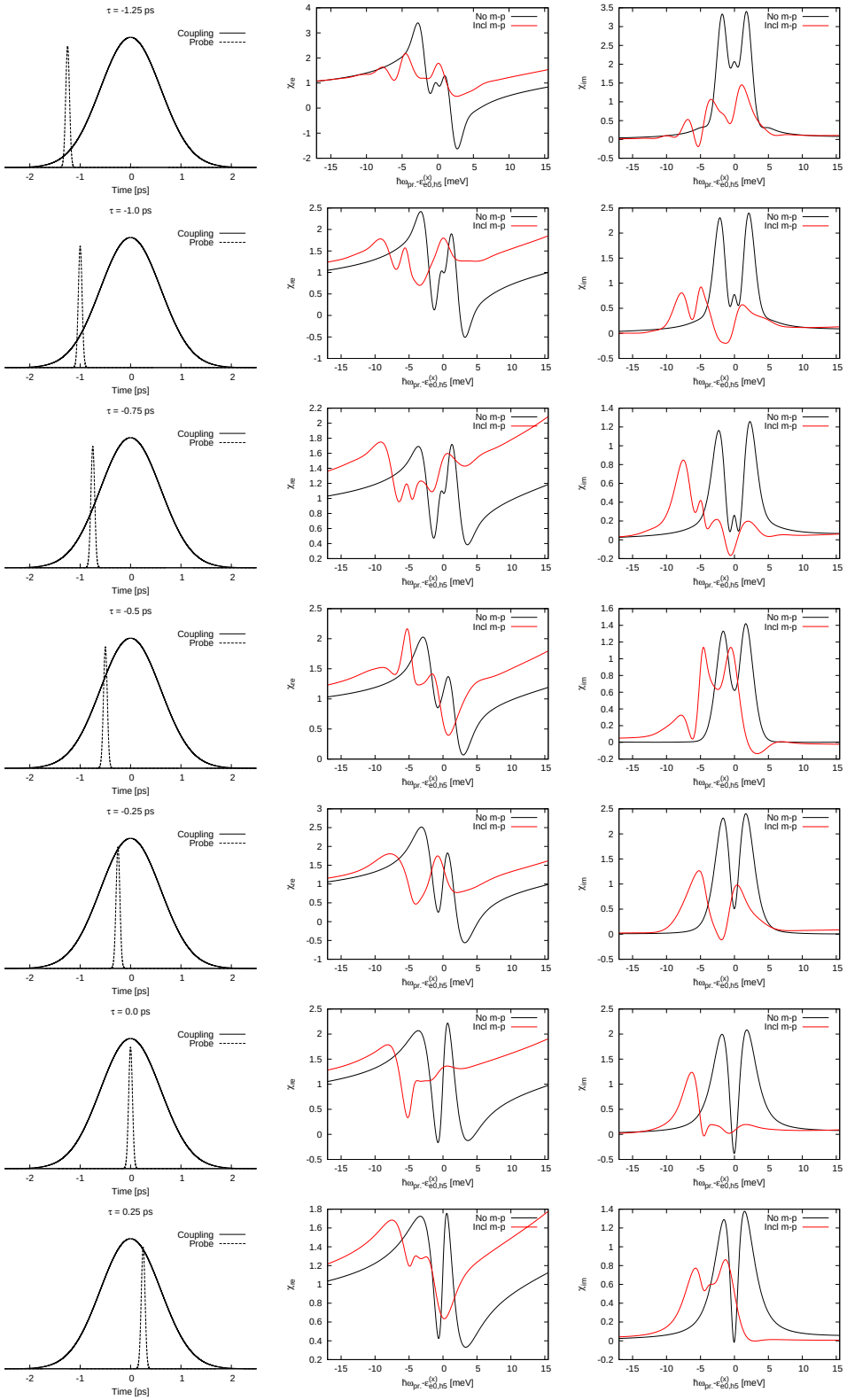

***Figure 6.26**: Time dependent susceptibility for Λ scheme at coupling intensity 9 MW/cm^2. Left panel shows an illustration of the envelopes of the probe and coupling field intensities. Middle panel shows the real part, rightmost the imaginary. The black curves are for the independent particles, while the red curves are including many-body interactions. In the interacting cases the coupling beam has been tuned to the zero density exciton resonance. The non-interacting results has been shifted in order to better enable a comparison of the spectral features.*

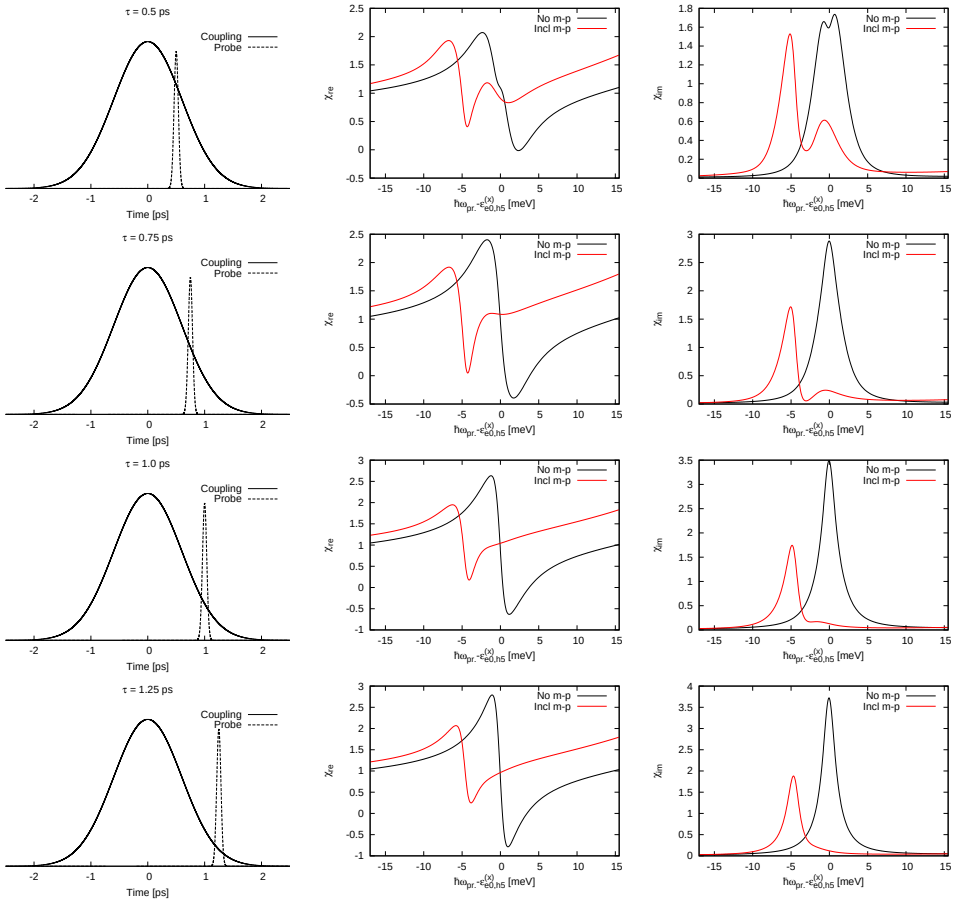

Figure 6.26: *Time dependent susceptibility for* Λ *scheme at coupling intensity* $9\ \mathrm{MW/cm^2}$. *Left panel shows an illustration of the envelopes of the probe and coupling field intensities. Middle panel shows the real part, rightmost the imaginary. The black curves are for the independent particles, while the red curves are including many-body interactions. In the interacting cases the coupling beam has been tuned to the zero density exciton resonance. The non-interacting results has been shifted in order to better enable a comparison of the spectral features.*

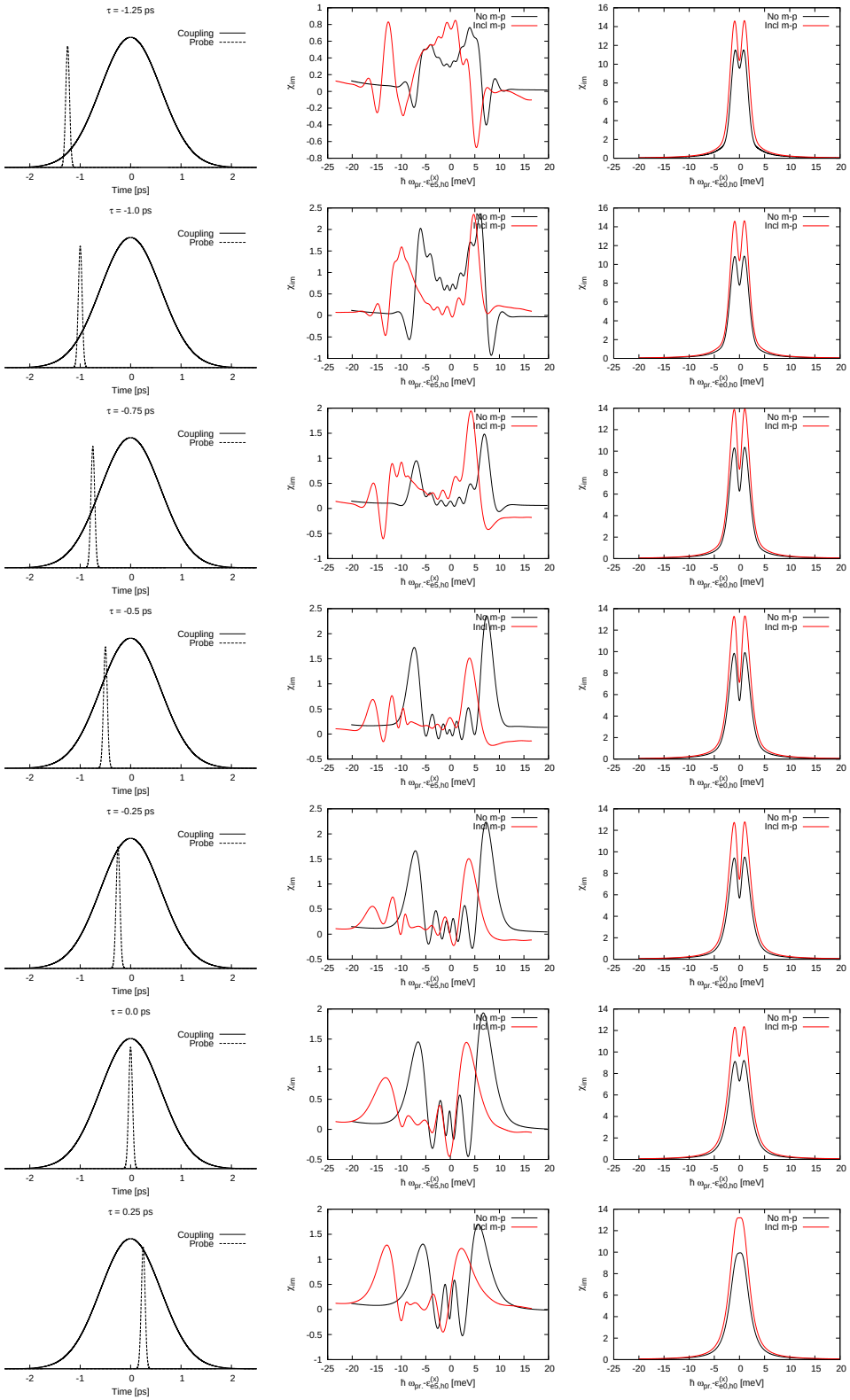

***Figure 6.27**: Time evolution of the imaginary part of the susceptibility at coupling intensity* 90 $\mathrm{MW/cm^2}$*. Left panel shows an illustration of the envelopes of the probe and coupling field intensities. Middle panel refers to V configuration, rightmost is Ladder. The black curves are for the independent particles, while the red curves are including many-body interactions. In the interacting cases the pump beam has been tuned to the zero density exciton resonance of the given transition. The non-interacting results has been shifted in order to better enable a comparison of the spectral features.*

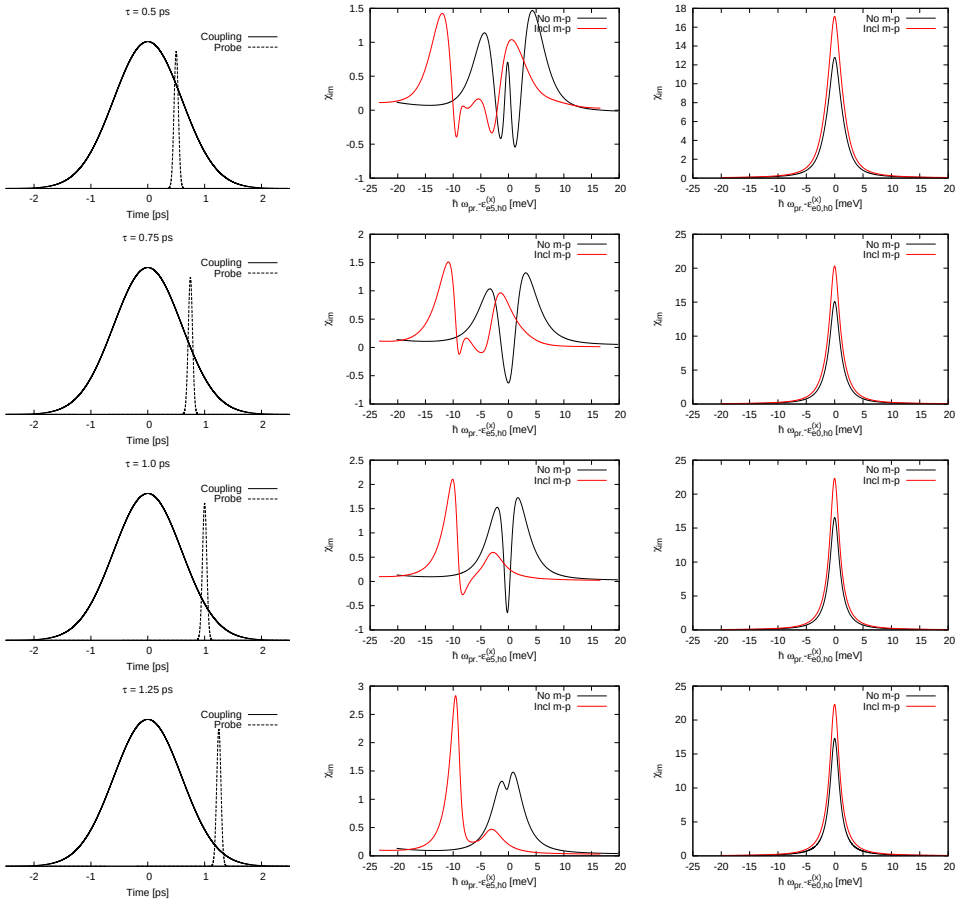

***Figure 6.27**: Time evolution of the imaginary part of the susceptibility at coupling intensity* $90\ \mathrm{MW/cm^2}$*. Left panel shows an illustration of the envelopes of the probe and coupling field intensities. Middle panel refers to V configuration, rightmost is Ladder. The black curves are for the independent particles, while the red curves are including many-body interactions. In the interacting cases the pump beam has been tuned to the zero density exciton resonance of the given transition. The non-interacting results has been shifted in order to better enable a comparison of the spectral features.*

Chapter 7

Conclusion and Outlook

In the present work we have studied the EIT phenomenon in self-assembled InAs quantum dots. The inclusion of the Coulomb effect is made on basis of the Hartree-Fock approximation. We identify the necessary conditions in which one can disregard solving the coupled Maxwell-Bloch equations and in stead rely solely on the microscopic description for extracting an effective susceptibility which can be used for calculating wave propagation characteristics. We find that this is only possible in the case where a c-w coupling beam is driving the system to a steady state. The transient case, one can only consider propagation through an optically thin sample.

The EIT properties are examined using three different coupling-probe schemes (Ladder, V and Λ , respectively). We find that for all schemes many-body interactions have an important impact on the EIT properties. Results obtained in steady state show that carrier exciting schemes (V and Λ) experience Coulomb enhancement of both the coupling- and the probe transition, whereas in the non-carrier exciting Ladder scheme we do not see an enhancement of the coupling transition. When comparing the slow light capabilities of the three schemes, the V-type scheme emerges as the most preferable for efficient EIT operation. This owes to the fact that the dissipative mechanisms that redistribute the excited carriers favors a V setup, which is reflected in a larger Pauli blocking factor. The reason for this is simply because the electron energy levels are split farther apart than the hole levels and therefore the excited states are less likely to be populated. This result is quite general and could act as a pointer for experimental realization of EIT mediated slow light.

The transient properties show interesting effects such as an increased robustness for quantum coherence effects and gain at the probe resonance frequency. We have identified the most favorable times at which to probe a transient system corresponding to a given duration of the coupling field. We have found that transient systems in the weak EIT regime are best probed at early times whereas systems in the strong EIT regime, where many oscillations are present in the absorption spectrum, provide the largest effects when probed around the peak time of the coupling pulse. Weather these observations could be utilized for

improved slowdown of a pulse propagating in a system during transients remains an open question, but the topic is being investigated.

The study of optical properties of conical dots including strain and up to eight band $k \cdot p$ theory identifies a QD of height $h \simeq 8$ nm and radius $r \simeq 16$ nm as having the best possibility for experimental realization of the EIT effect. Furthermore we find that, due to the separation of the heavy and light holes, band mixing effects are relatively small. This results in qualitative agreement between the optical transition strengths calculated using a single-band model and an eight-band model. The few exceptions we find are, however, transitions relevant for EIT operation.

The present model leaves room for improvement on many levels. First of all propagation of pulses in a transient regime is governed by the coupled Maxwell-Bloch equations and it would be natural to extend the present work in this direction.

The model employed in this work only uses a single effective dephasing rate for all transitions. An improved model would include different rates for different transitions as is done in the atomic EIT treatments, however experimental data on other than the groundstate to groundstate inter-band transition is difficult to come by. Otherwise one needs to go beyond the relaxation time approximation and utilize e.g. a Green's functions approach to model scattering terms. Including a quantum kinetic description of the carrier-phonon interaction would enable this and also allow access for studying the impact of e.g. excitation induced dephasing or excitation enlarged Rabi frequencies, which could have interesting effects on an EIT system. Also one could take into account the effect of a dynamically changing carrier density on the dephasing rates. Attempts at including Coulomb effects on H-F level along with a treatment of LO-phonons have proved more difficult than first anticipated, but are being pursued.

Bibliography

[1] U. Fano, Phys. Rev. **124**, 1866 (1961).

[2] S. E. Harris, J. E. Field, and A. Imamoglu, Phys. Rev. Lett. **64**, 1107 (1990).

[3] K.-J. Boller, A. Imamoglu, and S. E. Harris, Phys. Rev. Lett. **66**, 2593 (1991).

[4] S. H. Autler and C. H. Townes, Phys. Rev. **100**, 703 (1955).

[5] K. H. Hahn, D. A. King, and S. E. Harris, Phys. Rev. Lett. **65**, 2777 (1990).

[6] K. Hakuta, L. Marmet, and B. P. Stoicheff, Phys. Rev. A **45**, 5152 (1992).

[7] O. A. Kocharovskaya and Y. I. Khanin, JETP Letters **48**, 630 (1988).

[8] M. O. Scully, S.-Y. Zhu, and A. Gavrielides, Physical Review Letters **62**, 2813 (1989).

[9] A. S. Zibrov *et al.*, Phys. Rev. Lett. **75**, 1499 (1995).

[10] P. S. Bhatia, G. R. Welch, and M. O. Scully, J. Opt. Soc. Am. B **18**, 1587 (2001).

[11] J. Mompart and R. Corbalan, Journal of Optics B: Quantum and Semiclassical Optics **2**, R7 (2000).

[12] L. V. Hau, S. E. Harris, Z. Dutton, and C. H. Behroozi, Nature **397**, 594 (1999).

[13] C. Liu, Z. Dutton, C. H. Behroozi, and L. V. Hau, Nature **397**, 490 (2001).

[14] U. Leonhardt and P. Piwnicki, Phys. Rev. Lett. **84**, 822 (2000).

[15] M. D. Lukin and A. Imamoğlu, Phys. Rev. Lett. **84**, 1419 (2000).

[16] Y. Rostovtsev, O. Kocharovskaya, G. Welch, and M. Scully, Optics and Photonics News (2002).

[17] H. Schmidt and R. J. Ram, Applied Physics Letters **76**, 3173 (2000).

[18] C. J. Chang-Hasnain, P. C. Ku, J. Kim, and S. L. Chuang, Proc. IEEE **9**, 1884 (2003).

[19] J. Mørk *et al.*, Laser & Photon. Rev. , 1 (2008).

[20] Y. Zhao, C. Wu, B.-S. Ham, M. K. Kim, and E. Awad, Phys. Rev. Lett. **79**, 641 (1997).

[21] G. B. Serapiglia, E. Paspalakis, C. Sirtori, K. L. Vodopyanov, and C. C. Phillips, Phys. Rev. Lett. **84**, 1019 (2000).

[22] M. C. Philips and H. Wang, Phys. Rev. B **69**, 115337 (2004).

[23] H. Kang *et al.*, Opt. Express **16**, 15728 (2008).

[24] S.-M. Ma, H. Xu, and B. S. Ham, Opt. Express **17**, 14902 (2009).

[25] S. Marcinkevičius, A. Gushterov, and J. P. Reithmaier, Appl. Phys. Lett. **92**, 041113 (2008).

[26] V. I. Klimov *et al.*, Science **290**, 314 (2000), http://www.sciencemag.org/cgi/reprint/290/5490/314.pdf.

[27] L. P. Kouwenhoven, D. G. Austing, and S. Tarucha, Reports on Progress in Physics **64**, 701 (2001).

[28] W. Seifert *et al.*, Prog. Crystal Growth and Charact. **33**, 423 (1996).

[29] K. Jacobi, Prog. Surf. Sci. **71**, 185 (2003).

[30] S. Anders *et al.*, Phys. Rev. B **66**, 125309 (2002).

[31] S. Stobbe, J. Johansen, P. T. Kristensen, J. M. Hvam, and P. Lodahl, Physical Review B (Condensed Matter and Materials Physics) **80**, 155307 (2009).

[32] G. Park, O. Shchekin, D. Huffaker, and D. Deppe, Photonics Technology Letters, IEEE **12**, 230 (2000).

[33] D. Bimberg, Journal of Physics D: Applied Physics **38**, 2055 (2005).

[34] Q. Han *et al.*, Chin. Opt. Lett. **4**, 413 (2006).

[35] A. Kovsh *et al.*, Electronics Letters **38**, 1104 (2002).

[36] S. Schneider *et al.*, Quantum Electronics, IEEE Journal of **40**, 1423 (2004).

[37] V. M. Ustinov, A. E. Zhukov, A. Y. Egorov, and N. A. Maleev, *Quantum Dot Lasers* (Oxford University Press, 2003).

[38] H. Yokoyama and S. D. Brorson, Journal of Applied Physics **66**, 4801 (1989).

[39] Y. Yamamoto, S. Machida, and G. Björk, Phys. Rev. A **44**, 657 (1991).

[40] C. J. Chang-Hasnain, P. C. Ku, J. Kim, and S. L. Chuang, Proc. IEEE **91**, 1884 (2003).

[41] J. Kim, S. L. Chuang, P. C. Ku, and C. J. Chang-Hasnain, J. Phys.: Cond. Matt. **16**, 3727 (2004).

[42] P. Jänes, J. Tidström, and L. Thylén, J. Lightwave Technol. **23**, 3893 (2005).

[43] P. K. Nielsen, H. Thyrrestrup, J. Mørk, and B. Tromborg, Optics Express **15**, 6396 (2007).

[44] H. C. Schneider, W. W. Chow, and S. W. Koch, Phys. Rev. B **64**, 115315 (2001).

[45] W. W. Chow, S. Michael, and H. C. Schneider, J. Mod. Opt. **54**, 2413 (2007).

[46] S. Michael, W. W. Chow, and H. C. Schneider, Appl. Phys. Lett. **89**, 181114 (2006).

[47] W. W. Chow, H. C. Schneider, and M. C. Phillips, Phys. Rev. A **68**, 053802 (2003).

[48] M. Kira and S. Koch, Prog. Quantum Elec. **30**, 155 (2006).

[49] H. Haug and S. W. Koch, *Quantum theory of optical and electronic properties of semiconductors*, Third ed. (World scientific, 1990).

[50] M. Kira, F. Jahnke, W. Hoyer, and S. W. Koch, Progress in Quantum Electronics **23**, 189 (1999).

[51] H. Bruus and K. Flensberg, *Many-Body Quantum Theory in Condensed Matter Physics* (Oxford University Press, 2004), second reprint.

[52] H. Haug and A.-P. Jauho, *Quantum Kinetics in Transport and Optics of Semiconductors*, 2nd ed. (Springer, 2007).

[53] A. Krügel, V. Axt, T. Kuhn, P. Machnikowski, and A. Vagov, Applied Physics B: Lasers and Optics **81**, 897 (2005).

[54] J. Förstner, C. Weber, J. Danckwerts, and A. Knorr, Phys. Rev. Lett. **91**, 127401 (2003).

[55] V. M. Axt and T. Kuhn, Rep. Prog. Phys. **67**, 433 (2004).

[56] P. Borri *et al.*, IEEE J. Sel. Top. Quantum Elect. **8**, 984 (2002).

[57] P. Borri *et al.*, Phys. Rev. Lett. **87**, 157401 (2001).

[58] P. Borri *et al.*, Phys. Rev. B: Condens. Matter **60**, 7784 (1999).

[59] S. Sauvage *et al.*, Phys. Rev. B **66**, 153312 (2002).

[60] J. Shah, *Ultrafast spectroscopy of semiconductors and semiconductor nanostructures*, Second ed. (Springer, 1996).

[61] J. Mørk and A. Mecozzi, J. Opt. Soc. Am. B **72**, 1803 (1996).

[62] R. Boyd, *Nonlinear Optics* (Academic Press, San Diego, 1992).

[63] P. Meystre and M. Sargent, *Elements of Quantum Optics*, third ed. (Springer-Verlag, Heidelberg, Germany, 1998).

[64] M. E. Crenshaw and C. D. Cantrell, Phys. Rev. A **39**, 126 (1989).

[65] M. Grifoni and P. Hänggi, Physics Reports **304**, 229 (1998).

[66] M. Fleischhauer, A. Imamoglu, and J. P. Marangos, Rev. Mod. Phys. **75** (2005).

[67] M. O. Scully and M. S. Zubairy, *Quantum Optics* (Cambridge University Press, 1997).

[68] C. Cohen-Tannoudji, J. Dupont-Roc, and G. Grynberg, *Atom-Photon Interactions* (Wiley & Sons, 1998).

[69] J. Oshinowo, M. Nishioka, S. Ishicia, and Y. Arakawa, Appl. Phys. Lett. **65**, 1421 (1994).

[70] J. Marquez, L. Geelhaar, and K. Jacobi, Applied Physics Letters **78**, 2309 (2001).

[71] P. E. Lippens and M. Lannoo, Phys. Rev. B **41**, 6079 (1990).

[72] L.-W. Wang and A. Zunger, Phys. Rev. B **54**, 11417 (1996).

[73] L. C. L. Y. Voon and M. Willatzen, *The k·p Method: Electronic Properties of Semiconductors* (Springer, 2009).

[74] D. Bimberg, M. Grundmann, and N. N. Ledentsov, *Quantum Dot Heterostructures* (John Wiley & sons, 1999).

[75] N. Liu, J. Tersoff, O. Baklenov, A. L. Holmes, and C. K. Shih, Phys. Rev. Lett. **84**, 334 (2000).

[76] I. Kegel *et al.*, Phys. Rev. Lett. **85**, 1694 (2000).

[77] T. Inoue *et al.*, Appl. Phys. Lett **92**, 031902 (2008).

[78] P. Hawrylak and M. Korkusinski, in *Topics in Applied Physics*, edited by P. Michler Vol. 90, pp. 25–92, Springer-Verlag, Heidelberg, 2003.

[79] R. V. N. Melnik and M. Willatzen, Nanotechnology **15**, 1 (2004).

[80] R. V. N. Melnik and M. Willatzen, Nanotechnology **15**, 1 (2004).

[81] M. G. Burt, J. Phys. Condens. Matter **5**, 4091 (1993).

[82] T. R. Nielsen, *Carrier-Carrier and Carrier-Phonon Scattering in Self-Assembled Dots*, PhD thesis, Institute for Theoretical Physics, University of Bremen, Germany, http://elib.suub.uni-bremen.de/diss/docs/00010001.pdf, 2005.

[83] P. K. Nielsen, Fundamental properties of single photon sources, Master's thesis, DTU-photonics, Department of photonic engineering, Technical University of Denmark, 2008.

[84] T. R. Nielsen, P. Gartner, and F. Jahnke, Phys. Rev. B **69**, 235314 (2004).

[85] N. Baer, *Optical and Electronic Properties of InGaAs and Nitride Quantum Dots*, PhD thesis, Institute for Theoretical Physics, University of Bremen, Germany, http://elib.suub.uni-bremen.de/diss/docs/00010611.pdf, 2006.

[86] A. Wojs, P. Hawrylak, S. Fafard, and L. Jacak, Phys. Rev. B **54**, 5604 (1996).

[87] D. Barettin, *Multiphysic effects in quantum-dot structures*, PhD thesis, University of southern Denmark, 2009.

[88] E. P. Pokatilov, V. A. Fonoberov, V. M. Fomin, and J. T. Devreese, Phys. Rev. B **64**, 245328 (2001).

[89] Y. Zhang, Phys. Rev. B **49**, 14 352 (1994).

[90] I. V. J. Meyer and L. R. Ram-Mohan, J. Appl. Phys. **89**, 5815 (2001).

[91] G. L. Bir and G. E. Pikus, *Symmetry and Strain-Induced Effects In semiconductors* (Wiley, New York, 1974).

[92] V. A. Fonoberov and A. A. Balandin, J. Appl. Phys. **94**, 7178 (2003).

[93] O. Stier, M. Grundmann, and D. Bimberg, Phys. Rev. B **59**, 5688 (1999).

[94] D. Barettin *et al.*, To appear in: Phys. Rev. B **80** (2009).

[95] G. Bastard, *Wave mechanics applided to semiconductor heterostructures*les Editions de Physique (Wiley, New York, 1988).

[96] J. Houmark, T. R. Nielsen, J. Mørk, and A.-P. Jauho, Phys. Rev. B **79**, 115420 (2009).

[97] Y.-Q. Li and M. Xiao, Opt. Lett. **20**, 1489 (1995).

[98] S. R. de Echaniz *et al.*, Phys. Rev. A **64**, 013812 (2001).

[99] S. R. de Echaniz *et al.*, Phys. Rev. A **64**, 055801 (2001).

[100] S. Doniach and E. H. Sondheimer, *Green's functions for solid state physicists* (Imperial College Press, London, 1998).

[101] I. M. Lifshits, S. A. Gredeskul, and L. A. Pastur, *Introduction to the Theory of Disordered Systems* (John Wiley & Sons, 1988).

[102] T. Wimbauer and K. Oettinger, Phys. Rev. B **50**, 8889 (1994).

Appendix A

Hartree renormalization

We here show that the Hartree energy renormalization of a dot state $\alpha = (\boldsymbol{R}, l)$ of a dot position at $\boldsymbol{R}$ with band index b is independent of position. The index l covers all spatial quantum numbers, furthermore the spin is included tacitly in the band index. We start from Eq. (5.3.37)

$$\begin{aligned}\Delta^{\mathrm{H}}_{b,\alpha} &= \sum_{b_1,\alpha_1,\alpha_2} V^{bb_1}_{\alpha\alpha_1\alpha_2\alpha}\rho_{\alpha_1\alpha_2} + \sum_{b_1\boldsymbol{k}_1} V^{bb_1}_{\alpha\boldsymbol{k}_1\boldsymbol{k}_1\alpha} n^{b_1}_{\boldsymbol{k}_1} \\ &= \Delta^{\mathrm{H,QD}}_{b,\alpha} + \Delta^{\mathrm{H,WL}}_{b,\alpha} \end{aligned} \tag{A.0.1}$$

Since we have no intra-band WL dipole moment, only populations enter into $\Delta^{\mathrm{H,WL}}_{b,\alpha}$. The QD contribution looks like

$$\begin{aligned}\Delta^{\mathrm{H,QD}}_{b,\alpha} =& \sum_{\boldsymbol{R}_1}\sum_{b_1,l_1,l_2}\frac{1}{A}\sum_{\boldsymbol{q}} V^{bb_1}_{\sigma\sigma_1\sigma_1\sigma}(\boldsymbol{q})\rho^{b_1}_{l_1l_2} \\ &\times \langle l|e^{-i\boldsymbol{q}\cdot\boldsymbol{\rho}}|l\rangle \langle l_1|e^{i\boldsymbol{q}\cdot\boldsymbol{\rho}}|l_2\rangle\, e^{-i\boldsymbol{q}\cdot(\boldsymbol{R}-\boldsymbol{R}_1)}\,. \end{aligned} \tag{A.0.2}$$

The spatial position of the QDs enter through the phase factor. We can remove the explicit position dependence by considering a large quantization area encompassing a large number of dots N. By the law of large numbers, the distribution of different values for the above quantity is sharply peaked around the configurational averaged value. Thus allowing us to replace the QD contribution for a particular dot position $\Delta^{\mathrm{H,QD}}_{b,\alpha}$ by its averaged value $\Delta^{\mathrm{H,QD}}_{b,l}$ given by

$$\begin{aligned}\Delta^{\mathrm{H,QD}}_{b,l} =& \sum_{\boldsymbol{R},\boldsymbol{R}_1}\sum_{b_1,l_1,l_2}\frac{1}{A}\sum_{\boldsymbol{q}} V^{bb_1}_{\sigma\sigma_1\sigma_1\sigma}(\boldsymbol{q})\rho^{b_1}_{l_1l_2} \\ &\times \langle l|e^{-i\boldsymbol{q}\cdot\boldsymbol{\rho}}|l\rangle \langle l_1|e^{i\boldsymbol{q}\cdot\boldsymbol{\rho}}|l_2\rangle\, e^{-i\boldsymbol{q}\cdot(\boldsymbol{R}-\boldsymbol{R}_1)}\,. \end{aligned} \tag{A.0.3}$$

The summation over random positions $\boldsymbol{R}, \boldsymbol{R}_1$ is evaluated according to disordered system theory (see e.g. Ref. [100, 101])

$$\begin{aligned}\sum_{\boldsymbol{R},\boldsymbol{R}_1} f(\boldsymbol{R})g(\boldsymbol{R}_1) &= \sum_{\boldsymbol{R}\neq\boldsymbol{R}_1} f(\boldsymbol{R})g(\boldsymbol{R}_1) + \sum_{\boldsymbol{R}} f(\boldsymbol{R})g(\boldsymbol{R}) \\ &= N^2\,\langle\langle f\rangle\rangle\cdot\langle\langle g\rangle\rangle + N\,\langle\langle fg\rangle\rangle\,, \end{aligned} \tag{A.0.4}$$

where the configuration average of a function F is defined as $\langle\langle F\rangle\rangle = 1/A \int \mathrm{d}\boldsymbol{R}\, F(\boldsymbol{R})$. In the present case $f(\boldsymbol{R}) = e^{-i\boldsymbol{q}\cdot\boldsymbol{R}}$,$g(\boldsymbol{R}_1) = e^{i\boldsymbol{q}\cdot\boldsymbol{R}_1}$. We get $\langle\langle f\rangle\rangle = \langle\langle g\rangle\rangle = \delta_{\boldsymbol{q},0}$ and $\langle\langle fg\rangle\rangle = 1$, so we can write:

$$\begin{aligned}\Delta^{\mathrm{H,QD}}_{b,l} &= N_{\mathrm{dot}} \sum_{b_1,l_1,l_2} V^{bb_1}_{\sigma\sigma_1\sigma_1\sigma}(\boldsymbol{q}=0)\,\langle l|l\rangle\,\langle l_1|l_2\rangle\,\rho^{b_1}_{l_1l_2} + \sum_{b_1,l_1,l_2} V^{bb_1}_{ll_1l_2l}\rho^{b_1}_{l_1l_2} \\ &= N_{\mathrm{dot}} \sum_{b_1,l_1} V^{bb_1}_{\sigma\sigma_1\sigma_1\sigma}(\boldsymbol{q}=0) n^{b_1}_{l_1} + \sum_{b_1,l_1,l_2} V^{bb_1}_{ll_1l_2l}\rho^{b_1}_{l_1l_2} \qquad \text{(A.0.5)}\end{aligned}$$

For the Hartree part we end up with a term arising from the Coulomb interaction between different dots, which is proportional to the total QD charge and a second term describing the Hartree interaction inside the dot in question. Couplings to polarization components of other dots drop out due to the orthogonality requirement of states belonging to the same band.

The WL contribution to the Hartree energy shift can be easily evaluated

$$\begin{aligned}\Delta^{\mathrm{H,WL}}_{b,\alpha} &= \sum_{b_1,k_1} \frac{1}{A} \sum_{\boldsymbol{q}} V^{bb_1}_{\sigma\sigma_1\sigma_1\sigma}(\boldsymbol{q}) n^{b_1}_{\boldsymbol{k}_1}\,\langle l|e^{-i\boldsymbol{q}\cdot\boldsymbol{\rho}}|l\rangle\, e^{-i\boldsymbol{q}\cdot\boldsymbol{R}}\delta_{\boldsymbol{k}_1,\boldsymbol{k}_1+\boldsymbol{q}} \\ &= \frac{1}{A}\sum_{b_1,\boldsymbol{k}_1} V^{bb_1}_{\sigma\sigma_1\sigma_1\sigma}(\boldsymbol{q}=0) n^{b_1}_{\boldsymbol{k}_1}\,. \qquad \text{(A.0.6)}\end{aligned}$$

This result is independent of dot position and similar in structure to the first term of eq. (A.0.5) and is proportional to the WL charge density. Since we are considering $\boldsymbol{q}=0$, the form factor is the same in both expression and we shall write it as $V^{bb'}(\boldsymbol{q}=0)$. The total Hartree shift is

$$\Delta^{\mathrm{H}}_{b,l} = V^{bb'}(\boldsymbol{q}=0)\left(N_{\mathrm{dot}}\sum_{b_1l_1} n^{b_1}_{l_1} + \frac{1}{A}\sum_{b_1,\boldsymbol{k}_1} n^{b_1}_{\boldsymbol{k}_1}\right) \pm \sum_{b_1,l_1,l_2} V^{bb_1}_{ll_1l_2l}\rho^{b_1}_{l_1l_2}\,. \qquad \text{(A.0.7)}$$

Due to global charge neutrality the terms in the parenthesis must cancel each other, and the Hartree shift depends only on interactions inside the dot itself.

The WL Hartree shift is found in a similar manner

$$\begin{aligned}\Delta^{\mathrm{H}}_{b,\boldsymbol{k}} &= \sum_{b_1\alpha_1\alpha_2} B^{bb_1}_{\boldsymbol{k}\alpha_2\alpha_1\boldsymbol{k}}\rho^{b_1}_{\alpha_1\alpha_2} + \sum_{b_1\boldsymbol{k}_1} V^{bb_1}_{\boldsymbol{k}\boldsymbol{k}_1\boldsymbol{k}_1\boldsymbol{k}} n^{b_1}_{\boldsymbol{k}_1} \\ &= V^{bb'}(\boldsymbol{q}=0)\left(N_{\mathrm{dot}}\sum_{b_1l_1} n^{b_1}_{l_1} + \frac{1}{A}\sum_{b_1,\boldsymbol{k}_1} n^{b_1}_{\boldsymbol{k}_1}\right) \\ &= 0\,, \qquad \text{(A.0.8)}\end{aligned}$$

which also vanishes due to global charge neutrality.

For the Rabi energy renormalization Eq. (5.3.38) the $\delta_{bb'}$ requirement from the Coulomb interaction means that the Hartree term is only non-zero for intra-band polarizations ($b = b'$). Following a similar vein as for $\Delta^{\mathrm{H,QD}}_{b,\alpha}$ the $V(\boldsymbol{q}=0)$

contribution from other dots and the WL drop out completely as the term $\langle l|l'\rangle$ enters the expression. We then have

$$\Delta^{\mathrm{H,QD}}_{b,l,l'} = \sum_{b_1,l_1,l_2} V^{bb_1}_{ll_1l_2l'} \rho^{b_1}_{l_1l_2} \,. \tag{A.0.9}$$

Appendix B

Equations of motion e-h picture

In this appendix we derive the SBE using the electron-hole picture from Hamiltonian level. We will use a single label as a container for all quantum numbers, i.e. spin, wavenumber, subband number etc. The general labeling will be:

- **Specific state labels** are given in greek letters subscripts and refer to both dot -and wetting layer (WL) states:

  Electron: α and γ.

  Hole: β and κ.

- **General state labels** are given in english alphabet subscripts and refer to both dot -and WL states:

  Electron: n, n'.

  Hole: m, m'.

  Either hole or electron, depending on context: i, j, k, l.

- Second quantization creation and annihilation operators:

  Electron: $a^\dagger$ and a.

  Hole: $b^\dagger$ and b.

- **Wavefunctions** are taken within the envelope function approximation:

  $\Psi_i(\mathbf{r}) = \xi_i(\mathbf{r})u_i(\mathbf{r})$

We will later distinguish between WL and dot contributions. Here greek alphabet letters refer to (localized) quantum dot states, and $\mathbf{k}$ is used to label (delocalized) WL states with wavevector $\mathbf{k}$. At the end of the day we will limit ourselves to a two band model, the derivation is, however sufficiently general as to include subband structure.

B.1 Hamiltonian

For an interacting electron-hole plasma in a quantum-dot structure subjected to a coherent light field, the Hamiltonian in the e-h picture, neglecting constant terms, is

$$\hat{H} = \hat{H}_0 + \hat{H}_{c-f} + \hat{H}_C \,, \tag{B.1.1}$$

containing contributions from the free-carrier energy,

$$\hat{H}_0 = \sum_n \epsilon_n a_n^\dagger a_n + \sum_m \epsilon_m b_m^\dagger b_m \,, \tag{B.1.2}$$

the carrier-laser-field interaction energy,

$$\begin{aligned} \hat{H}_{c-f} \quad = \quad & -\Bigg[\sum_{n,n'} \mu_{nn'} a_n^\dagger a_{n'} + \sum_{m,m'} \mu_{mm'} b_m b_{m'}^\dagger \\ & + \sum_{n,m} \Big(\mu_{nm} a_n^\dagger b_m^\dagger + \mu_{nm}^* b_m a_n\Big)\Bigg] E(t) \,, \end{aligned} \tag{B.1.3}$$

and the Coulomb interaction energy,

$$\hat{H}_C = \frac{1}{2}\sum_{i,j,k,l} V_{kl}^{ij} a_i^\dagger a_j^\dagger a_k a_l + \frac{1}{2}\sum_{i,j,k,l} V_{kl}^{ij} b_i^\dagger b_j^\dagger b_k b_l - \sum_{i,j,k,l} V_{kl}^{ij} a_i^\dagger b_j^\dagger b_k a_l \,. \tag{B.1.4}$$

In the above equations ϵ_i is the free-carrier electron or hole energy, μ_{ij} is the projection of the dipole matrix element between states i and j onto the direction $\hat{\boldsymbol{e}}_{\boldsymbol{E}}$ of $E(t)$, the optical field(s). We treat the carrier-field interaction within the dipole approximation and thus disregard the spatial dependance of the field(s). Note that with the definition above, μ_{ij} is calculated as:

$$\mu_{ij} = \begin{cases} \int \mathrm{d}\boldsymbol{r}\ \Psi_i^*(\mathbf{r}) e\mathbf{r}\cdot\hat{\boldsymbol{e}}_{\boldsymbol{E}}\Psi_j(\mathbf{r}) & i,j\text{: electron states;} \\ \int \mathrm{d}\boldsymbol{r}\ \Psi_i(\mathbf{r}) e\mathbf{r}\cdot\hat{\boldsymbol{e}}_{\boldsymbol{E}}\Psi_j^*(\mathbf{r}) & i,j\text{: hole states;} \\ \int \mathrm{d}\boldsymbol{r}\ \Psi_i^*(\mathbf{r})\cdot\hat{\boldsymbol{e}}_{\boldsymbol{E}}\Psi_j^*(\mathbf{r}) & i\text{: electron state, } j\text{: hole state.} \end{cases} \tag{B.1.5}$$

The Coulomb interaction energy matrix element is defined as

$$V_{kl}^{ij} = \iint \mathrm{d}\, r \mathrm{d}\, r'\, \Psi_i^*(\mathbf{r})\Psi_j^*(\mathbf{r}') V(\mid \mathbf{r}-\mathbf{r}' \mid)\Psi_k(\mathbf{r}')\Psi_l(\mathbf{r}) \,, \tag{B.1.6}$$

where $V(\mid \mathbf{r}-\mathbf{r}' \mid)$ is the bare Coulomb potential. Note that we have omitted energetically unfavorable terms giving rise to inter-band scattering.

B.2 General approach

We wish to consider the time evolution of the coherences and populations of the combined dot-WL system, i.e. the elements of the reduced density matrix. In general the time development of the density matrix is given by the Liouville

equation

$$\frac{\partial \hat{\rho}_{ij}}{\partial t} = -\frac{i}{\hbar}\left[\hat{H}, \hat{\rho}\right]_{ij} . \tag{B.2.7}$$

However, since we seek to retain this discussion to second quantization, we will use the Heisenberg equation of motion on the second quantized operator equivalent of the density matrix. The corresponding matrix element is then found by taking the expectation value of the particular operator. Heisenberg's equation of motion reads

$$\frac{\partial \hat{A}(t)}{\partial t} = -\frac{i}{\hbar}\left[\hat{A}(t), \hat{H}\right] , \tag{B.2.8}$$

where $\hat{A}(t)$ represents an operator in the Heisenberg picture.

B.3 Coherences

B.3.1 Interband polarization: $P_{\alpha,\beta}$

$\underline{P_{\alpha,\beta} = \langle b_\beta a_\alpha \rangle}$.

$$\begin{aligned}\frac{\partial P_{\alpha,\beta}}{\partial t} &= -\frac{i}{\hbar}\left\langle\left[b_\beta a_\alpha, \hat{H}\right]\right\rangle \\ &= -\frac{i}{\hbar}\left\langle\left[b_\beta a_\alpha, \hat{H}_0\right] + \left[b_\beta a_\alpha, \hat{H}_{c-f}\right] + \left[b_\beta a_\alpha, \hat{H}_C\right]\right\rangle . \end{aligned} \tag{B.3.9}$$

$\underline{\left[b_\beta a_\alpha, \hat{H}_0\right]}$:

$$\left[b_\beta a_\alpha, \hat{H}_0\right] = b_\beta a_\alpha \hat{H}_0 - \hat{H}_0 b_\beta a_\alpha = A_1 - A_2 . \tag{B.3.10}$$

$$\begin{aligned} A_1 &= b_\beta a_\alpha \left(\sum_n \epsilon_n a_n^\dagger a_n + \sum_m \epsilon_m b_m^\dagger b_m\right) \\ &= \sum_n \epsilon_n b_\beta \left(\delta_{\alpha,n} - a_n^\dagger a_\alpha\right) a_n + \sum_m \epsilon_m \left(\delta_{\beta,m} - b_m^\dagger b_\beta\right) b_m a_\alpha \\ &= \sum_n \epsilon_n \left(b_\beta a_n \delta_{\alpha,n} + b_\beta a_n^\dagger a_n a_\alpha\right) + \sum_m \epsilon_m \left(b_m a_\alpha \delta_{\beta,m} + b_m^\dagger b_m b_\beta a_\alpha\right) \\ &= \epsilon_\alpha b_\beta a_\alpha + \epsilon_\beta b_\beta a_\alpha + \sum_n \epsilon_n a_n^\dagger a_n b_\beta a_\alpha + \sum_m \epsilon_m b_m^\dagger b_m b_\beta a_\alpha \\ &= (\epsilon_\alpha + \epsilon_\beta) b_\beta a_\alpha + A_2 . \end{aligned} \tag{B.3.11}$$

$$\left[b_\beta a_\alpha, \hat{H}_0\right] = (\epsilon_\alpha + \epsilon_\beta) b_\beta a_\alpha . \tag{B.3.12}$$

$\underline{\left[b_\beta a_\alpha, \hat{H}_{c-f}\right]}$:

$$\left[b_\beta a_\alpha, \hat{H}_{c-f}\right] = b_\beta a_\alpha \hat{H}_{c-f} - \hat{H}_{c-f} b_\beta a_\alpha = A_1 - A_2 . \tag{B.3.13}$$

$$
\begin{aligned}
A_1 &= -b_\beta a_\alpha \left[\sum_{n,n'} \mu_{nn'} a_n^\dagger a_{n'} + \sum_{m,m'} \mu_{mm'} b_m b_{m'}^\dagger \right. \\
&\quad \left. + \sum_{n,m} \left(\mu_{nm} a_n^\dagger b_m^\dagger + \mu_{nm}^* b_m a_n \right) \right] E(t) \\
&= \left[-\sum_{n,n'} \mu_{nn'} b_\beta \left(\delta_{\alpha,n} - a_n^\dagger a_\alpha \right) a_{n'} + \sum_{m,m'} \mu_{mm'} b_m \left(\delta_{\beta,m'} - b_{m'}^\dagger b_\beta \right) a_\alpha \right. \\
&\quad \left. - \sum_{n,m} \mu_{nm} b_\beta \left(\delta_{\alpha,n} - a_n^\dagger a_\alpha \right) b_m^\dagger - \sum_{n,m} \mu_{nm}^* b_m a_n b_\beta a_\alpha \right] E(t) \\
&= \left[-\sum_{n,n'} \mu_{nn'} b_\beta a_{n'} \delta_{\alpha,n} - \sum_{n,n'} \mu_{nn'} a_n^\dagger a_{n'} b_\beta a_\alpha + \sum_{m,m'} \mu_{mm'} b_m a_\alpha \delta_{\beta,m'} \right. \\
&\quad - \sum_{m,m'} \mu_{mm'} b_m b_{m'}^\dagger b_\beta a_\alpha - \sum_{n,m} \mu_{nm} \left[\delta_{\alpha,n} \left(\delta_{\beta,m} - b_m^\dagger b_\beta \right) - a_n^\dagger \left(\delta_{\beta,m} - b_m^\dagger b_\beta \right) a_\alpha \right] \\
&\quad \left. - \sum_{n,m} \mu_{nm}^* b_m a_n b_\beta a_\alpha \right] E(t) \\
&= \left[-\sum_{n'} \mu_{\alpha n'} b_\beta a_{n'} + \sum_m \mu_{m\beta} b_m a_\alpha - \sum_{n,m} \mu_{nm} \delta_{\alpha,n} \delta_{\beta,m} + \sum_{n,m} \mu_{nm} b_m^\dagger b_\beta \delta_{\alpha,n} \right. \\
&\quad + \sum_{n,m} \mu_{nm} a_n^\dagger a_\alpha \delta_{\beta,m} - \sum_{n,n'} \mu_{nn'} a_n^\dagger a_{n'} b_\beta a_\alpha - \sum_{m,m'} \mu_{mm'} b_m b_{m'}^\dagger b_\beta a_\alpha \\
&\quad \left. - \sum_{n,m} \mu_{nm} a_n^\dagger b_m^\dagger b_\beta a_\alpha - \sum_{n,m} \mu_{nm}^* b_m a_n b_\beta a_\alpha \right] E(t) \\
&= \left[-\sum_n \mu_{\alpha n} b_\beta a_n + \sum_m \mu_{m\beta} b_m a_\alpha - \mu_{\alpha\beta} + \sum_m \mu_{\alpha m} b_m^\dagger b_\beta \right. \\
&\quad \left. + \sum_n \mu_{n\beta} a_n^\dagger a_\alpha \right] E(t) + A_2 \,. \qquad \text{(B.3.14)}
\end{aligned}
$$

$$
\begin{aligned}
\left[b_\beta a_\alpha, \hat{H}_{c-f} \right] &= \left(-\sum_n \mu_{\alpha n} b_\beta a_n + \sum_m \mu_{m\beta} b_m a_\alpha \right. \\
&\quad \left. - \mu_{\alpha\beta} + \sum_m \mu_{\alpha m} b_m^\dagger b_\beta + \sum_n \mu_{n\beta} a_n^\dagger a_\alpha \right) E(t) \,. \qquad \text{(B.3.15)}
\end{aligned}
$$

$\underline{\left[b_\beta a_\alpha, \hat{H}_C \right]}$:

$$
\left[b_\beta a_\alpha, \hat{H}_C \right] = \left[b_\beta a_\alpha, \hat{H}_C^{ee} + \hat{H}_C^{hh} + \hat{H}_C^{eh} \right] . \qquad \text{(B.3.16)}
$$

$\underline{\left[b_\beta a_\alpha, \hat{H}_C^{ee}\right]}$:

$$\left[b_\beta a_\alpha, \hat{H}_C^{ee}\right] = b_\beta a_\alpha \hat{H}_C^{ee} - \hat{H}_C^{ee} b_\beta a_\alpha = A_1 - A_2\,. \tag{B.3.17}$$

$$\begin{aligned}
A_1 &= b_\beta a_\alpha \left(\frac{1}{2}\sum_{i,j,k,l} V_{kl}^{ij} a_i^\dagger a_j^\dagger a_k a_l\right) = \frac{1}{2}\sum_{i,j,k,l} V_{kl}^{ij} b_\beta a_\alpha a_i^\dagger a_j^\dagger a_k a_l \\
&= -\frac{1}{2}\sum_{i,j,k,l} V_{kl}^{ij}\left(\delta_{\alpha,i} - a_i^\dagger a_\alpha\right) a_j^\dagger a_k a_l b_\beta \\
&= -\frac{1}{2}\sum_{i,j,k,l} V_{kl}^{ij} a_j^\dagger a_k a_l b_\beta \delta_{\alpha,i} + \frac{1}{2}\sum_{i,j,k,l} V_{kl}^{ij} a_i^\dagger\left(\delta_{\alpha,j} - a_j^\dagger a_\alpha\right) a_k a_l b_\beta \\
&= -\frac{1}{2}\sum_{j,k,l} V_{kl}^{\alpha j} a_j^\dagger a_k a_l b_\beta + \frac{1}{2}\sum_{i,k,l} V_{kl}^{i\alpha} a_i^\dagger a_k a_l b_\beta + \frac{1}{2}\sum_{i,j,k,l} V_{kl}^{ij} a_i^\dagger a_j^\dagger a_k a_l b_\beta a_\alpha \\
&= -\frac{1}{2}\sum_{j,k,l} V_{kl}^{\alpha j} a_j^\dagger a_k a_l b_\beta + \frac{1}{2}\sum_{i,k,l} V_{kl}^{i\alpha} a_i^\dagger a_k a_l b_\beta + A_2\,.
\end{aligned} \tag{B.3.18}$$

$$\left[b_\beta a_\alpha, \hat{H}_C^{ee}\right] = -\frac{1}{2}\sum_{j,k,l} V_{kl}^{\alpha j} a_j^\dagger a_k a_l b_\beta + \frac{1}{2}\sum_{i,k,l} V_{kl}^{i\alpha} a_i^\dagger a_k a_l b_\beta\,. \tag{B.3.19}$$

$\underline{\left[b_\beta a_\alpha, \hat{H}_C^{hh}\right]}$:

$$\left[b_\beta a_\alpha, \hat{H}_C^{hh}\right] = b_\beta a_\alpha \hat{H}_C^{hh} - \hat{H}_C^{hh} b_\beta a_\alpha = A_1 - A_2\,. \tag{B.3.20}$$

$$\begin{aligned}
A_1 &= b_\beta a_\alpha \left(\frac{1}{2}\sum_{i,j,k,l} V_{kl}^{ij} b_i^\dagger b_j^\dagger b_k b_l\right) = \frac{1}{2}\sum_{i,j,k,l} V_{kl}^{ij} b_\beta a_\alpha b_i^\dagger b_j^\dagger b_k b_l \\
&= \frac{1}{2}\sum_{i,j,k,l} V_{kl}^{ij}\left(\delta_{\beta,i} - b_i^\dagger b_\beta\right) b_j^\dagger b_k b_l a_\alpha \\
&= \frac{1}{2}\sum_{i,j,k,l} V_{kl}^{ij} b_j^\dagger b_k b_l a_\alpha \delta_{\beta,i} - \frac{1}{2}\sum_{i,j,k,l} V_{kl}^{ij} b_i^\dagger\left(\delta_{\beta,j} - b_j^\dagger b_\beta\right) b_k b_l a_\alpha \\
&= \frac{1}{2}\sum_{j,k,l} V_{kl}^{\beta j} b_j^\dagger b_k b_l a_\alpha - \frac{1}{2}\sum_{i,k,l} V_{kl}^{i\beta} b_i^\dagger b_k b_l a_\alpha + \frac{1}{2}\sum_{i,j,k,l} V_{kl}^{ij} b_i^\dagger b_j^\dagger b_k b_l b_\beta a_\alpha \\
&= \frac{1}{2}\sum_{j,k,l} V_{kl}^{\beta j} b_j^\dagger b_k b_l a_\alpha - \frac{1}{2}\sum_{i,k,l} V_{kl}^{i\beta} b_i^\dagger b_k b_l a_\alpha + A_2\,.
\end{aligned} \tag{B.3.21}$$

$$\left[b_\beta a_\alpha, \hat{H}_C^{hh}\right] = \frac{1}{2}\sum_{j,k,l} V_{kl}^{\beta j} b_j^\dagger b_k b_l a_\alpha - \frac{1}{2}\sum_{i,k,l} V_{kl}^{i\beta} b_i^\dagger b_k b_l a_\alpha\,. \tag{B.3.22}$$

$\underline{\left[b_\beta a_\alpha, \hat{H}_C^{eh}\right]}$:

$$\left[b_\beta a_\alpha, \hat{H}_C^{eh}\right] = b_\beta a_\alpha \hat{H}_C^{eh} - \hat{H}_C^{eh} b_\beta a_\alpha = A_1 - A_2\,. \tag{B.3.23}$$

$$\begin{aligned}
A_1 &= b_\beta a_\alpha \left(- \sum_{i,j,k,l} V_{kl}^{ij} a_i^\dagger b_j^\dagger b_k a_l \right) = - \sum_{i,j,k,l} V_{kl}^{ij} b_\beta a_\alpha a_i^\dagger b_j^\dagger b_k a_l \\
&= - \sum_{i,j,k,l} V_{kl}^{ij} \left(\delta_{\alpha,i} - a_i^\dagger a_\alpha\right) \left(\delta_{\beta,j} - b_j^\dagger b_\beta\right) b_k a_l \\
&= - \sum_{i,j,k,l} V_{kl}^{ij} b_k a_l \delta_{\alpha,i} \delta_{\beta,j} + \sum_{i,j,k,l} V_{kl}^{ij} a_i^\dagger a_\alpha b_k a_l \delta_{\beta,j} + \sum_{i,j,k,l} V_{kl}^{ij} b_j^\dagger b_\beta b_k a_l \delta_{\alpha,i} \\
&\quad - \sum_{i,j,k,l} V_{kl}^{ij} a_i^\dagger a_\alpha b_j^\dagger b_\beta b_k a_l \\
&= - \sum_{k,l} V_{kl}^{\alpha\beta} b_k a_l + \sum_{i,k,l} V_{kl}^{i\beta} a_i^\dagger b_k a_l a_\alpha + \sum_{j,k,l} V_{kl}^{\alpha j} b_j^\dagger b_k a_l b_\beta \\
&\quad - \sum_{i,j,k,l} V_{kl}^{ij} a_i^\dagger b_j^\dagger b_k a_l b_\beta a_\alpha \\
&= - \sum_{k,l} V_{kl}^{\alpha\beta} b_k a_l + \sum_{i,k,l} V_{kl}^{i\beta} a_i^\dagger b_k a_l a_\alpha + \sum_{j,k,l} V_{kl}^{\alpha j} b_j^\dagger b_k a_l b_\beta + A_2\,.
\end{aligned} \tag{B.3.24}$$

$$\left[b_\beta a_\alpha, \hat{H}_C^{eh}\right] = - \sum_{k,l} V_{kl}^{\alpha\beta} b_k a_l + \sum_{i,k,l} V_{kl}^{i\beta} a_i^\dagger b_k a_l a_\alpha + \sum_{j,k,l} V_{kl}^{\alpha j} b_j^\dagger b_k a_l b_\beta \tag{B.3.25}$$

Taking the expectation value of all commutators we arrive at the following expression:

$$\begin{aligned}
\frac{\partial P_{\alpha,\beta}}{\partial t} &= -\frac{i}{\hbar}(\epsilon_\alpha + \epsilon_\beta)\langle b_\beta a_\alpha \rangle \\
&\quad -\frac{i}{\hbar}\left(- \sum_n \mu_{\alpha n} \langle b_\beta a_n \rangle + \sum_m \mu_{m\beta} \langle b_m a_\alpha \rangle - \mu_{\alpha\beta} + \sum_m \mu_{\alpha m} \langle b_m^\dagger b_\beta \rangle + \sum_n \mu_{n\beta} \langle a_n^\dagger a_\alpha \rangle \right) E(t) \\
&\quad -\frac{i}{\hbar}\left(-\frac{1}{2} \sum_{j,k,l} V_{kl}^{\alpha j} \langle a_j^\dagger a_k a_l b_\beta \rangle + \frac{1}{2} \sum_{i,k,l} V_{kl}^{i\alpha} \langle a_i^\dagger a_k a_l b_\beta \rangle \right) \\
&\quad -\frac{i}{\hbar}\left(\frac{1}{2} \sum_{j,k,l} V_{kl}^{\beta j} \langle b_j^\dagger b_k b_l a_\alpha \rangle - \frac{1}{2} \sum_{i,k,l} V_{kl}^{i\beta} \langle b_i^\dagger b_k b_l a_\alpha \rangle \right) \\
&\quad -\frac{i}{\hbar}\left(- \sum_{k,l} V_{kl}^{\alpha\beta} \langle b_k a_l \rangle + \sum_{i,k,l} V_{kl}^{i\beta} \langle a_i^\dagger b_k a_l a_\alpha \rangle + \sum_{j,k,l} V_{kl}^{\alpha j} \langle b_j^\dagger b_k a_l b_\beta \rangle \right)\,.
\end{aligned} \tag{B.3.26}$$

Hartree-Fock limit

In order to close the set of equations we truncate the four-operator terms. We separate the equation of motion into two parts; a Hartree-Fock part and a scattering part

$$\frac{\partial\langle\hat{A}\rangle}{\partial t} = \frac{\partial\langle\hat{A}\rangle_{HF}}{\partial t} + \left.\frac{\partial\hat{A}}{\partial t}\right|_{scatt} \tag{B.3.27}$$

where the scattering part contains all higher order correlations.
Within the Hartree-Fock approximation the four-operator terms become:
$\underline{\langle\left[b_\beta a_\alpha, \hat{H}_C^{ee}\right]\rangle_{HF}}$:

$$\begin{aligned} -\frac{1}{2}\sum_{j,k,l} V_{kl}^{\alpha j}\langle a_j^\dagger a_k a_l b_\beta\rangle + \frac{1}{2}\sum_{i,k,l} V_{kl}^{i\alpha}\langle a_i^\dagger a_k a_l b_\beta\rangle &= \\ -\frac{1}{2}\sum_{j,k,l} V_{kl}^{\alpha j}\langle a_j^\dagger b_\beta a_k a_l\rangle + \frac{1}{2}\sum_{i,k,l} V_{kl}^{i\alpha}\langle a_i^\dagger b_\beta a_k a_l\rangle &\simeq : \end{aligned} \tag{B.3.28}$$

$$\begin{aligned} \simeq & -\frac{1}{2}\sum_{j,k,l} V_{kl}^{\alpha j}\left(\langle a_j^\dagger a_l\rangle\langle b_\beta a_k\rangle - \langle a_j^\dagger a_k\rangle\langle b_\beta a_l\rangle\right) \\ & +\frac{1}{2}\sum_{i,k,l} V_{kl}^{i\alpha}\left(\langle a_i^\dagger a_l\rangle\langle b_\beta a_k\rangle - \langle a_i^\dagger a_k\rangle\langle b_\beta a_l\rangle\right) . \end{aligned} \tag{B.3.29}$$

The second term in both expressions is relabeled in the following manner: $k \to l$, $l \to k$

$$\begin{aligned} = & -\frac{1}{2}\sum_{j,k,l}\left(V_{kl}^{\alpha j} - V_{lk}^{\alpha j}\right)\langle a_j^\dagger a_l\rangle\langle b_\beta a_k\rangle \\ & +\frac{1}{2}\sum_{i,k,l}\left(V_{kl}^{i\alpha} - V_{lk}^{i\alpha}\right)\langle a_i^\dagger a_l\rangle\langle b_\beta a_k\rangle \\ = & -\sum_{j,k,l}\left(V_{kl}^{\alpha j} - V_{lk}^{\alpha j}\right)\langle a_j^\dagger a_l\rangle\langle b_\beta a_k\rangle , \end{aligned} \tag{B.3.30}$$

owing the last manipulation to the symmetry of the Coulomb matrix-element: $V_{kl}^{ij} = V_{lk}^{ji}$.

$\underline{\langle\left[b_\beta a_\alpha, \hat{H}_C^{hh}\right]\rangle_{HF}}$:

$$\frac{1}{2}\sum_{j,k,l} V_{kl}^{\beta j}\langle b_j^\dagger b_k b_l a_\alpha\rangle - \frac{1}{2}\sum_{i,k,l} V_{kl}^{i\beta}\langle b_i^\dagger b_k b_l a_\alpha\rangle \simeq : \tag{B.3.31}$$

$$\begin{aligned} \simeq & \frac{1}{2}\sum_{j,k,l} V_{kl}^{\beta j}\left(\langle b_j^\dagger b_k\rangle\langle b_l a_\alpha\rangle - \langle b_j^\dagger b_l\rangle\langle b_k a_\alpha\rangle\right) \\ & -\frac{1}{2}\sum_{i,k,l} V_{kl}^{i\beta}\left(\langle b_i^\dagger b_k\rangle\langle b_l a_\alpha\rangle - \langle b_i^\dagger b_l\rangle\langle b_k a_\alpha\rangle\right) . \end{aligned} \tag{B.3.32}$$

Following the same reasoning as above, we relabel the equations

$$\begin{aligned} &= \frac{1}{2}\sum_{j,k,l}\left(V_{lk}^{\beta j}-V_{kl}^{\beta j}\right)\langle b_j^\dagger b_l\rangle\langle b_k a_\alpha\rangle \\ &\quad -\frac{1}{2}\sum_{i,k,l}\left(V_{lk}^{i\beta}-V_{kl}^{\beta i}\right)\langle b_i^\dagger b_l\rangle\langle b_k a_\alpha\rangle \\ &= -\sum_{j,k,l}\left(V_{kl}^{\beta j}-V_{lk}^{\beta j}\right)\langle b_j^\dagger b_l\rangle\langle b_k a_\alpha\rangle\,. \end{aligned} \tag{B.3.33}$$

$\underline{\langle\left[b_\beta a_\alpha, \hat{H}_C^{eh}\right]\rangle_{HF}}$:

$$-\sum_{k,l}V_{kl}^{\alpha\beta}\langle b_k a_l\rangle+\sum_{i,k,l}V_{kl}^{i\beta}\langle a_i^\dagger b_k a_l a_\alpha\rangle+\sum_{j,k,l}V_{kl}^{\alpha j}\langle b_j^\dagger b_k a_l b_\beta\rangle \quad \simeq \quad : \tag{B.3.34}$$

$$\begin{aligned} &\simeq -\sum_{k,l}V_{kl}^{\alpha\beta}\langle b_k a_l\rangle+\sum_{i,k,l}V_{kl}^{i\beta}\left(\langle a_i^\dagger a_\alpha\rangle\langle b_k a_l\rangle-\langle a_i^\dagger a_l\rangle\langle b_k a_\alpha\rangle\right) \\ &\quad +\sum_{j,k,l}V_{kl}^{\alpha j}\left(\langle b_j^\dagger b_k\rangle\langle a_l b_\beta\rangle+\langle b_j^\dagger b_\beta\rangle\langle b_k a_l\rangle\right) \\ &= -\sum_{k,l}V_{kl}^{\alpha\beta}\langle b_k a_l\rangle+\sum_{i,k,l}V_{kl}^{i\beta}\left(\langle a_i^\dagger a_\alpha\rangle\langle b_k a_l\rangle-\langle a_i^\dagger a_l\rangle\langle b_k a_\alpha\rangle\right) \\ &\quad +\sum_{j,k,l}V_{kl}^{\alpha j}\left(\langle b_j^\dagger b_\beta\rangle\langle b_k a_l\rangle-\langle b_j^\dagger b_k\rangle\langle b_\beta a_l\rangle\right)\,. \end{aligned} \tag{B.3.35}$$

Collecting all terms we arrive at the following general expression for the inter-band polarization

$$\begin{aligned} i\hbar\frac{\partial P_{\alpha,\beta}}{\partial t} &= (\epsilon_\alpha+\epsilon_\beta)\langle b_\beta a_\alpha\rangle \\ &\quad \left(-\sum_n\mu_{\alpha n}\langle b_\beta a_n\rangle+\sum_m\mu_{m\beta}\langle b_m a_\alpha\rangle\ -\mu_{\alpha\beta}+\sum_m\mu_{\alpha m}\langle b_m^\dagger b_\beta\rangle+\sum_n\mu_{n\beta}\langle a_n^\dagger a_\alpha\rangle\right)E(t) \\ &\quad -\sum_{j,k,l}\left(V_{kl}^{\alpha j}-V_{lk}^{\alpha j}\right)\langle a_j^\dagger a_l\rangle\langle b_\beta a_k\rangle \\ &\quad -\sum_{j,k,l}\left(V_{kl}^{\beta j}-V_{lk}^{\beta j}\right)\langle b_j^\dagger b_l\rangle\langle b_k a_\alpha\rangle \\ &\quad -\sum_{k,l}V_{kl}^{\alpha\beta}\langle b_k a_l\rangle+\sum_{i,k,l}V_{kl}^{i\beta}\left(\langle a_i^\dagger a_\alpha\rangle\langle b_k a_l\rangle-\langle a_i^\dagger a_l\rangle\langle b_k a_\alpha\rangle\right) \\ &\quad +\sum_{j,k,l}V_{kl}^{\alpha j}\left(\langle b_j^\dagger b_\beta\rangle\langle b_k a_l\rangle-\langle b_j^\dagger b_k\rangle\langle b_\beta a_l\rangle\right) \\ &\quad +i\hbar\left.\frac{\partial P_{\alpha,\beta}}{\partial t}\right|_{scatt}\,. \end{aligned} \tag{B.3.36}$$

The above expression become more transparent when put in terms of populations and polarizations

$$
\begin{aligned}
i\hbar\frac{\partial P_{\alpha,\beta}}{\partial t} &= (\epsilon_\alpha+\epsilon_\beta)P_{\alpha,\beta} \\
&\quad \left(-\sum_{n\neq\alpha}\mu_{\alpha n}P_{n,\beta}+\sum_{m\neq\beta}\mu_{m\beta}P_{\alpha,m}\ +\mu_{\alpha\beta}\left(n_\alpha+n_\beta-1\right)\right. \\
&\quad \left.-\sum_{m\neq\beta}\mu_{\alpha m}\tilde{P}_{m,\beta}+\sum_{n\neq\alpha}\mu_{n\beta}\bar{P}_{\alpha,n}\right)E(t) \\
&\quad -\sum_{j,k}\left(V_{kj}^{\alpha j}-V_{jk}^{\alpha j}\right)n_j^e P_{k,\beta}-\sum_{\substack{j,k,l\\ l\neq j}}\left(V_{kl}^{\alpha j}-V_{lk}^{\alpha j}\right)\bar{P}_{l,j}P_{k,\beta} \\
&\quad -\sum_{j,k}\left(V_{kj}^{\beta j}-V_{jk}^{\beta j}\right)n_j^h P_{\alpha,k}+\sum_{\substack{j,k,l\\ l\neq j}}\left(V_{kl}^{\beta j}-V_{lk}^{\beta j}\right)\tilde{P}_{j,l}P_{\alpha,k} \\
&\quad +\sum_{k,l}V_{kl}^{\alpha\beta}\left(n_\alpha+n_\beta-1\right)P_{l,k}+\sum_{\substack{i,k,l\\ i\neq\alpha}}V_{kl}^{i\beta}\bar{P}_{\alpha,i}P_{l,k} \\
&\quad -\sum_{i,k}V_{ki}^{i\beta}n_i^e P_{\alpha,k}-\sum_{\substack{i,k,l\\ l\neq i}}V_{kl}^{i\beta}\bar{P}_{l,i}P_{\alpha,k}-\sum_{\substack{j,k,l\\ j\neq\beta}}V_{kl}^{\alpha j}\tilde{P}_{j,\beta}P_{l,k} \\
&\quad -\sum_{j,l}V_{jl}^{\alpha j}n_j^h P_{l,\beta}+\sum_{\substack{j,k,l\\ k\neq j}}V_{kl}^{\alpha j}\tilde{P}_{j,k}P_{l,\beta} \\
&\quad +i\hbar\left.\frac{\partial P_{\alpha,\beta}}{\partial t}\right|_{scatt}. \qquad \text{(B.3.37)}
\end{aligned}
$$

We introduced intraband polarizations involving electrons as $\bar{P}_{n,n'}=\langle a_{n'}^\dagger a_n\rangle$ and holes as $\tilde{P}_{m,m'}=\langle b_{m'}b_m^\dagger\rangle$.

B.3.2 Intraband hole-hole polarization: $\tilde{P}_{\beta,\kappa}$

$\underline{\tilde{P}_{\beta,\kappa}=\langle b_\kappa b_\beta^\dagger\rangle}$.

$$
\begin{aligned}
\frac{\partial\tilde{P}_{\beta,\kappa}}{\partial t} &= -\frac{i}{\hbar}\left\langle\left[b_\kappa b_\beta^\dagger,\hat{H}\right]\right\rangle \\
&= -\frac{i}{\hbar}\left\langle\left[b_\kappa b_\beta^\dagger,\hat{H}_0\right]+\left[b_\kappa b_\beta^\dagger,\hat{H}_{c-f}\right]+\left[b_\kappa b_\beta^\dagger,\hat{H}_C\right]\right\rangle. \qquad \text{(B.3.38)}
\end{aligned}
$$

$\underline{\left[b_\kappa b_\beta^\dagger,\hat{H}_0\right]}$:

$$
\left[b_\kappa b_\beta^\dagger,\hat{H}_0\right] = b_\kappa b_\beta^\dagger\hat{H}_0-\hat{H}_0 b_\kappa b_\beta^\dagger=A_1-A_2\,. \qquad \text{(B.3.39)}
$$

$$
\begin{aligned}
A_1 &= b_\kappa b_\beta^\dagger \left(\sum_n \epsilon_n a_n^\dagger a_n + \sum_m \epsilon_m b_m^\dagger b_m \right) \\
&= \sum_n \epsilon_n a_n^\dagger a_n b_\kappa b_\beta^\dagger - \sum_m \epsilon_m \left(\delta_{\kappa,m} - b_m^\dagger b_\kappa \right) \left(\delta_{\beta,m} - b_m b_\beta^\dagger \right) \\
&= \sum_n \epsilon_n a_n^\dagger a_n b_\kappa b_\beta^\dagger - \sum_m \epsilon_m \left(\delta_{\kappa,m}\delta_{\beta,m} - \delta_{\kappa,m} b_m b_\beta^\dagger - \delta_{\beta,m} b_m^\dagger b_\kappa - b_m b_m^\dagger b_\kappa b_\beta^\dagger \right) \\
&= -\sum_m \epsilon_m \left(\delta_{\kappa,m}\delta_{\beta,m} - \delta_{\kappa,m} b_m b_\beta^\dagger - \delta_{\beta,m} b_m^\dagger b_\kappa \right) + A_2 \\
&= \epsilon_\kappa b_\kappa b_\beta^\dagger - \epsilon_\beta b_\kappa b_\beta^\dagger + A_2 \qquad \text{(B.3.40)}
\end{aligned}
$$

$$
\left[b_\kappa b_\beta^\dagger, \hat{H}_0 \right] = \left(\epsilon_\kappa - \epsilon_\beta \right) b_\kappa b_\beta^\dagger \,. \qquad \text{(B.3.41)}
$$

$\underline{\left[b_\kappa b_\beta^\dagger, \hat{H}_{c-f} \right]}$:

$$
\left[b_\kappa b_\beta^\dagger, \hat{H}_{c-f} \right] = b_\kappa b_\beta^\dagger \hat{H}_{c-f} - \hat{H}_{c-f} b_\kappa b_\beta^\dagger = A_1 - A_2 \,. \qquad \text{(B.3.42)}
$$

$$
\begin{aligned}
A_1 &= -b_\kappa b_\beta^\dagger \Bigg[\sum_{n,n'} \mu_{nn'} a_n^\dagger a_{n'} + \sum_{m,m'} \mu_{mm'} b_m b_{m'}^\dagger \\
&\quad + \sum_{n,m} \left(\mu_{nm} a_n^\dagger b_m^\dagger + \mu_{nm}^* b_m a_n \right) \Bigg] E(t) \\
&= \Bigg[- \sum_{n,n'} \mu_{nn'} a_n^\dagger a_{n'} b_\kappa b_\beta^\dagger - \sum_{m,m'} \mu_{mm'} b_\kappa \left(\delta_{\beta,m} - b_m b_\beta^\dagger \right) b_{m'}^\dagger \\
&\quad + \sum_{n,m} \mu_{nm} a_n^\dagger \left(\delta_{\kappa,m} - b_m^\dagger b_\kappa \right) b_\beta^\dagger - \sum_{n,m} \mu_{nm}^* b_\kappa \left(\delta_{\beta,m} - b_m b_\beta^\dagger \right) a_n \Bigg] E(t) \\
&= \Bigg[- \sum_{n,n'} \mu_{nn'} a_n^\dagger a_{n'} b_\kappa b_\beta^\dagger - \sum_{m,m'} \mu_{mm'} \left[\delta_{\beta,m} b_\kappa b_{m'}^\dagger - b_m \left(\delta_{\kappa,m'} - b_{m'}^\dagger b_\kappa \right) b_\beta^\dagger \right] \\
&\quad + \sum_{n,m} \mu_{nm} \left(\delta_{\kappa,m} a_n^\dagger b_\beta^\dagger - a_n^\dagger b_m^\dagger b_\kappa b_\beta^\dagger \right) - \sum_{n,m} \mu_{nm}^* \left(\delta_{\beta,m} b_\kappa a_n + b_m a_n b_\kappa b_\beta^\dagger \right) \Bigg] E(t) \\
&= \Bigg[- \sum_{n,n'} \mu_{nn'} a_n^\dagger a_{n'} b_\kappa b_\beta^\dagger - \sum_{m'} \mu_{\beta m'} b_\kappa b_{m'}^\dagger + \sum_{m} \mu_{m\kappa} b_m b_\beta^\dagger - \sum_{m,m'} \mu_{mm'} b_m b_{m'}^\dagger b_\kappa b_\beta^\dagger \\
&\quad + \sum_{n} \mu_{n\kappa} a_n^\dagger b_\beta^\dagger - \sum_{n,m} \mu_{nn'} a_n^\dagger b_m^\dagger b_\kappa b_\beta^\dagger - \sum_{n} \mu_{n\beta}^* b_\kappa a_n - \sum_{n,m} \mu_{nm}^* b_m a_n b_\kappa b_\beta^\dagger \Bigg] E(t) \\
&= \Bigg[- \sum_{m'} \mu_{\beta m'} b_\kappa b_{m'}^\dagger + \sum_{m} \mu_{m\kappa} b_m b_\beta^\dagger \\
&\quad + \sum_{n} \mu_{n\kappa} a_n^\dagger b_\beta^\dagger - \sum_{n} \mu_{n\beta}^* b_\kappa a_n \Bigg] E(t) + A_2 \,. \qquad \text{(B.3.43)}
\end{aligned}
$$

$$
\begin{aligned}
\left[b_\kappa b_\beta^\dagger, \hat{H}_{c-f} \right] &= \Bigg(- \sum_{m'} \mu_{\beta m'} b_\kappa b_{m'}^\dagger + \sum_{m} \mu_{m\kappa} b_m b_\beta^\dagger \\
&\quad + \sum_{n} \mu_{n\kappa} a_n^\dagger b_\beta^\dagger - \sum_{n} \mu_{n\beta}^* b_\kappa a_n \Bigg) E(t) \,. \qquad \text{(B.3.44)}
\end{aligned}
$$

$\underline{\left[b_\kappa b_\beta^\dagger, \hat{H}_C \right]}$:

$$
\left[b_\kappa b_\beta^\dagger, \hat{H}_C \right] = \left[b_\kappa b_\beta^\dagger, \hat{H}_C^{ee} + \hat{H}_C^{hh} + \hat{H}_C^{eh} \right] . \qquad \text{(B.3.45)}
$$

$\underline{\left[b_\kappa b_\beta^\dagger, \hat{H}_C^{ee} \right]}$:

$$
\left[b_\kappa b_\beta^\dagger, \hat{H}_C^{ee} \right] = b_\kappa b_\beta^\dagger \hat{H}_C^{ee} - \hat{H}_C^{ee} b_\kappa b_\beta^\dagger = A_1 - A_2 \,. \qquad \text{(B.3.46)}
$$

$$\begin{aligned} A_1 &= b_\kappa b_\beta^\dagger \left(\frac{1}{2} \sum_{i,j,k,l} V_{kl}^{ij} a_i^\dagger a_j^\dagger a_k a_l \right) = \frac{1}{2} \sum_{i,j,k,l} V_{kl}^{ij} b_\kappa b_\beta^\dagger a_i^\dagger a_j^\dagger a_k a_l \\ &= \frac{1}{2} \sum_{i,j,k,l} V_{kl}^{ij} a_i^\dagger a_j^\dagger a_k a_l b_\kappa b_\beta^\dagger \\ &= A_2 \,. \end{aligned} \tag{B.3.47}$$

$$\left[b_\kappa b_\beta^\dagger, \hat{H}_C^{ee} \right] = 0 \,. \tag{B.3.48}$$

$\underline{\left[b_\kappa b_\beta^\dagger, \hat{H}_C^{hh} \right]}$:

$$\left[b_\kappa b_\beta^\dagger, \hat{H}_C^{hh} \right] = b_\kappa b_\beta^\dagger \hat{H}_C^{hh} - \hat{H}_C^{hh} b_\kappa b_\beta^\dagger = A_1 - A_2 \,. \tag{B.3.49}$$

$$\begin{aligned} A_1 &= b_\kappa b_\beta^\dagger \left(\frac{1}{2} \sum_{i,j,k,l} V_{kl}^{ij} b_i^\dagger b_j^\dagger b_k b_l \right) = \frac{1}{2} \sum_{i,j,k,l} V_{kl}^{ij} b_\kappa b_\beta^\dagger b_i^\dagger b_j^\dagger b_k b_l \\ &= \frac{1}{2} \sum_{i,j,k,l} V_{kl}^{ij} \left(\delta_{\kappa,i} - b_i^\dagger b_\kappa \right) b_j^\dagger \left(\delta_{\beta,k} - b_k b_\beta^\dagger \right) b_l \\ &= \frac{1}{2} \sum_{i,j,k,l} V_{kl}^{ij} \left[\delta_{\kappa,i} \delta_{\beta,k} b_j^\dagger b_l - \delta_{\beta,k} b_i^\dagger b_\kappa b_j^\dagger b_l - \delta_{\kappa,i} b_j^\dagger b_k b_\beta^\dagger \; b_l + b_i^\dagger b_\kappa b_j^\dagger b_k b_\beta^\dagger b_l \right] \\ &= \frac{1}{2} \sum_{i,j,k,l} V_{kl}^{ij} \left[\delta_{\kappa,i} \delta_{\beta,k} b_j^\dagger b_l - \delta_{\beta,k} b_i^\dagger \left(\delta_{\kappa,j} - b_j^\dagger b_\kappa \right) b_l - \delta_{\kappa,i} b_j^\dagger b_k \left(\delta_{\beta,l} - b_l b_\beta^\dagger \right) \right. \\ &\quad \left. + b_i^\dagger \left(\delta_{\kappa,j} - b_j^\dagger b_\kappa \right) b_k \left(\delta_{\beta,l} - b_l b_\beta^\dagger \right) \right] \\ &= \frac{1}{2} \sum_{i,j,k,l} V_{kl}^{ij} \left[\delta_{\kappa,i} \delta_{\beta,k} b_j^\dagger b_l - \delta_{\beta,k} \delta_{\kappa,j} b_i^\dagger b_l - \delta_{\beta,k} b_i^\dagger b_j^\dagger b_l b_\kappa - \delta_{\kappa,i} \delta_{\beta,l} b_j^\dagger b_k + \delta_{\kappa,i} b_j^\dagger b_k b_l b_\beta^\dagger \right. \\ &\quad \left. + \delta_{\kappa,j} \delta_{\beta,l} b_i^\dagger b_k - \delta_{\kappa,j} b_i^\dagger b_k b_l b_\beta^\dagger - \delta_{\beta,l} b_i^\dagger b_j^\dagger b_\kappa b_k + b_i^\dagger b_j^\dagger b_\kappa b_k b_l b_\beta^\dagger \right] \\ &= \frac{1}{2} \sum_{j,l} V_{\beta,l}^{\kappa,j} b_j^\dagger b_l - \frac{1}{2} \sum_{i,l} V_{\beta,l}^{i,\kappa} b_i^\dagger b_l - \frac{1}{2} \sum_{i,j,l} V_{\beta,l}^{i,j} b_i^\dagger b_j^\dagger b_l b_\kappa - \frac{1}{2} \sum_{j,k} V_{k,\beta}^{\kappa,j} b_j^\dagger b_k + \frac{1}{2} \sum_{j,k,l} V_{k,l}^{\kappa,j} b_j^\dagger b_k b_l b_\beta^\dagger \\ &\quad + \frac{1}{2} \sum_{i,k} V_{k,\beta}^{i,\kappa} b_i^\dagger b_k - \frac{1}{2} \sum_{i,k,l} V_{k,l}^{i,\kappa} b_i^\dagger b_k b_l b_\beta^\dagger + \frac{1}{2} \sum_{i,j,k} V_{k,\beta}^{i,j} b_i^\dagger b_j^\dagger b_k b_\kappa + A_2 \\ &= \sum_{j,l} \left(V_{\beta,l}^{\kappa,j} - V_{\beta,l}^{j,\kappa} \right) b_j^\dagger b_l + \frac{1}{2} \sum_{i,j,l} \left(V_{l,\beta}^{i,j} - V_{\beta,l}^{i,j} \right) b_i^\dagger b_j^\dagger b_l b_\kappa \\ &\quad + \frac{1}{2} \sum_{j,k,l} \left(V_{k,l}^{\kappa,j} - V_{k,l}^{j,\kappa} \right) b_j^\dagger b_k b_l b_\beta^\dagger \; + A_2 \,. \end{aligned} \tag{B.3.50}$$

$$\left[b_\kappa b_\beta^\dagger, \hat{H}_C^{hh}\right] = \sum_{j,l}\left(V_{\beta,l}^{\kappa,j} - V_{\beta,l}^{j,\kappa}\right) b_j^\dagger b_l + \frac{1}{2}\sum_{i,j,l}\left(V_{l,\beta}^{i,j} - V_{\beta,l}^{i,j}\right) b_i^\dagger b_j^\dagger b_l b_\kappa + \frac{1}{2}\sum_{j,k,l}\left(V_{k,l}^{\kappa,j} - V_{k,l}^{j,\kappa}\right) b_j^\dagger b_k b_l b_\beta^\dagger \ . \quad \text{(B.3.51)}$$

$\underline{\left[b_\kappa b_\beta^\dagger, \hat{H}_C^{eh}\right]}$:

$$\left[b_\kappa b_\beta^\dagger, \hat{H}_C^{eh}\right] = b_\kappa b_\beta^\dagger \hat{H}_C^{eh} - \hat{H}_C^{eh} b_\kappa b_\beta^\dagger = A_1 - A_2 \, . \quad \text{(B.3.52)}$$

$$\begin{aligned} A_1 &= b_\kappa b_\beta^\dagger \left(-\sum_{i,j,k,l} V_{kl}^{ij} a_i^\dagger b_j^\dagger b_k a_l\right) = -\sum_{i,j,k,l} V_{kl}^{ij} b_\kappa b_\beta^\dagger a_i^\dagger b_j^\dagger b_k a_l \\ &= \sum_{i,j,k,l} V_{kl}^{ij} a_i^\dagger \left(\delta_{\kappa,j} - b_j^\dagger b_\kappa\right)\left(\delta_{\beta,k} - b_k b_\beta^\dagger\right) a_l \\ &= \sum_{i,j,k,l} V_{kl}^{ij}\left[\delta_{\kappa,j}\delta_{\beta,k} a_i^\dagger a_l - \delta_{\kappa,j} a_i^\dagger b_k b_\beta^\dagger a_l - \delta_{\beta,k} a_i^\dagger b_j^\dagger b_\kappa a_l + a_i^\dagger b_j^\dagger b_\kappa b_k b_\beta^\dagger a_l\right] \\ &= \sum_{i,l} V_{\beta,l}^{i,\kappa} a_i^\dagger a_l + \sum_{i,k,l} V_{k,l}^{i,\kappa} a_i^\dagger b_k a_l b_\beta^\dagger + \sum_{i,j,l} V_{\beta,l}^{i,j} a_i^\dagger b_j^\dagger a_l b_\kappa + A_2 \, . \end{aligned} \quad \text{(B.3.53)}$$

$$\left[b_\kappa b_\beta^\dagger, \hat{H}_C^{eh}\right] = \sum_{i,l} V_{\beta,l}^{i,\kappa} a_i^\dagger a_l + \sum_{i,k,l} V_{k,l}^{i,\kappa} a_i^\dagger b_k a_l b_\beta^\dagger + \sum_{i,j,l} V_{\beta,l}^{i,j} a_i^\dagger b_j^\dagger a_l b_\kappa \, . \quad \text{(B.3.54)}$$

Collecting all terms and taking the expectation value

$$\begin{aligned} i\hbar\frac{\partial \tilde{P}_{\beta,\kappa}}{\partial t} &= (\epsilon_\kappa - \epsilon_\beta)\langle b_\kappa b_\beta^\dagger\rangle \\ &+ \left(-\sum_{m'} \mu_{\beta m'}\langle b_\kappa b_{m'}^\dagger\rangle + \sum_m \mu_{m\kappa}\langle b_m b_\beta^\dagger\rangle \right. \\ &\left. + \sum_n \mu_{n\kappa}\langle a_n^\dagger b_\beta^\dagger\rangle - \sum_n \mu_{n\beta}^*\langle b_\kappa a_n\rangle\right) E(t) \\ &+ \sum_{j,l}\left(V_{\beta,l}^{\kappa,j} - V_{\beta,l}^{j,\kappa}\right)\langle b_j^\dagger b_l\rangle + \frac{1}{2}\sum_{i,j,l}\left(V_{l,\beta}^{i,j} - V_{\beta,l}^{i,j}\right)\langle b_i^\dagger b_j^\dagger b_l b_\kappa\rangle \\ &+ \frac{1}{2}\sum_{j,k,l}\left(V_{k,l}^{\kappa,j} - V_{k,l}^{j,\kappa}\right)\langle b_j^\dagger b_k b_l b_\beta^\dagger \rangle + \sum_{i,l} V_{\beta,l}^{i,\kappa}\langle a_i^\dagger a_l\rangle \\ &+ \sum_{i,k,l} V_{k,l}^{i,\kappa}\langle a_i^\dagger b_k a_l b_\beta^\dagger\rangle + \sum_{i,j,l} V_{\beta,l}^{i,j}\langle a_i^\dagger b_j^\dagger a_l b_\kappa\rangle \, . \end{aligned} \quad \text{(B.3.55)}$$

Hartree-Fock limit

$\underline{\langle\left[b_\kappa b_\beta^\dagger, \hat{H}_C^{hh}\right]\rangle_{HF}}$:

$$\sum_{j,l}\left(V_{\beta,l}^{\kappa,j}-V_{\beta,l}^{j,\kappa}\right)\langle b_j^\dagger b_l\rangle+\frac{1}{2}\sum_{i,j,l}\left(V_{l,\beta}^{i,j}-V_{\beta,l}^{i,j}\right)\langle b_i^\dagger b_j^\dagger b_l b_\kappa\rangle$$
$$+\frac{1}{2}\sum_{j,k,l}\left(V_{k,l}^{\kappa,j}-V_{k,l}^{j,\kappa}\right)\langle b_j^\dagger b_k b_l b_\beta^\dagger\,\rangle\simeq: \qquad \text{(B.3.56)}$$

$$\begin{aligned}
\simeq\;& \sum_{j,l}\left(V_{\beta,l}^{\kappa,j}-V_{\beta,l}^{j,\kappa}\right)\langle b_j^\dagger b_l\rangle+\frac{1}{2}\sum_{i,j,l}\left(V_{l,\beta}^{i,j}-V_{\beta,l}^{i,j}\right)\left(\langle b_i^\dagger b_\kappa\rangle\langle b_j^\dagger b_l\rangle-\langle b_i^\dagger b_l\rangle\langle b_j^\dagger b_\kappa\rangle\right)\\
&+\frac{1}{2}\sum_{j,k,l}\left(V_{k,l}^{\kappa,j}-V_{k,l}^{j,\kappa}\right)\left(\langle b_j^\dagger b_k\rangle\langle b_l b_\beta^\dagger\rangle-\langle b_j^\dagger b_l\rangle\langle b_k b_\beta^\dagger\rangle\right)\\
=\;& \sum_{j,l}\left(V_{\beta,l}^{\kappa,j}-V_{\beta,l}^{j,\kappa}\right)\langle b_j^\dagger b_l\rangle+\sum_{i,j,l}\left(V_{l,\beta}^{i,j}-V_{\beta,l}^{i,j}\right)\langle b_i^\dagger b_\kappa\rangle\langle b_j^\dagger b_l\rangle\\
&+\sum_{j,k,l}\left(V_{k,l}^{\kappa,j}-V_{k,l}^{j,\kappa}\right)\langle b_j^\dagger b_k\rangle\langle b_l b_\beta^\dagger\rangle\\
=\;& \sum_{j,l}\left(V_{\beta,l}^{\kappa,j}-V_{\beta,l}^{j,\kappa}\right)\langle b_j^\dagger b_l\rangle+\sum_{i,j,l}\left(V_{l,\beta}^{i,j}-V_{\beta,l}^{i,j}\right)\langle b_i^\dagger b_\kappa\rangle\langle b_j^\dagger b_l\rangle\\
&+\sum_{j,k,l}\left(V_{k,l}^{\kappa,j}-V_{k,l}^{j,\kappa}\right)\langle b_j^\dagger b_k\rangle\left(\delta_{\beta,l}-\langle b_\beta^\dagger b_l\rangle\right)\\
=\;& \sum_{i,j,l}\left(V_{l,\beta}^{i,j}-V_{\beta,l}^{i,j}\right)\langle b_i^\dagger b_\kappa\rangle\langle b_j^\dagger b_l\rangle-\sum_{j,k,l}\left(V_{k,l}^{\kappa,j}-V_{k,l}^{j,\kappa}\right)\langle b_j^\dagger b_k\rangle\langle b_\beta^\dagger b_l\rangle\,. \qquad \text{(B.3.57)}
\end{aligned}$$

$\underline{\langle\left[b_\kappa b_\beta^\dagger, \hat{H}_C^{eh}\right]\rangle_{HF}}$:

$$\sum_{i,l}V_{\beta,l}^{i,\kappa}\langle a_i^\dagger a_l\rangle+\sum_{i,k,l}V_{k,l}^{i,\kappa}\langle a_i^\dagger b_k a_l b_\beta^\dagger\rangle+\sum_{i,j,l}V_{\beta,l}^{i,j}\langle a_i^\dagger b_j^\dagger a_l b_\kappa\rangle\;\simeq\;: \qquad \text{(B.3.58)}$$

$$\begin{aligned}
\simeq\;& \sum_{i,l}V_{\beta,l}^{i,\kappa}\langle a_i^\dagger a_l\rangle+\sum_{i,k,l}V_{k,l}^{i,\kappa}\left(\langle a_i^\dagger b_\beta^\dagger\rangle\langle b_k a_l\rangle-\langle a_i^\dagger a_l\rangle\langle b_k b_\beta^\dagger\rangle\right)\\
&+\sum_{i,j,l}V_{\beta,l}^{i,j}\left(\langle a_i^\dagger b_j^\dagger\rangle\langle a_l b_\kappa\rangle-\langle a_i^\dagger a_l\rangle\langle b_j^\dagger b_\kappa\rangle\right)\\
=\;& \sum_{i,k,l}V_{k,l}^{i,\kappa}\left(\langle a_i^\dagger b_\beta^\dagger\rangle\langle b_k a_l\rangle+\langle a_i^\dagger a_l\rangle\langle b_\beta^\dagger b_k\rangle\right)\\
&+\sum_{i,j,l}V_{\beta,l}^{i,j}\left(\langle a_i^\dagger b_j^\dagger\rangle\langle a_l b_\kappa\rangle-\langle a_i^\dagger a_l\rangle\langle b_j^\dagger b_\kappa\rangle\right)\,. \qquad \text{(B.3.59)}
\end{aligned}$$

The full expression in the Hartree-Fock limit becomes

$$
\begin{aligned}
i\hbar\frac{\partial \tilde{P}_{\beta,\kappa}}{\partial t} &= (\epsilon_\kappa - \epsilon_\beta)\,\langle b_\kappa b_\beta^\dagger\rangle \\
&+ \left(-\sum_{m'} \mu_{\beta m'}\langle b_\kappa b_{m'}^\dagger\rangle + \sum_m \mu_{m\kappa}\langle b_m b_\beta^\dagger\rangle \right. \\
&\left. + \sum_n \mu_{n\kappa}\langle a_n^\dagger b_\beta^\dagger\rangle - \sum_n \mu_{n\beta}^*\langle b_\kappa a_n\rangle \right) E(t) \\
&+ \sum_{i,j,l} \left(V_{l,\beta}^{i,j} - V_{\beta,l}^{i,j} \right) \langle b_i^\dagger b_\kappa\rangle\langle b_j^\dagger b_l\rangle - \sum_{j,k,l} \left(V_{k,l}^{\kappa,j} - V_{k,l}^{j,\kappa} \right) \langle b_j^\dagger b_k\rangle\langle b_\beta^\dagger b_l\rangle \\
&+ \sum_{i,k,l} V_{k,l}^{i,\kappa} \left(\langle a_i^\dagger b_\beta^\dagger\rangle\langle b_k a_l\rangle + \langle a_i^\dagger a_l\rangle\langle b_\beta^\dagger b_k\rangle \right) \\
&+ \sum_{i,j,l} V_{\beta,l}^{i,j} \left(\langle a_i^\dagger b_j^\dagger\rangle\langle a_l b_\kappa\rangle - \langle a_i^\dagger a_l\rangle\langle b_j^\dagger b_\kappa\rangle \right) \\
&+ i\hbar \left.\frac{\partial \tilde{P}_{\beta,\kappa}}{\partial t}\right|_{scatt} . \qquad \text{(B.3.60)}
\end{aligned}
$$

We write this expression in terms of polarizations and populations

$$
\begin{aligned}
i\hbar\frac{\partial\tilde{P}_{\beta,\kappa}}{\partial t} &= (\epsilon_\kappa-\epsilon_\beta)\,\tilde{P}_{\beta,\kappa} \\
&+\left(-\sum_{m\neq\kappa,\beta}\mu_{\beta m}\tilde{P}_{m,\kappa}+\sum_{m\neq\kappa,\beta}\mu_{m\kappa}\tilde{P}_{\beta,m}+\mu_{\beta\kappa}(n^h_\kappa-n^h_\beta)\right. \\
&\left.+\sum_n\mu_{n\kappa}P_{\beta,n}-\sum_n\mu^*_{n\beta}P_{n,\kappa}\right)E(t) \\
&+\sum_j\left(V^{\kappa,j}_{j,\beta}-V^{\kappa,j}_{\beta,j}\right)n^h_\kappa n^h_j-\sum_{\substack{i,j\\ i\neq\kappa}}\left(V^{i,j}_{j,\beta}-V^{i,j}_{\beta,j}\right)\tilde{P}_{i,\kappa}n^h_j \\
&+\sum_{\substack{i,j,l\\ i\neq\kappa,l\neq j}}\left(V^{i,j}_{l,\beta}-V^{i,j}_{\beta,l}\right)\tilde{P}_{i,\kappa}\tilde{P}_{j,l}-\sum_{\substack{j,l\\ l\neq j}}\left(V^{\kappa,j}_{l,\beta}-V^{\kappa,j}_{\beta,l}\right)n^h_\kappa\tilde{P}_{j,l} \\
&-\sum_j\left(V^{\kappa,j}_{j,\beta}-V^{j,\kappa}_{j,\beta}\right)n^h_\beta n^h_j+\sum_{\substack{j,l\\ l\neq\beta}}\left(V^{\kappa,j}_{j,l}-V^{j,\kappa}_{j,l}\right)\tilde{P}_{\beta,l}n^h_j \\
&-\sum_{\substack{j,k,l\\ j\neq k,l\neq\beta}}\left(V^{\kappa,j}_{k,l}-V^{j,\kappa}_{k,l}\right)\tilde{P}_{\beta,l}\tilde{P}_{j,k}+\sum_{\substack{j,k\\ j\neq k}}\left(V^{\kappa,j}_{k,\beta}-V^{j,\kappa}_{k,\beta}\right)n^h_\beta\tilde{P}_{j,k} \\
&+\sum_{n,n',m}V^{n,\kappa}_{m,n'}P_{\beta,n}P_{n',m}+\sum_i V^{i,\kappa}_{\beta,i}n^h_\beta n^e_i-\sum_{\substack{i,k\\ k\neq\beta}}V^{i,\kappa}_{k,i}\tilde{P}_{\beta,k}n^e_i \\
&+\sum_{\substack{i,l\\ l\neq i}}V^{i,\kappa}_{\beta,l}n^h_\beta\bar{P}_{l,i}-\sum_{\substack{i,k,l\\ k\neq\beta,l\neq i}}V^{i,\kappa}_{k,l}\tilde{P}_{\beta,k}\bar{P}_{l,i} \\
&-\sum_{n,n',m}V^{n,m}_{\beta,n'}P_{m,n}P_{n',\kappa}-\sum_i V^{i,\kappa}_{\beta,i}n^h_\kappa n^e_i+\sum_{\substack{i,j\\ j\neq\kappa}}V^{i,j}_{\beta,i}\tilde{P}_{j,\kappa}n^e_i \\
&-\sum_{\substack{i,l\\ l\neq i}}V^{i,\kappa}_{\beta,l}n^h_\kappa\bar{P}_{l,i}+\sum_{\substack{i,j,l\\ j\neq\kappa,l\neq i}}V^{i,j}_{\beta,l}\tilde{P}_{j,\kappa}\bar{P}_{l,i} \\
&+i\hbar\left.\frac{\partial\tilde{P}_{\beta,\kappa}}{\partial t}\right|_{scatt}. \qquad \text{(B.3.61)}
\end{aligned}
$$

where we used the definition $\langle a^\dagger_n b^\dagger_m\rangle\equiv P_{m,n}$.

B.3.3 Intraband electron-electron polarization: $\bar{P}_{\alpha,\gamma}$

$\underline{\bar{P}_{\alpha,\gamma} = \langle a_\gamma^\dagger a_\alpha \rangle}$.

$$\begin{aligned}\frac{\partial \bar{P}_{\alpha,\gamma}}{\partial t} &= -\frac{i}{\hbar}\left\langle \left[a_\gamma^\dagger a_\alpha, \hat{H}\right]\right\rangle \\ &= -\frac{i}{\hbar}\left\langle \left[a_\gamma^\dagger a_\alpha, \hat{H}_0\right] + \left[a_\gamma^\dagger a_\alpha, \hat{H}_{c-f}\right] + \left[a_\gamma^\dagger a_\alpha, \hat{H}_C\right]\right\rangle . \end{aligned} \tag{B.3.62}$$

$\underline{\left[a_\gamma^\dagger a_\alpha, \hat{H}_0\right]}$:

$$\left[a_\gamma^\dagger a_\alpha, \hat{H}_0\right] = a_\gamma^\dagger a_\alpha \hat{H}_0 - \hat{H}_0 a_\gamma^\dagger a_\alpha = A_1 - A_2 . \tag{B.3.63}$$

$$\begin{aligned} A_1 &= a_\gamma^\dagger a_\alpha \left(\sum_n \epsilon_n a_n^\dagger a_n + \sum_m \epsilon_m b_m^\dagger b_m\right) \\ &= \sum_n \epsilon_n a_\gamma^\dagger \left(\delta_{\alpha,n} - a_n^\dagger a_\alpha\right) a_n + \sum_m \epsilon_m b_m^\dagger b_m a_\gamma^\dagger a_\alpha \\ &= \sum_n \epsilon_n \left(\delta_{\alpha,n} a_\gamma^\dagger a_n - a_n^\dagger \left(\delta_{\gamma,n} - a_n a_\gamma^\dagger\right) a_\alpha\right) + \sum_m \epsilon_m b_m^\dagger b_m a_\gamma^\dagger a_\alpha \\ &= \epsilon_\alpha a_\gamma^\dagger a_\alpha - \epsilon_\gamma a_\gamma^\dagger a_\alpha + \sum_n \epsilon_n a_n^\dagger a_n a_\gamma^\dagger a_\alpha + \sum_m \epsilon_m b_m^\dagger b_m a_\gamma^\dagger a_\alpha \\ &= \epsilon_\alpha a_\gamma^\dagger a_\alpha - \epsilon_\gamma a_\gamma^\dagger a_\alpha + A_2 . \end{aligned} \tag{B.3.64}$$

$$\left[a_\gamma^\dagger a_\alpha, \hat{H}_0\right] = \left(\epsilon_\alpha - \epsilon_\gamma\right) a_\gamma^\dagger a_\alpha . \tag{B.3.65}$$

$\underline{\left[a_\gamma^\dagger a_\alpha, \hat{H}_{c-f}\right]}$:

$$\left[a_\gamma^\dagger a_\alpha, \hat{H}_{c-f}\right] = a_\gamma^\dagger a_\alpha \hat{H}_{c-f} - \hat{H}_{c-f} a_\gamma^\dagger a_\alpha = A_1 - A_2 . \tag{B.3.66}$$

$$
\begin{aligned}
A_1 &= -a_\gamma^\dagger a_\alpha \left[\sum_{n,n'} \mu_{nn'} a_n^\dagger a_{n'} + \sum_{m,m'} \mu_{mm'} b_m b_{m'}^\dagger \right. \\
&\quad \left. + \sum_{n,m} \left(\mu_{nm} a_n^\dagger b_m^\dagger + \mu_{nm}^* b_m a_n \right) \right] E(t) \\
&= \left[-\sum_{n,n'} \mu_{nn'} a_\gamma^\dagger \left(\delta_{\alpha,n} - a_n^\dagger a_\alpha \right) a_{n'} - \sum_{m,m'} \mu_{mm'} b_m b_{m'}^\dagger a_\gamma^\dagger a_\alpha \right. \\
&\quad \left. - \sum_{n,m} \left(\mu_{nm} a_\gamma^\dagger \left(\delta_{\alpha,n} - a_n^\dagger a_\alpha \right) b_m^\dagger - \mu_{nm}^* b_m \left(\delta_{\gamma,n} - a_n a_\gamma^\dagger \right) a_\alpha \right) \right] E(t) \\
&= \left[-\sum_{n'} \mu_{\alpha n'} a_\gamma^\dagger a_{n'} + \sum_{n,n'} \mu_{nn'} a_n^\dagger \left(\delta_{\gamma,n'} - a_{n'} a_\gamma^\dagger \right) a_\alpha - \sum_{m,m'} \mu_{mm'} b_m b_{m'}^\dagger a_\gamma^\dagger a_\alpha \right. \\
&\quad \left. - \sum_{m} \mu_{\alpha m} a_\gamma^\dagger b_m^\dagger - \sum_{n,m} \mu_{nm} a_n^\dagger b_m^\dagger a_\gamma^\dagger a_\alpha + \sum_{m} \mu_{\gamma m}^* b_m a_\alpha - \sum_{nm} \mu_{nm}^* b_m a_n a_\gamma^\dagger a_\alpha \right] E(t) \\
&= \left[-\sum_{n'} \mu_{\alpha n'} a_\gamma^\dagger a_{n'} + \sum_{n} \mu_{n\gamma} a_n^\dagger a_\alpha \right. \\
&\quad \left. - \sum_{m} \mu_{\alpha m} a_\gamma^\dagger b_m^\dagger + \sum_{m} \mu_{\gamma m}^* b_m a_\alpha \right] E(t) + A_2 \,. \qquad \text{(B.3.67)}
\end{aligned}
$$

$$
\begin{aligned}
\left[a_\gamma^\dagger a_\alpha, \hat{H}_{c-f} \right] &= \left[-\sum_{n'} \mu_{\alpha n'} a_\gamma^\dagger a_{n'} + \sum_{n} \mu_{n\gamma} a_n^\dagger a_\alpha \right. \\
&\quad \left. - \sum_{m} \mu_{\alpha m} a_\gamma^\dagger b_m^\dagger + \sum_{m} \mu_{\gamma m}^* b_m a_\alpha \right] E(t) \,. \qquad \text{(B.3.68)}
\end{aligned}
$$

$\underline{\left[a_\gamma^\dagger a_\alpha, \hat{H}_C \right]}$:

$$
\left[a_\gamma^\dagger a_\alpha, \hat{H}_C \right] = \left[a_\gamma^\dagger a_\alpha, \hat{H}_C^{ee} + \hat{H}_C^{hh} + \hat{H}_C^{eh} \right] . \qquad \text{(B.3.69)}
$$

$\underline{\left[a_\gamma^\dagger a_\alpha, \hat{H}_C^{ee} \right]}$:

$$
\left[a_\gamma^\dagger a_\alpha, \hat{H}_C^{ee} \right] = a_\gamma^\dagger a_\alpha \hat{H}_C^{ee} - \hat{H}_C^{ee} a_\gamma^\dagger a_\alpha \,. \qquad \text{(B.3.70)}
$$

We here use the result from eq. (B.3.50) by switching to electron operators, while changing sign overall and letting $\beta \to \gamma$ and $\kappa \to \alpha$

$$
\begin{aligned}
\left[a_\gamma^\dagger a_\alpha, \hat{H}_C^{ee} \right] &= -\sum_{j,l} \left(V_{\gamma,l}^{\alpha,j} - V_{\gamma,l}^{j,\alpha} \right) a_j^\dagger a_l - \frac{1}{2} \sum_{i,j,l} \left(V_{l,\gamma}^{i,j} - V_{\gamma,l}^{i,j} \right) a_i^\dagger a_j^\dagger a_l a_\alpha \\
&\quad - \frac{1}{2} \sum_{j,k,l} \left(V_{k,l}^{\alpha,j} - V_{k,l}^{j,\alpha} \right) a_j^\dagger a_k a_l a_\gamma^\dagger \,. \qquad \text{(B.3.71)}
\end{aligned}
$$

$\underline{\left[a^\dagger_\gamma a_\alpha, \hat{H}^{hh}_C\right]}$:

$$\left[a^\dagger_\gamma a_\alpha, \hat{H}^{hh}_C\right] = 0\,. \tag{B.3.72}$$

The result follows from the similar calculation for hole-hole polarization.

$\underline{\left[a^\dagger_\gamma a_\alpha, \hat{H}^{eh}_C\right]}$:

$$\left[a^\dagger_\gamma a_\alpha, \hat{H}^{eh}_C\right] = a^\dagger_\gamma a_\alpha \hat{H}^{eh}_C - \hat{H}^{eh}_C a^\dagger_\gamma a_\alpha = A_1 - A_2\,. \tag{B.3.73}$$

$$\begin{aligned}
A_1 =& a^\dagger_\gamma a_\alpha \left(- \sum_{i,j,k,l} V^{ij}_{kl} a^\dagger_i b^\dagger_j b_k a_l \right) = - \sum_{i,j,k,l} V^{ij}_{kl} a^\dagger_\gamma a_\alpha a^\dagger_i b^\dagger_j b_k a_l \\
=& - \sum_{i,j,k,l} V^{ij}_{kl} a^\dagger_\gamma \left(\delta_{\alpha,i} - a^\dagger_i a_\alpha\right) b^\dagger_j b_k a_l \\
=& - \sum_{i,j,k,l} V^{ij}_{kl} \delta_{\alpha,i} a^\dagger_\gamma b^\dagger_j b_k a_l + \sum_{i,j,k,l} V^{ij}_{kl} a^\dagger_\gamma a^\dagger_i a_\alpha b^\dagger_j b_k a_l \\
=& - \sum_{i,j,k,l} V^{ij}_{kl} \delta_{\alpha,i} b^\dagger_j b_k \left(\delta_{\gamma,l} - a_l a^\dagger_\gamma\right) + \sum_{i,j,k,l} V^{ij}_{kl} a^\dagger_i b^\dagger_j b_k \left(\delta_{\gamma,l} - a_l a^\dagger_\gamma\right) a_\alpha \\
=& - \sum_{j,k} V^{\alpha,j}_{k,\gamma} b^\dagger_j b_k + \sum_{j,k,l} V^{\alpha,j}_{k,l} b^\dagger_j b_k a_l a^\dagger_\gamma + \sum_{i,j,k} V^{i,j}_{k,\gamma} a^\dagger_i b^\dagger_j b_k a_\alpha + A_2\,.
\end{aligned} \tag{B.3.74}$$

$$\left[a^\dagger_\gamma a_\alpha, \hat{H}^{eh}_C\right] = - \sum_{j,k} V^{\alpha,j}_{k,\gamma} b^\dagger_j b_k + \sum_{j,k,l} V^{\alpha,j}_{k,l} b^\dagger_j b_k a_l a^\dagger_\gamma + \sum_{i,j,k} V^{i,j}_{k,\gamma} a^\dagger_i b^\dagger_j b_k a_\alpha\,. \tag{B.3.75}$$

Collecting terms we end up with

$$\begin{aligned}
i\hbar \frac{\partial \bar{P}_{\alpha,\gamma}}{\partial t} \quad = \quad & (\epsilon_\alpha - \epsilon_\gamma) \langle a^\dagger_\gamma a_\alpha \rangle \\
& \left[- \sum_{n'} \mu_{\alpha n'} \langle a^\dagger_\gamma a_{n'} \rangle + \sum_n \mu_{n\gamma} \langle a^\dagger_n a_\alpha \rangle \right. \\
& \left. - \sum_m \mu_{\alpha m} \langle a^\dagger_\gamma b^\dagger_m \rangle + \sum_m \mu^*_{\gamma m} \langle b_m a_\alpha \rangle \right] E(t) \\
& - \sum_{j,l} \left(V^{\alpha,j}_{\gamma,l} - V^{j,\alpha}_{\gamma,l} \right) \langle a^\dagger_j a_l \rangle - \frac{1}{2} \sum_{i,j,l} \left(V^{i,j}_{l,\gamma} - V^{i,j}_{\gamma,l} \right) \langle a^\dagger_i a^\dagger_j a_l a_\alpha \rangle \\
& - \frac{1}{2} \sum_{j,k,l} \left(V^{\alpha,j}_{k,l} - V^{j,\alpha}_{k,l} \right) \langle a^\dagger_j a_k a_l a^\dagger_\gamma \rangle - \sum_{j,k} V^{\alpha,j}_{k,\gamma} \langle b^\dagger_j b_k \rangle \\
& + \sum_{j,k,l} V^{\alpha,j}_{k,l} \langle b^\dagger_j b_k a_l a^\dagger_\gamma \rangle + \sum_{i,j,k} V^{i,j}_{k,\gamma} \langle a^\dagger_i b^\dagger_j b_k a_\alpha \rangle\,.
\end{aligned} \tag{B.3.76}$$

Hartree-Fock limit

$\underline{\langle\left[a_\gamma^\dagger a_\alpha, \hat{H}_C^{ee}\right]\rangle_{HF}}$:

$$
\begin{aligned}
&-\sum_{j,l}\left(V_{\gamma,l}^{\alpha,j}-V_{\gamma,l}^{j,\alpha}\right)\langle a_j^\dagger a_l\rangle-\frac{1}{2}\sum_{i,j,l}\left(V_{l,\gamma}^{i,j}-V_{\gamma,l}^{i,j}\right)\langle a_i^\dagger a_j^\dagger a_l a_\alpha\rangle\\
&-\frac{1}{2}\sum_{j,k,l}\left(V_{k,l}^{\alpha,j}-V_{k,l}^{j,\alpha}\right)\langle a_j^\dagger a_k a_l a_\gamma^\dagger\,\rangle\simeq: \qquad \text{(B.3.77)}
\end{aligned}
$$

$$
\begin{aligned}
\simeq\;& -\sum_{j,l}\left(V_{\gamma,l}^{\alpha,j}-V_{\gamma,l}^{j,\alpha}\right)\langle a_j^\dagger a_l\rangle-\frac{1}{2}\sum_{i,j,l}\left(V_{l,\gamma}^{i,j}-V_{\gamma,l}^{i,j}\right)\left(\langle a_i^\dagger a_\alpha\rangle\langle a_j^\dagger a_l\rangle-\langle a_i^\dagger a_l\rangle\langle a_j^\dagger a_\alpha\rangle\right)\\
&-\frac{1}{2}\sum_{j,k,l}\left(V_{k,l}^{\alpha,j}-V_{k,l}^{j,\alpha}\right)\left(\langle a_j^\dagger a_k\rangle\langle a_l a_\gamma^\dagger\rangle-\langle a_j^\dagger a_l\rangle\langle a_k a_\gamma^\dagger\rangle\right)\\
=\;& -\sum_{j,l}\left(V_{\gamma,l}^{\alpha,j}-V_{\gamma,l}^{j,\alpha}\right)\langle a_j^\dagger a_l\rangle-\sum_{i,j,l}\left(V_{l,\gamma}^{i,j}-V_{\gamma,l}^{i,j}\right)\langle a_i^\dagger a_\alpha\rangle\langle a_j^\dagger a_l\rangle\\
&-\sum_{j,k,l}\left(V_{k,l}^{\alpha,j}-V_{k,l}^{j,\alpha}\right)\langle a_j^\dagger a_k\rangle\langle a_l a_\gamma^\dagger\rangle\\
=\;& -\sum_{i,j,l}\left(V_{l,\gamma}^{i,j}-V_{\gamma,l}^{i,j}\right)\langle a_i^\dagger a_\alpha\rangle\langle a_j^\dagger a_l\rangle+\sum_{j,k,l}\left(V_{k,l}^{\alpha,j}-V_{k,l}^{j,\alpha}\right)\langle a_j^\dagger a_k\rangle\langle a_\gamma^\dagger a_l\rangle\,. \qquad \text{(B.3.78)}
\end{aligned}
$$

$\underline{\langle\left[a_\gamma^\dagger a_\alpha, \hat{H}_C^{eh}\right]\rangle_{HF}}$:

$$
-\sum_{j,k}V_{k,\gamma}^{\alpha,j}\langle b_j^\dagger b_k\rangle+\sum_{j,k,l}V_{k,l}^{\alpha,j}\langle b_j^\dagger b_k a_l a_\gamma^\dagger\rangle+\sum_{i,j,k}V_{k,\gamma}^{i,j}\langle a_i^\dagger b_j^\dagger b_k a_\alpha\rangle\simeq: \qquad \text{(B.3.79)}
$$

$$
\begin{aligned}
\simeq\;& -\sum_{j,k}V_{k,\gamma}^{\alpha,j}\langle b_j^\dagger b_k\rangle+\sum_{i,j,k,l}V_{k,l}^{\alpha,j}\left(\langle b_j^\dagger b_k\rangle\langle a_l a_\gamma^\dagger\rangle+\langle b_j^\dagger a_\gamma^\dagger\rangle\langle b_k a_l\rangle\right)\\
&+\sum_{i,j,k}V_{k,\gamma}^{i,j}\left(\langle a_i^\dagger b_j^\dagger\rangle\langle b_k a_\alpha\rangle+\langle a_i^\dagger a_\alpha\rangle\langle b_j^\dagger b_k\rangle\right)\\
=\;& \sum_{j,k,l}V_{k,l}^{\alpha,j}\left(\langle b_j^\dagger a_\gamma^\dagger\rangle\langle b_k a_l\rangle-\langle b_j^\dagger b_k\rangle\langle a_\gamma^\dagger a_l\rangle\right)\\
&+\sum_{i,j,k}V_{k,\gamma}^{i,j}\left(\langle a_i^\dagger b_j^\dagger\rangle\langle b_k a_\alpha\rangle+\langle a_i^\dagger a_\alpha\rangle\langle b_j^\dagger b_k\rangle\right)\,. \qquad \text{(B.3.80)}
\end{aligned}
$$

The equation of motion for $\bar{P}_{\alpha,\gamma}$ becomes

$$
\begin{aligned}
i\hbar\frac{\partial \bar{P}_{\alpha,\gamma}}{\partial t} &= (\epsilon_\alpha - \epsilon_\gamma)\,\langle a_\gamma^\dagger a_\alpha\rangle \\
&\quad \Bigg[-\sum_{n'}\mu_{\alpha n'}\langle a_\gamma^\dagger a_{n'}\rangle + \sum_{n}\mu_{n\gamma}\langle a_n^\dagger a_\alpha\rangle \\
&\quad -\sum_{m}\mu_{\alpha m}\langle a_\gamma^\dagger b_m^\dagger\rangle + \sum_{m}\mu_{\gamma m}^*\langle b_m a_\alpha\rangle\Bigg]\,E(t) \\
&\quad -\sum_{i,j,l}\left(V_{l,\gamma}^{i,j} - V_{\gamma,l}^{i,j}\right)\langle a_i^\dagger a_\alpha\rangle\langle a_j^\dagger a_l\rangle + \sum_{j,k,l}\left(V_{k,l}^{\alpha,j} - V_{k,l}^{j,\alpha}\right)\langle a_j^\dagger a_k\rangle\langle a_\gamma^\dagger a_l\rangle \\
&\quad +\sum_{j,k,l}V_{k,l}^{\alpha,j}\left(\langle b_j^\dagger a_\gamma^\dagger\rangle\langle b_k a_l\rangle - \langle b_j^\dagger b_k\rangle\langle a_\gamma^\dagger a_l\rangle\right) \\
&\quad +\sum_{i,j,k}V_{k,\gamma}^{i,j}\left(\langle a_i^\dagger b_j^\dagger\rangle\langle b_k a_\alpha\rangle + \langle a_i^\dagger a_\alpha\rangle\langle b_j^\dagger b_k\rangle\right) \\
&\quad +i\hbar\left.\frac{\partial \tilde{P}_{\alpha,\gamma}}{\partial t}\right|_{scatt}. \qquad \text{(B.3.81)}
\end{aligned}
$$

In terms of populations and polarizations

$$
\begin{aligned}
i\hbar\frac{\partial \bar{P}_{\alpha,\gamma}}{\partial t} &= (\epsilon_\alpha - \epsilon_\gamma)\,\bar{P}_{\alpha,\gamma} \\
&\quad \Bigg[- \sum_{n\neq\alpha,\gamma} \mu_{\alpha n}\bar{P}_{n,\gamma} + \sum_{n\neq\alpha,\gamma} \mu_{n\gamma}\bar{P}_{\alpha,n} + \mu_{\alpha\gamma}\left(n^e_\alpha - n^e_\gamma\right) \\
&\quad - \sum_m \mu_{\alpha m}P_{m,\gamma} + \sum_m \mu^*_{\gamma m}P_{\alpha,m} \Bigg] E(t) \\
&\quad - \sum_j \left(V^{\alpha,j}_{j,\gamma} - V^{\alpha,j}_{\gamma,j}\right) n^e_\alpha n^e_j - \sum_{\substack{j,l \\ l\neq j}} \left(V^{\alpha,j}_{l,\gamma} - V^{\alpha,j}_{\gamma,l}\right) n^e_\alpha \bar{P}_{l,j} - \sum_{\substack{i,j \\ i\neq\alpha}} \left(V^{i,j}_{j,\gamma} - V^{i,j}_{\gamma,j}\right) \bar{P}_{\alpha,i} n^e_j \\
&\quad - \sum_{\substack{i,j,l \\ i\neq\alpha, l\neq j}} \left(V^{i,j}_{l,\gamma} - V^{i,j}_{\gamma,l}\right) \bar{P}_{\alpha,i}\bar{P}_{l,j} + \sum_j \left(V^{\alpha,j}_{j,\gamma} - V^{j,\alpha}_{j,\gamma}\right) n^e_\gamma n^e_j + \sum_{\substack{j,k \\ k\neq j}} \left(V^{\alpha,j}_{k,\gamma} - V^{j,\alpha}_{k,\gamma}\right) n^e_\gamma \bar{P}_{k,j} \\
&\quad + \sum_{\substack{j,l \\ l\neq\gamma}} \left(V^{\alpha,j}_{j,l} - V^{j,\alpha}_{j,l}\right) \bar{P}_{l,\gamma} n^e_j + \sum_{\substack{j,k,l \\ k\neq j, l\neq\gamma}} \left(V^{\alpha,j}_{k,l} - V^{j,\alpha}_{k,l}\right) \bar{P}_{l,\gamma}\bar{P}_{k,j} - \sum_{n,m,m'} V^{\alpha,m}_{m',n} P_{m,\gamma} P_{n,m'} \\
&\quad - \sum_j V^{\alpha,j}_{j,\gamma} n^e_\gamma n^h_j + \sum_{\substack{j,k \\ k\neq j}} V^{\alpha,j}_{k,\gamma} n^e_\gamma \tilde{P}_{j,k} - \sum_{\substack{j,l \\ l\neq\gamma}} V^{\alpha,j}_{k,l} \bar{P}_{l,\gamma} n^h_j + \sum_{\substack{j,k,l \\ k\neq j, l\neq\gamma}} V^{\alpha,j}_{k,l} \bar{P}_{l,\gamma} \tilde{P}_{j,k} \\
&\quad + \sum_{n,m,m'} V^{n,m}_{m',\gamma} P_{m,n} P_{\alpha,m'} + \sum_j V^{\alpha,j}_{j,\gamma} n^e_\alpha n^h_j - \sum_{\substack{j,k \\ k\neq j}} V^{\alpha,j}_{k,\gamma} n^e_\alpha \tilde{P}_{j,k} + \sum_{\substack{i,j \\ i\neq\alpha}} V^{i,j}_{j,\gamma} \bar{P}_{\alpha,i} n^h_j \\
&\quad - \sum_{\substack{i,j,k \\ i\neq\alpha, k\neq j}} V^{i,j}_{k,\gamma} \bar{P}_{\alpha,i} \tilde{P}_{j,k} + i\hbar \left.\frac{\partial \tilde{P}_{\alpha,\gamma}}{\partial t}\right|_{scatt} . \qquad \text{(B.3.82)}
\end{aligned}
$$

B.4 Populations

B.4.1 Electron: n^e_α

$\underline{n^e_\alpha = \langle a^\dagger_\alpha a_\alpha \rangle}$:

$$\begin{aligned}\frac{\partial n^e_\alpha}{\partial t} &= -\frac{i}{\hbar}\left\langle \left[a^\dagger_\alpha a_\alpha, \hat{H}\right]\right\rangle \\ &= -\frac{i}{\hbar}\left\langle \left[a^\dagger_\alpha a_\alpha, \hat{H}_0\right] + \left[a^\dagger_\alpha a_\alpha, \hat{H}_{c-f}\right] + \left[a^\dagger_\alpha a_\alpha, \hat{H}_C\right]\right\rangle . \end{aligned} \tag{B.4.83}$$

$\underline{\left[a^\dagger_\alpha a_\alpha, \hat{H}_0\right]}$:

$$\left[a^\dagger_\alpha a_\alpha, \hat{H}_0\right] = a^\dagger_\alpha a_\alpha \hat{H}_0 - \hat{H}_0 a^\dagger_\alpha a_\alpha = A_1 - A_2 . \tag{B.4.84}$$

$$\begin{aligned} A_1 &= a^\dagger_\alpha a_\alpha \left(\sum_n \epsilon_n a^\dagger_n a_n + \sum_m \epsilon_m b^\dagger_m b_m\right) \\ &= \sum_n \epsilon_n a^\dagger_\alpha \left(\delta_{\alpha,n} - a^\dagger_n a_\alpha\right) a_n + \sum_m \epsilon_m b^\dagger_m b_m a^\dagger_\alpha a_\alpha \\ &= \sum_n \epsilon_n \delta_{\alpha,n} a^\dagger_\alpha a_n - \sum_n \epsilon_n a^\dagger_n \left(\delta_{\alpha,n} - a_n a^\dagger_\alpha\right) a_\alpha + \sum_m \epsilon_m b^\dagger_m b_m a^\dagger_\alpha a_\alpha \\ &= A_2 . \end{aligned} \tag{B.4.85}$$

$$\left[a^\dagger_\alpha a_\alpha, \hat{H}_0\right] = 0 . \tag{B.4.86}$$

$\underline{\left[a^\dagger_\alpha a_\alpha, \hat{H}_{c-f}\right]}$:

We carry over the result from $\bar{P}_{\alpha,\gamma}$ and let $\gamma \to \alpha$

$$\begin{aligned}\left[a^\dagger_\alpha a_\alpha, \hat{H}_{c-f}\right] = \Bigg[&-\sum_n \mu_{\alpha n} a^\dagger_\alpha a_n + \sum_n \mu_{n\alpha} a^\dagger_n a_\alpha \\ &- \sum_m \mu_{\alpha m} a^\dagger_\alpha b^\dagger_m + \sum_m \mu^*_{\alpha m} b_m a_\alpha \Bigg] E(t) . \end{aligned} \tag{B.4.87}$$

$\underline{\left[a^\dagger_\alpha a_\alpha, \hat{H}_C\right]}$:

$$\left[a^\dagger_\alpha a_\alpha, \hat{H}_C\right] = \left[a^\dagger_\alpha a_\alpha, \hat{H}^{ee}_C + \hat{H}^{hh}_C + \hat{H}^{eh}_C\right] . \tag{B.4.88}$$

Again we will make extensive use of the electron-electron polarization result.

$\underline{\left[a^\dagger_\alpha a_\alpha, \hat{H}^{ee}_C\right]}$:

$$\begin{aligned}\left[a^\dagger_\alpha a_\alpha, \hat{H}^{ee}_C\right] &= -\sum_{j,l}\left(V^{\alpha,j}_{\alpha,l} - V^{j,\alpha}_{\alpha,l}\right) a^\dagger_j a_l - \frac{1}{2}\sum_{i,j,l}\left(V^{i,j}_{l,\alpha} - V^{i,j}_{\alpha,l}\right) a^\dagger_i a^\dagger_j a_l a_\alpha \\ &\quad -\frac{1}{2}\sum_{j,k,l}\left(V^{\alpha,j}_{k,l} - V^{j,\alpha}_{k,l}\right) a^\dagger_j a_k a_l a^\dagger_\alpha \ . \qquad \text{(B.4.89)}\end{aligned}$$

$\underline{\left[a^\dagger_\alpha a_\alpha, \hat{H}^{hh}_C\right]}$:

$$\left[a^\dagger_\alpha a_\alpha, \hat{H}^{hh}_C\right] = 0\,. \qquad \text{(B.4.90)}$$

$\underline{\left[a^\dagger_\alpha a_\alpha, \hat{H}^{eh}_C\right]}$:

$$\begin{aligned}\left[a^\dagger_\gamma a_\alpha, \hat{H}^{eh}_C\right] &= -\sum_{j,k} V^{\alpha,j}_{k,\alpha} b^\dagger_j b_k + \sum_{j,k,l} V^{\alpha,j}_{k,l} b^\dagger_j b_k a_l a^\dagger_\alpha + \sum_{i,j,k} V^{i,j}_{k,\alpha} a^\dagger_i b^\dagger_j b_k a_\alpha \\ &= -\sum_{j,k,l} V^{\alpha,j}_{k,l} b^\dagger_j b_k a^\dagger_\alpha a_l + \sum_{i,j,k} V^{i,j}_{k,\alpha} a^\dagger_i b^\dagger_j b_k a_\alpha\,. \qquad \text{(B.4.91)}\end{aligned}$$

The general expression for n^e_α is then

$$\begin{aligned}i\hbar\frac{\partial n^e_\alpha}{\partial t} &= \left[-\sum_n \mu_{\alpha n}\langle a^\dagger_\alpha a_n\rangle + \sum_n \mu_{n\alpha}\langle a^\dagger_n a_\alpha\rangle\right. \\ &\quad \left. -\sum_m \mu_{\alpha m}\langle a^\dagger_\alpha b^\dagger_m\rangle + \sum_m \mu^*_{\alpha m}\langle b_m a_\alpha\rangle\right] E(t) \\ &\quad -\sum_{j,l}\left(V^{\alpha,j}_{\alpha,l} - V^{j,\alpha}_{\alpha,l}\right)\langle a^\dagger_j a_l\rangle - \frac{1}{2}\sum_{i,j,l}\left(V^{i,j}_{l,\alpha} - V^{i,j}_{\alpha,l}\right)\langle a^\dagger_i a^\dagger_j a_l a_\alpha\rangle \\ &\quad -\frac{1}{2}\sum_{j,k,l}\left(V^{\alpha,j}_{k,l} - V^{j,\alpha}_{k,l}\right)\langle a^\dagger_j a_k a_l a^\dagger_\alpha\rangle \\ &\quad -\sum_{j,k,l} V^{\alpha,j}_{k,l}\langle b^\dagger_j b_k a^\dagger_\alpha a_l\rangle + \sum_{i,j,k} V^{i,j}_{k,\alpha}\langle a^\dagger_i b^\dagger_j b_k a_\alpha\rangle\,. \qquad \text{(B.4.92)}\end{aligned}$$

Hartree-Fock limit

$\underline{\langle\left[a^\dagger_\alpha a_\alpha, \hat{H}^{ee}_C\right]\rangle_{HF}}$:

$$\begin{aligned}&-\sum_{j,l}\left(V^{\alpha,j}_{\alpha,l} - V^{j,\alpha}_{\alpha,l}\right)\langle a^\dagger_j a_l\rangle - \frac{1}{2}\sum_{i,j,l}\left(V^{i,j}_{l,\alpha} - V^{i,j}_{\alpha,l}\right)\langle a^\dagger_i a^\dagger_j a_l a_\alpha\rangle \\ &-\frac{1}{2}\sum_{j,k,l}\left(V^{\alpha,j}_{k,l} - V^{j,\alpha}_{k,l}\right)\langle a^\dagger_j a_k a_l a^\dagger_\alpha\rangle \simeq : \qquad \text{(B.4.93)}\end{aligned}$$

$$\begin{aligned}
&\simeq -\sum_{j,l}\left(V^{\alpha,j}_{\alpha,l}-V^{j,\alpha}_{\alpha,l}\right)\langle a^\dagger_j a_l\rangle-\frac{1}{2}\sum_{i,j,l}\left(V^{i,j}_{l,\alpha}-V^{i,j}_{\alpha,l}\right)\left(\langle a^\dagger_i a_\alpha\rangle\langle a^\dagger_j a_l\rangle-\langle a^\dagger_i a_l\rangle\langle a^\dagger_j a_\alpha\rangle\right)\\
&\quad -\frac{1}{2}\sum_{j,k,l}\left(V^{\alpha,j}_{k,l}-V^{j,\alpha}_{k,l}\right)\left(\langle a^\dagger_j a_k\rangle\langle a_l a^\dagger_\alpha\rangle-\langle a^\dagger_j a_l\rangle\langle a_k a^\dagger_\alpha\rangle\right)\\
&= -\sum_{i,j,l}\left(V^{i,j}_{l,\alpha}-V^{i,j}_{\alpha,l}\right)\langle a^\dagger_i a_\alpha\rangle\langle a^\dagger_j a_l\rangle+\sum_{j,k,l}\left(V^{\alpha,j}_{k,l}-V^{j,\alpha}_{k,l}\right)\langle a^\dagger_j a_k\rangle\langle a^\dagger_\alpha a_l\rangle\,. \qquad \text{(B.4.94)}
\end{aligned}$$

$\underline{\langle\left[a^\dagger_\alpha a_\alpha,\hat{H}^{eh}_C\right]\rangle_{HF}}$:

$$-\sum_{j,k,l}V^{\alpha,j}_{k,l}\langle b^\dagger_j b_k a^\dagger_\alpha a_l\rangle+\sum_{i,j,k}V^{i,j}_{k,\alpha}\langle a^\dagger_i b^\dagger_j b_k a_\alpha\rangle\simeq: \qquad \text{(B.4.95)}$$

$$\begin{aligned}
&\simeq -\sum_{j,k,l}V^{\alpha,j}_{k,l}\left(\langle b^\dagger_j b_k\rangle\langle a^\dagger_\alpha a_l\rangle-\langle b^\dagger_j a^\dagger_\alpha\rangle\langle b_k a_l\rangle\right)\\
&\quad +\sum_{i,j,k}V^{i,j}_{k,\alpha}\left(\langle a^\dagger_i b^\dagger_j\rangle\langle b_k a_\alpha\rangle+\langle a^\dagger_i a_\alpha\rangle\langle b^\dagger_j b_k\rangle\right)\,. \qquad \text{(B.4.96)}
\end{aligned}$$

We end up with

$$\begin{aligned}
i\hbar\frac{\partial n^e_\alpha}{\partial t} &= \Bigg[-\sum_n\mu_{\alpha n}\langle a^\dagger_\alpha a_n\rangle+\sum_n\mu_{n\alpha}\langle a^\dagger_n a_\alpha\rangle\\
&\quad -\sum_m\mu_{\alpha m}\langle a^\dagger_\alpha b^\dagger_m\rangle+\sum_m\mu^*_{\alpha m}\langle b_m a_\alpha\rangle\Bigg]E(t)\\
&\quad -\sum_{i,j,l}\left(V^{i,j}_{l,\alpha}-V^{i,j}_{\alpha,l}\right)\langle a^\dagger_i a_\alpha\rangle\langle a^\dagger_j a_l\rangle+\sum_{j,k,l}\left(V^{\alpha,j}_{k,l}-V^{j,\alpha}_{k,l}\right)\langle a^\dagger_j a_k\rangle\langle a^\dagger_\alpha a_l\rangle\\
&\quad -\sum_{j,k,l}V^{\alpha,j}_{k,l}\left(\langle b^\dagger_j b_k\rangle\langle a^\dagger_\alpha a_l\rangle-\langle b^\dagger_j a^\dagger_\alpha\rangle\langle b_k a_l\rangle\right)\\
&\quad +\sum_{i,j,k}V^{i,j}_{k,\alpha}\left(\langle a^\dagger_i b^\dagger_j\rangle\langle b_k a_\alpha\rangle+\langle a^\dagger_i a_\alpha\rangle\langle b^\dagger_j b_k\rangle\right)\\
&\quad +i\hbar\left.\frac{\partial n^e_\alpha}{\partial t}\right|_{scatt}\,, \qquad \text{(B.4.97)}
\end{aligned}$$

which can be put in the following form

$$
\begin{aligned}
i\hbar\frac{\partial n_\alpha^e}{\partial t} \;=\; & \Bigg[-\sum_{n\neq\alpha}\mu_{\alpha n}\bar{P}_{n,\alpha}+\sum_{n\neq\alpha}\mu_{n\alpha}\bar{P}_{\alpha,n} \\
& -\sum_{m}\mu_{\alpha m}P_{m,\alpha}+\sum_{m}\mu^*_{\alpha m}P_{\alpha,m}\Bigg]E(t) \\
& -\sum_{j}\left(V^{\alpha,j}_{j,\alpha}-V^{\alpha,j}_{\alpha,j}\right)n^e_\alpha n^e_j-\sum_{\substack{j,l\\ l\neq j}}\left(V^{\alpha,j}_{l,\alpha}-V^{\alpha,j}_{\alpha,l}\right)n^e_\alpha\bar{P}_{l,j}-\sum_{\substack{i,j\\ i\neq\alpha}}\left(V^{i,j}_{j,\alpha}-V^{i,j}_{\alpha,j}\right)\bar{P}_{\alpha,i}n^e_j \\
& -\sum_{\substack{i,j,l\\ i\neq\alpha,l\neq j}}\left(V^{i,j}_{l,\alpha}-V^{i,j}_{\alpha,l}\right)\bar{P}_{\alpha,i}\bar{P}_{l,j}+\sum_{j}\left(V^{\alpha,j}_{j,\alpha}-V^{j,\alpha}_{j,\alpha}\right)n^e_\alpha n^e_j+\sum_{\substack{j,k\\ k\neq j}}\left(V^{\alpha,j}_{k,\alpha}-V^{j,\alpha}_{k,\alpha}\right)n^e_\alpha\bar{P}_{k,j} \\
& +\sum_{\substack{j,l\\ l\neq\alpha}}\left(V^{\alpha,j}_{j,l}-V^{j,\alpha}_{j,l}\right)\bar{P}_{l,\alpha}n^e_j+\sum_{\substack{j,k,l\\ l\neq\alpha,k\neq j}}\left(V^{\alpha,j}_{k,l}-V^{j,\alpha}_{k,l}\right)\bar{P}_{l,\alpha}\bar{P}_{k,j} \\
& -\sum_{j}V^{\alpha,j}_{j,\alpha}n^e_\alpha n^h_j+\sum_{\substack{j,k\\ k\neq j}}V^{\alpha,j}_{k,\alpha}n^e_\alpha\tilde{P}_{j,k}-\sum_{\substack{j,k\\ l\neq\alpha}}V^{\alpha,j}_{j,l}\bar{P}_{l,\alpha}n^h_j+\sum_{\substack{j,k,l\\ k\neq jl\neq\alpha}}V^{\alpha,j}_{k,l}\bar{P}_{l,\alpha}\tilde{P}_{j,k} \\
& -\sum_{n,m,m'}V^{\alpha,m}_{m',n}P_{m,\alpha}P_{n,m'}+\sum_{n,m,m'}V^{n,m}_{m',\alpha}P_{m,n}P_{\alpha,m'}+\sum_{j}V^{\alpha,j}_{j,\alpha}n^e_\alpha n^h_j-\sum_{\substack{j,k\\ k\neq j}}V^{\alpha,j}_{k,\alpha}n^e_\alpha\tilde{P}_{j,k} \\
& +\sum_{i,ji\neq\alpha}V^{i,j}_{j,\alpha}\bar{P}_{\alpha,i}n^h_j-\sum_{\substack{i,j,k\\ i\neq\alpha,k\neq j}}V^{i,j}_{k,\alpha}\bar{P}_{\alpha,i}\tilde{P}_{j,k}+i\hbar\left.\frac{\partial n^e_\alpha}{\partial t}\right|_{scatt}. \qquad \text{(B.4.98)}
\end{aligned}
$$

Terms involving n^e_α cancel each other

$$
\begin{aligned}
i\hbar\frac{\partial n_\alpha^e}{\partial t} \;=\; & \Bigg[-\sum_{n\neq\alpha}\mu_{\alpha n}\bar{P}_{n,\alpha}+\sum_{n\neq\alpha}\mu_{n\alpha}\bar{P}_{\alpha,n} \\
& -\sum_{m}\mu_{\alpha m}P_{m,\alpha}+\sum_{m}\mu^*_{\alpha m}P_{\alpha,m}\Bigg]E(t) \\
& -\sum_{\substack{i,j\\ i\neq\alpha}}\left(V^{i,j}_{j,\alpha}-V^{i,j}_{\alpha,j}\right)\bar{P}_{\alpha,i}n^e_j+\sum_{\substack{j,l\\ l\neq\alpha}}\left(V^{\alpha,j}_{j,l}-V^{j,\alpha}_{j,l}\right)\bar{P}_{l,\alpha}n^e_j \\
& -\sum_{\substack{i,j,l\\ i\neq\alpha,l\neq j}}\left(V^{i,j}_{l,\alpha}-V^{i,j}_{\alpha,l}\right)\bar{P}_{\alpha,i}\bar{P}_{l,j}+\sum_{\substack{j,k,l\\ l\neq\alpha,k\neq j}}\left(V^{\alpha,j}_{k,l}-V^{j,\alpha}_{k,l}\right)\bar{P}_{l,\alpha}\bar{P}_{k,j} \\
& -\sum_{\substack{j,k\\ l\neq\alpha}}V^{\alpha,j}_{j,l}\bar{P}_{l,\alpha}n^h_j+\sum_{\substack{j,k,l\\ k\neq jl\neq\alpha}}V^{\alpha,j}_{k,l}\bar{P}_{l,\alpha}\tilde{P}_{j,k}-\sum_{n,m,m'}V^{\alpha,m}_{m',n}P_{m,\alpha}P_{n,m'} \\
& +\sum_{i,ji\neq\alpha}V^{i,j}_{j,\alpha}\bar{P}_{\alpha,i}n^h_j-\sum_{\substack{i,j,k\\ i\neq\alpha,k\neq j}}V^{i,j}_{k,\alpha}\bar{P}_{\alpha,i}\tilde{P}_{j,k}+\sum_{n,m,m'}V^{n,m}_{m',\alpha}P_{m,n}P_{\alpha,m'} \\
& +i\hbar\left.\frac{\partial n^e_\alpha}{\partial t}\right|_{scatt}. \qquad \text{(B.4.99)}
\end{aligned}
$$

B.4.2 Hole: n^h_β

$\underline{n^h_\beta = \langle b^\dagger_\beta b_\beta \rangle}$:

$$\begin{aligned}\frac{\partial n^h_\beta}{\partial t} &= -\frac{i}{\hbar}\left\langle \left[b^\dagger_\beta b_\beta, \hat{H} \right] \right\rangle \\ &= -\frac{i}{\hbar}\left\langle \left[b^\dagger_\beta b_\beta, \hat{H}_0 \right] + \left[b^\dagger_\beta b_\beta, \hat{H}_{c-f} \right] + \left[b^\dagger_\beta b_\beta, \hat{H}_C \right] \right\rangle . \end{aligned} \tag{B.4.100}$$

$\underline{\left[b^\dagger_\beta b_\beta, \hat{H}_0 \right]}$:

$$\left[b^\dagger_\beta b_\beta, \hat{H}_0 \right] = 0 , \tag{B.4.101}$$

which follows from the similar calculation for n^e_α.

$\underline{\left[b^\dagger_\beta b_\beta, \hat{H}_{c-f} \right]}$:

$$\left[b^\dagger_\beta b_\beta, \hat{H}_{c-f} \right] = b^\dagger_\beta b_\beta \hat{H}_{c-f} - \hat{H}_{c-f} b^\dagger_\beta b_\beta = A_1 - A_2 . \tag{B.4.102}$$

$$\begin{aligned} A_1 &= -b^\dagger_\beta b_\beta \left[\sum_{n,n'} \mu_{nn'} a^\dagger_n a_{n'} + \sum_{m,m'} \mu_{mm'} b_m b^\dagger_{m'} \right. \\ &\quad \left. + \sum_{n,m} \left(\mu_{nm} a^\dagger_n b^\dagger_m + \mu^*_{nm} b_m a_n \right) \right] E(t) \\ &= \left[-\sum_{n,n'} \mu_{nn'} a^\dagger_n a_{n'} b^\dagger_\beta b_\beta + \sum_{m,m'} \mu_{mm'} \left(\delta_{\beta,m} - b_m b^\dagger_\beta \right) \left(\delta_{\beta,m'} - b^\dagger_{m'} b_\beta \right) \right. \\ &\quad \left. - \sum_{n,m} \left(\mu_{nm} a^\dagger_n b^\dagger_\beta \left(\delta_{\beta,m} - b^\dagger_m b_\beta \right) + \mu^*_{nm} \left(\delta_{\beta,m} - b_m b^\dagger_\beta \right) a_n b_\beta \right) \right] E(t) \\ &= \left[-\sum_{n,n'} \mu_{nn'} a^\dagger_n a_{n'} b^\dagger_\beta b_\beta + \sum_{m,m'} \mu_{mm'} \delta_{\beta,m} \delta_{\beta,m'} - \sum_{m,m'} \mu_{mm'} \delta_{\beta,m} b^\dagger_{m'} b_\beta \right. \\ &\quad - \sum_{m,m'} \mu_{mm'} \delta_{\beta,m'} b_m b^\dagger_\beta + \sum_{m,m'} \mu_{mm'} b_m b^\dagger_\beta b^\dagger_{m'} b_\beta - \sum_{n,m} \mu_{nm} \delta_{\beta,m} a^\dagger_n b^\dagger_\beta \\ &\quad \left. + \sum_{n,m} \mu_{nm} a^\dagger_n b^\dagger_\beta b^\dagger_m b_\beta - \sum_{n,m} \mu^*_{nm} \delta_{\beta,m} a_n b_\beta + \sum_{n,m} \mu^*_{nm} b_m b^\dagger_\beta a_n b_\beta \right] E(t) \\ &= \left[-\sum_{m'} \mu_{\beta m'} b^\dagger_{m'} b_\beta - \sum_{m} \mu_{m\beta} b_m b^\dagger_\beta \right. \\ &\quad \left. - \sum_{n} \mu_{n\beta} a^\dagger_n b^\dagger_\beta - \sum_{n} \mu^*_{n\beta} a_n b_\beta \right] E(t) + A_2 . \end{aligned} \tag{B.4.103}$$

$$\left[b_\beta^\dagger b_\beta, \hat{H}_{c-f}\right] = \left[-\sum_{m\neq\beta}\mu_{\beta m} b_m^\dagger b_\beta + \sum_{m\neq\beta}\mu_{m\beta} b_\beta^\dagger b_m - \sum_n \mu_{n\beta} a_n^\dagger b_\beta^\dagger + \sum_n \mu_{n\beta}^* b_\beta a_n\right] E(t)\,. \tag{B.4.104}$$

$\underline{\left[b_\beta^\dagger b_\beta, \hat{H}_C\right]}$:

$$\left[b_\beta^\dagger b_\beta, \hat{H}_C\right] = \left[b_\beta^\dagger b_\beta, \hat{H}_C^{ee} + \hat{H}_C^{hh} + \hat{H}_C^{eh}\right]. \tag{B.4.105}$$

$\underline{\left[b_\beta^\dagger b_\beta, \hat{H}_C^{ee}\right]}$:

$$\left[b_\beta^\dagger b_\beta, \hat{H}_C^{ee}\right] = 0\,. \tag{B.4.106}$$

$\underline{\left[b_\beta^\dagger b_\beta, \hat{H}_C^{hh}\right]}$:

$$\left[b_\beta^\dagger b_\beta, \hat{H}_C^{hh}\right] = -\sum_{j,l}\left(V_{\beta,l}^{\beta,j} - V_{\beta,l}^{j,\beta}\right) b_j^\dagger b_l - \frac{1}{2}\sum_{i,j,l}\left(V_{l,\beta}^{i,j} - V_{\beta,l}^{i,j}\right) b_i^\dagger b_j^\dagger b_l b_\beta - \frac{1}{2}\sum_{j,k,l}\left(V_{k,l}^{\beta,j} - V_{k,l}^{j,\beta}\right) b_j^\dagger b_k b_l b_\beta^\dagger\ . \tag{B.4.107}$$

$\underline{\left[b_\beta^\dagger b_\beta, \hat{H}_C^{eh}\right]}$:

$$\left[b_\beta^\dagger b_\beta, \hat{H}_C^{eh}\right] = = b_\beta^\dagger b_\beta \hat{H}_C^{eh} - \hat{H}_C^{eh} b_\beta^\dagger b_\beta = A_1 - A_2\,. \tag{B.4.108}$$

$$
\begin{aligned}
A_1 &= b^\dagger_\beta b_\beta \left(- \sum_{i,j,k,l} V^{ij}_{kl} a^\dagger_i b^\dagger_j b_k a_l \right) = - \sum_{i,j,k,l} V^{ij}_{kl} b^\dagger_\beta b_\beta a^\dagger_i b^\dagger_j b_k a_l \\
&= - \sum_{i,j,k,l} V^{ij}_{kl} a^\dagger_i b^\dagger_\beta \left(\delta_{\beta,j} - b^\dagger_j b_\beta \right) b_k a_l \\
&= - \sum_{i,j,k,l} V^{ij}_{kl} \delta_{\beta,j} a^\dagger_i \left(\delta_{\beta,k} - b_k b^\dagger_\beta \right) a_l + \sum_{i,j,k,l} V^{ij}_{kl} a^\dagger_i b^\dagger_\beta b^\dagger_j b_\beta b_k a_l \\
&= - \sum_{i,j,k,l} V^{ij}_{kl} \delta_{\beta,j} \delta_{\beta,k} a^\dagger_i a_l + \sum_{i,j,k,l} V^{ij}_{kl} \delta_{\beta,j} a^\dagger_i b_k b^\dagger_\beta a_l \\
&\quad - \sum_{i,j,k,l} V^{ij}_{kl} a^\dagger_i b^\dagger_j \left(\delta_{\beta,k} - b_k b^\dagger_\beta \right) a_l b_\beta \\
&= - \sum_{i,l} V^{i,\beta}_{\beta,l} a^\dagger_i a_l + \sum_{i,k,l} V^{i,\beta}_{k,l} a^\dagger_i b_k b^\dagger_\beta a_l - \sum_{i,j,l} V^{i,j}_{\beta,l} a^\dagger_i b^\dagger_j a_l b_\beta \\
&\quad - \sum_{i,j,k,l} V^{ij}_{kl} a^\dagger_i b^\dagger_j b_k a_l b^\dagger_\beta b_\beta \\
&= - \sum_{i,k,l} V^{i,\beta}_{k,l} a^\dagger_i b^\dagger_\beta b_k a_l - \sum_{i,j,l} V^{i,j}_{\beta,l} a^\dagger_i b^\dagger_j a_l b_\beta + A_2 \,. \qquad \text{(B.4.109)}
\end{aligned}
$$

$$
\left[b^\dagger_\beta b_\beta, \hat{H}^{eh}_C \right] = - \sum_{i,k,l} V^{i,\beta}_{k,l} a^\dagger_i b^\dagger_\beta b_k a_l - \sum_{i,j,l} V^{i,j}_{\beta,l} a^\dagger_i b^\dagger_j a_l b_\beta \,. \qquad \text{(B.4.110)}
$$

All in all we get

$$
\begin{aligned}
i\hbar \frac{\partial n^h_\beta}{\partial t} &= \Bigg[- \sum_{m \neq \beta} \mu_{\beta m} \langle b^\dagger_m b_\beta \rangle + \sum_{m \neq \beta} \mu_{m\beta} \langle b^\dagger_\beta b_m \rangle \\
&\quad - \sum_n \mu_{n\beta} \langle a^\dagger_n b^\dagger_\beta \rangle + \sum_n \mu^*_{n\beta} \langle b_\beta a_n \rangle \Bigg] E(t) \\
&\quad - \sum_{j,l} \left(V^{\beta,j}_{\beta,l} - V^{j,\beta}_{\beta,l} \right) \langle b^\dagger_j b_l \rangle - \frac{1}{2} \sum_{i,j,l} \left(V^{i,j}_{l,\beta} - V^{i,j}_{\beta,l} \right) \langle b^\dagger_i b^\dagger_j b_l b_\beta \rangle \\
&\quad - \frac{1}{2} \sum_{j,k,l} \left(V^{\beta,j}_{k,l} - V^{j,\beta}_{k,l} \right) \langle b^\dagger_j b_k b_l b^\dagger_\beta \rangle \\
&\quad - \sum_{i,k,l} V^{i,\beta}_{k,l} \langle a^\dagger_i b^\dagger_\beta b_k a_l \rangle - \sum_{i,j,l} V^{i,j}_{\beta,l} \langle a^\dagger_i b^\dagger_j a_l b_\beta \rangle \,. \qquad \text{(B.4.111)}
\end{aligned}
$$

Hartree-Fock limit

$\underline{\langle\left[b_\beta^\dagger b_\beta, \hat{H}_C^{hh}\right]\rangle_{HF}}$:

$$-\sum_{j,l}\left(V_{\beta,l}^{\beta,j}-V_{\beta,l}^{j,\beta}\right)\langle b_j^\dagger b_l\rangle-\frac{1}{2}\sum_{i,j,l}\left(V_{l,\beta}^{i,j}-V_{\beta,l}^{i,j}\right)\langle b_i^\dagger b_j^\dagger b_l b_\beta\rangle$$
$$-\frac{1}{2}\sum_{j,k,l}\left(V_{k,l}^{\beta,j}-V_{k,l}^{j,\beta}\right)\langle b_j^\dagger b_k b_l b_\beta^\dagger\,\rangle\simeq: \tag{B.4.112}$$

$$\begin{aligned}\simeq\;& -\sum_{j,l}\left(V_{\beta,l}^{\beta,j}-V_{\beta,l}^{j,\beta}\right)\langle b_j^\dagger b_l\rangle-\frac{1}{2}\sum_{i,j,l}\left(V_{l,\beta}^{i,j}-V_{\beta,l}^{i,j}\right)\left(\langle b_i^\dagger b_\beta\rangle\langle b_j^\dagger b_l\rangle-\langle b_i^\dagger b_l\rangle\langle b_j^\dagger b_\beta\rangle\right)\\ &-\frac{1}{2}\sum_{j,k,l}\left(V_{k,l}^{\beta,j}-V_{k,l}^{j,\beta}\right)\left(\langle b_j^\dagger b_k\rangle\langle b_l b_\beta^\dagger\rangle-\langle b_j^\dagger b_l\rangle\langle b_k b_\beta^\dagger\rangle\right)\\ =\;& -\sum_{i,j,l}\left(V_{l,\beta}^{i,j}-V_{\beta,l}^{i,j}\right)\langle b_i^\dagger b_\beta\rangle\langle b_j^\dagger b_l\rangle\\ &+\sum_{j,k,l}\left(V_{k,l}^{\beta,j}-V_{k,l}^{j,\beta}\right)\langle b_j^\dagger b_k\rangle\langle b_\beta^\dagger b_l\rangle\,.\end{aligned} \tag{B.4.113}$$

$\underline{\langle\left[b_\beta^\dagger b_\beta, \hat{H}_C^{eh}\right]\rangle_{HF}}$:

$$-\sum_{i,k,l}V_{k,l}^{i,\beta}\langle a_i^\dagger b_\beta^\dagger b_k a_l\rangle-\sum_{i,j,l}V_{\beta,l}^{i,j}\langle a_i^\dagger b_j^\dagger a_l b_\beta\rangle\simeq: \tag{B.4.114}$$

$$\begin{aligned}\simeq\;& -\sum_{i,k,l}V_{k,l}^{i,\beta}\left(\langle a_i^\dagger b_\beta^\dagger\rangle\langle b_k a_l\rangle+\langle a_i^\dagger a_l\rangle\langle b_\beta^\dagger b_k\rangle\right)\\ &-\sum_{i,j,l}V_{\beta,l}^{i,j}\left(\langle a_i^\dagger b_j^\dagger\rangle\langle a_l b_\beta\rangle-\langle a_i^\dagger a_l\rangle\langle b_j^\dagger b_\beta\rangle\right)\\ =\;& -\sum_{i,k,l}V_{k,l}^{i,\beta}\left(\langle a_i^\dagger b_\beta^\dagger\rangle\langle b_k a_l\rangle+\langle a_i^\dagger a_l\rangle\langle b_\beta^\dagger b_k\rangle\right)\\ &+\sum_{i,j,l}V_{\beta,l}^{i,j}\left(\langle a_i^\dagger b_j^\dagger\rangle\langle b_\beta a_l\rangle+\langle a_i^\dagger a_l\rangle\langle b_j^\dagger b_\beta\rangle\right)\,.\end{aligned} \tag{B.4.115}$$

The full expression in the Hartree-Fock limit thus becomes

$$
\begin{aligned}
i\hbar\frac{\partial n^h_\beta}{\partial t} &= \Bigg[-\sum_{m\neq\beta}\mu_{\beta m}\langle b^\dagger_m b_\beta\rangle+\sum_{m\neq\beta}\mu_{m\beta}\langle b^\dagger_\beta b_m\rangle \\
&\quad -\sum_n \mu_{n\beta}\langle a^\dagger_n b^\dagger_\beta\rangle+\sum_n \mu^*_{n\beta}\langle b_\beta a_n\rangle\Bigg]E(t) \\
&\quad -\sum_{i,j,l}\left(V^{i,j}_{l,\beta}-V^{i,j}_{\beta,l}\right)\langle b^\dagger_i b_\beta\rangle\langle b^\dagger_j b_l\rangle+\sum_{j,k,l}\left(V^{\beta,j}_{k,l}-V^{j,\beta}_{k,l}\right)\langle b^\dagger_j b_k\rangle\langle b^\dagger_\beta b_l\rangle \\
&\quad -\sum_{i,k,l}V^{i,\beta}_{k,l}\left(a^\dagger_i b^\dagger_\beta\rangle\langle b_k a_l\rangle+\langle a^\dagger_i a_l\rangle\langle b^\dagger_\beta b_k\rangle\right) \\
&\quad +\sum_{i,j,l}V^{i,j}_{\beta,l}\left(\langle a^\dagger_i b^\dagger_j\rangle\langle b_\beta a_l\rangle+\langle a^\dagger_i a_l\rangle\langle b^\dagger_j b_\beta\rangle\right) \\
&\quad +i\hbar\left.\frac{\partial n^h_\beta}{\partial t}\right|_{scatt}. \qquad \text{(B.4.116)}
\end{aligned}
$$

In terms of polarizations and populations:

$$
\begin{aligned}
i\hbar\frac{\partial n^h_\beta}{\partial t} &= \left[\sum_{m\neq\beta}\mu_{\beta m}\tilde{P}_{m,\beta}-\sum_{m\neq\beta}\mu_{m\beta}\tilde{P}_{\beta,m}-\sum_n\mu_{n\beta}P_{\beta,n}+\sum_n\mu^*_{n\beta}P_{n,\beta}\right]E(t) \\
&\quad -\sum_j\left(V^{\beta,j}_{j,\beta}-V^{\beta,j}_{\beta,j}\right)n^h_\beta n^h_j+\sum_{\substack{i,j\\ i\neq\beta}}\left(V^{i,j}_{j,\beta}-V^{i,j}_{\beta,j}\right)\tilde{P}_{i,\beta}n^h_j \\
&\quad +\sum_{\substack{j,l\\ l\neq j}}\left(V^{\beta,j}_{l,\beta}-V^{\beta,j}_{\beta,l}\right)n^h_\beta\tilde{P}_{j,l}-\sum_{\substack{i,j,l\\ i\neq\beta,l\neq j}}\left(V^{i,j}_{l,\beta}-V^{i,j}_{\beta,l}\right)\tilde{P}_{i,\beta}\tilde{P}_{j,l} \\
&\quad +\sum_j\left(V^{\beta,j}_{j,\beta}-V^{j,\beta}_{j,\beta}\right)n^h_\beta n^h_j-\sum_{\substack{j,l\\ l\neq\beta}}\left(V^{\beta,j}_{j,l}-V^{j,\beta}_{j,l}\right)\tilde{P}_{\beta,l}n^h_j \\
&\quad -\sum_{\substack{j,k\\ k\neq j}}\left(V^{\beta,j}_{k,\beta}-V^{j,\beta}_{k,\beta}\right)n^h_\beta\tilde{P}_{j,k}+\sum_{\substack{j,k,l\\ k\neq j,l\neq\beta}}\left(V^{\beta,j}_{k,l}-V^{j,\beta}_{k,l}\right)\tilde{P}_{\beta,l}\tilde{P}_{j,k} \\
&\quad -\sum_{n,n',m}V^{n,\beta}_{m,n'}P_{\beta,n}P_{n',m}-\sum_i V^{i,\beta}_{\beta,i}n^h_\beta n^e_i-\sum_{\substack{i,l\\ l\neq i}}V^{i,\beta}_{\beta,l}n^h_\beta\bar{P}_{l,i} \\
&\quad +\sum_{\substack{i,k\\ k\neq\beta}}V^{i,\beta}_{k,i}\tilde{P}_{\beta,k}n^e_i+\sum_{\substack{i,k,l\\ k\neq\beta,l\neq i}}V^{i,\beta}_{k,l}\tilde{P}_{\beta,k}\bar{P}_{l,i}+\sum_{n,n',m,}V^{n,m}_{\beta,n'}P_{m,n}P_{n',\beta} \\
&\quad +\sum_i V^{i,\beta}_{\beta,i}n^h_\beta n^e_i+\sum_{\substack{i,l\\ l\neq i}}V^{i,\beta}_{\beta,l}n^h_\beta\bar{P}_{l,i}-\sum_{\substack{i,j\\ j\neq\beta}}V^{i,j}_{\beta,i}\tilde{P}_{j,\beta}n^e_i \\
&\quad -\sum_{\substack{i,j,l\\ i\neq\beta,j\neq i}}V^{i,j}_{\beta,l}\tilde{P}_{j,\beta}\bar{P}_{l,i}+i\hbar\left.\frac{\partial n^h_\beta}{\partial t}\right|_{scatt}. \qquad \text{(B.4.117)}
\end{aligned}
$$

Terms involving n^h_β drop out, and we are left with

$$
\begin{aligned}
i\hbar\frac{\partial n^h_\beta}{\partial t} \quad = \quad & \left[\sum_{m\neq\beta}\mu_{\beta m}\tilde{P}_{m,\beta} \; - \sum_{m\neq\beta}\mu_{m\beta}\tilde{P}_{\beta,m}\right. \\
& \left. -\sum_{n}\mu_{n\beta}P_{\beta,n} + \sum_{n}\mu^*_{n\beta}P_{n,\beta}\right] E(t) \\
& + \sum_{\substack{i,j\\ i\neq\beta}}\left(V^{i,j}_{j,\beta} - V^{i,j}_{\beta,j}\right)\tilde{P}_{i,\beta}n^h_j - \sum_{\substack{j,l\\ l\neq\beta}}\left(V^{\beta,j}_{j,l} - V^{j,\beta}_{j,l}\right)\tilde{P}_{\beta,l}n^h_j \\
& - \sum_{\substack{i,j,l\\ i\neq\beta,l\neq j}}\left(V^{i,j}_{l,\beta} - V^{i,j}_{\beta,l}\right)\tilde{P}_{i,\beta}\tilde{P}_{j,l} + \sum_{\substack{j,k,l\\ k\neq j,l\neq\beta}}\left(V^{\beta,j}_{k,l} - V^{j,\beta}_{k,l}\right)\tilde{P}_{\beta,l}\tilde{P}_{j,k} \\
& - \sum_{n,n',m} V^{n,\beta}_{m,n'}P_{\beta,n}P_{n',m} + \sum_{\substack{i,k\\ k\neq\beta}} V^{i,\beta}_{k,i}\tilde{P}_{\beta,k}n^e_i + \sum_{\substack{i,k,l\\ k\neq\beta,l\neq i}} V^{i,\beta}_{k,l}\tilde{P}_{\beta,k}\bar{P}_{l,i} \\
& + \sum_{n,n',m,} V^{n,m}_{\beta,n'}P_{m,n}P_{n',\beta} - \sum_{\substack{i,j\\ j\neq\beta}} V^{i,j}_{\beta,i}\tilde{P}_{j,\beta}n^e_i - \sum_{\substack{i,j,l\\ i\neq\beta,j\neq i}} V^{i,j}_{\beta,l}\tilde{P}_{j,\beta}\bar{P}_{l,i} \\
& + i\hbar\left.\frac{\partial n^h_\beta}{\partial t}\right|_{scatt} . \qquad \text{(B.4.118)}
\end{aligned}
$$

Appendix C

Material parameters

C.1 InAs/GaAs

Parameter	Value
QD material	InAs
Barrier material	GaAs
Kane energy (E_P) InAs	21.5 eV
Dielectric constant (ϵ_r) InAs	14.6
Band gap GaAs (300 K)	1.4225 eV
Band gap InAs (300 K)	0.3543 eV
CBO (ΔE_c)	705 meV
VBO (ΔE_v)	363 meV
m_e^{GaAs}	0.067 m_0
m_{hh}^{GaAs}	0.15 m_0
m_e^{InAs}	0.067 m_0
m_{hh}^{InAs}	0.15 m_0

***Table C.1**: Parameters used for QD modeling. Material parameters are taken from Ref. [90], except the InAs heavy hole mass. According to Ref. [102] the mass is reduced to 0.15 m_0 due to strain. Furthermore we have assumed a 60/40 splitting for the conduction/valence band offset (CBO/VBO).*

C.2 QD and QD array parameters

Parameter	Value
QD radius (r)	9 nm
QD height (h)	3 nm
WL thickness (d)	1.2 nm
Dot density (N_{dot})	$5 \cdot 10^{10}$ cm^{-2}
Thickness of active region (w)	2.5 nm

Table C.2: *Quantum dot and quantum dot array parameters.*

Appendix D

Computational parameters

The wetting layer states are discretized into 100 k-points. The quantum dot contains six states in each band, which means that the density matrix has 212 entries for which only select components are solved.

To solve the differential equation involving the density matrix we use a fourth order Runge-Kutta scheme. The Runge-Kutta method for a differential equation of the type

$$\frac{\partial}{\partial t} f = g[f(t), t]\,, \tag{D.0.1}$$

has the following appearance

$$f_n = f_{n-1} + \frac{h}{6}(k_1 + 2k_2 + 2k_3 + k_4) + O(h^5)\,, \tag{D.0.2}$$

where

$$\begin{aligned} k_1 =& g[f_{n-1}, t_{n-1}] \\ k_2 =& g[f_{n-1} + \frac{h}{2}k_1, t_{n-1} + \frac{h}{2}] \\ k_3 =& g[f_{n-1} + \frac{h}{2}k_2, t_{n-1} + \frac{h}{2}] \\ k_4 =& g[f_{n-1} + hk_3, t_{n-1} + h]\,, \end{aligned}$$

for the time-step size h and $f_n = f(t_n)$.